Study of a non-Galilean Hamiltonian liquid : collective motion without activity

Mathias Casiulis

THÈSE DE DOCTORAT
DE SORBONNE UNIVERSITÉ

Spécialité : Physique

École doctorale n°564: Physique en Île-de-France

réalisée

au Laboratoire de Physique Théorique et de la Matière Condensée

sous la direction de Marco TARZIA & Leticia F. CUGLIANDOLO

présentée par

Mathias Casiulis

pour obtenir le grade de :

DOCTEUR DE SORBONNE UNIVERSITÉ

Sujet de la thèse :

Etude d'un modèle Hamiltonien de liquide non-Galiléen : du mouvement collectif sans activité

soutenue le 21 novembre 2019

devant le jury composé de :

M^{me}	Silke HENKES	Rapporteuse
M.	Peter C. W. HOLDSWORTH	Rapporteur
M.	Eric BERTIN	Examinateur
M.	Florent KRZĄKAŁA	Examinateur
M.	Julien TAILLEUR	Examinateur
M^{me}	Leticia F. CUGLIANDOLO	Co-directrice de thèse
M.	Marco TARZIA	Directeur de thèse
M.	Olivier DAUCHOT	Invité

Acknowledgements

> For once in your life, take a stand with pride! I don't understand how you stand to the side.
>
> Lin Manuel Miranda, *Hamilton: an American musical*

A bit more than three years ago, a few months before deciding on the topic of my thesis, I decided to go on an adventure. I decided to leave the world of experimental physics and try myself at theoretical statistical mechanics, mostly on a whim, because a man in a funny shirt told me about relativistic gnus forming herds at low temperatures. Therefore, I would first like to thank Olivier Dauchot, for leading me to the topic that started as an internship at the Gulliver lab. His undying enthusiasm and curiosity about physics, as well as his candid yet deep look at theory have made every discussion both encouraging and deeply instructional for the last three years. From my time at the Gulliver, I would also like to thank Michael Schindler, who has been both a great help when I started using simulations, and a great colleague with whom I had many fascinating conversations about physics, maths, and life. I would also like to thank Guillaume Briand, Thomas Salez, David Lacoste, and Vincent Démery for their enthusiastic questions on my work, and the directions they suggested.

After this internship, having been forever tainted by statistical physics, I decided to work on the same topic for my PhD thesis. To do so, I turned to two wonderful scientists, colleagues, and now friends, Leticia Cugliandolo and Marco Tarzia, and started working at LPTMC. I would like to thank them for cheerfully accepting to join me on this adventure. They provided me with the tools I needed to write this thesis, gave me directions when I was simply a blunt instrument only fit to be thrown at a problem, and most importantly made my workplace one that was always welcoming, lively – and full of coffee. Without them, I would never have got this far, and I might have lost my taste for research already. From the time I spent at LPTMC, I would also like to thank Jean-Noël Fuchs, Olivier Bénichou, Raphaël Voituriez, Jean-Marc Victor, Maria Barbi, Pascal Viot, Matthieu Micoulaut, Nicolas Sator, Nicolas Dupuis, Matthieu Tissier, Ivan Dornic, Alex Solon, and Hélène Berthoumieux for the insightful discussions we had on my work, and the ideas that stemmed from those. Furthermore, I would like to thank all the external researchers who showed interest for my research and helped me make sense of it, during seminars or summer schools. A probably incomplete list would include Eric Bertin, Jorge Kurchan, Guilhem Semerjian, Francesco Zamponi, Alessandro Manacorda, Yariv Kafri,

Guy Bunin, Dov Levine, Nir Gov, Sam Safran, Julien Tailleur, Piyush Garg, Hayden Nunley, Asaf Miron, Alexis Poncet, Hisao Hayakawa, and Hajime Yoshino.

I would also like to thank all of those who supported me, and cheered me up all the way. These include fellow students, especially Mélody Merle who had to cope with sharing my office, my (many) joys and (few) sorrows, and my addiction to caffeine, but also Antony Lesage, Léopold Carron, Greg Page, and Jean-Baptiste Morlot. In this category, I would also like to thank co-organizers of the "Physics for All" lectures, Tony, Alex and Louis; but also volunteers on the Lutetium Project, Hoon Kwon, Guillaume Durey, Quentin Magdelaine; and private friends – Sam, Saj, Chris, Matthieu, Yquem, Vincent, Clém, Lise, Ben, Ju, Marion, Ori, Lona, Delphine, and many others that I am probably forgetting here. Last but not least, I would like to thank my beloved parents, my wonderful wife, and my stupid cat, who all had to suffer my ramblings, my late nights at the lab and my sometimes low morale.

Finally, I would like to warmly thank all of the members of my jury, for accepting to spend some of their time listening to my PhD project, and in particular my referees, Pr. Peter Holdsworth and Dr. Silke Henkes, who kindly accepted to go through the ordeal of carefully reading this manuscript and thus improving it.

Short Outline

> "Would you tell me, please, which way I ought to go from here?" / "That depends a good deal on where you want to get to," said the Cat.
>
> Lewis Carroll, *Alice in Wonderland*

This thesis is organized as follows. In Chapter I, I recall the state of the art and main results on collective motion, starting from observations in nature and moving on to experiments, then abstract models. I then introduce the conservative model that I study in this thesis, and why it is relevant to the field of collective motion. In Chapter II, I present the concepts of analytical mechanics, statistical mechanics, spin magnetism, and of the physics of liquids that one should be comfortable with in order to fully understand the scope of this thesis. In Chapter III, I discuss the physics of a Hamiltonian liquid of particles that carry unit length vectors (spins), coupled by short-ranged ferromagnetic interactions. In Chapter IV, I add a spin-velocity coupling to the previous model, and discuss the consequences on the phase diagram, including the emergence of spontaneous collective motion at equilibrium, or Hamiltonian flocking. In Chapter V, I present the dynamical properties of Hamiltonian flocks, and I discuss their links with the usual active flocks. Finally, in Chapter VI, I summarise the main results of this thesis and propose directions for future research.

Appendices A, B, C and D respectively present a simple example of a model with a non-quadratic kinetic energy, the detailed calculation of the virial coefficients of the fluid described in Chapter III, the exact computation of the displacement-displacement correlations in a homogeneous rotating disk used in Chapter V, and the derivation of simple hydrodynamic equations describing the model studied in Chapters IV and V.

Contents

Chapter I

Introduction

> Je sais que je ne sais pas ce que je ne sais pas.
>
> Marguerite Yourcenar, *L'Œuvre au noir*

I.1 Collective Motion, a Physicist's View

I.1.1 Collective Motion as Physics?

Systems of many particles have been one of the main concerns of modern physics, since the birth of statistical physics in the late 19th century. The reason behind the interest of such systems is that they often display surprising macroscopic properties, that emerge from the collective ordering of particles at the microscopic scale. Such collective behaviours are notably responsible for phase transitions, the most famous of which are the transitions between the "canonical" phases of matter (gas, liquid, solid) [1]. However, the concepts of collective behaviour and phase transitions go well beyond these well-known examples: they apply to other fields of physics, like the description of magnets [2], or that of molecules that present more complicated phases like liquid crystals and polymers [3, 4], but also beyond physics, to describe the complexity of classes of problems in computer science [5], the evolution of a financial system in econophysics [6, 7], or even the mixing of populations in social systems [8]. In particular, there has been a growing interest in recent years for the phenomenology of collective motion, the spontaneous, macroscopic ordering of the velocities of a system of many particles. Examples that immediately come to mind belong to the natural world: from colonies of bacteria to large human crowds, animals of all sizes form groups that move together. But why should those biological and social systems be of any concern to physicists? After all, living beings look much more complicated to describe with equations than inanimate molecules made of a few atoms, all the more so when they interact with each other according to social rules and biochemical signals. The answer lies in the concept of universality classes: throughout systems that are very different at the microscopic scale, phase transitions can behave in similar ways that mostly depend on the symmetries of the system, and very little on the precise shape of the microscopic

interactions. For instance, a collection of arrows pointing up or down with an aligning interaction, when it magnetises, has the same critical behaviour as an attractive fluid that phase-separates between a liquid and a gas [9]. Therefore, there is hope that the transition from disorderly motion to collective motion might be characterised by universal properties across very different systems, because the symmetries and basic interactions underlying the transition are sufficiently similar. The reason why it is not obvious that this concept of universality applies to systems of collective motion is that most of the systems that feature collective escape the realm of equilibrium physics, so that the usual reasonings based on the minimization of a potential of some kind that roughly retains the same shape across different systems do not apply to them. In fact, most systems that display collective motion are non-equilibrium not only at a macroscopic scale, like a fluid driven by an external force would be, but also at a microscopic scale, since they are able to convert energy into mechanical work at the scale of a single particle, thus making them "active" particles. Furthermore, groups of collectively moving particles like animals are often able to process sensorial information and to react to it, so that their interactions are generically more complicated than physical interactions. There is therefore very little hope that these highly peculiar systems can be grasped using conceptual tools that are usually justified by the existence of underlying conservation rules like the conservation of an energy or of a momentum. Nevertheless, common behaviours between groups of moving animals and physical experiments of collective motion have fostered the hope of discovering universal, non-equilibrium transitions to collective motion; which fueled many studies in the last 25 years. In the rest of this section, I shall briefly review these studies to help uncover the commonalities between collectively moving systems. In order to do so, I classify these studies into three categories. First, I present the main observations of collective motion in living systems. Then, I focus on experiments of collective motion in inanimate systems that were designed to move together. Finally, I briefly present the types of models that have been proposed to describe collective motion from a theoretical point of view.

I.1.2 Collective Motion in Nature

Many studies on collective motion have focused on natural occurrences of collective motion, in groups of animals. These groups can be observed across wildly different time and length scales, ranging from tens of micrometers to tens or even hundreds of meters, and time scales ranging from fractions of a second to several days. For instance, one can think of groups of microswimmers, swarms of insects, herds of Mammals, flocks of birds, schools of fish, human crowds, etc. The most famous and complete example of those is perhaps that of flocks of starlings [10–14]. These birds present several advantages: they spontaneously gather in rather large groups, of sizes typically ranging from a few hundreds to a few thousands, they can be observed with usual cameras, and they move in a low-viscosity fluid (air), in free $3d$ space without interacting with obstacles. They therefore constitute a good model system of collective motion, in which only gravity and internal interactions between birds play a significant role. Using photographs taken from 2 angles and tracking algorithms, experimentalists have been able to reconstruct the position and velocity fields of flocks accurately (see Fig. I.1). From these fields, it is possible to study the properties

of the motion in the flock. One of these properties is the *polarity* Φ of the flock,

$$\Phi \equiv \frac{1}{N}\left|\sum_{i=1}^{N}\frac{\boldsymbol{v}_i}{|\boldsymbol{v}_i|}\right|,$$

that counts how well the velocities $\boldsymbol{v}_i$ are aligned together in a flock of N birds. This polarity is typically very high in flocks, $\Phi \approx 0.9 - 1.0$ [11], revealing that they are very polar objects or, in other words, that birds very effectively align their velocities together. This high degree of alignment prompted studies regarding the fluctuations of the velocities across a flock, and their correlations. If one considers the fluctuations $\delta\boldsymbol{v}$ around the mean velocity of the flock, as in Fig. I.1(*e*), one finds that they are strongly anti-correlated across the flock. The associated correlation function is defined by

$$C(r) = \frac{1}{c_0}\frac{\sum_{i,j=1}^{N}\delta\boldsymbol{v}_i\cdot\delta\boldsymbol{v}_j\delta(\boldsymbol{r}-\boldsymbol{r}_{ij})}{\sum_{i,j=1}^{N}\delta(\boldsymbol{r}-\boldsymbol{r}_{ij})},$$

where the δ function is a smoothed Dirac delta that selects particles separated by a distance close to r, and c_0 is a renormalisation constant which ensures that $C(0) = 1$. One finds that this correlation function does not depend on any microscopic length scale, but simply on the size of the flock: it is a scale-free function [11]. In other words, the plots of C obtained for several flock sizes can be collapsed into one master curve if they are plotted against the distance divided by the linear size of the flock, as in Fig. I.1(*f*), which was adapted from Cavagna *et al.* [11]. That last property is rather unusual in physical systems: one usually expects correlation functions to decrease on a length scale that only depends on the nature of the interactions and the temperature. In the context of birds, several groups were intrigued by the scale-free behaviour of correlations, and proposed that the interactions themselves might be different from the ones that are usually observed in microscopic physical systems. Since birds use visual information to navigate in a flock, it was proposed that the interactions between birds themselves might in fact not decay with a metric distance, but are in fact "topological" interactions, meaning that each bird interacts with its first n (in practice 7) neighbours regardless of the distance to them [13, 15]. Long-range correlations of the velocity fluctuations also led to studies regarding the way in which flocks of birds coherently turn, and select a new direction. These studies showed that the information of the imminent rotation of the velocities propagated through the flock like a wave, leading to fast, coherent turns [14] that happen without the flock breaking up. Other studies of the collective motion of large animals from the perspective of physics (as opposed to behavioural biology) are still rather uncommon, mostly due to the difficulties of observing and measuring their motions in the lab, or in well-controlled environments. Note however that seminal works on the motion of fish, placed in an aquarium and exposed to a school of virtual fish (using virtual reality techniques) [16] might open new perspectives of well-controlled experiments in this field.

Going down a couple of orders of magnitudes in size, quite a few studies have focused on the collective behaviour of flying insects, and in particular of midges [17–22], as they are much easier to observe in a controlled environment. These swarms do not move collectively [17], in the sense that their velocities do not order, but it was shown that

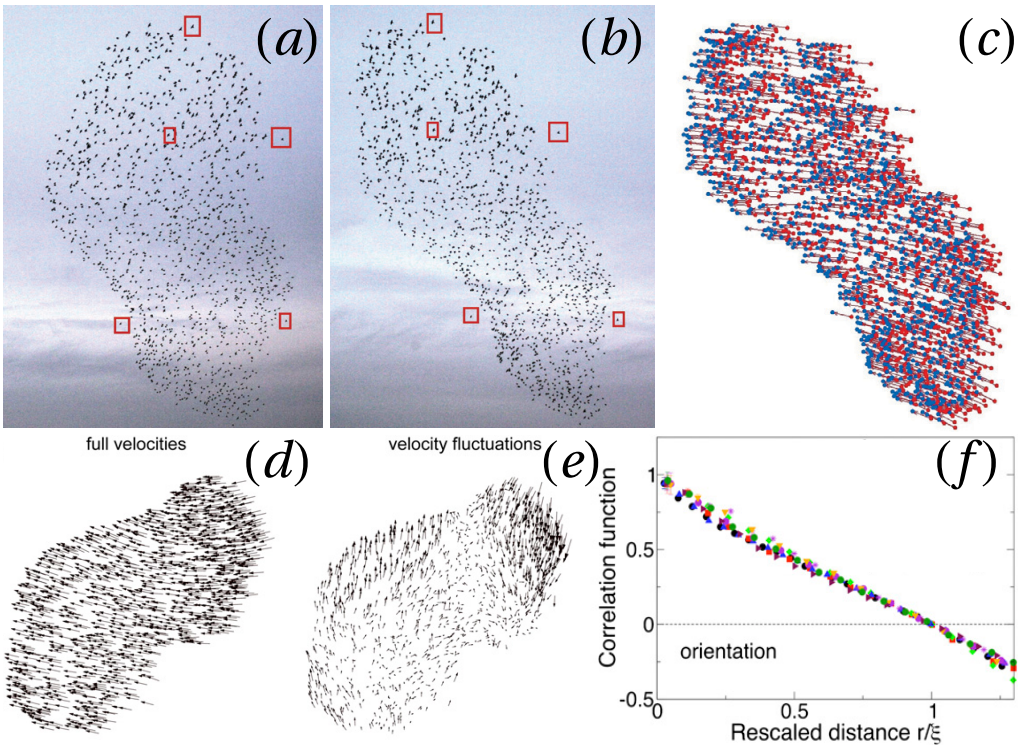

Fig. I.1 **Flocks of Starlings.** $(a-b)$ Example of a flock of starlings, here photographed from two angles taken from Refs. [10, 13] (red boxes indicate the same birds in both pictures). (c) Corresponding velocity field, as retrieved from successive shots using a tracking algorithm. $(d)-(e)$ Full velocities and (rescaled) velocity fluctuations in a flock. (f) Spatial correlation of velocity fluctuations against the distance, for several flocks with different numbers of individuals (in the range $[122; 4268]$), rescaled by a length proportional to the size of the flock. Panels $(d-f)$ were adapted from Ref. [11].

the motion of individual insects is strongly correlated at the scale of the swarm, and that the dynamical correlation functions in these swarms were described by scaling laws reminiscent of magnetic systems near their magnetisation transition [18]. This result prompted research on the nature of interactions between midges, and the reason behind the cohesion of swarms. These interactions were shown to be transported by acoustic waves, so that they are well-described in $3d$ by a gravitation-like interaction [20–22]. While studies also exist on the collective motion and cooperation behaviours of non-flying insects like ants [23] or locusts [24], these often rely on more complicated interactions, that combine visual, tactile, hydrodynamic, chemical, and auditory communication [23], thus making their systematic study much harder.

Finally, most of the experiments on living systems have been performed not with macroscopic animals, but with bacteria [26, 28, 29] (or, recently, microscopic nematods [30]). There are many advantages linked to the choice of bacteria: they are much smaller than birds or insects, so that large groups of individuals can be studied in a lab, the medium that they evolve in can be controlled very precisely, and they are much sim-

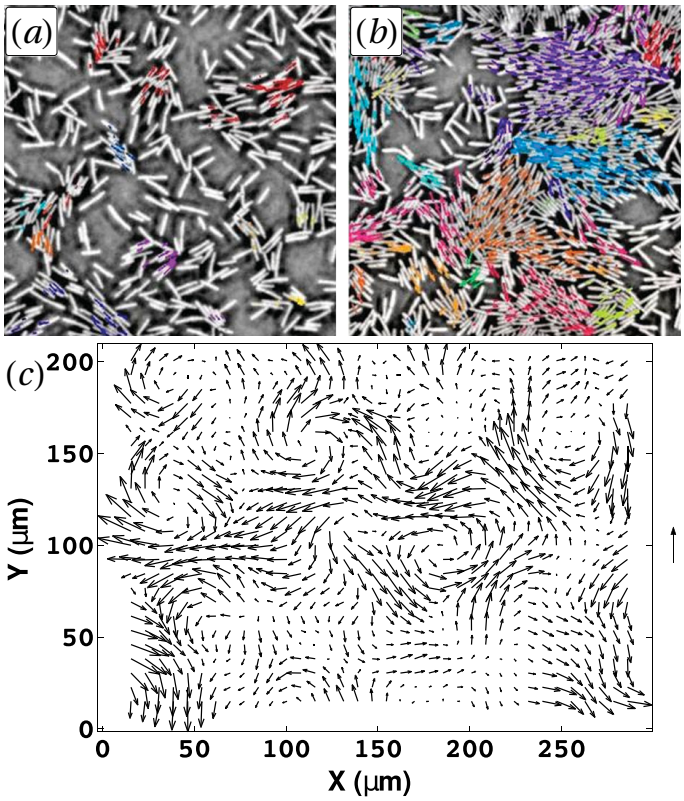

Fig. I.2 **Collective motion of bacteria.** $(a)-(b)$ Velocity fields (coloured arrows) superimposed on snapshots of suspensions of bacteria in the (a) low-, and (b) high-density regimes, adapted from Refs. [25, 26]. The colour of velocity arrows is used to show groups of bacteria moving in the same direction. (c) Larger-scale velocity field of a bacterial suspension, featuring vortex structures. Adapted from Ref. [27].

pler beings so that no visual or auditory processing of information happens. Furthermore, bacteria can be genetically engineered so that they are rigorously identical, and that their functions can be edited *à la carte*. Therefore, one can hope to vary control parameters (like the density of bacteria, or the shape of their environment), while experiments on larger animals are essentially confined to the realm of *observations* of uncontrolled phenomena. The motion of bacteria is generally studied in confined quasi-2d geometries, so that their motion is also easy to track. One can therefore measure the individual displacements of bacteria and draw their velocity fields, like in the example of Fig. I.2$(a)-(b)$, adapted from Refs. [25, 26], which shows typical velocity fields in the low- and high-density regimes of a suspension of *Bacillus Subtilis* bacteria. These pictures show that, at high enough densities, bacteria start moving in groups [25, 31]. Furthermore, most bacteria are shaped like rods and propelled by a flagellum located at one end of the rod, so that their velocities are generally well aligned onto that internal direction, in the same way that the velocity of a bird is generally aligned with their tail-to-head axis. When unzooming and considering larger ensembles of bacteria, the nematic steric interactions between bacteria and the polar propulsion along the axis of the rod lead to vortices in the bacterial flow, as

shown in Fig. I.2(*c*), which was adapted from Dombrowski *et al.* [27]. These spontaneous flows of the bacteria interact non-trivially with the fluid that surrounds them, leading for example to a reduction of its measured viscosity [32, 33]. The understanding of dense bacterial suspensions is therefore made more complicated by the strong hydrodynamical effects in the system. Finally, although bacterial experiments are much more flexible than observations of flocks of birds, they are still marred by flaws that are inherent to living systems. For instance, it is hard to ensure that their environment has a perfectly homogeneous concentration of food and oxygen, or to tune the speed of their propulsion.

I.1.3 Engineered Collective Motion Experiments

As explained above, carrying out experiments with living beings such as birds or bacteria presents a number of drawbacks in the context of physical modelling. The most fundamental of these drawbacks is that interactions between animals are in general very complicated. Indeed, they generally integrate several sensory inputs (visual, auditory, tactile, chemical, ...) when selecting a direction of motion. Even bacteria, that are supposedly well-controlled "particles" to work with, move in response to the concentration of chemicals, the flow of the surrounding fluid, and so on. These interactions are generally hard to model, and sometimes even to tune experimentally. Consequently, there has been significant effort to design non-living experiments of collective motion. To reach this goal, it is important to understand what the minimal ingredients that could lead to collective motion. In living systems, there are three ingredients that seem relevant, although they might not all be necessary. The first ingredient is that each individual particle (animal) is a polar object, with a well-defined front (a head) and rear (a tail) that define a direction in which motion is more likely, or at least more persistent. The second ingredient is that each individual particle is able to transform an internal source of energy (e.g. chemical energy accumulated from meals) into mechanical work, used to move: this is self-propulsion. The third ingredient is that interactions should align the velocities of individual particles together. The experimental challenge is therefore to design polar, self-propelled particles that align their velocities together.

A very natural realisation of such a system is found in the field of swarm robotics. Indeed, one can design robots that are able to move on a $2d$ plane (in a polar direction that is fixed by their design), and that can wirelessly communicate with each other. Then, one can program the robots in such a way that they broadcast their positions and orientations to each other at all times, and code interaction rules. For instance, requiring that robots are repulsive at short-range and should align their velocities together leads to collective motion [34]. While using robotics is a rather easy way out of the living world, this solution is not entirely satisfactory. Indeed, programming velocity-velocity alignment ensures that collective motion can happen, but it is perhaps even more interesting to check whether this alignment can emerge from simpler physical interactions.

Another way to create inanimate collective motion is to use shaken granular matter [35, 36]. The idea is then to create millimetric objects that have an asymmetric contact with the surface below them. An example of a possible design is shown in the inset of Fig. I.3. This design consist of a metallic disk, that is placed on top of a thin metallic foot (white) and a large rubber foot (blue), both shaped so that the grain loses its front-back symmetry but retains a left-right symmetry. It was shown that one of these grains, when

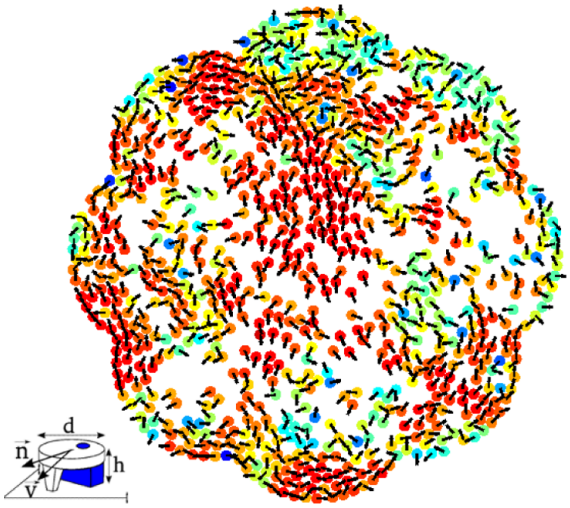

Fig. I.3 **Collective motion in shaken grains.** Inset: A possible design of shaken grains that leads to collective motion. Main panel: experimental realization of a velocity-ordered state. The colour codes for the alignment between the velocities of neighbouring particles (red = perfect alignment, blue = perfect anti-alignment), and the intrinsic polarity of each grain is shown as a black arrow. Figure taken from Deseigne *et al.* [35]

placed on a plate and shaken perfectly vertically, moves persistently along the axis defined by these feet, and randomly turns over time [35]. They are therefore a good effective realisation of polar, self-propelled particles. Furthermore, the interactions between these grains are hardcore exclusions, which were shown to have an aligning effect on the internal polarity of colliding grains [35, 37, 38]. Therefore, this system has all three ingredients needed to display collective motion. Experimental realisations resemble the snapshot shown in Fig. I.3: grains form groups that move together, and also align with walls at the boundaries of the system. Moreover, in the collectively moving regime, the "fluid" of grains is not spatially homogeneous: in fact, it seems to phase separate between low- and high-density regions. This feature is surprising since phase separations are usually expected only in fluids of attractive particles, whereas here the grains are purely repulsive. Even more exotic properties appear at higher densities, when solid phases are expected: instead of crystallising homogeneously, this system was shown to form crystallites that continuously form and dissolve into a fast-moving fluid of self-propelled particles [39]. At yet higher densities, the system eventually forms a single crystal, but with very unusual, synchronised defect dynamics that cause intermittent rotations of the whole system [40]. This experiment therefore sheds light on the fact that self-propelled and aligning polar particles not only feature collective motion, but also very surprising properties in dense phases.

Many other possible realisations of self-propelled, polar particles were proposed in the field of colloids, micrometric particles immersed in a solvent. The most famous example is that of so-called Janus particles, spheres whose surface is divided into two hemispheres that are coated in different chemicals, thereby inducing polarity. Typical examples are polymer spheres with hematite attached on one side [41], or silica spheres coated with

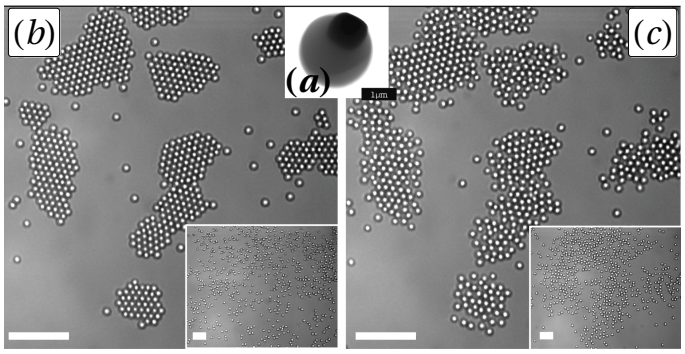

Fig. I.4 **Clusters of Janus Particles.** (a) Scanning electron microscopy picture of a colloidal Janus particle made of a ball of polymer attached to a cube of hematite. (b) Clusters obtained by switching on self-propulsion from a homogeneous configuration, shown in the inset. (c) Effect of switching off self-propulsion in a cluster state: the main panel shows a picture 10s after the switch, and the inset 100s after the switch. The scale bars indicate 10μ m. Figure adapted from Palacci *et al.* [41]

platinum on one side [42, 43]. With these specific choices of coating, these particles can self-propel in the right conditions. For instance, in the case of the $SiO_2 - Pt$ Janus particles, platinum (but not silica) catalyses the dissociation of hydrogen peroxide, H_2O_2, into O_2 and H_2O. As a result, when put into a solution of H_2O_2, $SiO_2 - Pt$ Janus particles develop a gradient of concentration of H_2O_2 around them, which leads to a local difference of osmotic pressure between the platinum and silica side (diffusiophoresis). Consequently, the particles self-propel in the direction of the silica-platinum axis. Other possible designs include polymer spheres with a protruding hematite cube [41] (see Fig. I.4), that also catalyses the $H_2O_2 \rightarrow H_2O + 0.5O_2$ reaction, but this time only when illuminated with blue-violet light, or polystyrene spheres coated on one side with gold, so that a strong temperature gradient develops around the particle when the gold is illuminated with a laser [44], leading to thermophoretic motion. In these cases, self-propulsion is light-activated, so that one can easily compare the passive and self-propelled situations by switching the light on or off. In particular, it was demonstrated that self-propulsion was responsible for the formation of cohesive clusters, that disassemble when the light is turned off (see Fig. I.4). However, such particles generally do not display collectively moving phases, as interactions apparently do not lead to the alignment of their internal polarity. Similar principles of phoretic self-propulsion have led to other related designs, like for instance droplets of water in oil that swim due to an inhomogeneous concentration of surfactants around them [45], or camphor boats moving at the surface of water [46].

Many other designs of self-propelled colloidal objects have been proposed. An interesting example is that of so-called Quincke rollers, or *rolloids*. These colloids are micrometer-sized beads of an insulating material (typically polymer beads). When sedimented in a conducting fluid and subjected to a strong enough vertical electric field, an electrohydrodynamic instability called the Quincke effect causes these colloids to start rolling in a random direction, that carries the horizontal component of their dielectric polarization [47]. These particles are therefore polar, self-propelled particles. Furthermore,

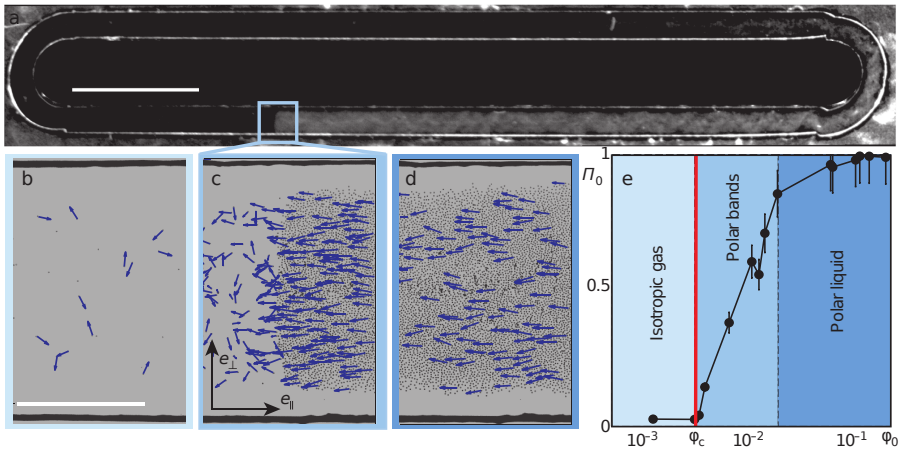

Fig. I.5 **Phases of Quincke rollers.** (*a*) Full experimental system: Quincke rollers are here placed in an oblong arena, and subjected to an electric field perpendicular to the picture. (*b*) – (*d*) Isotropic gas, polar band, and homogeneous polar liquid obtained at low-, intermediate-, and high-densities. The blue arrows represent the velocities of a few particles. (*e*) Polarity of the system versus its density, labeled with the type of phase that is observed at each density. Figure taken from Bricard *et al.* [47]

their polarity is really a dielectric polarity, so that particles are coupled by (aligning) dipolar interactions, in addition to hardcore exclusion and hydrodynamic interactions. As a result, at high enough densities, these particles form collectively moving "flocks", first in the shape of bands that coexist with a low-density gas, then in the shape of a homogeneous polar liquid in collective motion, as shown in Fig. I.5.

Finally, a last family of relevant experiments is the group of so-called "motility assays" [48]. These experiments, taking inspiration from the inner works of living cells, consist in grafting so-called molecular motors to a plane substrate. Molecular motors are biological molecules that can essentially be seen as a pair of arms, with hands at their ends, that can attach specifically to a given biological polymer and exert a force on it. This action comes at the cost of chemical energy, in the form of a reaction that uses ATP, the gasoline of biochemistry. By grafting one arm of these molecular motors on a substrate, one therefore obtains a crowd of upward arms, ready to heave polymers in exchange for ATP. A typical example of polymer that can be used to that end is microtubules, rigid chains of a few tens of micrometers that have a polarity due to their chemical structure. The associated molecular motors are typically molecules of dynein, that propel microtubules in the direction of their polarity. A system of microtubules on a motility assay is therefore similar to a system of self-propelled polar rods. These rods typically interact through steric interactions, that result in nematic alignment, [48] so that similar systems are an example of self-propelled nematics. Typical observations in such systems is that the rods organise into regular structures, such as the lattice of vortices of collectively moving microtubules shown in Fig. I.6. Similar experiments can be performed with other polymer-motor pairs, for instance actin filaments heaved by myosin molecules [49]. Another way to design active nematics using molecular motor-biopolymer pairs is to place

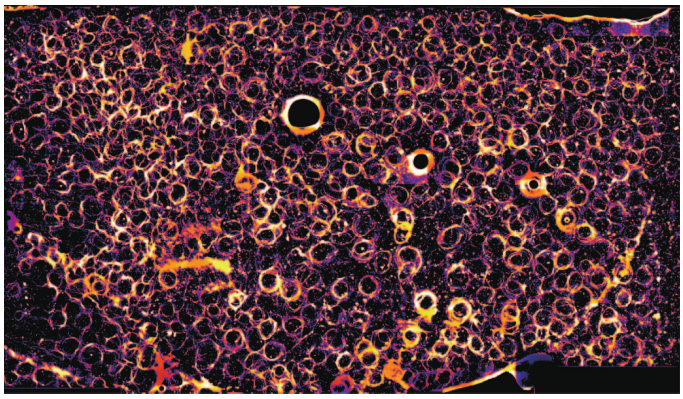

Fig. I.6 **Lattice of vortices in a motility assay.** The system consists in microtubules, tagged with fluorescent molecules, and carried by grafted molecular motors, in a solution of ATP. The false colours code for the intensity of fluorescence, and the scale bar is 2mm long. Figure taken from Sumino *et al.* [48]

the motors directly in solution, so that their two arms bind to two different filaments and exert force dipoles. This experimental protocol leads to the formation of bundles of active fibres that may this time move freely in three-dimensional space, although they are generally studied in a quasi-2d geometry, in which they develop topological defects reminiscent of nematic liquid crystals [50].

In summary, many experiments on non-living systems have established that collective motion could be obtained in a wide variety of simple physical systems, provided that they used polar, self-propelled particles with aligning interactions. It is important to realise that the interactions themselves are here much simpler than in the context of living systems: unlike animals, that process a number of very different sensory information, self-propelled particles interact through physical collisions, or physical fields (concentration fields, electric fields,...). Furthermore, such systems often display unusual properties when compared to usual ensembles of particles: they phase-separate without any attraction, they can spontaneously form large structures like bands or arrays of vortices, and their dense phases seem to be highly peculiar.

I.1.4 Models of Self-Propelled Particles

Because of the very peculiar properties of both natural and engineered systems of self-propelled particles, there has been in recent years a lot of interest in designing abstract models that feature collective motion. Again, it seems that the minimal ingredients of such a model should be that it considers an ensemble of polar, self-propelled particles, interacting in such a way that polarities align together. The simplest, and oldest example of such a model is the *Vicsek model* [51, 52], which is defined as follows. Consider N point-like particles in two dimensions, each moving with a fixed speed v_0, encoding a nominal self-propulsion speed. The velocity of each particle, $\boldsymbol{v}_i = v_0\hat{\boldsymbol{e}}_i$ is therefore simply parametrized by the direction θ_i of a unit vector $\hat{\boldsymbol{e}}_i$. Each of these particles interacts with all its neighbours at a finite range R_0, by aligning its unit vector on the mean direction of all the particles in this ball, so that the evolution of θ_i can be written in discrete time

as

$$\theta_i(t+\delta t) = \langle \theta_i \rangle_{R_0} + \delta\theta_i(t),$$

where $\langle\cdot\rangle_R$ is the mean value in the ball of radius R_0, and $\delta\theta_i$ is a random noise that takes the velocity away from perfect alignment. A sketch representing these evolution rules is shown in Fig. I.7(a), which was adapted from Ginelli [53]. In Vicsek's original formulation, $\delta\theta$ was a random number drawn uniformly in an interval $[-\eta/2;\eta/2]$. Using this definition, the polarity of the system reduces to

$$\Phi = \frac{1}{Nv_0}\left|\sum_{i=1}^{N} \boldsymbol{v}_i\right|.$$

This polarity can be plotted at fixed density against the width of the collision noise η, which plays the same role as a temperature, revealing a phase transition to collective motion at a finite value η_c [52]. This phase transition resembles that of a model of spins that align together and form a magnetic phase. In the case of a two-dimensional space, however, this result might come up as surprising, as it was shown by Mermin and Wagner [54, 55] that systems of spins with a continuous rotational symmetry do not display a phase transition from a disordered to an ordered phase at equilibrium. Furthermore, varying the density reveals a rich behaviour, featuring the formation of multiple polar bands [56], reminiscent of the Quincke roller experiments, and the formation at even higher densities of a single flock. The numerical phase diagram is shown in Fig. I.7(b), and an example of a state of polar bands, which can be interpreted as a microphase separation, is shown in Fig. I.7(c) (both panels are adapted from Solon *et al.* [57]). Like in the experiments of colloids or grains described above, a phase separation also occurs without attraction, and is simply due to the alignment of the velocities (particles "grab" their neighbours as they go). The apparent violation of Mermin's and Wagner's argument, as well as the occurrence of a phase separation without any attraction, are in fact both allowed because the Vicsek model is a non-equilibrium model. Indeed, unlike in a usual gas, the moduli of the velocities are all the same, and do not equilibrate with the effective temperature. Furthermore, collisions do not conserve the momentum. Because of this, the macroscopic properties of the Vicsek model are *a priori* not prescribed by principles as general as those that govern usual gases and liquids. In particular, the precise shape of the noise and of the interactions between particles may change the behaviour of the model. For instance, a noise acting directly on the vector that carries the velocity instead of the angle changes the nature of the transition to collective motion [56], and replacing the continuous $2d$ velocities by Ising-like $1d$ velocities turns the microphase separation into a usual phase separation [57, 58]. Furthermore, non-equilibrium models are in general much more difficult to describe theoretically than equilibrium models, since a variety of tools used in equilibrium rely on the conservation of energy or momentum. Nevertheless, studies of the Vicsek model at the level of hydrodynamic equations [59], and of a closely related on-lattice model [58] have shown that the gas-bands-flock pattern is in fact akin to a liquid-gas phase separation, the critical point of which is sent to infinite density. Intuitively, it has to be the case because the symmetries of the polar liquid and of the isotropic gas are different, so that a transition line has to separate them at all densities (see sketch in Fig. I.7(d)).

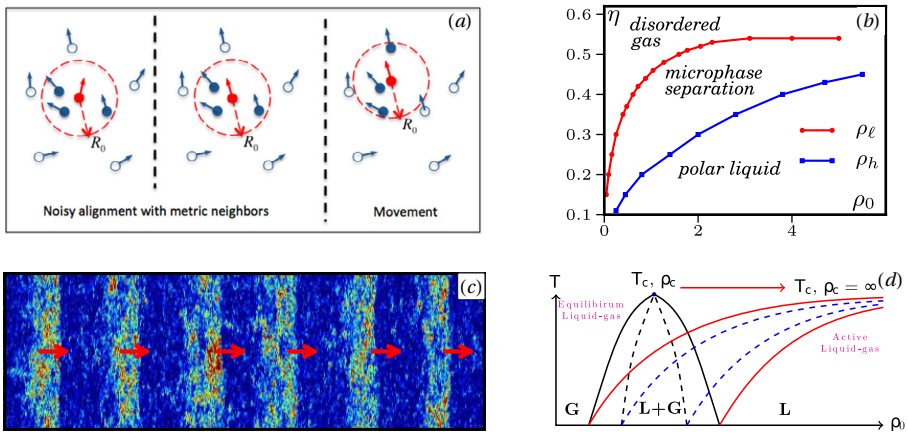

Fig. I.7 **Main observations in the Vicsek model.** (*a*) Sketch of the dynamics in the Vicsek model, adapted from Ref. [53]. (*b*) Numerical phase diagram of the Vicsek model, in the density-collisional noise amplitude plane, adapted from Ref. [57] (*c*) Snapshot of a Vicsek model in the microphase separation regime. The density is colour-coded from blue (low) to red (high), and the arrows represent the velocity of each moving band. Figure adapted from Ref. [57]. (*d*) Sketch of the phase separation in the Vicsek model as an equilibrium phase separation, with a critical point sent to infinite density. Figure adapted from Ref. [58].

Since the first occurrence of the Vicsek model, a number of other models of self-propelled particles have been proposed, so as to make both the individual dynamics and the interactions between particles more realistic than point-particles with a fixed speed that align their velocities directly. They are generally divided into two classes, models of dry self-propelled particles, that describe systems which only interact at close range without a mediation by a surrounding fluid, and models of wet self-propelled particles, that interact with a surrounding fluid and through hydrodynamic interactions. In this thesis, I only focus on dry models. Many of these models are essentially variations on so-called *Active Brownian Particles* (ABPs). These ABPs were first defined through stochastic equations of motion by Fily *et al.* [60]

$$\begin{aligned} \dot{\boldsymbol{v}}_i &= v_0 \hat{\boldsymbol{e}}(\theta_i) + \sum_{j \neq i} \boldsymbol{F}_{ji} + \boldsymbol{\xi}_i \\ \dot{\theta}_i &= \sum_{j \neq i} \Gamma_{ji} + \eta_i, \end{aligned} \tag{I.1}$$

where $\boldsymbol{F}_{ji}$ and Γ_{ji} are, respectively, the forces exerted by other particles on particle i, and the effective torques acting on the self-propulsion direction of particle i due to the other particles. I also defined random noises acting on the velocities, $\boldsymbol{\xi}_i$, and on the angles, η_i. They are generally chosen to be Gaussian white noises,

$$\begin{aligned} \langle \eta_i(t)\eta_j(t') \rangle &= 2D_r \delta_{ij} \delta(t-t'), \\ \left\langle \xi_i^a(t)\xi_j^b(t') \right\rangle &= 2D \delta_{ij} \delta_{ab} \delta(t-t'), \end{aligned}$$

where the superscripts a, b indicate Cartesian components of vectors, and D_r, D are rotational and translational diffusion constants, respectively. Assuming that the bath is at

equilibrium, these diffusion constants are often rewritten as functions of the temperature of the bath (see Sec.II.4.3),

$$D_r = k_B T/\gamma_r,$$
$$D = k_B T/\gamma,$$

where γ, γ_r are damping coefficients acting on the velocity and angle, respectively, and T is the temperature of the bath. In this model, interactions can be made more realistic than in the Vicsek model by considering short-range repulsive interactions, that confer a typical exclusion size to particles, as well as attractive interactions akin to those observed in real-life liquids and colloids. In the simple case with no torques and no attractive interactions, where no collective motion is expected, this model features a phase separation [60]. This is surprising since liquid-gas phase separations are usually expected when attraction is present. Furthermore, there is no alignment of the velocities in this model, meaning that the mechanism underlying the phase separation is not the same as in the case of the Vicsek model. Nevertheless, the phase separation itself can be understood on the basis of intuitive arguments. The idea is that if the coarse-grained velocity of a fluid of self-propelled particles decreases sufficiently fast as the local density increases, for instance because two particles meeting head-on get blocked due to hardcore interactions, particles will gather in a denser phase in parts of space. A careful description of the equations that control the evolution of the coarse-grained field even leads to a thermodynamic-like potential from which the coexisting densities can be recovered [61, 62]. A major difference with usual gases is that this coexistence does not imply that the usual pressure and chemical potential are equal in both phases, they are replaced by more complicated functions of the density. This mechanism for phase separation without attraction was coined Motility-Induced Phase Separation (MIPS), which can be thought of as opposed to the usual "Attraction-Induced" Phase Separations[1]. Even beyond this very peculiar phase-separated regime, that typically happens when the self-propulsion velocity v_0 is high compared to the intensity of the noises, ABP-like models do not simply have the exact same phase diagrams as their equilibrium counterparts. Similar models have for instance been studied in the high-density regime, revealing very rich phase diagrams, that strongly depend on the precise shape of the potential. For instance, considering hard disks, or hard dumbbells lead to very different phenomenologies [64, 65].

Richer behaviours are expected in ABP-like models with the addition of aligning interactions, that should resemble more closely physics experiments of collective motion. These models have mostly been studied numerically, and have very rich and different behaviours depending on the precise interactions. For instance, they have been considered (both numerically and at the level of the hydrodynamic equations) in order to explain the behaviour of microtubules, bacteria and nematods [30, 66–68]. All these systems can, in the right region of parameter space, organise into large regular patterns, vortices or lattices of vortices, in each of which particles are collectively moving.[2]

[1] Interestingly, it has been shown that MIPS can be seen as the consequence of an effective attraction, that appears as a direct consequence of self-propulsion terms in the differential equation on the density field [63].

[2] To obtain those, it is often necessary to add a second time derivative of the angle to Eq. (I.1), indicating that there is a finite inertia.

I.2 The Role of Activity

I.2.1 Active matter and collective motion

Both ABP-like and Vicsek-like models describe non-equilibrium systems constituted of self-propelled, polar particles. Indeed, it is not only impossible to define a conserved energy in the models described above, but they also in general do not conserve momentum during their interactions. In fact, the way in which they are non-equilibrium is also quite unusual. Indeed, most non-equilibrium systems are driven out of equilibrium by the application of an external field: for instance, a fluid subjected to a stress starts flowing. In the case of all the models presented in this introduction, however, equilibrium laws are violated not because an operator imposes an external field, but because individual particles themselves are able to turn an internal source of energy into mechanical work (like birds), or to turn some energy from their medium into mechanical work (like Janus particle or walking grains). Such particles, that break the rules of equilibrium even at the microscopic level, are called active particles, and systems consisting of active particles constitute so-called active matter. The field of active matter goes way beyond that of collective motion alone, as it also encompasses biological tissues, for instance, the mechanical properties of which are deeply linked to the ability of cells to pull on their neighbours, to divide, and to die [26].

In the context of collective motion alone, while it is natural to consider active particles when seeking to observe collective motion resembling that of flocks of birds, if only because experimental realisations of flocking are themselves active, it is far from obvious that it is necessary to do so. Indeed, the difference between the phenomenology of aligning active matter (Vicsek-like) and non-aligning active matter (like the original ABPs) shows that collective motion might not so much be a property linked to activity as it is a property of aligning interactions. In particular, the fact that the polarity of Vicsek-like models behaves a lot like spins in a magnet suggests that coupling the velocities of a usual gas to internal spins that align together might lead to collective motion in a setting such that there is in fact a conserved energy in the system.

I.2.2 Collective Motion without Activity?

This idea recently led to the definition of a conservative model of polar particles that can feature collective motion [69]. The model is defined as follows. Consider N particles, placed in a d-dimensional space, each of which carrying an internal degree of freedom that takes the form of a d-dimensional unit vector $\boldsymbol{s}_i$, and thus encodes a direction in space, much like the internal polarity of walking grains. In the language of magnetism and field theory, this direction can be thought of as a classical $O(n)$ spin with $n = d$ [2, 70], and it is in this sense natural to couple them through aligning (ferromagnetic) interactions. Then, one can seek to couple this internal polarity to the velocity in the simplest possible way: namely, a ferromagnetic-like interaction between the velocity and the spin. The model that contains these ingredients, with the additions of kinetic energy associated to both translation and rotation, and of a purely repulsive pair potential, can be defined in

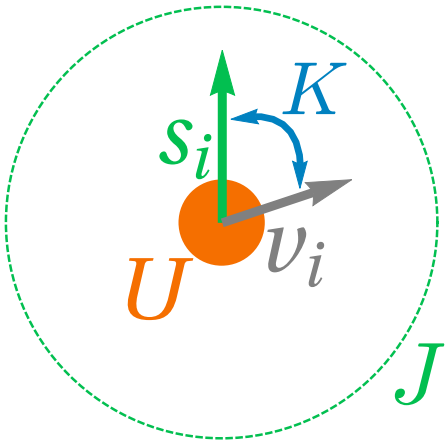

Fig. I.8 **Sketch of the ingredients of the model of Bore *et al.*** [69]. Each particle carries a unit vector, or spin (green), and a velocity (grey), that are coupled with each other through a linear coupling with a coupling constant K (blue). Particles interact with each other through a core repulsion U (orange) and a finite-range ferromagnetic interaction J (dashed, green).

the Lagrangian formalism [69],

$$\mathcal{L} = \sum_{i=1}^{N} \frac{m}{2}\dot{\boldsymbol{r}}_i^2 + \sum_{i=1}^{N} \frac{I}{2}\dot{\boldsymbol{s}}_i^2 + \sum_{i=1}^{N} K\dot{\boldsymbol{r}}_i \cdot \boldsymbol{s}_i - \frac{U_0}{2}\sum_{k\neq i} U(r_{ik}) + \frac{J_0}{2}\sum_{k\neq i} J(r_{ik})\boldsymbol{s}_i \cdot \boldsymbol{s}_k \ . \quad \text{(I.2)}$$

The terms of this Lagrangian are sketched in Fig. I.8. The position of the i-th particle is denoted $\boldsymbol{r}_i$ and its velocity $\boldsymbol{v}_i = \dot{\boldsymbol{r}}_i$, while $r_{ik} = |\boldsymbol{r}_i - \boldsymbol{r}_k|$ is the distance between the centers of particles i and k; $\boldsymbol{s}_i$ is the spin degree of freedom, a vector of unit modulus. The time derivative of the spin vector is indicated by $\dot{\boldsymbol{s}}_i$. Furthermore, m is the mass of each particle and I its moment of inertia. U is a short-ranged, isotropic and purely repulsive two-body interaction potential and J is a short-ranged and isotropic ferromagnetic coupling between the spins. For future convenience, I made explicit the typical amplitudes of the two-body potential, U_0, and the ferromagnetic coupling, J_0. K is the parameter that controls the strength of the spin-velocity coupling, that favours alignment between the spin and the velocity. Following Ref. [69], I introduce dimensionless variables according to the transformations $\boldsymbol{r}/\sqrt{I/m} \to \boldsymbol{r}$, $t/\sqrt{I/J_0} \to t$, $K/\sqrt{mJ_0} \to K$, $L/J_0 \to L$, $U_0/J_0 \to U_0$ and, in the notation hereafter, I absorb U_0 in the definition of the two-body potential U, so that the Lagrangian (I.2) is rewritten as

$$\mathcal{L} = \sum_{i=1}^{N} \frac{1}{2}\dot{\boldsymbol{r}}_i^2 + \sum_{i=1}^{N} \frac{1}{2}\dot{\boldsymbol{s}}_i^2 + \sum_{i=1}^{N} K\dot{\boldsymbol{r}}_i \cdot \boldsymbol{s}_i - \frac{1}{2}\sum_{k\neq i} U(r_{ik}) + \frac{1}{2}\sum_{k\neq i} J(r_{ik})\boldsymbol{s}_i \cdot \boldsymbol{s}_k \ .$$

This Lagrangian is associated to a conserved energy, that can be written as a Hamiltonian,

$$\mathcal{H} = \sum_{i=1}^{N} \frac{1}{2}\boldsymbol{p}_i^2 + \sum_{i=1}^{N} \frac{1}{2}\omega_i^2 - \sum_{i=1}^{N} K\boldsymbol{p}_i \cdot \boldsymbol{s}_i + \frac{1}{2}\sum_{k\neq i} U(r_{ik}) - \frac{1}{2}\sum_{k\neq i} J(r_{ik})\boldsymbol{s}_i \cdot \boldsymbol{s}_k \ , \quad \text{(I.3)}$$

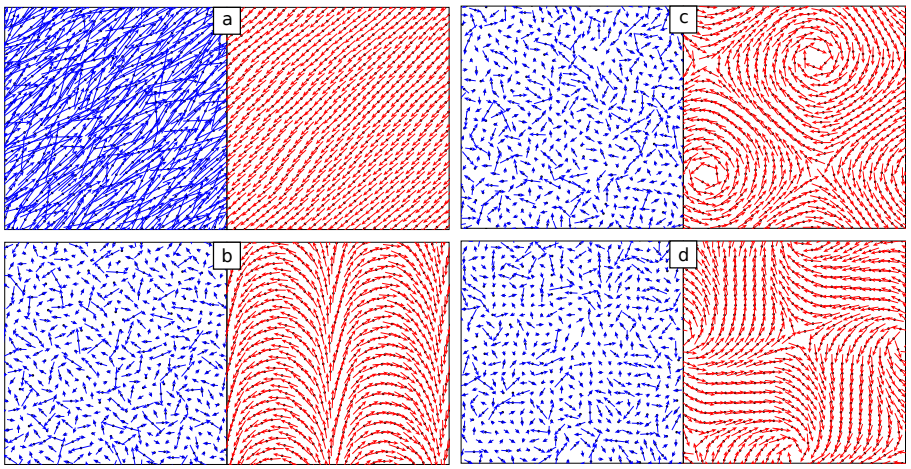

Fig. I.9 **Numerical ground states of the spin-velocity coupled model.** In all panels, the velocities are plotted in blue on the left, and the spins in red on the right. (a) Collectively moving, magnetised state. (b) Arched state. $(c) - (d)$ Vortex states. Figure adapted from Bore *et al.* [69].

where I defined the canonical momenta $\omega_i = \dot{\theta}_i$ and $\boldsymbol{p}_i = \dot{\boldsymbol{r}} + K\boldsymbol{s}_i$. The total momentum, $\boldsymbol{P} = \sum_i \boldsymbol{p}_i$ is, likewise, conserved. Notice that the linear momenta $\boldsymbol{p}_i$ and the total momentum $\boldsymbol{P}$ are not conventional, as they are not simply proportional to the velocities, but also contain some spin information. Due to the alignment interactions between spins and to the spin-velocity coupling, it was shown in Bore *et al.* [69], both at the mean-field level and with seminal numerical simulations in $2d$, that this model can feature collective motion at low energies or temperatures, as recalled in Fig. I.9. Although one expects this ordering of the velocities to vanish in the $N \to \infty$ limit due to the Mermin-Wagner argument, it is thus a model of polar particles, with alignment interactions, that displays finite-size collective motion without the addition of any activity. Instead of activity, the original ingredient compared to standard models of equilibrium liquids is that the spin-velocity coupling breaks Galilean invariance: shifting all the velocities by a constant vector creates an additional field acting on the spins. This invariance is in fact usually broken in models of self-propelled particles, as many of their properties depend on the amplitude of the self-propulsion velocity compared to that of the noise [64, 65].

This conservative setting for collective motion is interesting both conceptually, as it was not obvious that it could exist, and practically, as it enables one to use the standard analytical and numerical tools of equilibrium physics. However, Bore *et al.* [69] also showed that this collective motion is accompanied by several unforeseen behaviours. The most striking one is that, when one chooses to simulate a spatially homogeneous system with a zero total momentum (so that the high-temperature phase is a usual still gas), due to momentum conservation, the low-temperature collectively moving phase has to anti-align the mean magnetisation and the mean velocity, so that

$$\boldsymbol{P} = \boldsymbol{0} = \sum_i \boldsymbol{v}_i + K \sum_i \boldsymbol{s}_i.$$

Therefore, although the coupling between the spin and the velocity in the Lagrangian

was designed to promote an alignment of the velocity onto the spin, the velocities of the collectively moving phase instead *anti-align* with the spins so as to conserve momentum. Such a low-temperature moving state is shown in Fig. I.9(a). Furthermore, when increasing the value of K, Bore *et al.* also observed the formation of states with a zero total magnetisation, featuring arch shapes and vortices (see Fig. I.9(b) – (d)). These states were attributed to a frustration between the conservation of the total momentum, and the associated cost of the total kinetic energy, that grows with ${v_G}^2 = K^2 m^2$, but their shapes and their domain of existence remained unexplained.

In summary, Bore *et al.* [69] suggested that collective motion could emerge as a finite-size equilibrium property of a conservative model at low temperatures, at the cost of breaking Galilean invariance in a fluid of polar, aligning particles. However, several important questions remained open: what is the effect of tuning the density? Can one observe conservative, collectively moving droplets? What are the origin and domain of existence of non-moving states? And last but not least, how do collectively moving phases compare to active flocks? In this thesis, I shall explore these heretofore unexplored questions by studying the model from the crossed perspectives of the theory of fluids, magnetism, and models of self-propelled particles.

I.3 Main Results

In this thesis, I show that a fluid of particles that each carry a continuous spin, that interact with finite-range ferromagnetic interactions generically feature a liquid-gas phase separation between an isotropic gas and a ferromagnetic liquid due to spin-mediated attraction. This result is instructive in the light of the observations on aligning active matter, as it indicates that aligning interactions between polar particles are enough to phase separate, and that the case of the Vicsek model might be a special, non-equilibrium case of a more general result. Furthermore, I show that the selected way to avoid collective motion in the large K and large N limits is the generation of topological defects in the magnetic field. I show that these defects are not linked to the usual defects of $2d$ continuous spins (as captured by the Berezinskii-Kosterlitz-Thouless scenario [71–74]), but to an unusual order-by-disorder scenario that enables the system to escape a high kinetic energy cost. The creation of these defects is reminiscent of the frequent observation of topological structures in systems of self-propelled particles, and could indicate a common mechanism leading to the unstability of polar phases. Then, I discuss the dynamical properties of the system, and I show that the collective motion can be understood as an emergent self-propulsion of the center of mass. This self-propulsion is entirely dictated by the value of the total magnetization, so that the motion of a droplet of the system is well-described by an inertial Langevin-like equation on the orientation of the self-propulsion velocity, that is reminiscent of models that were proposed to describe polar, self-propelled systems like microtubules or nematods [30, 48, 67]. Finally, I show that the conservation of a generalized angular momentum in the system leads to spontaneous rigid rotations of droplets without any external torque, as a response to fluctuations of the magnetization. This result, which is rather unusual in isolated systems, leads to displacement-displacement correlations that are scale-free, like the ones observed in flocks of birds [11].

I.4 Structure of the Thesis

This thesis is organised as follows. In Chapter II, I introduce in detail the standard tools and concepts that are useful to understand this thesis. It is divided into three sections. Sec. II.2 presents the construction of analytical mechanics and statistical mechanics from a Lagrangian, with a strong emphasis on the special case of non-Galilean models in general, and a more detailed discussion on models with spin-velocity couplings. At then end of the section, I also present the simulation methods used in the rest of the thesis, and justify them through the peculiarities of spin-velocity couplings. Sec. II.3 summarises the usual vocabulary and tools of spin magnetism. In particular, I recall how one usually defines and predicts the critical properties of a magnetisation transition at mean-field level, then apply this formalism to the model at hand in the simplest possible setting. Then, I discuss how a model in finite size and finite dimension differs from its mean-field description, and I describe at length the very peculiar example of the square-lattice XY model. Finally, in Sec. II.4, I discuss the various phases that are usually expected in the context of the theory of liquids, both passive and active, and I briefly discuss the special case $d = 2$. I then describe how to predict such phase diagrams for a passive liquid, discussing the effect of adding internal spin variables coupled by isotropic interactions. Finally, I briefly discuss the dynamical properties of the displacements of particles in fluids, both active and passive.

In Chapter III, I present the results I obtained in the benchmark case of a fluid of particles carrying spins in $d = 2$, without spin-velocity couplings ($K = 0$), which were published in Ref. [75]. I first discuss in detail the model I consider as well as the questions that were still open before this thesis. Then, I present a detailed numerical analysis of the properties of the model, both from the point of view of magnetism and from that of the physics of fluids. In particular, I show that, even if the pair potential is chosen to be purely repulsive, finite-range ferromagnetic interactions result in a Ferromagnetism-Induced Phase Separation (FIPS). Finally, I present original mean-field-level derivations of the phase diagram of the model, adapting standard tools from the physics of liquids and of magnetism.

Then, in Chapter IV, reproducing the results that were published in Ref. [76], I discuss in detail the full phase diagram of the model with a spin-velocity coupling ($K \neq 0$), as well as the effects of varying several control parameters. I first discuss and predict the shape of the low-temperature states, showing that they depend on both the size of the system and on the amplitude of the spin-velocity coupling, through an energetic trade-off between the kinetic and magnetic energies. Then, a numerical study at finite temperatures reveals an unusual order-by-disorder scenario that is observed in a finite range of the control parameters, and can be qualitatively explained by constructing a simple approximation for the free energy of the system. I also discuss how the spin-velocity coupling affects the phase-separated phases of the model. I also discuss the ordering properties of the velocities, that are shown to align only at very low temperatures. Finally, I discuss the generality of these results by considering other forms of the spin-velocity coupling, as well as the effect of the geometry and dimensionality of space.

In Chapter V, I discuss the dynamics of the collectively moving phases of the model, in order to compare it to more usual systems of self-propelled particles. These results were published in Ref. [77]. I first show that, in cases in which a FIPS is observed, the model

presents a very rich phenomenology that is reminiscent of more standard realisations of collective motion. I then discuss the relatively simpler properties of homogeneous moving states, and show that, when collective motion emerges at low temperatures, the system effectively behaves like an ABP with memory. I then proceed to show that, at low densities, the conservation of angular momentum also leads to spontaneous rotations of droplets, that are reminiscent of similar properties observed in active matter.

Finally, in Chapter VI, I summarise the results of the thesis in the context of collective motion, and give perspectives for future research.

Chapter II
Useful Tools and Concepts

> No man ever wetted clay and left it, as if there would be bricks by chance and fortune.
>
> Plutarch, *Of Fortune*

II.1 Why this chapter?

The model introduced in Sec. I.2.2, and that I shall discuss in this whole thesis, is a rather unusual one from several points of view. First and foremost, from the point of view of statistical mechanics, it contains a coupling between the velocity and an internal degree of freedom that encodes a polarity. This coupling, as it breaks Galilean invariance, raises many fundamental questions regarding the very construction of statistical mechanics for this system: what are the conserved quantities in the system? What are the conditions on the new coupling for the system to be well-behaved? Can a canonical ensemble be defined in the usual way? If so, is the Gibbs-Boltzmann measure affected by the loss of Galilean invariance? What are the practical implications when designing numerical simulations? These questions are addressed in Sec. II.2, where I show that the standard framework of statistical mechanics is preserved, albeit with a more general formulation of the Gibbs-Boltzmann measure, as long as the spin-velocity coupling takes a simple enough form.

Second, from the point of view of magnetism, this model is also an off-lattice $O(n)$ model placed in an $n-$dimensional space. To characterise its magnetic behaviour, one should therefore have in mind the general characteristics of standard, on-lattice $O(n)$ models. In particular, since I focus on the case of a two-dimensional space, most of the results of this thesis should be compared to the specific case of the $O(2)$ model, or *XY model* in $2d$. The latter is known to be highly peculiar: although it does not feature a critical transition from a disordered to a polar state at any finite temperature, it presents another kind of transition, called the *Berezinskii-Kosterlitz-Thouless* (BKT) transition, which is marked by the excitation of topological defects throughout the system [71–74, 78]. In the context of this thesis, it is therefore natural to investigate whether this BKT behaviour is recovered in the context of an off-lattice fluid of particles carrying spins

and velocities. Thus, in Sec. II.3, I provide an overview of the properties of $O(n)$ models, starting from a general, mean-field view, and progressively moving towards the special case of a finite-size XY model.

Finally, the system I consider is a polar fluid. From the point of view of the theory of liquids, it is expected to order structurally as the temperature and density are tuned. This ordering can be predicted analytically in the case of "simple" liquids, that is to say ensembles of particles that are not endowed with internal degrees of freedom other than their positions and velocities, so that they only interact through isotropic potentials [1]. In this thesis, I consider the somewhat unusual case of particles that do carry additional degrees of freedom, namely a polarity and a rotational velocity, but still interact through isotropic potentials (unlike, for example, in the case of dipolar interactions). Therefore, in Sec. II.4, I describe the standard tools of the physics of simple liquids, and how they are modified by the addition of a polarity that interacts isotropically. Furthermore, since the purpose of this model is to obtain collective motion in a setting that is not active, one should be aware of the basic dynamical properties of both conservative liquids and simple models of self-propelled particles. I therefore briefly discuss these aspects in Sec. II.4.

II.2 Lagrangian and Hamiltonian Mechanics

In order to fully understand the particularities of the model studied in this thesis, and of velocity terms in Lagrangian mechanics in general, it is worth spending some time on general considerations about Lagrangian and Hamiltonian mechanics. In Sec. II.2.1, I start by reminding the reader of the definition of the Lagrangian and Hamiltonian formalisms, I highlight the interest of these two descriptions, and I define the framework of statistical mechanics, including the case of non-Galilean theories. Then, in Sec. II.2.2, I discuss the consequences of adding spin-velocity coupling terms in a Lagrangian. Finally, in Sec. II.2.3, I present the simulation method used throughout this thesis, the choice of which heavily relies on the notions presented in Sec. II.2.1 and II.2.2.

II.2.1 General Definitions

The most general formulation of mechanics, describing the motion of particles in a fluid for instance, is the principle of least action [79]. According to this principle, any mechanical system with degrees of freedom $\boldsymbol{q}$ can be characterised by a function of these degrees of freedom, of their time derivative, and of time. This function is called the Lagrangian, and I shall note it $\mathcal{L}(\boldsymbol{q}, \dot{\boldsymbol{q}}; t)$. The principle of least action then states that, when time runs from a value t_1 to a value t_2, the system described by $\mathcal{L}$ chooses the trajectory such that the action,

$$\mathcal{S} = \int_{t_1}^{t_2} \mathcal{L}(\boldsymbol{q}, \dot{\boldsymbol{q}}, t) dt, \tag{II.1}$$

takes the lowest possible value. Differentiating Eq. (II.1), one finds that the principle of least action can be cast into a set of differential equations on the Lagrangian,

$$\frac{d}{dt}\left(\frac{\partial \mathcal{L}}{\partial \dot{q}_a}\right) - \frac{\partial \mathcal{L}}{\partial q_a} = 0, \tag{II.2}$$

where q_a is any degree of freedom. This equation is called Lagrange's equation, or the Euler-Lagrange equation.

In the simple example of a usual system of N point-like particles, each carrying a mass m, located at positions $\{\boldsymbol{r}_i\}_{1\leq i\leq N}$ and coupled by an isotropic pairwise interaction potential $V(r_{ij})$, where $r_{ij} = |\boldsymbol{r}_i - \boldsymbol{r}_j|$, the Lagrangian that yields the right equations of motion reads

$$\mathcal{L} = \sum_{i=1}^{N} \left[\frac{1}{2} m \dot{\boldsymbol{r}}_i{}^2 - \sum_{j<i} V(r_{ij}) \right].$$

Indeed, one can check that the associated Euler-Lagrange equation for any particle is Newton's equation,

$$m\ddot{\boldsymbol{r}}_i = -\sum_{j\neq i} \frac{\partial}{\partial \boldsymbol{r}_i} V(r_{ij}).$$

Notice that the Lagrangian is here given by the usual kinetic energy, minus the potential energy. This decomposition can be performed for any system, by defining the potential energy $\mathcal{V}$ as the part of the Lagrangian that does not depend on time derivatives of degrees of freedom, and the kinetic energy $\mathcal{T}$ as the rest:

$$\mathcal{L}(\boldsymbol{q}, \dot{\boldsymbol{q}}, t) = \mathcal{T}(\boldsymbol{q}, \dot{\boldsymbol{q}}, t) - \mathcal{V}(\boldsymbol{q}, t).$$

a) Conservation and Symmetries

One of the main interests of the Lagrangian formalism is that it greatly facilitates the systematic writing of conserved quantities in a mechanical system. If one spots a continuous transformation of the $\boldsymbol{q}_i$'s that leaves the value of $\mathcal{L}$ unchanged (a symmetry), according to Noether's theorem, it is associated to a conserved quantity (see, for instance, Landau [79]). This conserved quantity is simply sought by considering an infinitesimal version of this symmetry (an infinitesimal translation of all positions, for instance), and writing that the associated infinitesimal change of the value of the Lagrangian must be zero. The simplest, and perhaps the most important example of this theorem, is provided by the invariance under a time translation. Assuming that the Lagrangian does not depend explicitly on time, which physically means that he system is not subjected to time-dependent fields, one can write that the time-derivative of the Lagrangian should be zero,

$$\frac{d\mathcal{L}}{dt} = \sum_a \left[\frac{\partial \mathcal{L}}{\partial q_a} \dot{q}_a + \frac{\partial \mathcal{L}}{\partial \dot{q}_a} \ddot{q}_a \right],$$

which can be recast into the form

$$\frac{d}{dt} \left(\sum_a \dot{q}_a \frac{\partial \mathcal{L}}{\partial \dot{q}_a} - \mathcal{L} \right) = 0.$$

This last equation defines the conserved quantity associated to the symmetry with respect to a time-translation,

$$E \equiv \sum_a \dot{q}_a \frac{\partial \mathcal{L}}{\partial \dot{q}_a} - \mathcal{L}, \tag{II.3}$$

that is called the energy of the system. One can check that if the kinetic energy that is a quadratic function of the velocities, $E = \mathcal{T} + \mathcal{V}$ is indeed the total energy of the system. The case of non-quadratic kinetic energies is discussed in Sec. II.2.2.

Another fundamental conservation law is that associated to the invariance under a space translation of the whole system. Consider an infinitesimal translation of the whole system by a vector $\boldsymbol{\epsilon}$. The associated conservation law only concerns the derivatives of $\mathcal{L}$ with respect to position variables among the degrees of freedom, and reads,

$$\delta L = \sum_i \frac{\partial \mathcal{L}}{\partial \boldsymbol{r}_i} \cdot \boldsymbol{\epsilon} = 0,$$

which is equivalent to

$$\sum_i \frac{\partial \mathcal{L}}{\partial \boldsymbol{r}_i} = \boldsymbol{0},$$

Using Eq. (II.2), this last equation can be rewritten as

$$\frac{d}{dt} \sum_i \frac{\partial \mathcal{L}}{\partial \dot{\boldsymbol{r}}_i} = 0,$$

which defines a second conserved quantity, the total momentum

$$\boldsymbol{P} = \sum_i \frac{\partial \mathcal{L}}{\partial \dot{\boldsymbol{r}}_i}.$$

In the case of a usual quadratic kinetic energy, one can check that this momentum is indeed the usual momentum, $\boldsymbol{P} = \sum_i m\dot{\boldsymbol{r}}_i$. By extension, one also defines the canonical momentum of one particle,

$$\boldsymbol{p}_i \equiv \frac{\partial \mathcal{L}}{\partial \dot{\boldsymbol{r}}_i}.$$

Similarly, one can define the canonical momenta associated to degrees of freedom other than the positions.

Finally, a last symmetry that is often considered is the invariance by rotation around any axis. This time, I consider an infinitesimal rotation vector $\boldsymbol{\delta\vartheta}$, the amplitude of which is an angle $\delta\vartheta$, and pointing into the direction of the axis of rotation. A particle at position $\boldsymbol{r}$ undergoing that rotation is displaced by a vector $\boldsymbol{\delta r} = \boldsymbol{\delta\vartheta} \times \boldsymbol{r}$, where $\times$ is a vector product. Likewise, a velocity $\boldsymbol{v} = \dot{\boldsymbol{r}}$ is displaced of $\boldsymbol{\delta v} = \boldsymbol{\delta\vartheta} \times \boldsymbol{v}$. The perturbation of the Lagrangian by this rotation then reads

$$\delta L = \sum_i \left(\frac{\partial \mathcal{L}}{\partial \boldsymbol{r}_i} \cdot \boldsymbol{\delta r}_i + \frac{\partial \mathcal{L}}{\partial \boldsymbol{v}_i} \cdot \boldsymbol{\delta v}_i \right) = 0.$$

To lighten the notations, I introduce the canonical momenta $\boldsymbol{p}_i$, and notice that the Euler-Lagrange equation yields $\dot{\boldsymbol{p}}_i = \partial\mathcal{L}/\partial\boldsymbol{r}_i$. Using the expressions of $\boldsymbol{\delta r}_i$ and $\boldsymbol{\delta v}_i$ given above, the conservation relation can be rewritten as

$$\sum_i \left(\dot{\boldsymbol{p}}_i \cdot \boldsymbol{\delta\vartheta} \times \boldsymbol{r}_i + \boldsymbol{p}_i \cdot \boldsymbol{\delta\vartheta} \times \boldsymbol{v}_i \right) = 0.$$

Permuting the terms in the cross-products so as to take out the rotation vector yields

$$\boldsymbol{\delta\vartheta} \cdot \sum_i \left(\boldsymbol{r}_i \times \dot{\boldsymbol{p}}_i + \boldsymbol{v}_i \times \boldsymbol{p}_i \right) = 0,$$

an equation that contains a total time derivative:

$$\boldsymbol{\delta\vartheta} \cdot \frac{d}{dt} \sum_i \boldsymbol{r}_i \times \boldsymbol{p}_i = 0.$$

It is therefore possible to define the conserved quantity

$$\boldsymbol{L} \equiv \sum_i \boldsymbol{r}_i \times \boldsymbol{p}_i,$$

called the angular momentum.

b) The Hamiltonian Description

The Lagrangian formalism is a representation of a mechanical system as a function of the degrees of freedom q_a and of the associated generalised velocities $\dot{q}_a$. It is also useful, in some situations, to change variables and use the generalised momenta p_a instead of the generalised velocities. In order to operate this change of variables, assuming that it has no explicit time dependence, one writes the total derivative of the Lagrangian in terms of the q_a's and $\dot{q}_a$'s,

$$d\mathcal{L} = \sum_a \left(\frac{\partial \mathcal{L}}{\partial q_a} dq_a + \frac{\partial \mathcal{L}}{\partial \dot{q}_a} d\dot{q}_a \right),$$

which can, introducing p_a and $\dot{p}_a$ like in the previous subsection, be rewritten as

$$d\mathcal{L} = \sum_a \left(\dot{p}_a dq_a + p_a d\dot{q}_a \right). \tag{II.4}$$

To get rid of the $d\dot{q}_a$ dependence, I rewrite

$$p_a d\dot{q}_a = d\left(p_a \dot{q}_a\right) - \dot{q}_a dp_a,$$

so that Eq. (II.4) can be recast into the form

$$d\left(\sum_a p_a \dot{q}_a - L \right) = -\sum_a \left(\dot{q}_a dp_a - \dot{p}_a dq_a \right). \tag{II.5}$$

The left-hand side of Eq. (II.5) is the differential of the conserved energy of the system, as defined in Eq. (II.3), here expressed as a function of the degrees of freedom and canonical momenta of the system. This energy function is called the Hamiltonian of the system,

$$\mathcal{H}(\boldsymbol{q}, \boldsymbol{p}, t) = \sum_a p_a \dot{q}_a - \mathcal{L}. \tag{II.6}$$

The transformation that turns the Lagrangian into the Hamiltonian is called the Legendre transformation. Geometrically, notice that the definition (II.6) of the Hamiltonian in fact defines a family of tangents of $\mathcal{L}$, seen as a function of velocities, these tangents being

parameterised by their slope $\boldsymbol{p}$. I shall come back to this geometric interpretation in Sec. II.2.2, in particular to discuss the cases when the Hamiltonian cannot be defined unequivocally from the transformation that is detailed here.

Using Eq. (II.5), one gets, for all degrees of freedom, the equations

$$\dot{q}_a = \frac{\partial \mathcal{H}}{\partial p_a},$$
$$\dot{p}_a = -\frac{\partial \mathcal{H}}{\partial q_a}.$$

These equations are called the Hamiltonian equations of motion, or simply Hamilton's equations. They form a set of first-order differential equations, that replace the second-order differential equations obtained with the Euler-Lagrange equation. This replacement is, in particular, interesting in the context of numerical simulations, since first-order differential equations are easier to integrate numerically, in ways that I shall describe in Sec. II.2.3. Because of the symmetry between the roles played by p_a and q_a in the Hamiltonian formalism, they are usually called pairs of conjugate variables.

c) Statistical Mechanics

For an isolated system with energy E_0, momentum $\boldsymbol{P}_0$, and angular momentum $\boldsymbol{L}_0$, at equilibrium, one generally assumes that the probability distribution of microscopic configurations in phase space is such that all configurations with the same values of the conserved quantities are equiprobable [80–82]. This assumption is reasonable if the system is composed of "sufficiently" interacting particles, meaning that the microscopic dynamics are chaotic enough to ensure that all microstates are explored.[1] The associated probability distribution of microscopic configurations in phase space reads

$$\mathcal{P}_{mc}(\mathcal{C}) = \frac{1}{\Omega(E, \boldsymbol{P}, \boldsymbol{L})} \delta\left(E - E_0\right) \delta\left(\boldsymbol{P} - \boldsymbol{P}_0\right) \delta\left(\boldsymbol{L} - \boldsymbol{L}_0\right),$$

where the subscript mc indicates that the setting of an isolated system is called the microcanonical ensemble in the context of statistical mechanics, $\mathcal{C}$ is a configuration of the degrees of freedom and momenta of particles, and Ω is the microcanonical partition function, that normalizes $\mathcal{P}_{mc}(\mathcal{C})$ in such a way that its sum over all configurations is 1.

The microcanonical setting, while it is the most natural to define, is the least practical to work with for calculations. I therefore introduce the canonical ensemble, that corresponds to the statistics of a system that is allowed to exchange some of the conserved quantities defining the microcanonical ensemble, but not particles, with a much larger reservoir. The ensemble is introduced as follows: consider the total system $\mathcal{T}$, composed of the small system $\mathcal{S}$ that I wish to study, and of the reservoir $\mathcal{R}$. This total system is isolated and Hamiltonian, so that it is described in the microcanonical setting by the distribution

$$\mathcal{P}^{\mathcal{T}}_{mc}(\mathcal{C}^{\mathcal{T}}) = \frac{1}{\Omega^{\mathcal{T}}(E^{\mathcal{T}}, \boldsymbol{P}^{\mathcal{T}}, \boldsymbol{L}^{\mathcal{T}})} \delta\left(E^{\mathcal{T}} - E_0\right) \delta\left(\boldsymbol{P}^{\mathcal{T}} - \boldsymbol{P}_0\right) \delta\left(\boldsymbol{L}^{\mathcal{T}} - \boldsymbol{L}_0\right),$$

[1] While the validity of this "ergodic" hypothesis cannot in general be proved, even in simple systems, it is frequent to justify it from the so-called Liouville equation: if one summarily assumes that the distribution of states in phase-space is explicitly a function of the conserved quantities, one finds that a flat distribution is compatible with Hamiltonian dynamics at equilibrium [81–83].

which is a joint probability that describes both $\mathcal{S}$ and $\mathcal{R}$. The canonical distribution of the configurations of $\mathcal{S}$ alone is recovered when summing $\mathcal{P}^{\mathcal{T}}_{mc}$ over all the configurations of the reservoir $\mathcal{R}$ such that a configuration $\mathcal{C}^{\mathcal{S}}$ is observed,

$$\mathcal{P}(\mathcal{C}^{\mathcal{S}}) = \sum_{\{\mathcal{C}^{\mathcal{R}}|\mathcal{C}^{\mathcal{S}}\}} \mathcal{P}^{\mathcal{T}}_{mc}(\mathcal{C}^{\mathcal{T}}). \tag{II.7}$$

Since the distribution $\mathcal{P}^{\mathcal{T}}_{mc}$ is flat over the surface of constant E, $\boldsymbol{P}$ and $\boldsymbol{L}$, the sum in Eq. (II.7) simply yields

$$\mathcal{P}(\mathcal{C}^{\mathcal{S}}) = \frac{\Omega^{\mathcal{R}}(E^{\mathcal{R}}, \boldsymbol{P}^{\mathcal{T}} - \boldsymbol{P}^{\mathcal{S}}, \boldsymbol{L}^{\mathcal{T}} - \boldsymbol{L}^{\mathcal{S}})}{\Omega^{\mathcal{T}}(E^{\mathcal{T}}, \boldsymbol{P}^{\mathcal{T}}, \boldsymbol{L}^{\mathcal{T}})},$$

where I called $\Omega^{\mathcal{R}}$ the number of configurations of the reservoir, and I explicitly write its dependence on the energy, momentum and angular momentum of the reservoir. While the linear and angular momenta of the reservoir can be decomposed as a difference by linearity, the same is not directly true of the energy. Indeed, the total energy can be written as

$$E^{\mathcal{T}} = E^{\mathcal{R}} + E^{\mathcal{S}} + E^{\mathcal{R}-\mathcal{S}},$$

where $E^{\mathcal{R}-\mathcal{S}}$ is the energy corresponding to the interactions between the reservoir and the system. In the case of short-range interactions, the interaction energy grows much slower than the other two terms as the number of particles increases in both $\mathcal{S}$ and $\mathcal{R}$. It can therefore be neglected in the limit of large systems,[2] leading to $E^{\mathcal{R}} \approx E^{\mathcal{T}} - E^{\mathcal{S}}$. I now define the microcanonical entropy of a system via Boltzmann's equation, $S = k_B \log \Omega$, where k_B is Boltzmann's constant that fixes the physical unit of the temperature, so that

$$\mathcal{P}(\mathcal{C}^{\mathcal{S}}) = \frac{1}{\Omega^{\mathcal{T}}(E^{\mathcal{T}}, \boldsymbol{P}^{\mathcal{T}}, \boldsymbol{L}^{\mathcal{T}})} \exp\left[\frac{1}{k_B} S^{\mathcal{R}}\left(E^{\mathcal{T}} - E^{\mathcal{S}}, \boldsymbol{P}^{\mathcal{T}} - \boldsymbol{P}^{\mathcal{S}}, \boldsymbol{L}^{\mathcal{T}} - \boldsymbol{L}^{\mathcal{S}}\right)\right].$$

Assuming that the reservoir is much bigger than $\mathcal{S}$, so that its energy, momentum and angular momentum are much bigger than that of the system I want to study, the entropy can be Taylor-expanded up to first order in the last expression. Dropping the prefactors that only depend on the total quantities to improve readability, one gets

$$\mathcal{P}(\mathcal{C}^{\mathcal{S}}) \propto \exp\left[-\frac{E^{\mathcal{S}}}{k_B}\frac{\partial S^{\mathcal{R}}}{\partial E}\bigg|_{\mathcal{T}} - \frac{\boldsymbol{P}^{\mathcal{S}}}{k_B}\cdot\frac{\partial S^{\mathcal{R}}}{\partial \boldsymbol{P}}\bigg|_{\mathcal{T}} - \frac{\boldsymbol{L}^{\mathcal{S}}}{k_B}\cdot\frac{\partial S^{\mathcal{R}}}{\partial \boldsymbol{L}}\bigg|_{\mathcal{T}}\right],$$

where $|_{\mathcal{T}}$ indicates that the function is evaluated at $(E^{\mathcal{T}}, \boldsymbol{P}^{\mathcal{T}}, \boldsymbol{L}^{\mathcal{T}})$. By definition, $\partial S^{\mathcal{R}}/\partial E$ is the temperature T of the reservoir, that is also imposed to $\mathcal{S}$ at equilibrium. Therefore, following the notations of Bore *et al.* [69], for any Hamiltonian system in contact with a large reservoir of energy, momentum and angular momentum, the canonical distribution of configurations can be written as

$$\mathcal{P}(\mathcal{C}) = \frac{1}{Z(\beta, \boldsymbol{\alpha}, \boldsymbol{\lambda})} e^{-\beta(E - \boldsymbol{\alpha}\cdot\boldsymbol{P} - \boldsymbol{\lambda}\cdot\boldsymbol{L})},$$

[2] For a more detailed discussion on the corrections to this approximation in the case of small systems, and on its breakdown in the presence of long-range interactions, see for instance Mukamel [84].

where $\beta = 1/k_B T$, $Z(\beta, \boldsymbol{\alpha}, \boldsymbol{\lambda})$ is the canonical partition function, that normalises the probability distribution, and

$$\boldsymbol{\alpha} = -T \left.\frac{\partial S^{\mathcal{R}}}{\partial \boldsymbol{P}}\right|_{\mathcal{T}},$$
$$\boldsymbol{\lambda} = -T \left.\frac{\partial S^{\mathcal{R}}}{\partial \boldsymbol{L}}\right|_{\mathcal{T}},$$

are the intensive control parameters of the reservoir that control the thermal averages of $\boldsymbol{P}$, and $\boldsymbol{L}$.[3] This is the most general writing of the canonical distribution of configurations of a mechanical system. This might look a bit surprising, as one does not usually write down the momentum and angular momentum dependencies.

In fact, assuming that the system is a Galilean invariant, the microcanonical entropy should not depend on the referential of study. As a result, in the case of a standard kinetic energy, the microcanonical entropy should only be a function of the internal energy [81, 85],

$$E_{int} = E - \frac{P^2}{2M} - \frac{L^2}{2I},$$

where M is the total mass of the system, and I its total moment of inertia, so that $S(E, \boldsymbol{P}, \boldsymbol{L}) = S(E_{int})$. As a result,

$$\begin{aligned}\boldsymbol{\alpha} &= -T \left.\frac{\partial S^{\mathcal{R}}}{\partial E_{int}}\right|_{\mathcal{T}} \frac{\partial E^{\mathcal{T}}_{int}}{\partial \boldsymbol{P}}, \\ &= \boldsymbol{P}/M.\end{aligned}$$

Therefore, noticing that $\boldsymbol{P}/M$ is the velocity of the centre of mass of the system, $\boldsymbol{v}_G$, I find $\boldsymbol{\alpha} = \boldsymbol{v}_G$. Likewise, one finds $\boldsymbol{\lambda} = \boldsymbol{L}/I = \boldsymbol{\omega}_G$, the macroscopic rotational velocity vector of the system. Using these results, for a usual system, I find

$$\mathcal{P}(\mathcal{C}) = \frac{1}{Z(\beta, \boldsymbol{v}_G, \boldsymbol{\omega}_G)} e^{-\beta(E - \boldsymbol{v}_G \cdot \boldsymbol{P} - \boldsymbol{\omega}_G \cdot \boldsymbol{L})}.$$

Therefore, while the most general definition of the canonical distribution does depend on the total momentum and angular momentum, one can usually set $\boldsymbol{v}_G = \boldsymbol{0}$ due to Galilean invariance. As for the angular momentum term, it is usually also set to zero arbitrarily, this time arguing that the considered system is a very small part of a reservoir [81]. Consequently, its angular momentum relative to its own centre of mass is very small compared to its angular momentum relative to the centre of mass of the whole system, including the reservoir. Additionally, one can argue that neither momentum nor angular momentum are actually conserved in real-life experiments, since experimental systems are placed in still containers [85]. Finally, for a Galilean invariant system with a quadratic kinetic energy, one finds that the canonical distribution law is well-described by the usual Gibbs-Boltzmann law,

$$\mathcal{P}(\mathcal{C}) = \frac{1}{Z(\beta)} e^{-\beta E}.$$

[3] I here follow Bore and co-workers [69] in the definition of the canonical measure when factorising β in the exponent, but one could also define the control parameters $\tilde{\boldsymbol{\alpha}} = \beta \boldsymbol{\alpha}$ and $\tilde{\boldsymbol{\lambda}} = \beta \boldsymbol{\lambda}$, that may be defined even in systems that do not conserve an energy, but do conserve linear and angular momenta.

However, as soon as Galilean invariance is lost *or* as the kinetic energy becomes non-quadratic, one should *a priori* check, case by case, whether $\boldsymbol{\alpha}$ and $\boldsymbol{\lambda}$ can be dropped from the most general definition of this probability measure. In the following, I discuss how well the construction of statistical mechanics presented in this section survives in the context of models that contain spin-velocity couplings.

II.2.2 Spin-Velocity Coupled Theories

a) Linear Spin-Velocity Coupling

I first want to discuss the properties of the model introduced by Bore et al. [69] and discussed in Sec. I.2.2. It is defined at the Lagrangian level by

$$\mathcal{L} = \sum_{i=1}^{N} \frac{m}{2}\dot{\boldsymbol{r}}_i^2 + \sum_{i=1}^{N} \frac{I}{2}\dot{\boldsymbol{s}}_i^2 + \sum_{i=1}^{N} K\dot{\boldsymbol{r}}_i \cdot \boldsymbol{s}_i - \frac{U_0}{2}\sum_{k\neq i} U(r_{ik}) + \frac{J_0}{2}\sum_{k\neq i} J(r_{ik})\cos\theta_{ik} \ , \quad \text{(II.8)}$$

where the position $\boldsymbol{r}_i$ of the i-th particle sits in a $2d$ periodic square box of linear size L; θ_i is the angle that the spin forms with a reference axis and fully parameterises the continuous $2d$ spin $\boldsymbol{s}_i$ of unit modulus. The time derivative of the spin vector is indicated by $\dot{\boldsymbol{s}}_i$; θ_{ik} is the angle between the spin of particle i and the one of particle k. Furthermore, m is the mass of each particle and I its moment of inertia. U is a short-ranged, isotropic and purely repulsive two-body interaction potential and J is a short-ranged and isotropic ferromagnetic coupling between the spins. For future convenience I made explicit the typical amplitudes of the two-body potential, U_0, and the ferromagnetic coupling, J_0. K is the parameter that controls the strength of the spin-velocity coupling. Before discussing the properties of this model in detail, I first introduce dimensionless variables according to the transformations $\boldsymbol{r}/\sqrt{I/m} \to \boldsymbol{r}$, $t/\sqrt{I/J_0} \to t$, $K/\sqrt{mJ_0} \to K$, $L/J_0 \to L$, $U_0/J_0 \to U_0$ and, in the notation hereafter, I absorb U_0 in the definition of the two-body potential U. Using these rescaled variables, the Lagrangian (II.8) can be rewritten in the simpler form

$$\mathcal{L} = \sum_{i=1}^{N} \frac{1}{2}\dot{\boldsymbol{r}}_i^2 + \sum_{i=1}^{N} \frac{1}{2}\dot{\boldsymbol{s}}_i^2 + \sum_{i=1}^{N} K\dot{\boldsymbol{r}}_i \cdot \boldsymbol{s}_i - \frac{1}{2}\sum_{k\neq i} U(r_{ik}) + \frac{1}{2}\sum_{k\neq i} J(r_{ik})\cos\theta_{ik} \ . \quad \text{(II.9)}$$

Furthermore, throughout this thesis, I will only consider the case $K \geq 0$ as the case $K \leq 0$ can be recovered by simply flipping all the spins.

This model is invariant under a translation of time, a translation of space, and a joint rotation of space and of spins. As a consequence, one can seek a conserved energy, momentum, and angular momentum. A straightforward reproduction of the technique introduced in Sec. II.2.1a) yields the conserved spatial momentum

$$\boldsymbol{P} = \sum_{i=1}^{N} \frac{\partial \mathcal{L}}{\partial \dot{\boldsymbol{r}}_i} = \sum_{i=1}^{N} (\dot{\boldsymbol{r}}_i + K\boldsymbol{s}_i) \, ,$$

which also enables me to define the canonical momentum of one particle,

$$\boldsymbol{p}_i = \dot{\boldsymbol{r}}_i + K\boldsymbol{s}_i .$$

This momentum contains the usual "kinetic" term proportional to the velocity, but also a term proportional to the spin of the particle, in a way that is reminiscent of the conserved momentum of charged particles in magnetic fields [81, 82]. Regarding the conserved angular momentum, one here needs to consider the joint rotation of spins and space. The calculation of the value of this conserved quantity however still exactly follows the calculation of Sec. II.2.1a), that was written for generalised positions and momenta, yielding

$$\begin{aligned}\boldsymbol{L} &= \sum_{i=1}^{N} \left(\boldsymbol{r}_i \times \boldsymbol{p}_i + \boldsymbol{r}_i \times \dot{\boldsymbol{s}}_i\right), \\ &= \sum_{i=1}^{N} \left(\boldsymbol{r}_i \times \boldsymbol{p}_i + \dot{\theta}_i \boldsymbol{e}_z\right),\end{aligned}$$

where $\boldsymbol{e}_z \equiv \boldsymbol{e}_x \times \boldsymbol{e}_y$ is the out of plane unit vector that completes a $3d$ standard basis. Finally, the conserved energy can also be written in a standard way,

$$\begin{aligned}E &= \sum_{i=1}^{N} \left[\boldsymbol{v}_i \cdot \frac{\partial \mathcal{L}}{\partial \boldsymbol{v}_i} + \dot{\boldsymbol{s}}_i \cdot \frac{\partial \mathcal{L}}{\partial \dot{\boldsymbol{s}}_i} - \mathcal{L}\right], \\ &= \sum_{i=1}^{N} \left[\frac{1}{2}\boldsymbol{v}_i^2 + \frac{1}{2}\dot{\boldsymbol{s}}_i^2 + \frac{1}{2}\sum_{k\neq i} U(r_{ik}) - \frac{1}{2}\sum_{k\neq i} J(r_{ik}) \cos\theta_{ik}\right]. \end{aligned} \tag{II.10}$$

A striking feature of this energy is that it does not contain any spin-velocity coupling term, although the Lagrangian did. This is even more surprising when noticing that the Lagrangian, due to the spin-velocity coupling, is not invariant under a Galilean transformation. Indeed, shifting all velocities by a constant value $\boldsymbol{v}_0$ creates an additional spin-velocity term

$$\mathcal{L}_{Gal} = \sum_{i=1}^{N} K \boldsymbol{v}_0 \cdot \boldsymbol{s}_i,$$

so that $K\boldsymbol{v}_0$ plays the same role as a field acting on spins. In simple words, this model should magnetise when it is set in motion.

A visual consequence of the non-Galilean behaviour is the aspect of the trajectories of free particles described by the Lagrangian (II.9): such particles follow equations of motion found by writing the system of Euler-Lagrange equations written for the generalised coordinates $\boldsymbol{r}$ and $\boldsymbol{\theta}$,

$$\begin{aligned}\ddot{\boldsymbol{r}} &= -K\dot{\theta}\boldsymbol{s}_\perp, \\ \ddot{\theta} &= K\dot{\boldsymbol{r}} \cdot \boldsymbol{s}_\perp = K\boldsymbol{p} \cdot \boldsymbol{s}_\perp,\end{aligned}$$

where $\boldsymbol{s}_\perp = \partial \boldsymbol{s}/\partial\theta$ is the unit vector obtained by rotating $\boldsymbol{s}$ of an anticlockwise $\pi/2$ angle. The first of these equations states that free particle trajectories conserve momentum, so that $\boldsymbol{p} = \dot{\boldsymbol{r}} + K\boldsymbol{s}$ is a constant vector $\boldsymbol{p}_0$. Using this result, the second equation of motion can be rewritten using the axis of the (conserved) momentum as an angle reference,

$$\ddot{\theta} = -Kp_0 \sin\theta,$$

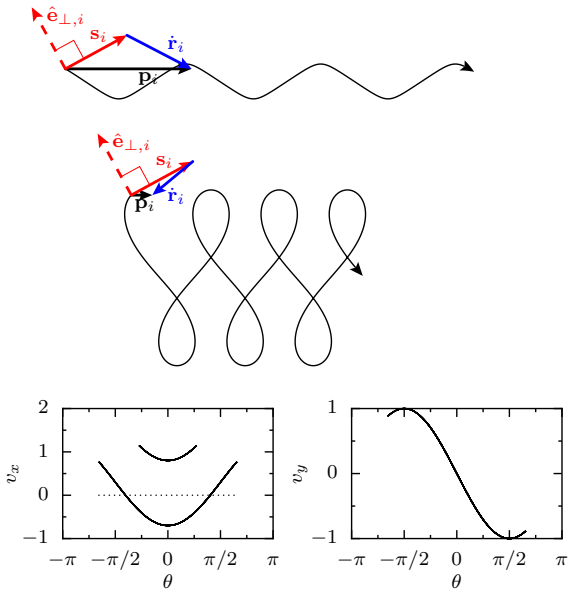

Fig. II.1 **Trajectories of Free Particles.** I show a trajectory in the case $Kp_0 > 1$ (top) and in the case $Kp_0 < 1$ (middle), with the same value of p_0. In both cases, the spin oscillates around the momentum at a frequency $\sqrt{Kp_0}$, and the conservation of momentum then sets the value of the velocity from the value of the spin. The bottom row shows that, between the two trajectories, only the $x-$component differs, while the $y-$component follows the exact same trajectory. Figure taken from Ref. [69]

which states that the spin behaves like a pendulum oscillating around the direction of the velocity with a frequency $\sqrt{Kp_0}$. Finally, calling x the axis of $\boldsymbol{p}_0$ and y the axis perpendicular to it, one can write equations describing the trajectory. Using the conservation of the angular momentum $\boldsymbol{L} = (-y(t)p_0 + \dot{\theta})\hat{\boldsymbol{e}}_z$, one gets an equation for y,

$$y(t) = y(0) + \frac{1}{p_0}\left(\dot{\theta}(t) - \dot{\theta}(0)\right),$$

which states that the motion perpendicular to the momentum simply follows the oscillatory motion of $\dot{\theta}$. While the motion along x is more complicated, the trajectory can be qualitatively understood when writing down the momentum conservation equation,

$$\dot{x} = p_0 - K\cos\theta.$$

Indeed, this equation shows that there are two regimes of motion: for $p_0 > K$, the particle always moves in the direction of its momentum, but with oscillations of its velocity. For larger K, such that $K > p_0$, however, there are velocity reversals, and the trajectory strongly depends on the dynamics of θ. Typical free particle trajectories are shown in Fig. II.1, in both regimes. They are obviously *not* the straight lines that one would expect in a Galilean invariant setting. Note however that straight trajectories are recovered in the special case $p_0 = 0$.

The apparent discrepancy between the expression of E and the non-Galilean properties of this system is in fact linked to the definition of the canonical momentum. Indeed, the

object that defines the dynamics in such a way that equations of motion and statistical mechanics can be properly defined is not the energy expressed as a function of velocities, but the Hamiltonian. In order to write it, I define the canonical momentum associated to the angular velocity of spins,

$$\omega_i \equiv \frac{\partial \mathcal{L}}{\partial \dot{\theta}_i} = \dot{\theta}_i,$$

then rewrite the conserved energy solely in terms of canonical momenta to obtain the Hamiltonian

$$\mathcal{H} = NK^2 + \sum_{i=1}^{N} \left[\frac{1}{2}\boldsymbol{p}_i^2 + \frac{1}{2}\omega_i^2 - K\boldsymbol{p}_i \cdot \boldsymbol{s}_i + \frac{1}{2}\sum_{k\neq i} U(r_{ik}) - \frac{1}{2}\sum_{k\neq i} J(r_{ik}) \cos\theta_{ik} \right].$$

In that last expression, the constant term NK^2 can be discarded by shifting the energy reference, yielding

$$\mathcal{H} = \sum_{i=1}^{N} \left[\frac{1}{2}\boldsymbol{p}_i^2 + \frac{1}{2}\omega_i^2 - K\boldsymbol{p}_i \cdot \boldsymbol{s}_i + \frac{1}{2}\sum_{k\neq i} U(r_{ik}) - \frac{1}{2}\sum_{k\neq i} J(r_{ik}) \cos\theta_{ik} \right].$$

This Hamiltonian, unlike the energy expressed in terms of the velocities, features a spin-momentum coupling in the kinetic energy.

Since I have shown that the present model is described by a well-defined Hamiltonian, the whole route to the construction of statistical mechanics described in Sec. II.2.1 applies. Consequently, the present model has a well-defined statistical mechanics description in the canonical ensemble, that follows the distribution

$$\mathcal{P}(\mathcal{C}) = \frac{1}{Z(\beta, \boldsymbol{\alpha}, \boldsymbol{\lambda})} \exp\left[-\beta\left(E - \boldsymbol{\alpha}\cdot\boldsymbol{P} - \boldsymbol{\lambda}\cdot\boldsymbol{L}\right)\right], \tag{II.11}$$

with $\mathcal{C}$ a configuration of the microscopic variables of the system, $\beta = 1/k_B T$, and the expressions of the intensive parameters $\boldsymbol{\alpha}$ and $\boldsymbol{\lambda}$ are *a priori* to be determined in this non-Galilean setting. Unlike in the usual setting, there is no reason to believe that the microcanonical entropy and the internal energy of the system do not depend explicitly on the momentum and angular momentum, so that one should check explicitly the effects of $\boldsymbol{\alpha}$ and $\boldsymbol{\lambda}$ on the moments of $\mathcal{P}$. I therefore introduce the canonical mean value of an observable as

$$\langle\cdot\rangle = \int_\Gamma d^{2N}\boldsymbol{R} d^{2N}\boldsymbol{P} d^N\boldsymbol{\Theta} d^N\boldsymbol{\Omega}(\cdot)\mathcal{P}(\mathcal{C}),$$

where I noted the phase space Γ, and introduced the short-hand notations

$$d^{2N}\boldsymbol{R} = \prod_{i=1}^{N} d^2\boldsymbol{r}_i, \qquad d^{2N}\boldsymbol{P} = \prod_{i=1}^{N} d^2\boldsymbol{p}_i,$$
$$d^{N}\boldsymbol{\Theta} = \prod_{i=1}^{N} d\theta_i, \qquad d^{N}\boldsymbol{\Omega} = \prod_{i=1}^{N} d\omega_i,$$

so that, for instance, the mean magnetisation per spin is defined through $\boldsymbol{m} = \langle \boldsymbol{s}_i \rangle$. Computing such mean values would prove to be very challenging in the full setting defined

by Eq. (II.11), so that I will henceforth assume, following standard hypotheses [81], that the angular momentum is here irrelevant because I am only considering a system that is very small compared to the reservoir.[4] In this case, the canonical distribution is described by

$$\mathcal{P}(\mathcal{C}) = \frac{1}{Z(\beta, \boldsymbol{\alpha})} \exp\left[-\beta \left(E - \boldsymbol{\alpha} \cdot \boldsymbol{P}\right)\right].$$

In this simpler setting, one can easily compute the mean value of an individual momentum, $\langle \boldsymbol{p}_i \rangle$, that only contains a Gaussian integral of the momentum. One finds

$$\langle \boldsymbol{p}_i \rangle = \boldsymbol{\alpha} + K \langle \boldsymbol{s}_i \rangle,$$

an expression that can be combined with the definition of the momentum to find $\boldsymbol{\alpha} = \langle \dot{\boldsymbol{r}}_i \rangle$. When summed over all particles and divided by N, this result yields $\boldsymbol{\alpha} = \boldsymbol{v}_G$, the velocity of the centre of mass, so that

$$\mathcal{P}(\mathcal{C}) = \frac{1}{Z(\beta, \boldsymbol{v}_G)} \exp\left[-\beta \left(E - \boldsymbol{v}_G \cdot \boldsymbol{P}\right)\right].$$

Therefore, for this model, one recovers the result obtained in the context of Galilean theories that $\boldsymbol{\alpha} = \boldsymbol{v}_G$. This result might be linked to the fact that the energy, when expressed as a function of the velocities alone, takes the same form as that of a Galilean system. Indeed, looking at the energy written in Eq. (II.10), one could argue that the microcanonical entropy should still depend on $E_{int} = E - N v_G^2/2$, or equivalently $E_{int} = E - (\boldsymbol{P} - K\boldsymbol{m})^2/(2N)$, which yields $\partial E_{int}/\partial \boldsymbol{P} = -\boldsymbol{v}_G$ and $\boldsymbol{\alpha} = \boldsymbol{v}_G$ like in the Galilean case. However, unlike in Galilean theories, here one cannot set $\boldsymbol{v}_G$ to zero and hope to capture every aspect of the physics of the system.

Besides, it is useful to compute the second moment of $\boldsymbol{p}_i$ and the first two moments of ω_i. A calculation very similar to that of $\langle \boldsymbol{p}_i \rangle$ yields

$$\langle \boldsymbol{p}_i^2 \rangle - \langle \boldsymbol{p}_i \rangle^2 - K^2 \left(\langle \boldsymbol{s}_i^2 \rangle - \langle \boldsymbol{s}_i \rangle^2 \right) = 2 k_B T, \tag{II.12}$$

meaning that the fluctuations of momenta and spins are correlated, and that the kinetic energy is not directly proportional to the temperature. Regarding the angular velocity, it is easy to show that $\langle \omega_i \rangle = 0$, and that

$$\langle \omega_i^2 \rangle = k_B T.$$

Therefore, the angular velocities are the only variables the fluctuations of which directly yield the temperature: they are the only "good thermometer".

Finally, using only the definition of the conserved quantities and the fluctuation relations obtained in this section, it is possible to reach an intuitive understanding of the behaviour of this model. Consider the special case of a zero total momentum, $\boldsymbol{P} = \boldsymbol{0}$ or equivalently $\boldsymbol{v}_G = -K\boldsymbol{m}$. At high temperatures or energies, where the spins are disordered, this choice ensures that the system is still. Looking at the expression (II.10) of E,

[4] In the context of this thesis, it is also justified by the fact that the simulations I use, that are described in Sec. II.2.3, are performed in a periodic box, so that the conserved angular momentum is ill-defined in cases in which particles fill the whole box.

and seeing it as a function that the system seeks to minimise, one expects the ferromagnetic couplings to fuel a growth of $\boldsymbol{m}$ at low temperatures. Consequently, because of the conservation of momentum, the velocity of the centre of mass should grow. However, a growth of $\boldsymbol{v}_G$ leads to an increase of the kinetic energy. There is therefore a frustration between a tendency to align, due to the magnetic part of the energy, and the high associated kinetic energy cost caused by the conservation of momentum. In practice, since v_G grows like K, one would expect collective motion to exist only up to a finite value of K. Furthermore, in the thermodynamic limit, as discussed in detail in Sec. II.3, the Mermin-Wagner argument [54, 55] *a priori* prevents a transition to a ferromagnetic phase at finite temperatures. Therefore, one also expects collective motion to be suppressed as the number of particles increases. The precise effects of K and N on the ordering of the spins and velocities at various temperatures and densities are discussed at length in Chapter IV.

b) More General Coupling: Degree-Two Polynomial

It is natural at this point to wonder whether more complicated spin-velocity couplings would lead to equally well-defined dynamics and, hopefully, to an interesting phenomenology. A first remark is that, due to the rotational invariance of the spins and velocities, any linear spin-velocity coupling with a shape

$$\mathcal{L}_{sv} = K\boldsymbol{v_i} \cdot \mathcal{R}_\varphi \left[\boldsymbol{s_i}\right] \ ,$$

where $\mathcal{R}_\varphi$ is a rotation by an angle φ, would be equivalent to the previous linear coupling. Indeed, the momentum conservation would now impose a fixed angle determined by φ between the velocities and spins at low energies.

The next most natural extension is the addition of a quadratic spin-velocity coupling. Indeed, one could hope that such a term could actually play a role in the conserved energy by decreasing the cost of the kinetic energy. I therefore consider the Lagrangian spin-velocity interaction terms defined by

$$\mathcal{L}_{sv} = \sum_{i=1}^{N} K_1 \boldsymbol{v_i} \cdot \boldsymbol{s_i} - \sum_{i=1}^{N} K_2 \left(\boldsymbol{v_i} \cdot \boldsymbol{s_i}\right)^2 \ ,$$

where I called K_1 the coupling constant of the linear term and K_2 the one in front of the quadratic coupling for clarity. For positive values of K_2, this coupling decreases the kinetic cost of velocities aligned with the spins. With this coupling, the canonical linear momentum reads

$$\boldsymbol{p}_i = \dot{\boldsymbol{r}}_i + K_1 \boldsymbol{s}_i - 2K_2 \left(\dot{\boldsymbol{r}}_i \cdot \boldsymbol{s}_i\right) \boldsymbol{s}_i \ ,$$

from which one can write down the definitions of the conserved linear and angular momenta, $\boldsymbol{P} = \sum_i \boldsymbol{p}_i$ and $\boldsymbol{L} = \sum_i \boldsymbol{r}_i \times \boldsymbol{p}_i + \omega_i \hat{\boldsymbol{e}}_z$, like before. I also write an expression for the energy that is conserved by this model, in the same way as before,

$$E = \sum_{i=1}^{N} \left[\frac{1}{2}\dot{\theta}_i^2 + \frac{1}{2}v_i^2 - K_2 \left(\boldsymbol{v}_i \cdot \boldsymbol{s}_i\right)^2 + \frac{1}{2}\sum_{k\neq i} U(r_{ik}) - \frac{1}{2}\sum_{k\neq i} J(r_{ik}) \cos\theta_{ik} \right] \ .$$

The quadratic term in the Lagrangian decreases the cost of the kinetic energy, even when the energy is expressed as a function of the velocities. Hence, such terms could in principle favour the formation of equilibrium moving states. However, one can clearly see that problems arise for $K_2 \geq 1/2$, since in this range of values the energy can be made arbitrarily low for $v_i \to \infty$. In fact, in this regime, the dynamics themselves are ill-defined, because the Lagrangian is no longer convex with respect to the velocities, and this leads to unphysical results like infinite accelerations or velocities even for a single particle system, as briefly discussed in App. A. While there are ways to exploit such theories using path integral formulations [86] as well as interpretations of their peculiarities in quantum models, I will here restrict ourselves to $K_2 < 1/2$. Note that the convexity condition imposed by $K_2 < 1/2$ would lead to similar restrictions for other non-linear couplings, with several forbidden intervals for their corresponding coupling constants.

Another issue is to rewrite the Hamiltonian in terms of its canonical variables. It is here more complicated than usual, as the only way to do so is to project the canonical momentum onto the vectors of interest, $\boldsymbol{v}_i$, $\boldsymbol{s}_i$, and $\boldsymbol{p}_i$. After some algebra, I obtain

$$\begin{aligned} \boldsymbol{v}_i \cdot \boldsymbol{s}_i &= \frac{\boldsymbol{p}_i \cdot \boldsymbol{s}_i - K_1}{1 - 2K_2}, \\ \boldsymbol{v}_i \cdot \boldsymbol{p}_i &= v_i^2 + K_1 \boldsymbol{v}_i \cdot \boldsymbol{s}_i - 2K_2 \left(\boldsymbol{v}_i \cdot \boldsymbol{s}_i\right)^2 , \\ v_i^2 &= p_i^2 + A \boldsymbol{p}_i \cdot \boldsymbol{s}_i + B \left(\boldsymbol{p}_i \cdot \boldsymbol{s}_i\right)^2 + C , \end{aligned} \tag{II.13}$$

where I defined the constants

$$A = -\frac{2K_1}{(1-2K_2)^2} , \qquad B = \frac{4K_2(1-K_2)}{(1-2K_2)^2} , \qquad C = \frac{K_1^2}{(1-2K_2)^2} .$$

Using these projections, after some more algebra, I can finally rewrite the Hamiltonian as a function of the canonical variables only

$$\mathcal{H} = \sum_{i=1}^{N} \left[\frac{1}{2}\omega_i^2 + \frac{1}{2}p_i^2 - \tilde{K}_1 \boldsymbol{p}_i \cdot \boldsymbol{s}_i + \tilde{K}_2 \left(\boldsymbol{p}_i \cdot \boldsymbol{s}_i\right)^2 + \frac{1}{2}\sum_{k \neq i} U(r_{ik}) - \frac{1}{2}\sum_{k \neq i} J(r_{ik}) \cos\theta_{ik} \right] ,$$

where the Hamiltonian coupling constants $\tilde{K}_1$ and $\tilde{K}_2$ are, interestingly, defined differently from the Lagrangian ones,

$$\tilde{K}_1 = \frac{K_1}{1-2K_2} , \qquad \tilde{K}_2 = \frac{K_2}{1-2K_2} ,$$

and where I discarded a constant term E_0 defined as

$$E_0 = \frac{K_1^2}{2(1-2K_2)} .$$

It is a priori much more difficult and maybe even impossible to perform this inversion analytically for any other non-linear couplings, as the vector projections used here no longer yield linear equations between the terms of interest. In particular, it is tempting to choose a coupling of the form $\hat{\boldsymbol{v}}_i \cdot \boldsymbol{s}_i$, where $\hat{\boldsymbol{v}}_i = \boldsymbol{v}_i / v_i$, since it would favour pure alignment between the spins and the velocities, that would not become weaker as the

typical speeds decrease. However, such a coupling yields a system of equations that do not allow to write a Hamiltonian in terms of the corresponding canonical momentum. Also note that higher order polynomials in $\boldsymbol{v}_i \cdot \boldsymbol{s}_i$ yield, instead of Eq. (II.13), polynomial equations in $\boldsymbol{v}_i \cdot \boldsymbol{s}_i$ with degree higher or equal to two, so that several roots can exist.

Therefore, the only two reasonable couplings one can imagine to get unequivocal, analytical Hamiltonian dynamics with a spin-velocity coupling are the linear and quadratic couplings. Any other non-linear term will lead either to convexity or to $\boldsymbol{p} \leftrightarrow \boldsymbol{v}$ inversion issues. An important message is that velocity terms in a conservative model are very constrained, so that it is in general much easier to take the system out of equilibrium to impose an ordering of the velocities. Note however that within these limitations, one could choose coupling strengths K_1 and K_2 that depend on the values of the spins and on the positions of the particles. Intuitively, such couplings could lead to density-dependent spin-velocity alignment, for instance. Although I do not explore this variant in this thesis, it would doubtless be an interesting direction for future research.

Regarding the statistical description, like in the case $K_2 = 0$, I will discard the angular momentum conservation term. The determination of the value of $\boldsymbol{\alpha}$, as it is more technical to perform than in the case $K_2 = 0$, is postponed to the calculation of the mean-field properties of this model, that is reported in Sec. IV.6.1. One finds, just like in the $K_2 = 0$ case, $\boldsymbol{\alpha} = \boldsymbol{v}_G$.

Regarding the physical importance of the quadratic coupling introduced in this part, it does not seem to make the system simpler nor to lead to new physics relevant to collective motion for $K_1 > 0$. Indeed, if I reproduce the discussion at the end of the previous section, and consider only cases with $\boldsymbol{P} = \boldsymbol{0}$, I expect collective motion only for magnetised states. In these states, assuming that I only consider states with $\boldsymbol{s}_i = \boldsymbol{m}, \forall i$ the momentum conservation constraint is now $\boldsymbol{v}_G = -\tilde{K}_1 \boldsymbol{m}$, so that the velocity of the centre of mass will just be rescaled in the same way as the coupling constants in the Hamiltonian. Therefore, I roughly expect to observe the same states as in the case $K_2 = 0$. Further proof that I do not expect any significant qualitative change when adding K_2 can be obtained by computing the partition function and observables in a mean-field approximation. The full calculation is reported in Sec. IV.6.1, and shows that the results are essentially the same as those obtained with K_1 only [69]. In particular, the magnetisation curves remain almost unaltered by the addition of K_2.

The case $K_1 = 0, K_2 > 0$, however, might be interesting to study on its own, as it favours nematic order between the velocity and the spins. This is reminiscent of a recent model of active matter in which velocities are allowed to switch between alignment and anti-alignment with an internal spin degree of freedom [87]. A similar nematic spin-velocity coupling was also considered in systems of active disks with nematic spin alignment [88], and led to the destruction of perfectly aligned nematic states, that are replaced by "turbulent" states containing many topological defects. These two recent incursions into the world of nematic spin-velocity couplings suggest that it would be interesting to study their conservative counterpart. It however looks like a different problem than the one of collective motion, as I do not expect any spontaneous flow of particles to arise in the case $K_1 = 0$, whatever the value of K_2. In light of these results, I am confident that the model with a single K_1 should contain all the physics related to the addition of a conservative, and polar spin-velocity coupling.

II.2.3 Simulation Method

In this section, I describe in detail the simulation method used throughout this thesis whenever numerical results are presented, and I justify the choice of the method I use, called Molecular Dynamics (MD).

a) Molecular Dynamics Simulations: Definition

Consider a Hamiltonian system, with canonical variables $\boldsymbol{q}$ and $\boldsymbol{p}$, described by a Hamiltonian $\mathcal{H}$ and a Lagrangian $\mathcal{L}$. The Hamiltonian equations of motion are

$$\dot{\boldsymbol{q}} = \frac{\partial \mathcal{H}}{\partial \boldsymbol{p}},$$
$$\dot{\boldsymbol{p}} = -\frac{\partial \mathcal{H}}{\partial \boldsymbol{q}}.$$

Since these equations are first-order differential equations, they can rather easily be integrated numerically over a finite but small time step dt, starting from a given initial condition. A direct integration of the Hamiltonian equations describing an isolated system is called Molecular Dynamics. By definition, this scheme describes the evolution of a whole isolated system, and conserves, in the limit $dt \to 0$, the energy and total momentum of the system up to numerical errors[5]. This method therefore samples the microcanonical ensemble, as opposed to numerical schemes that draw each step using the canonical measure to mimic the effect of a thermostat. In practice, I integrate the equations of motion using a standard fourth order Runge-Kutta method. This method is defined as follows. Consider an initial value problem defined by

$$\dot{y} = f(t, y), \qquad y(t_0) = y_0,$$

and a discretized time step dt such that I only compute y at discrete times defined recursively by

$$t_{n+1} = t_n + dt.$$

It is easy to show that the evolution of y between these time steps can be approximated by [89]

$$y(t_{n+1}) \equiv y_{n+1} = y_n + \frac{1}{6}\left(k_1 + 2k_2 + 2k_3 + k_4\right) + O(dt^5),$$

with

$$\begin{aligned}
k_1 &= dt f(t_n, y_n),\\
k_2 &= dt f\left(t_n + \frac{dt}{2}, y_n + \frac{k_1}{2}\right),\\
k_3 &= dt f\left(t_n + \frac{dt}{2}, y_n + \frac{k_2}{2}\right),\\
k_4 &= dt f(t_n + dt, y_n + k_3).
\end{aligned}$$

[5] Note, however, that if the bounding box of the system has periodic boundary conditions, the angular momentum is a priori not conserved, since positions "jump" from one side to the other

These increments are evaluations of the slope at four different points in the time window dt.

Note that many authors rather resort to so-called leapfrog, or Verlet methods, following the definition provided by Verlet himself [90]. These methods consist in evaluating the updates of positions and velocities of a system at different times, using the fact that the velocity does not explicitly depend on the position. The interest of using them is that they are so-called symplectic methods, meaning that they exactly conserve energy and momentum. In the context of spin-velocity couplings, however, the space momentum explicitly depends on the spin, which is a position-like variable. For instance, in the case of a linear spin-velocity coupling, the Hamiltonian equations of motion read

$$\begin{aligned}
\dot{\boldsymbol{r}}_i &= \boldsymbol{p}_i - K\boldsymbol{s}_i, \\
\dot{\boldsymbol{p}}_i &= \sum_{k(\neq i)} \left(\frac{\partial J(r_{ik})}{\partial \boldsymbol{r}_i} \cos\theta_{ik} - \frac{\partial U(r_{ik})}{\partial \boldsymbol{r}_i} \right), \\
\dot{\theta}_i &= \omega_i, \\
\dot{\omega}_i &= K\boldsymbol{p}_i \cdot \boldsymbol{s}_{\perp,i} + \sum_{k(\neq i)} J(r_{ik}) \sin\theta_{ik}.
\end{aligned}$$

Because $\dot{\boldsymbol{p}}_i$ depends explicitly on $\boldsymbol{s}_i$, Verlet-like algorithms cannot be applied directly here.

b) Choice of Molecular Dynamics

In the context of this thesis, the choice of Molecular Dynamics was made because it samples the microcanonical distribution. Indeed, as discussed in Sec. II.2.2, the non-Galilean character of the present model forces to consider the canonical distribution defined by

$$\mathcal{P}_{\beta,\boldsymbol{v}_G}[\mathcal{C}] \propto e^{-\beta(\mathcal{H}[\mathcal{C}] - \boldsymbol{v}_G \cdot \boldsymbol{P}[\mathcal{C}])},$$

where both the inverse temperature β and the velocity of the centre of mass $\boldsymbol{v}_G$ are imposed by the bath and, in the context of simulations, chosen at the start of the simulation. As a consequence, usual canonical ensemble sampling via a Monte Carlo-like scheme is not expected to be the most interesting setting since the aim of the model is to demonstrate the *emergence* of a spontaneous $\boldsymbol{v}_G$ as a response to a lowering of the temperature or energy. It seems more natural, instead, to impose a total momentum $\boldsymbol{P}$. In practice, in order for collective motion to emerge at low temperatures, one should choose $\boldsymbol{P} = \boldsymbol{0}$, which ensures that the high-temperature isotropic phase does not move.

Another possibility would be to impose a temperature and a total momentum, that is to say, to work in an intermediary ensemble that lies between the microcanonical (conserved energy and momentum) and the canonical (conserved temperature and momentum) ensembles. However, little is known on the peculiarities of non-Galilean statistical mechanics, so that I choose the simpler setting of the microcanonical ensemble. This also enables me to see the actual dynamics of the system, and for instance physical displacement of particles over long times.

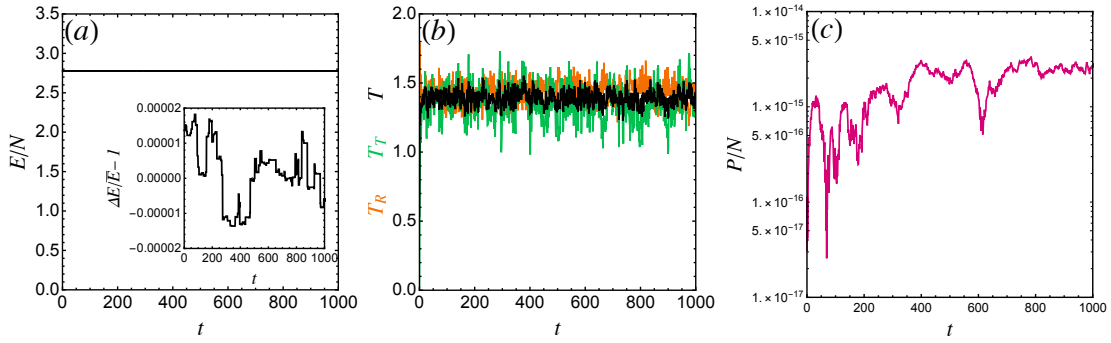

Fig. II.2 **Energy and Temperature in Simulated Conservative Dynamics.** (*a*) Free evolution of the energy per particle E/N. (*b*) Free evolution of the rotational (orange) and translational (green) temperatures, and of the average of the two (black). (*c*) Free evolution of the modulus of the momentum (in lin-log scale). All three panels are obtained starting from random initial conditions (uniform positions and spin orientations, unit-variance Gaussian-distributed momenta and angular velocities), and $P(0) = 0$. In the inset of (*a*), I plot the evolution of the relative fluctuations $E(t)/\overline{E} - 1$ of the energy around the time-averaged value $\overline{E}$.

c) Numerical Recipes

Having specified the kind of simulations used in this thesis, I now describe in detail the precise numerical recipes used to obtain the results that I present in Chapters III,IV, and V. First off, since MD simulations sample the microcanonical ensemble, one should specify the considered values of the total momentum $\boldsymbol{P}$ and of the total energy E. In all the rest of this work, I choose a total momentum $\boldsymbol{P} = \boldsymbol{0}$. Since the spins are disordered at high energies, this choice ensures that high-energy states are also still. Concerning the energy, it is set by the following choice of initial conditions: positions are drawn uniformly anywhere in the simulation box, and spins uniformly on the circle, while momenta and angular velocities of the spins are drawn from centered, reduced gaussian distributions. The obtained states equilibrate after a very short time following the Hamiltonian dynamics, since they are at rather high energies.

As an illustration, I plot in Fig. II.2 a typical run of the system at a fixed energy obtained from random initial conditions (uniform positions and angles, unit-variance Gaussian-distributed momenta and angular velocities), for $N = 512$ particles, at a packing fraction $\phi = 0.55$, and with $K = 1$. Fig. II.2(*a*) shows that the Runge-Kutta integrator indeed approximately conserves the energy as the dynamics are run, with fluctuations ΔE from the time-averaged value value $\overline{E}$ of the energy of the order of 1 per $100,000$. Fig. II.2(*b*) illustrates the fact that the rotational temperature, measured from fluctuations of ω, and the translational temperature, obtained from fluctuations of momenta and spins, fluctuate around the same mean value. Fig. II.2(*c*) represents the modulus of the momentum per particle P/N against time, showing that it departs from zero momentum since the algorithm I used is not symplectic, but does not grow beyond values of the order of 10^{-15}.

Then, lower-energy equilibrated states are obtained by performing a simulated an-

nealing, following the strategy used in Bore *et al.* [69]. The idea is to lower the rotational kinetic energy by multiplying all the ω_i's by a factor $\lambda < 1$ every now and then. If the annealing factor λ is sufficiently close to 1, and the annealing events are sufficiently spaced in time, the system smoothly re-equilibrates at a new, lower energy with a typical time called the equilibration time. In cases in which the system crosses a critical point, this equilibration time typically becomes large, so that λ should be chosen very close to 1 to obtain equilibrated data (see for instance Refs. [91–94]). In practice, λ is chosen close enough to 1 that the observables of the system do not depend on its value any more, and such that two-time correlations in the system do not depend on the choice of the initial time (there is no "aging"). The choice of lowering only the ω_i's originates from the fluctuation relation $\langle \omega_i^2 \rangle = k_B T$, established in the canonical ensemble in Sec. II.2.2. Indeed, the angular velocities are here the only good thermometer, so that lowering them should be directly equivalent to cooling the system down. Note, however, that in the microcanonical setting used here, the temperature is not fixed, but fluctuates around its mean value $\langle T \rangle$ defined by the values of the energy and momentum.

In practice, using the rescaled units introduced at the beginning of Sec. II.2.2, annealings are performed by multiplying angular velocities by a factor of 0.9999 every 100 time units, using a time step $dt = 10^{-3}$. I checked that this rate, which is also the one that was used and checked in Ref. [69], yielded curves similar to those obtained for slower annealing rates for the usual observables, and that no ageing was visible at reasonable time scales.

In Chapter III, where $K = 0$, I also subject the system to quenches, violent events that cool the system down. The procedure when performing these quenches is this time different: in order to make sure that all degrees of freedom are cooled down, both the angular velocities and the moduli of momenta are multiplied by a quench factor $\lambda_Q = 0.1$ once.

d) The $3d$ case

In order to simulate the system in 3 dimensions, which I discuss in Chapter IV, I also used the Runge-Kutta Molecular Dynamics method. In this higher dimensional case the proper Hamiltonian dynamics are given by

$$\begin{aligned}
\dot{\boldsymbol{r}}_{\boldsymbol{i}} &= \boldsymbol{p_i} - K_1 \boldsymbol{s_i} \,, \\
\dot{\boldsymbol{p}}_{\boldsymbol{i}} &= \frac{1}{2} \sum_{k \neq i} \left(j'(r_{ik}) \boldsymbol{s_i} \cdot \boldsymbol{s_k} - u'(r_{ik}) \right) \hat{\boldsymbol{r}}_{\boldsymbol{i}} \,, \\
\dot{\theta}_i &= p_{\theta_i} \,, \\
\dot{p}_{\theta_i} &= \frac{p_{\phi_i}^2 cos\theta_i}{\sin^3 \theta_i} - \frac{\partial H_{int}}{\partial \theta_i} \,, \\
\dot{\phi}_i &= \frac{p_{\phi_i}}{\sin^2 \theta_i} \,, \\
\dot{p}_{\phi_i} &= -\frac{\partial H_{int}}{\partial \phi_i} \,,
\end{aligned}$$

where I called H_{int} the interaction part of the Hamiltonian. These equations pose a major problem to their numerical integration, as divergences at the poles of the sphere appear

in the evolution equations for ϕ_i and p_{θ_i}, at each time step. This problem, which is usual for simulations of rotors on spheres, is here rather tricky to solve [95], and a variety of strategies can be tested. In my case, I chose to write modified evolution equations in which I consider spins to be arbitrary Cartesian vectors, but that should (within numerical accuracy) conserve the spin normalisation. The idea, adapted from previous works on Heisenberg spins [96] and dynamics in a spherical geometry [95] consists in writing

$$H \equiv \sum_{i=1}^{N} \left[\frac{\boldsymbol{p_i}^2}{2} + \frac{\boldsymbol{L_i^2}}{2} - K_1 \boldsymbol{p_i} \cdot \boldsymbol{s_i} - \frac{1}{2} \sum_{k(\neq i)} \left(j(r_{ik}) \boldsymbol{s_i} \cdot \boldsymbol{s_k} - u(r_{ik}) \right) \right] ,$$

where $\boldsymbol{L_i} = \boldsymbol{s_i} \wedge \boldsymbol{p s_i}$ is the usual angular momentum of the spins. For unit spins, $L_i^2 = \boldsymbol{p}_{\boldsymbol{s_i}}^2 = \dot{\boldsymbol{s}}_{\boldsymbol{i}}^2$, as their time derivative should be perpendicular to them. I then write the evolution equations:

$$\begin{aligned} \dot{\boldsymbol{s}}_{\boldsymbol{i}} &= \boldsymbol{L_i} \wedge \boldsymbol{s_i} \, , \\ \dot{\boldsymbol{L}}_{\boldsymbol{i}} &= \boldsymbol{s_i} \wedge \left(-\frac{\partial H}{\partial \boldsymbol{s_i}} \right) . \end{aligned}$$

These equations are natural consequences of the definition of $\boldsymbol{L}_i$ with respect to $\boldsymbol{p}_{\boldsymbol{s}_i}$, the actual canonical momentum associated to the spins. The advantage of this way of writing the evolution is that, even though it is not strictly symplectic in 3 dimensions, it does conserve the modulus of the spins up to numerical errors.

II.3 Continuous-Spin Magnetism: At Mean-Field and Beyond

In this section, I review the known properties of systems of continuous spins. I start by describing in Sec. II.3.1 the concept of critical transitions in such models at the so-called mean-field level, which corresponds to the limit in which the dimension of space is taken to infinity. I also discuss the usual methods to obtain a mean-field description from a microscopic description. I then apply such methods to models containing a spin-velocity coupling in Sec. II.3.2. Then, in Sec. II.3.3, I discuss the reasons behind the deviations from the mean-field description in finite-size, finite-dimensional simulations. Finally, in Sec. II.3.4, I discuss at length the very specific case of systems of $2d$ continuous spins placed on a $2d$ square lattice, and the BKT transition. This last part is essential to understand the discussion of the presence or absence of a BKT transition in the case of particles moving in continuous space that I present in Chapter III, and its implications on the nature of the topological defects observed in the case $K > 0$, that I describe at length in Chapter IV.

II.3.1 Critical Phenomena

a) Definitions: Continuous-Spin Models

Consider a collection of N unit vectors of arbitrary dimension d_s, $\boldsymbol{s}_i$, placed on a d-dimensional hypercubic lattice. In the simplest setting, they are assumed to interact only with their nearest neighbours with a ferromagnetic (aligning) interaction of amplitude

$J > 0$, that is described by the Hamiltonian

$$\mathcal{H} = -\frac{J}{2}\sum_{i=1}^{N}\sum_{j\in\partial i}\boldsymbol{s}_i\cdot\boldsymbol{s}_j - \boldsymbol{h}\cdot\sum_{i=1}^{N}\boldsymbol{s}_i, \tag{II.22}$$

where ∂i is a short-hand notation for the nearest-neighbours of site i, and $\boldsymbol{h}$ is a constant external field. Such systems are generally studied in contact with a thermostat at temperature T, so that they are described by the canonical distribution

$$\mathcal{P}(\mathcal{C}) = \frac{1}{Z(\beta,\boldsymbol{h})}e^{-\beta\mathcal{H}},$$

where $\beta = 1/k_BT$ and Z is the partition function at the considered temperature. The canonical ensemble, as defined by this distribution of configurations, can be sampled numerically to study the property of such models depending on their temperature T, the intensity of the coupling J, the dimension of space d, the dimension of spins d_s, the number of particles N.

The most usual observables in the context of systems of spins are the mean total magnetisation,

$$\boldsymbol{M} \equiv \left\langle\sum_{i=1}^{N}\boldsymbol{s}_i\right\rangle,$$

and the corresponding intensive observable $\boldsymbol{m} = \boldsymbol{M}/N$. If one considers a system of spins described by the Hamiltonian (II.22) at zero field ($\boldsymbol{h} = \boldsymbol{0}$), and cools it down from a high temperature, in general, the magnetisation will switch from a high-temperature regime with $|\boldsymbol{M}| \sim N^{1/2}$, corresponding to a situation in which the magnetisation is simply a sum of independent random variables, to a low-temperature regime with $|\boldsymbol{M}| \sim N$, corresponding to a situation in which spins are aligned together. The high-temperature phase is often called the paramagnetic phase, while the low-temperature phase is called the ferromagnetic phase. In the limit $N \to \infty$ (the "thermodynamic limit"), this change of behaviour is associated to a singularity of the intensive magnetisation modulus $m = |\boldsymbol{m}|$ at a temperature T_c called the critical temperature, and is called a critical phase transition. A sketch usual aspect of the magnetisation versus the temperature at zero field is shown in Fig. II.3.

The singularity at T_c is characterised by an algebraic behaviour of the intensive magnetisation right below the critical temperature, $m \sim |t|^{\beta}$, where $t = (T - T_c)/T_c$ is the reduced temperature, and β is called a critical exponent. Similar exponents can be defined for different quantities, that also exhibit a singular behaviour at the critical temperature. For instance, one often defines the zero-field magnetic susceptibility on both sides of the critical temperature,

$$\chi_{m,T} \equiv \left.\frac{\partial\boldsymbol{M}}{\partial\boldsymbol{h}}\right|_{h=0}.$$

The subscript m indicates that this is the susceptibility associated to the magnetisation, and I add the subscript T to emphasise that this definition in fact contains a trivial temperature factor,

$$\chi_{m,T} = \frac{\beta}{N}\left(\left\langle\boldsymbol{M}^2\right\rangle - \langle\boldsymbol{M}\rangle^2\right),$$

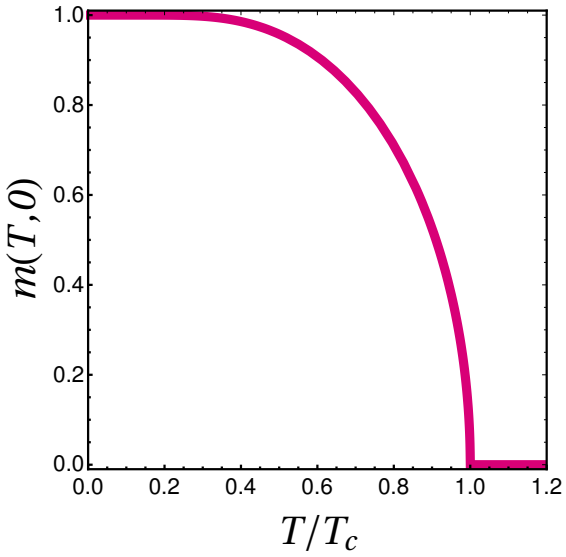

Fig. II.3 **Sketch of the critical behaviour of a magnet at zero-field.**

so that it is common to discuss the "reduced" susceptibility $\chi_m = k_B T \chi_{m,T}$, which is simply the second moment of the extensive magnetisation. In the thermodynamic limit, the susceptibility $\chi_{m,T}$ diverges at the critical temperature, and behaves algebraically close to T_c following

$$\chi_\pm \sim |t|^{-\gamma_\pm},$$

where the exponent is a priori different on each side of the critical point, but is in fact in general the same so that $\gamma_+ = \gamma_- = \gamma$ [2]. Finally, one often defines the spatial spin-spin correlation function, $C(r)$, defined by

$$C(r) \equiv \langle \boldsymbol{s}_i \cdot \boldsymbol{s}_j \delta(r - r_{ij}) \rangle - \langle \boldsymbol{s}_i \rangle \cdot \langle \boldsymbol{s}_j \rangle,$$

where the δ function is a Dirac delta that selects spins separated by a distance r. That function, close to the critical temperature, behaves like [97]

$$C(r) \sim r^{-(d-2+\eta)} G(r/\xi), \tag{II.23}$$

where d is the dimension, η is a critical exponent, G is a scaling function that typically decreases exponentially, with a typical decay rate that defines the correlation length ξ. This correlation length diverges at the critical temperature, and also depends on the temperature algebraically according to

$$\xi_\pm \sim |t|^{-\nu_\pm},$$

where the exponents on each side of T_c can be different, but are very often the same $\nu_+ = \nu_- = \nu$.

A set of critical exponents (which only depends on the symmetries of the model) defines so-called universality classes, groups of models that behave in the same way close

to their critical transitions. These exponents are not independent of each other, they are linked to each other by so-called hyperscaling relations [97, 98],

$$\gamma = (2 - \eta)\nu, \tag{II.24}$$
$$d\nu = \gamma + 2\beta. \tag{II.25}$$

In general, these exponents are very hard to predict analytically for an arbitrary set of d_s and d. It is however rather easy to predict a set of properties, like the magnetisation, as well as critical exponents in a specific setting, the so-called mean-field description.

b) Mean-field Description

In order to predict the properties of a model of spins, it is sufficient to compute the partition function,

$$Z \equiv \sum_{\mathcal{C}} e^{-\beta \mathcal{H}(\mathcal{C})}.$$

Indeed, the mean values of observables can in general be expressed as derivatives of the logarithm of Z, using the definition of the canonical distribution. For instance, one can check that

$$\boldsymbol{M}(T, \boldsymbol{h}) = k_B T \frac{\partial \ln Z}{\partial \boldsymbol{h}},$$
$$\chi_{m,T}(T) = k_B T \left. \frac{\partial^2 \ln Z}{\partial \boldsymbol{h}^2} \right|_{h=0}.$$

However, in general, Z cannot be computed exactly due to the nearest-neighbour interactions. One thus needs to use some kind of approximation to make some progress. The simplest approximation consists in the Curie-Weiss mean-field treatment [99]. The spirit of the approximation is to assume that each spin $\boldsymbol{s}_i$ feels a "molecular field" (as defined by Weiss [100])

$$\boldsymbol{h}_{eff,i} = \boldsymbol{h} + J \sum_{j \in \partial i} \boldsymbol{s}_j,$$

that can be approximated by its mean value

$$\langle \boldsymbol{h}_{eff,i} \rangle = \boldsymbol{h} + Jz \langle \boldsymbol{s}_j \rangle,$$

where z is the number of nearest neighbours of a site, and by definition $\langle \boldsymbol{s}_i \rangle = \boldsymbol{m}$. In this description, spin i therefore literally feels a "mean field", created by all other spins. This spin is then described by the statistics described by the distribution

$$\mathcal{P}_{MF}(\boldsymbol{s}_i) = \frac{1}{Z_{MF}(d_s)} e^{-\beta \langle \boldsymbol{h}_{eff,i} \rangle \cdot \boldsymbol{s}_i},$$

with the mean-field particle function

$$Z_{MF}(d_s) \equiv \int d^{d_s} \boldsymbol{s}_i e^{-\beta \langle \boldsymbol{h}_{eff,i} \rangle \cdot \boldsymbol{s}_i}.$$

In particular, one can check that for $d_s = 1$ (Ising spins), one finds

$$Z_{MF}(d_s = 1) = 2\cosh\left(\beta\langle h_{eff,i}\rangle\right),$$

and that for $d_s = 2$ (XY spins),

$$Z_{MF}(d_s = 2) = 2\pi I_0\left(\beta\,|\langle \boldsymbol{h}_{eff,i}\rangle|\right), \tag{II.26}$$

where I_0 is a modified Bessel function of the first kind [101]. From this expression of the partition function as a function of the mean field, one can write down a self-consistent expression for the mean value of the magnetisation by computing

$$\boldsymbol{m} = \langle \boldsymbol{s}_i\rangle = k_B T \frac{\partial \ln Z_{MF}}{\partial \boldsymbol{h}}.$$

For instance, for Ising spins, one finds the equation

$$m = \tanh\left(\beta\left(h + Jzm\right)\right). \tag{II.27}$$

This equation can be solved numerically, for example yielding the curve that was shown in Fig. II.3 for $h = 0$ and $Jz = 1$: at $T_c = Jz$, the magnetisation goes from the high-temperature solution $m = 0$ a the low-temperature solution $m > 0$. The self-consistent equation (II.27) can then also be Taylor-expanded, slightly under the critical temperature, yielding

$$|t|m = h - \frac{1}{3}m^3 + O(h^3, m^5),$$

which grants access to the behaviour of the zero-field magnetisation close to the critical temperature,

$$m \sim |t|^{1/2}.$$

Therefore, this simple calculation yields a value for a critical exponent, $\beta = 1/2$. Similarly, one can compute the susceptibility exponent by writing

$$\chi_{m,T}^{-1} = \left.\frac{\partial h}{\partial m}\right|_{h=0} = t + m^2.$$

Using $m = 0$ for $T > T_c$ and $m \sim |t|^{1/2}$ for $T \leq T_c$, this equation yields, in both regimes, $\chi_{m,T} \sim |t|^{-1}$. One therefore finds $\gamma = 1$. The same exponents are found in the case $d_s = 2$ and, in fact, for any value of d_s: these exponents define a mean-field universality class.

Many other techniques can be used to study a model at mean-field level, such as the Bethe approximation or variational formulations. These other techniques yield the same mean-field exponents, but can yield different prefactors for the thermodynamic functions of interest. Among the other techniques, I would like to mention two in particular in this part.

The first one consists in replacing the Hamiltonian (II.22) by the following Hamiltonian

$$\mathcal{H}_{FC} = -\frac{J}{N}\sum_{i=1}^{N}\sum_{j\neq i}\boldsymbol{s}_i\cdot\boldsymbol{s}_j - \boldsymbol{h}\cdot\sum_{i=1}^{N}\boldsymbol{s}_i,, \tag{II.28}$$

in which I replaced the sum over nearest neighbours by a sum over all other spins, and rescaled the interaction constant J by a factor of N so that the energy remains proportional to N, and not to N^2. This Hamiltonian is often called the fully-connected Hamiltonian, as the underlying lattice of Hamiltonian (II.22) is here replaced by a complete (or "fully-connected") graph. It is equivalent to the previous approach, as the sum over interactions can be rewritten as

$$\sum_{i=1}^{N}\sum_{j\neq ii} \boldsymbol{s}_i \cdot \boldsymbol{s}_j = \frac{1}{N}\left(\sum_{i=1}^{N} \boldsymbol{s}_i\right)^2 - 1,$$

which only depends on the sum of all spins. Indeed, defining the average of spins in a configuration $\boldsymbol{m} = \sum_{i=1}^{N} \boldsymbol{s}_i/N$, the Hamiltonian can be rewritten as a function of this single variable,

$$\mathcal{H}_{FC}(\boldsymbol{m}) = -Jm^2 - N\boldsymbol{h}\cdot\boldsymbol{m},$$

where I discarded a constant term J. This description therefore considers the effect of interactions on an effective "mean spin", and computing the leading term in the mean value of $\boldsymbol{m}$ yields the same kind of self-consistent equations as in the Curie-Weiss setting. A derivation of these equations in the context of the models containing spin-velocity couplings is presented in more details in Sec. II.3.2.

The second standard technique is applicable to Hamiltonians written in field-theoretical terms, so that I must first write an approximate theory for the coarse-grained magnetisation $\boldsymbol{m}(\boldsymbol{x})$, that is then considered as a field in continuous space,

$$\beta\mathcal{H}_{LG} = \int d^d\boldsymbol{x}\left(\Phi\left[\boldsymbol{x}, \boldsymbol{m}(\boldsymbol{x}), \nabla\boldsymbol{m}(\boldsymbol{x}), \nabla^2\boldsymbol{m}(\boldsymbol{x}), ...\right] - \boldsymbol{h}\cdot\boldsymbol{m}\right),$$

where Φ is a free energy density around point $\boldsymbol{x}$, that depends on the value $\boldsymbol{m}(\boldsymbol{x})$, but also on its gradients due to interactions between spins. The field term was here kept explicitly out of Φ, as it is easy to show by linearity that it retains this form. The form of Φ can be inferred solely from symmetry arguments [2]. If the considered magnet is uniform in space, Φ contains no explicit $\boldsymbol{x}$ dependency, so that this dependency can be dropped. Assuming that there are no long-range interactions, one can hope that retaining only a few terms in a polynomial expansion of Φ provides an accurate description of the system. In the absence of an external field, one should only keep terms that are invariant under a rotation of all spins, meaning that only even terms should be kept in Φ. Finally, assuming that the coarse-graining scale is sufficiently large that there are many spins participating to the averaging in $\boldsymbol{m}$, one expects to find a theory that is close to a Gaussian theory due to the central limit theorem, with higher powers of m and its gradients being corrections. Using these arguments, one can write the effective theory up to order 4 in m and 2 in the gradients, introducing phenomenological parameters a, u, K that depend on the temperature,

$$\beta\mathcal{H}_{LG} = \int d^d\boldsymbol{x}\left(\frac{a}{2}m^2 + um^4 + \frac{K}{2}(\nabla m)^2 - \boldsymbol{h}\cdot\boldsymbol{m}\right), \tag{II.29}$$

which is called the Landau-Ginzburg theory.[6] The mean-field level description of this theory is obtained by considering only solutions that are uniform in space. Calling the volume of the system V, such solutions are associated to a partition function

$$Z_{MF} = \int d^{d_s}\boldsymbol{m} \exp\left[-V\left(\frac{a}{2}m^2 + um^4 - \boldsymbol{h}\cdot\boldsymbol{m}\right)\right].$$

In the limit of a large volume, $V \to \infty$, the integral is dominated by the value of $\boldsymbol{m}$ that maximizes the exponent of the integrand, also called the "saddle point",

$$Z_{MF} \approx Z_{sp} = \exp\left[-V \min_{\boldsymbol{m}} \Psi(\boldsymbol{m})\right],$$

where

$$\Psi = \frac{a}{2}m^2 + um^4 - \boldsymbol{h}\cdot\boldsymbol{m}.$$

The value of $\boldsymbol{m}$ that minimizes Ψ, and therefore dominates Z_{MF}, is the most likely value of $\boldsymbol{m}$. It verifies the equation obtained by derivating Ψ with respect to $\boldsymbol{m}$,

$$a\boldsymbol{m} + 4u\boldsymbol{m}^3 - \boldsymbol{h} = \boldsymbol{0}. \tag{II.30}$$

Very close to the critical temperature, t and u can be Taylor expanded up to first order,

$$a \approx a_0 + a_1(T - T_c),$$
$$u \approx u_0 + u_1(T - T_c),$$

where one should have $a_0 = 0$, $a_1 > 0$, and $u > 0$ for the magnetisation to match the mean-field aspect shown in Fig. II.3. Using these expressions and Eq. (II.30), one recovers the mean-field results discussed above. A similar field-theoretical formulation will be briefly discussed in Chapter IV, in the context of models that contain spin-velocity couplings, to see how they modify this picture.

Note that an additional advantage of this mean-field Landau-Ginzburg formulation is that Ψ is the effective mean-field free energy density felt by the magnet. It is therefore interesting to plot $\Psi(m)$ at different temperatures, and to interpret it as the potential energy landscape of a mechanical system, to get an intuitive picture of the behaviour of the system. Examples of such curves, both with (a) and without (b) an external field, are shown in Fig. II.4. For instance, Fig. II.4(a) immediately shows that, in the case $h = 0$ and at low temperatures, all directions of the magnetisation are equivalent, while the presence of a field tilts the energy landscape shown in (b). The shape of this free energy, with an axisymmetric double well, is often compared to that of a wine bottle, or Mexican hat, because of its shape in the case of a $2d$ magnetisation (see the inset of Fig. II.4(a)). Similar sketches of an effective free energy are presented in Sec. II.3.2, as well as in Chapter IV to discuss the peculiarities of the magnetisation in systems with a spin-velocity coupling.

[6] Note that this description can be recovered from the microscopic theory, by computing an explicit form for the coarse-grained fully-connected free energy and Taylor-expanding the entropic terms up to order m^4, then adding the lowest-order gradient term that is compatible with the symmetries. For the example of the Ising model see, for instance, Chaikin and Lubensky [4].

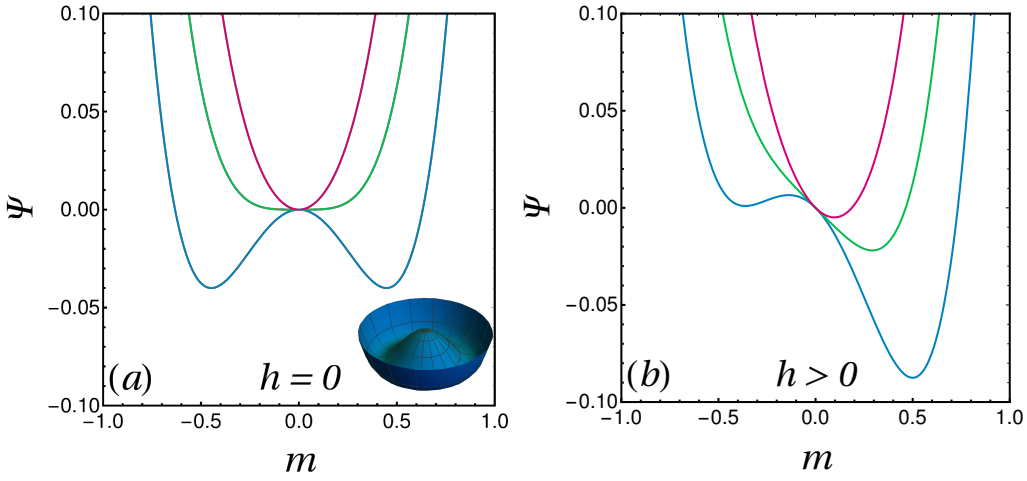

Fig. II.4 **Mean-Field Landau-Ginzburg Free Energy Density.** (a) Without an external field, $h = 0$, and (b) with an external field $h > 0$. In both panels, I chose $a = (T - T_c)$, $u = u_0 = 1$, $T_c = 1$, and I plotted three temperatures, $T = T_c/5$ (blue), $T = T_c$ (green), and $T = 2T_c$. In panel (b), $h = 0.1$. In the inset of (a), I replot the blue curve of the main panel as a function of the $2d$ magnetisation for $d_s = 2$.

c) Continuous Symmetries and Goldstone modes

A peculiarity of the models defined in Hamiltonian (II.22) for spins of dimension $d_s \geq 2$ and at zero field is that, while they are described by a Hamiltonian that has full rotational symmetry, their low-temperature phase does not: any given sample chooses a direction for its magnetisation $\boldsymbol{m}$. This phenomenon is a spontaneous symmetry breaking. However, as pointed out while commenting Fig. II.4, there is still no favoured direction for this net magnetisation, even in magnetised phases, so that the low-temperature energy landscape should be axisymmetric. Consequently, the magnetisation has access to a line of connected, equivalent minima corresponding to different orientations of the total magnetisation. Since these minima are connected, it has a zero potential energy cost for the total magnetisation to turn in this potential. Such collective excitations are called "Goldstone modes," or "soft modes." They are present in all systems with a broken continuous symmetries, and are for example the origin of phonons in solids [2].

In order to model these excitations, consider a system described by an effective Landau-Ginzburg Hamiltonian with a gradient term, as given by Eq. (II.29). To study rotations at the bottom of the Mexican hat, one can assume that the modulus of the magnetisation is fixed by the mean-field treatment described above, but that the magnetisation also carries a slowly varying set of "phase" coordinates $\boldsymbol{\theta}$,

$$\boldsymbol{m}(\boldsymbol{x}) = m_{MF}\hat{\boldsymbol{e}}(\boldsymbol{\theta}(\boldsymbol{x})).$$

Typically, in the context of a d_s-dimensional magnetisation, θ is one angle in $2d$, encoding a polar orientation, 2 angles in $3d$, encoding an orientation on a sphere, and the $d_s - 1$ angles necessary to define the hyperspherical coordinates in general. Once inserted into

the Landau-Ginzburg Hamiltonian, this magnetisation yields an energy

$$\beta\mathcal{H}_{sw} = \frac{\overline{K}}{2}\int d^d\boldsymbol{x}\sum_{a=1}^{ds-1}\left(\nabla\theta_a\right)^2,$$

where $\overline{K} = Km_{MF}^2$ is called the stiffness, and a is an index that runs over the coordinates of $\boldsymbol{\theta}$. This Hamiltonian is often called the spin-wave Hamiltonian, as it describes a superposition of plane-wave excitations of the magnetisation pattern. I shall discuss these excitations in more details in the case $d_s = d = 2$ in Sec. II.3.4.

II.3.2 Application: Mean-Field Treatment with a linear spin-velocity term

Using the concepts introduced in Sec. II.3.1, I here derive a mean-field description of the model defined in the Lagrangian (I.2), seeking only to describe its magnetic properties in phases with a homogeneous density, following the method used in Ref. [69]. In order to do so, I drop the repulsive interaction U and consider the fully-connected variant of the ferromagnetic interaction, so that I consider the mean-field Hamiltonian

$$\mathcal{H}_{FC} = \sum_{i=1}^{N}\left[\frac{1}{2}\boldsymbol{p}_i^2 + \frac{1}{2}\omega_i^2 - K\boldsymbol{p}_i\cdot\boldsymbol{s}_i - \frac{J}{2N}\sum_{k\neq i}\boldsymbol{s}_i\cdot\boldsymbol{s}_k - \boldsymbol{h}\cdot\boldsymbol{s}_i\right],$$

where J is a constant coupling, that was rescaled by N so that the total energy remains extensive, and $\boldsymbol{h}$ is a constant external field. As discussed in Sec. II.2.2, the canonical distribution that describes the statistical mechanics of this model is given by

$$\mathcal{P}\left(\mathcal{C}\right) = \frac{1}{Z(\beta,\boldsymbol{v_G})}e^{-\beta(\mathcal{H}_{FC}(\mathcal{C})-\boldsymbol{v}_G\cdot\boldsymbol{P}(\mathcal{C}))},$$

where $\mathcal{C}$ is a configuration of the Hamiltonian microscopic variables, $\boldsymbol{P}$ is the total momentum, β is the inverse temperature, $\boldsymbol{v}_G$ is the velocity of the centre of mass, and Z is the partition function. The partition function is defined by

$$Z = \frac{1}{N!}\int d^{2N}\boldsymbol{R}d^{2N}\boldsymbol{P}d^N\boldsymbol{\Theta}d^N\boldsymbol{\Omega}e^{-\beta(\mathcal{H}_{FC}(\mathcal{C})-\boldsymbol{v}_G\cdot\boldsymbol{P}(\mathcal{C}))},$$

where I use short-hand notations for the integration over the microscopic variables of all N particles, like in Sec. II.2.2. Since there is no space dependence in the fully-connected version of the Hamiltonian, each integration over the positions is straightforward and yields a factor equal to the volume of the system, V. Likewise, the integrals over angular velocities is easy to compute, since they are simply Gaussian integrals,

$$\int_{-\infty}^{+\infty} d\omega_i e^{-\beta\frac{\omega_i^2}{2}} = \sqrt{\frac{2\pi}{\beta}}.$$

the partition function can therefore be rewritten as

$$Z = \frac{1}{N!}\left(\sqrt{\frac{2\pi}{\beta}}V\right)^N\int d^N\boldsymbol{\Theta}Z_p(\boldsymbol{\Theta})\prod_{i=1}^{N}\exp\left[\beta\left(\frac{J}{2N}\sum_{k\neq i}\boldsymbol{s}_i\cdot\boldsymbol{s}_k + \boldsymbol{h}\cdot\boldsymbol{s}_i\right)\right],$$

with

$$Z_p(\boldsymbol{\Theta}) \equiv \prod_{i=1}^{N} \int d^2\boldsymbol{p}_i e^{-\beta\left(\frac{p_i^2}{2} - (\boldsymbol{v}_G + K\boldsymbol{s}_i)\cdot\boldsymbol{p}_i\right)}.$$

The integrals are also Gaussian and can be computed in a standard way, yielding

$$\begin{aligned} Z_p(\boldsymbol{\Theta}) &= \left(\frac{2\pi}{\beta}\right)^N \prod_{i=1}^{N} \left(e^{\frac{\beta}{2}(\boldsymbol{v}_G + K\boldsymbol{s}_i)^2}\right), \\ &= \left(\frac{2\pi}{\beta}\right)^N e^{-N\frac{\beta}{2}\left(v_G^2 + K^2\right)} \prod_{i=1}^{N} \left(e^{-\beta K \boldsymbol{v}_G \cdot \boldsymbol{s}_i}\right). \end{aligned}$$

The partition function can therefore be rewritten as

$$Z = \frac{V^N}{N!}\left(\frac{2\pi}{\beta}\right)^{\frac{3N}{2}} e^{N\frac{\beta}{2}\left(v_G^2 + K^2\right)} Z_\theta, \tag{II.31}$$

where I defined

$$Z_\theta = \int d^N\boldsymbol{\Theta} \prod_{i=1}^{N} \exp\left[\beta\left(\frac{J}{2N}\sum_{k\neq i} \boldsymbol{s}_i \cdot \boldsymbol{s}_k + (\boldsymbol{h} + K\boldsymbol{v}_G)\cdot\boldsymbol{s}_i\right)\right].$$

The sum over interactions can then be rewritten by introducing $\boldsymbol{m} = \sum_i \boldsymbol{s}_i/N$, the magnetisation per spin of a given configuration, as

$$\frac{1}{N}\sum_{i=1}^{N}\sum_{k\neq i} \boldsymbol{s}_i \cdot \boldsymbol{s}_k = N\boldsymbol{m}^2 - 1,$$

so that the integral over all angles can be cast into the form

$$Z_\theta = \int d^N\boldsymbol{\Theta} e^{\beta N\left(\frac{J}{2}\boldsymbol{m}^2 + (\boldsymbol{h} + K\boldsymbol{v}_G)\cdot\boldsymbol{m}\right)} \delta\left(N\boldsymbol{m} - \sum_{i=1}^{N}\boldsymbol{s}_i\right).$$

This partial partition function takes the same form as the full partition function of the mean-field XY model, with an effective external field $\boldsymbol{h}_{eff} = \boldsymbol{h} + K\boldsymbol{v}_G$ [4]. In order to compute Z_θ, it is useful to resort to a so-called Hubbard-Stratonovich transformation, which is simply a rewriting of a Gaussian as the integral of another Gaussian,

$$e^{\frac{b^2}{2a}} = \sqrt{\frac{a}{2\pi}} \int_{-\infty}^{\infty} du\, e^{-\frac{1}{2}au^2 + bu}.$$

Applying this transformation to both components of $\boldsymbol{m}$ in Z_θ yields

$$Z_\theta = \frac{N\beta}{2\pi}\int d^2\boldsymbol{u} d^N\boldsymbol{\Theta} e^{-\beta N\left(\frac{u^2}{2} - \boldsymbol{\gamma}(\boldsymbol{u})\cdot\boldsymbol{m}\right)} \delta\left(N\boldsymbol{m} - \sum_{i=1}^{N}\boldsymbol{s}_i\right),$$

where I introduced $\boldsymbol{\gamma}(\boldsymbol{u}) \equiv K\boldsymbol{v}_G + \boldsymbol{h} + \boldsymbol{u}$. Using the direction of $\boldsymbol{\gamma}$ as the origin for all angles θ_i, I rewrite the scalar product $\boldsymbol{\gamma}(\boldsymbol{u}) \cdot \boldsymbol{m}$ as

$$\boldsymbol{\gamma}(\boldsymbol{u}) \cdot \boldsymbol{m} = \frac{1}{N} \sum_{i=1}^{N} \gamma(\boldsymbol{u}) \cos\theta_i,$$

with $\gamma = |\boldsymbol{\gamma}|$. Using this replacement, Z_θ can be rewritten as

$$Z_\theta = \frac{N\beta}{2\pi} \int d^2\boldsymbol{u} e^{-\beta N u^2/2} \prod_{i=1}^{N} \int_{-\pi}^{\pi} d\theta_i e^{\beta N \gamma(\boldsymbol{u}) \cos\theta_i}.$$

Introducing the function $\mathcal{F}(\boldsymbol{u})$ defined by

$$\mathcal{F}(\boldsymbol{u}) \equiv \frac{u^2}{2} - \frac{1}{\beta} \ln\left[2\pi I_0\left(\beta\gamma(\boldsymbol{u})\right)\right], \tag{II.32}$$

where

$$I_n(x) \equiv \frac{1}{2\pi} \int_{-\pi}^{\pi} d\theta e^{x\cos\theta} \cos n\theta$$

is the modified Bessel function of the first kind of order n [101], Z_θ can be cast into the form

$$Z_\theta = \frac{N\beta}{2\pi} \int d^2\boldsymbol{u} e^{-\beta N \mathcal{F}(\boldsymbol{u})}.$$

In the limit $\beta N \to \infty$, the integral over $\boldsymbol{u}$ can be computed resorting to the saddle-point approximation, which, at leading order, states that

$$Z_\theta \approx \frac{N\beta}{2\pi} e^{-\beta N \mathcal{F}(\boldsymbol{u}^\star)}, \tag{II.33}$$

where the saddle point, $\boldsymbol{u}^\star$, is the value of $\boldsymbol{u}$ that minimises $\mathcal{F}$. Possible values of $\boldsymbol{u}^\star$ are given by the extremisation condition

$$\boldsymbol{0} = \frac{\partial \mathcal{F}}{\partial \boldsymbol{u}}(\boldsymbol{u}^\star) = \boldsymbol{u}^\star - \frac{I_1(\beta\gamma(\boldsymbol{u}^\star))}{I_0(\beta\gamma(\boldsymbol{u}^\star))} \hat{\boldsymbol{\gamma}}(\boldsymbol{u}^\star), \tag{II.34}$$

where $\hat{\boldsymbol{\gamma}} = \boldsymbol{\gamma}/\gamma$ is the unit vector pointing in the direction of $\boldsymbol{\gamma}$.

Before solving this self-consistent equation numerically, it is useful to derive the mean values of observables as functions of $\boldsymbol{u}^\star$. In order to do so, I first define the free energy density f,

$$f(\beta, \boldsymbol{v}_G, N/V) \equiv -\frac{1}{\beta N} \ln Z(\beta, \boldsymbol{v}_G, N, V),$$

which can be evaluated at leading order in N using Eqs. (II.31) and (II.33), as well as Stirling's approximation, leading to

$$f(\beta, \boldsymbol{v}_G, N/V) \approx \mathcal{F}(\boldsymbol{u}^\star) - \frac{1}{\beta}\left(\frac{3}{2}\ln\frac{2\pi}{\beta} - \ln\frac{N}{V} + 1\right) - \frac{\boldsymbol{v}_G^2}{2}.$$

The mean values of various observables can be computed from this expression. For instance, the mean magnetisation $\boldsymbol{m} = \langle \overline{\boldsymbol{m}} \rangle$ reads

$$\boldsymbol{m} = -\frac{\partial f}{\partial \boldsymbol{h}} = -\frac{\partial \boldsymbol{u}^\star}{\partial \boldsymbol{h}} \frac{\partial \mathcal{F}}{\partial \boldsymbol{u}}(\boldsymbol{u}^\star) - \frac{\partial \mathcal{F}}{\partial \boldsymbol{h}}(\boldsymbol{u}^\star).$$

By definition of the saddle point, $\partial \mathcal{F}/\partial \boldsymbol{u}(\boldsymbol{u}^\star) = \boldsymbol{0}$. Therefore, using the expression of $\mathcal{F}$ given in Eq. (II.32) as well as the definition of $\boldsymbol{\gamma}$, one gets

$$\boldsymbol{m} = -\frac{\partial \mathcal{F}}{\partial \boldsymbol{h}}(\boldsymbol{u}^\star) = \boldsymbol{u}^\star.$$

The self-consistent equation that defines $\boldsymbol{u}^\star$ is therefore also the mean-field self-consistent equation of $\boldsymbol{m}$. Note that this equation on $\boldsymbol{m}$ takes the exact same form as the Curie-Weiss mean-field equation for the XY model, obtained from the partition function (II.26). The other observables of interest here are the mean momentum per particle, $\langle \boldsymbol{p} \rangle$,

$$\langle \boldsymbol{p} \rangle \equiv -\frac{\partial f}{\partial \boldsymbol{v}_G},$$

which here reads

$$\langle \boldsymbol{p} \rangle = \boldsymbol{v}_G + K\boldsymbol{m},$$

as already described in Sec. II.2.2. Finally, one can also compute the average energy per particle, $\langle e \rangle$ using the fact that

$$\langle e \rangle \equiv -\frac{1}{N}\frac{\partial \ln Z}{\partial \beta} + \boldsymbol{v}_G \cdot \langle \boldsymbol{p} \rangle,$$

yielding

$$\langle e \rangle = \frac{3}{2\beta} + \frac{\boldsymbol{v}_G^2 - \boldsymbol{m}^2}{2} - \boldsymbol{h} \cdot \boldsymbol{m}.$$

The average magnetisation can be computed numerically as a function of the canonical control parameters β and $\boldsymbol{v}_G$, by solving the self-consistent equation (II.34). To do so, one can assume that $\boldsymbol{v}_G = v_{G,x}\hat{\boldsymbol{e}}_x$ so that $\boldsymbol{m} = m_x\hat{\boldsymbol{e}}_x$ without any loss of generality. Examples of curves of m versus the temperature $T = \beta^{-1}$ for a few values of v_G and a zero external field, $\boldsymbol{h} = \boldsymbol{0}$, are shown in Fig. II.5(a). In the case $\boldsymbol{v}_G = \boldsymbol{0}$, I recover a standard symmetry breaking with symmetric branches of non-zero magnetisation in all directions (black line). When the velocity of the centre of mass is cranked up, since it plays the same role as an external magnetic field, the direction of $\boldsymbol{v}_G$ is favoured, leading to a branch of solutions with a higher magnetisation. This branch corresponds to the global minimum of the effective free energy, which is plotted against the projection of the magnetisation for a few values of the temperature and a positive velocity of the centre of mass in Fig. II.5(b). However, this branch of solutions cannot yield states with a total momentum $\boldsymbol{P} = \boldsymbol{0}$, like those I seek in simulations. Indeed, for $\boldsymbol{P}$ to be zero, the magnetisation and velocity need to point in opposite directions. Therefore, it is also interesting to seek other solutions of the self-consistent equation (II.34). At low temperatures, one indeed finds a branch of solutions of this equation such that $\boldsymbol{m} \cdot \boldsymbol{v}_G < 0$. At a fixed value of $\boldsymbol{v}_G$, and starting

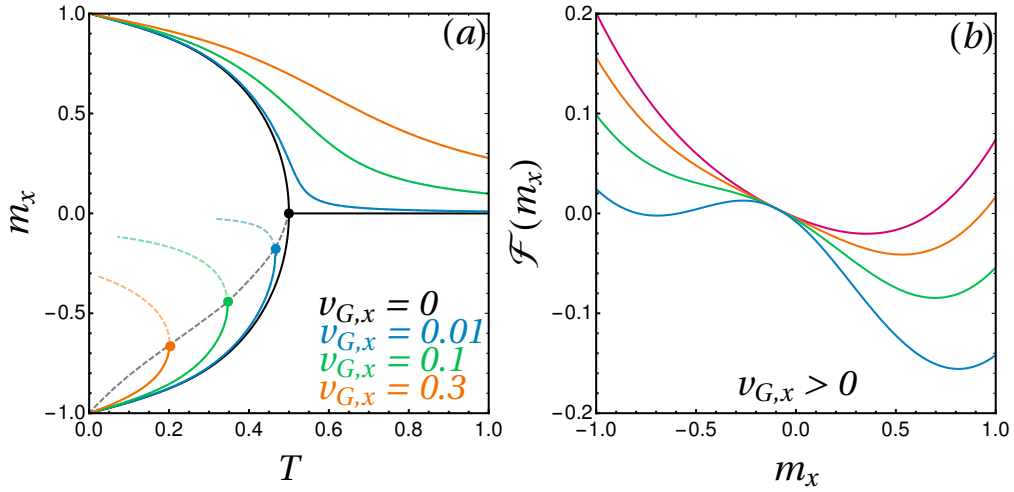

Fig. II.5 **Mean-field magnetisation with a linear spin-velocity coupling.**(a) Projection of the magnetisation onto the direction of the velocity $v_{G,x}$.The solid lines are found by a numerical minimisation of $\mathcal{F}(\boldsymbol{u})$ for various values of the velocity.At low temperatures, there are two branches of solution with different signs of the magnetisation.The lower branch is a minimum only under a breakline, that is here represented as a dashed gray line.Above the breakline, solutions of the self-consistent equation (II.34) describe a local maximum of $\mathcal{F}$ (dashed colored lines).(b) $\mathcal{F}$ against m_x for a positive value of the velocity $v_{G,x} = 0.1$ and $K = 1$, at temperatures $T = 0.3$,0.4,0.5,0.6 (blue to red).

from low values of the magnetisation, this branch of solutions first follows the secondary minimum of $\mathcal{F}$, and then the local maximum lying between the minima. Therefore, for each value of $\boldsymbol{v}_G$, there is a line of stable solutions with a negative magnetisation up to a (spinodal) line, that corresponds to the point where the minimum and maximum meet and form an inflexion point. In Fig. II.5(a), the lower branches of stable solutions are represented as solid lines, the spinodal as a gray dashed line, and I show solutions of Eq. (II.34) corresponding to a maximum of $\mathcal{F}$ as dashed coloured lines. In microcanonical simulations with $\boldsymbol{P} = \boldsymbol{0}$, the system selects solutions from the lower branches, by tuning $\boldsymbol{v}_G$ and $\boldsymbol{m}$ together. This is a rather unusual situation: in the canonical picture, because of the conservation of momentum, the system does not choose the global minimum of the free energy, but a secondary minimum instead. It was also shown in Ref. [69] that one can numerically perform an inversion between the variables $(\beta, \boldsymbol{v}_G)$ and the variables $(\langle e \rangle, \langle \boldsymbol{p} \rangle)$, leading to very similar curves of the magnetisation at a fixed momentum. Note, however, that this mechanism cannot survive in the thermodynamic limit: indeed, in finite dimension of space, metastability does not exist in the limit $N \to \infty$. Therefore, moving magnetised states such as those predicted in the mean-field ($d \to \infty$) limit can only be seen in simulations at finite values of N.[7]

[7]Note, however, that a different choice for $\boldsymbol{P}$ can lead to states that move even for $N \to \infty$. This situation, that I do not consider at length in my thesis since I want collective motion to emerge spontaneously at low temperatures only, might actually be more relevant when compared to actual active systems.

II.3.3 Deviations from the Mean-Field Picture

a) Effect of the dimension of space

When using a mean-field-level description, the whole system of N spins is approximated by one variable subjected to an effective interaction. A by-product of this approximation is that one completely loses the notion of positions of different spins in space: this is particularly obvious in fully-connected descriptions like the one of Eq. (II.28). As such, one can wonder whether a mean-field description can, in fact, be a good picture of a system of spins on a lattice, since lattices are very structured graphs. A way to check this is to measure the critical exponents of a model of spins, keeping the dimension of the spins d_s fixed, but varying the dimension of the underlying lattice d.

Consider, for instance, the Ising model ($d_s = 1$). For a one-dimensional chain ($d = 1$), it was shown on general grounds by Peierls [102] that the ferromagnetic order is destroyed at all finite temperatures, meaning that the critical temperature T_c is zero. Furthermore, one can easily check [2] that the shape of the spin-spin correlation function is not described by an algebraic law multiplied by a scaling law, as expressed by Eq. (II.23), but simply by an exponential law. Therefore, the Ising model is not critical in $d = 1$. This result can also be understood as follows: a critical transition happens when long-range order sets in. For $d = 1$, this order is easily destroyed by low-energy excitations, namely domain walls. Indeed, it is enough to flip half the system to go from $m = 1$ to $m = 0$, at the cost of only one anti-aligned pair. In the thermodynamic limit, this $O(1)$ cost is very small compared to terms that grow with N, so that ferromagnetic order is destroyed by thermal fluctuations at all finite temperatures.[8] Similar local disorder is expected in any classical system with short-range interactions in $d = 1$.

In higher dimension, however, creating a domain wall that brings the magnetisation to 0 costs an energy that scales like L, the linear size of the system, so that one recovers a critical transition at a finite temperature, with critical exponents that can be predicted analytically and measured numerically. The values of the critical exponents that I defined in Sec. II.3.1a) are reported in Table II.1. Looking at these values, one sees that the critical exponents are different from the mean-field ones for $d = 2$ and $d = 3$, but that they become equal to their mean-field values for $d \geq 4$.

d	β	γ	η	ν	Refs.
2	1/8	7/4	1/4	1	[104, 105]
3	0.326419(3)	1.237075(10)	0.036298(2)	0.629971(4)	[106, 107]
4+	1/2	1	0	1/2	[108, 109]

Table II.1: **Critical Exponents of the Ising model.**

This phenomenology is in fact general: the mean-field description corresponds to the $d \to \infty$ limit of a model, as each particle typically interacts with a number of other particles that scales like the size of the system. Furthermore, the mean-field values of the critical exponents become correct for all dimensions of space above a value d_u that is model-dependent, and is called the "upper critical dimension". From the results above, the upper critical dimension of the Ising model is $d_u = 4$. Finally, critical properties

[8] For an in-depth discussion of these excitations as the system size increases, see Rulquin [103]

emerge only strictly above another value of the dimension of space, d_l, that is called the "lower critical dimension". For the Ising model, $d_l = 1$. In general, when performing simulations of a model while expecting a critical transition, care should be taken of the values of these special dimensions in order to know what to expect. In the special case $d_s = 2$ (the XY model), which is of particular interest in this thesis, more details are given in Sec. II.3.4.

b) Finite-Size Scalings

Finally, all the results given above concerning the critical properties of the Ising model were obtained under in the thermodynamic limit, $N \to \infty$. However, in practice, all experimental and numerical results are obtained for finite values of N. In many experiments, this fact is overlooked since, typically, $N \sim 10^{23}$. However, in simulations, as well as in experiments of colloidal, granular, or active matter one generally uses $N \sim 10^2 - 10^9$, so that finite-size effects can play an important role. In this context, it is therefore crucial to understand the effect of a finite N on the magnetisation properties of a system of spins.

If the dimension of space is larger than the lower critical dimension, the effect of N on the transition can be understood using the critical scalings that I introduced before. In particular, while in the limit $N \to \infty$, the correlation length of a critical system diverges at the critical temperature, it is bounded by the size of the system in finite size. As a result, in finite size, one observes a value of the critical temperature $T_c(L)$ that is different from the thermodynamic value. Indeed, one state is selected across the whole system at the temperature at which the thermodynamic ξ reaches L, not infinity. In this section, I therefore introduce the reduced temperature $t = T/T_c(L) - 1$. Using this notation, one often assumes that the free energy F of the system can be written in a scaling form as a function of L and t [110, 111],

$$F = L^{-(2-\alpha)/\nu} \mathcal{F}_s \left(t L^{1/\nu} \right),$$

where α is the critical exponent associated to the specific heat C at the critical point, such that $C \sim t^{-\alpha}$. $\mathcal{F}_s$ is a scaling function, and the choice of the scaling variable $tL^{1/\nu}$ is motivated by the fact that ξ is limited by L: it is therefore interesting to express thermodynamic functions in terms of $L/\xi \sim t^\nu L$. Taking derivatives of F yields finite-size scalings for other thermodynamic quantities, for instance

$$m \sim L^{-\beta/\nu} \mathcal{M} \left(t L^{1/\nu} \right),$$
$$\chi_{m,T} \sim L^{\gamma/\nu} \mathcal{X} \left(t L^{1/\nu} \right),$$

with $\mathcal{M}$ and $\mathcal{X}$ two scaling functions. The scalings at $T_c(L)$, that are obtained at $t = 0$, can equivalently be written by using the critical scalings introduced in Sec. II.3.1a) to first write the magnetisation and magnetic susceptibility as functions of the correlation length,

$$m \sim \xi^{-\beta/\nu},$$
$$\chi_{m,T} \sim \xi^{\gamma/\nu}.$$

Since $\xi = L$ at the transition, one can write that, at $t = 0$,

$$m \sim L^{-\beta/\nu}, \tag{II.35}$$

$$\chi_{m,T} \sim L^{\gamma/\nu}. \tag{II.36}$$

These algebraic scalings at the transition, that are often called finite-size scalings themselves, although they do not contain the temperature and size dependence of the thermodynamic functions away from the transition. In practice, Eqs. (II.35) and (II.36) are often used to measure critical exponents of a system by varying its size [112]. For instance, one often plots the maximum value of $\chi_{m,T}$, χ_{max}, as a function of the system size, so as to measure the exponent γ/ν. In this context, it is usual to use the hyperscaling relation (II.24) to write

$$\chi_{m,T} \sim L^{2-\eta},$$

where η is the "anomalous dimension", that measures the deviation of $\chi_{m,T}$ from extensivity at the critical point. Note that $\eta = 0$ in the mean-field limit.

II.3.4 The Square-lattice XY Model

In this Section, I discuss in details the special case that is most useful in this thesis: the case of the XY model ($d_s = 2$), in two-dimensional space, and in the particular setting of a square lattice. I first discuss the absence of true long-range ferromagnetic order in this special case in Sec. a), then the very special transition that nevertheless occurs in this system in Sec. b), and finally the properties of a finite-size XY model in Sec. c). Having these results in mind is essential to understand the discussion about the presence or absence of BKT behaviour in the cqse of repulsive, ferromagnetically coupled particles moving in free space that is presented in Chapter III.

a) The Mermin-Wagner Argument

When studying the XY model in $d = 2$, it is instructive to focus on the effects of the spin-waves introduced in Sec. c) on the ordered phase. Consider a situation in which the coarse-grained magnetisation has a uniform amplitude, but is oriented in a direction encoded by an angle $\theta(\boldsymbol{r})$ at position $\boldsymbol{r}$. The probability of a given configuration is then given by the exponential of the spin-wave Hamiltonian given in Sec. c),

$$\mathcal{P}\left[\theta(\boldsymbol{r})\right] \propto \exp\left[-\frac{\overline{K}}{2}\int d^2\boldsymbol{r}\,(\nabla\theta)^2\right].$$

This probability can be rewritten in terms of Fourier components,

$$\mathcal{P}\left[\theta(\boldsymbol{q})\right] \propto \exp\left[-\frac{\overline{K}}{2}\sum_{\boldsymbol{q}} q^2\,|\theta(\boldsymbol{q})|^2\right].$$

This probability can therefore be rewritten as a product of Gaussians,

$$\mathcal{P}\left[\theta(\boldsymbol{q})\right] \propto \prod_{\boldsymbol{q}} \exp\left[-\frac{\overline{K}}{2}q^2\,|\theta(\boldsymbol{q})|^2\right],$$

meaning that each mode $\theta_{\boldsymbol{q}}$ behaves like an independent, Gaussian random variable. As a consequence, one can compute the correlation between two modes,

$$\langle \theta_{\boldsymbol{q}} \theta_{\boldsymbol{q}'} \rangle = \frac{\delta(\boldsymbol{q}+\boldsymbol{q}')}{\overline{K} q^2}.$$

This expression can be used to compute the values of the correlation function in real-space,

$$\langle \theta(\boldsymbol{r})\theta(\boldsymbol{r}') \rangle = \frac{1}{V} \sum_{\boldsymbol{q},\boldsymbol{q}'} e^{i\boldsymbol{q}\cdot\boldsymbol{r}+i\boldsymbol{q}'\cdot\boldsymbol{r}'} \langle \theta_{\boldsymbol{q}} \theta_{\boldsymbol{q}'} \rangle$$

where V is the volume of space. In the continuum limit (in which the sum over modes can be approximated by an integral) reads

$$\langle \theta(\boldsymbol{r})\theta(\boldsymbol{r}') \rangle = \frac{1}{\overline{\overline{K}}} \int \frac{d^2\boldsymbol{q}}{4\pi^2} \frac{e^{i\boldsymbol{q}\cdot(\boldsymbol{r}-\boldsymbol{r}')}}{q^2}.$$

The integral

$$\Phi(\boldsymbol{r}) \equiv -\int \frac{d^2\boldsymbol{q}}{4\pi^2} \frac{e^{i\boldsymbol{q}\cdot\boldsymbol{r}}}{q^2}$$

verifies Poisson's equation

$$\nabla^2 \Phi(\boldsymbol{r}) = \delta(\boldsymbol{r}),$$

and is therefore the Coulombian potential created by a unit charge placed at the origin. Computing this potential is a standard exercise in electromagnetism, and one finds, in $d = 2$ [2],

$$\Phi(\boldsymbol{r}) = \frac{\ln r}{2\pi}.$$

Therefore, one finds

$$\langle \theta(\boldsymbol{r})\theta(\boldsymbol{r}') \rangle = -\frac{\ln |\boldsymbol{r}-\boldsymbol{r}'|}{2\pi\overline{\overline{K}}}.$$

This value can be used to compute the value of the 2-point correlation function of the magnetisation,

$$\begin{aligned} \langle \boldsymbol{m}(\boldsymbol{r}) \cdot \boldsymbol{m}(\boldsymbol{0}) \rangle &= m^2 \langle \cos\left(\theta(\boldsymbol{r}) - \theta(\boldsymbol{0})\right) \rangle, \\ &= m^2 \mathrm{Re} \left\langle e^{i(\theta(\boldsymbol{r})-\theta(\boldsymbol{0}))} \right\rangle, \end{aligned}$$

where the amplitude of the magnetisation is, by hypothesis, homogeneous here. I finally use the fact that, for any collection of Gaussian distributed variables [2, 4],

$$\langle e^{\alpha\theta} \rangle = e^{\frac{\alpha^2}{2}\langle\theta^2\rangle},$$

so that

$$\langle \boldsymbol{m}(\boldsymbol{r}) \cdot \boldsymbol{m}(\boldsymbol{0}) \rangle = m^2 \exp\left[-\frac{1}{2} \langle (\theta(\boldsymbol{r}) - \theta(\boldsymbol{0}))^2 \rangle \right].$$

This formulation yields the long-range limit of the correlation function,

$$\lim_{r\to\infty} \langle \boldsymbol{m}(\boldsymbol{r}) \cdot \boldsymbol{m}(\boldsymbol{0}) \rangle = 0,$$

which means that the phase fluctuations of the magnetisation, created by spin-waves, prevent the system from developing long-range order. This proof can be repeated straightforwardly for a higher value of d_s, which simply adds more components in the correlations. In other words, a model with a continuous symmetry that is well-described in the low-temperature domain by the spin-wave Hamiltonian does not feature a phase transition to a ferromagnetic phase at any finite temperature in $2d$. Such models therefore have a lower critical dimension $d_l \geq 2$ (and, in particular, it was shown by field-theoretical calculations [113] that, for the XY model, $d_l = 2$). This result is known, in field theory, as the Mermin-Wagner theorem (also sometimes called the Mermin-Wagner-Berezinskii theorem, the Mermin-Wagner-Hohenberg theorem, or even the Coleman theorem).

Note, however, that the name "theorem" is misleading. While the Mermin-Wagner *argument* holds at the field-theoretical level considered here, it does *not* state, as one often reads, that "two-dimensional systems with a continuous symmetry cannot have a broken symmetry at finite temperature". In fact, the original proofs by Mermin and Wagner [54, 55] state that this result holds in a number of precise examples, such as superfluids, superconductors, the square-lattice XY magnet with nearest-neighbour interactions, or crystallization in $2d$. However, several other systems are known not to follow this rule. For instance, it is known that liquids can spontaneously break orientational order in $2d$ in the context of the hexatic transition [114, 115], as I will discuss in Sec. II.4.1. Moreover, this result holds, even in the context of the XY model, only if the spin-wave description is a good picture of the low-temperature physics: in particular, interactions have to be short-ranged for the gradient expansion to quadratic order to be correct.

Furthermore, Mermin's and Wagner's result, while it forbids continuous symmetry breaking in a number of cases, does not forbid phase transitions as characterised by a diverging correlation length. This fact is important in the specific example of the square-lattice XY model, since it does, in fact, feature a phase transition at a finite temperature, called the Berezinskii-Kosterlitz-Thouless transition.

b) The Berezinskii-Kosterlitz-Thouless Transition

The argument in Sec. a) shows that, in a square-lattice XY model with nearest-neighbour interactions, and in the thermodynamic limit, $m(T) = \delta(T)$. However, it was shown by Berezinskii [78], and by Kosterlitz and Thouless [71, 73] that the square-lattice XY model presents a static phase transition at a temperature T_{KT} between a high-temperature disordered paramagnet and a low-temperature phase characterised by an infinite correlation length and susceptibility.

Phenomenologically, while the phase below T_{KT} displays locally ordered spins that are smoothly disaligned at long range by spin-wave excitations, the phase above T_{KT} is characterised by the proliferation of topological defects, that suppress the spin-spin correlation much faster than spin waves. These topological defects are, from the point of view of the magnetisation field, structures at the centre of which the magnetisation is zero, and around which the magnetisation field winds. In the context of the XY model, only two kinds of such defects are observed: vortices and antivortices, like the ones shown

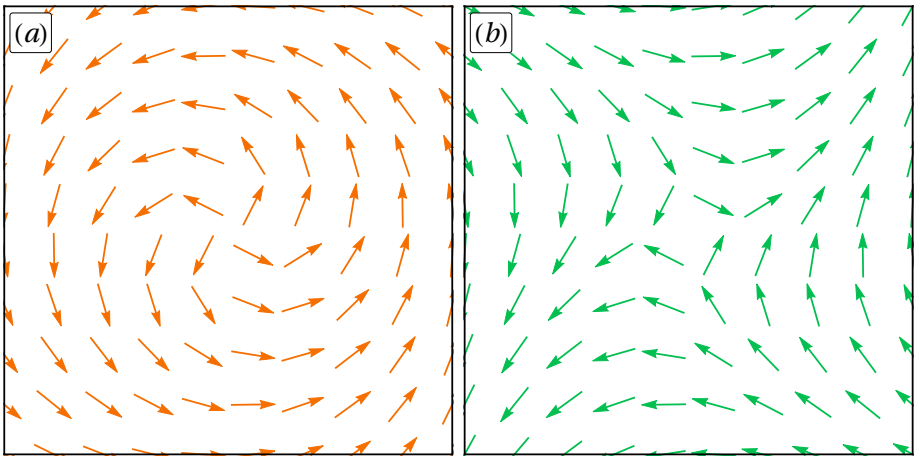

Fig. II.6 **Topological Defects of the XY model.**(a) a vortex, and (b) an antivortex.

in Fig. II.6. The difference between a vortex and an antivortex is the topological charge n, defined by

$$\oint \nabla\theta(\boldsymbol{r}) \cdot d\boldsymbol{\ell} = 2\pi n,$$

where the integral is computed over a closed contour that contains a defect, and $d\boldsymbol{\ell}$ is an oriented element of that contour. For a vortex, one gets $n = +1$, while for an antivortex, one gets $n = -1$. The name *charge* is in fact particularly appropriate, since the interaction between these defects can be mapped onto the Coulombian interactions between point electric charges [71]: vortices and antivortices attract each other, and annihilate when they meet. Furthermore, like in the case of Coulombian systems, the total charge of a system is constant, and is in fact here imposed by the topology of the supporting space. In particular, in a flat (Euclidean) space, the total charge has to be zero. This Coulombian picture is in fact commonly used to describe the nature of the BKT transition: below T_{KT}, defects are all bound together by their mutual attraction, but at T_{KT} these charges get enough kinetic energy to unbind, and thus each roam freely throughout the system. Note that this behaviour is reminiscent of the creation of domain walls in the $1d$ Ising model: vortices and antivortices are low-cost, local alignment defects that efficiently suppress the magnetisation of a system.

In terms of the usual observables, the BKT transition is characterised by a diverging correlation length ξ, like other critical transitions. However, unlike usual critical transitions, the scaling of ξ close to T_{KT} against the temperature is not algebraic, but exponential, so that

$$\begin{aligned} \ln \xi &\sim t^{-\nu}, \ (t > 0) \\ &= \infty, \ \ (t < 0) \end{aligned}$$

with $t = T/T_{KT} - 1$ and $\nu = 1/2$ [73]. Note that an exponential scaling is also expected for any model at its lower critical dimension near $T = 0$: for instance, the Ising model in $d = 1$ features a similar scaling, but with $t = T$ and $\nu = 1$ [2, 102]. In other words, in the

case of the BKT transition, both the fact that $\nu = 1/2$ and that $T_{KT} > 0$ are surprising, but the fact that ξ scales like an exponential function of the temperature is not. The correlation length is related to the susceptibility through the more usual scaling law

$$\chi_{m,T} \sim \xi^{2-\eta},$$

with $\eta = 1/4$ [73]. From the values of these exponents, and using the hyperscaling relation (II.25) for $d = 2$, one can also deduce the values of the exponents $\beta = 1/8$ and $\gamma = 7/8$. An unusual characteristic of these observables is that ξ and $\chi_{m,T}$ are infinite over a whole interval of temperatures, while in usual critical transitions they are infinite only at the critical temperature. Because of this characteristic, that can be rationalised in the context of the Renormalisation Group (RG) study of the model [73], the low-temperature phase of the square-lattice XY model is called a critical phase.

c) The Square-Lattice XY Model in Finite Size

Finally, in order to discuss the presence or absence of BKT physics in experiments or simulations, one should be aware of the finite-size properties of the square-lattice XY model. The first property that I would like to comment on is the magnetisation. While, in the limit $N \to \infty$, the average modulus of the magnetisation $m = \langle |\boldsymbol{m}| \rangle = 0$ at all finite values of the temperature, the finite-size magnetisation of the XY model displays a much richer behaviour. Indeed, it is suppressed by two very different mechanisms on each side of the BKT transition. Below the finite-size value of the BKT transition, $T^\star(L) \equiv T_{KT}(L)$, the mean modulus of the magnetisation $m = \langle |\boldsymbol{m}| \rangle$ is only suppressed by spin-wave excitations.

The calculations of Sec. a) can be repeated, but this time taking into account the finite size of the system, as well as the shape of the square lattice [116]. In order to do so, I write the on-lattice Hamiltonian,

$$\mathcal{H} = -J \sum_{i=1}^{N} \sum_{j \in \partial i} \cos\left(\theta_i - \theta_j\right),$$

then focus on the low-temperature regime, in which the spins are almost aligned, so that the cos can be expanded,

$$\mathcal{H} = \frac{J}{2} \sum_{i=1}^{N} \sum_{j \in \partial i} \left(\theta_i - \theta_j\right)^2, \tag{II.37}$$

where I also omitted a constant term. This Hamiltonian can be rewritten in Fourier space,

$$\mathcal{H} = J \sum_{q} |\phi_q|^2 \gamma_q,$$

where I introduced the Fourier series representation

$$\theta_r = \frac{1}{\sqrt{N}} \sum_{q} e^{-iqr} \phi_q, \qquad \phi_q = \frac{1}{\sqrt{N}} \sum_{r} e^{+iqr} \theta_r,$$

with $\sqrt{N} = L$ the side-length of the lattice, and $\boldsymbol{r}$ the position of the considered spin. I also define the Fourier coefficients, that reflect the structure of the square lattice [116],

$$\gamma_q = 4 - 2\cos q_x - 2\cos q_y.$$

Using this expression, one can write the partition function, that is given by a product of Gaussians just like in Sec. a),

$$Z = \prod_q Z_q = \prod_q \int \frac{d\phi_q}{2\pi\sqrt{N}} e^{-\frac{\beta J}{2}|\phi_q|^2\gamma_q}.$$

The case $q = 0$ needs to be treated separately, since $\gamma_0 = 0$, leading to

$$Z_0 = \int_{-\pi\sqrt{N}}^{\pi\sqrt{N}} \frac{d\phi_0}{2\pi\sqrt{N}} = 1.$$

The other "modes" of the partition function are well-approximated, at low temperatures, by taking the integration limits to infinity. The integrals are then full Gaussian integrals, and one finds

$$Z_q = \sqrt{\frac{T}{2\pi J\gamma_q}},$$

leading to the free energy, expressed in units of J,

$$F = \frac{T}{2J}\sum_{q\neq 0} \ln\left(\frac{2\pi J\gamma_q}{T}\right).$$

Furthermore, one can compute explicitly the finite-size values of the magnetisation and magnetic susceptibility. In order to do so, I define $\overline{\theta}$, the direction of the instantaneous magnetisation $\overline{\boldsymbol{m}}$, and $\psi_r = \theta_r - \overline{\theta}$ the direction of spin r relative to $\overline{\boldsymbol{m}}$. Then, I introduce the spatial correlation function of these relative angles, expressed in Fourier space,

$$\langle\psi_0\psi_r\rangle = \frac{1}{N}\sum_{q,q'} e^{-iqr}\langle\psi_q\psi_{q'}\rangle.$$

Using the definition of ψ_r, one easily finds that $\psi_q = \phi_q\,(1 - \delta(q))$, leading to

$$\langle\psi_0\psi_r\rangle = \frac{1}{N}\sum_{q,q'\neq 0} e^{-iqr}\langle\phi_q\phi_{q'}\rangle.$$

Since the ϕ_q's are independent Gaussian random variables, the only non-zero terms of the double-sum are those such that $q = -q'$, which leads to

$$\langle\psi_0\psi_r\rangle = \frac{1}{N}\sum_{q\neq 0} e^{-iqr}\langle|\phi_q|^2\rangle.$$

Finally, the average value is easy to compute (assuming that the integration bounds can be made infinite again),

$$\langle|\phi_q|^2\rangle = \frac{1}{Z_q}\int \frac{d\phi_q}{2\pi\sqrt{N}}|\phi_q|^2 e^{-\frac{\beta J}{2}|\phi_q|^2\gamma_q} = \frac{\beta J}{\gamma_q},$$

so that the 2-point correlation reads

$$\langle\psi_0\psi_r\rangle = \frac{\beta J}{N}\sum_{q\neq 0}\frac{e^{-iqr}}{\gamma_q}.$$

Using field-theoretical notations, one often defines $G(r) = \langle\psi_0\psi_r\rangle/\beta J$, the propagator or Green's function of the theory, so that

$$G(r) = \frac{1}{N}\sum_{q\neq 0}\frac{e^{-iqr}}{\gamma_q}. \tag{II.38}$$

This result is directly used to compute an exact expression for the magnetisation at finite N and low, finite T. The trick is to write a projection of the instantaneous magnetisation as

$$\overline{m}_x = \frac{1}{N}\sum_r \cos\psi_r,$$

and to notice that the instantaneous magnetisation modulus differs from the expression above only by corrections with a higher order in $1/N$ [116], so that

$$\overline{m} \equiv |\overline{\boldsymbol{m}}| \approx \frac{1}{N}\sum_r \cos\psi_r.$$

One can therefore approximate the average modulus of the magnetisation, $m = \langle\overline{m}\rangle$, by

$$m = \langle\cos\psi_0\rangle = \sum_{p=0}^{\infty}\frac{(-1)^p}{(2p)!}\left\langle\psi_0^{2p}\right\rangle,$$

where I used the Taylor series expression of the cosine. As the average is performed over Gaussian statistics, the $2p$-th moment used in this expression can be expressed as a function of the first two moments only, a result known as Wick's theorem [2], which here leads to

$$\left\langle\psi_0^{2p}\right\rangle = (2p-1)!!\left\langle\psi_0^2\right\rangle^p = (2p-1)!!\left(\frac{G(0)}{\beta J}\right)^p.$$

Finally, the mean modulus of the magnetisation can be rewritten as

$$m = \sum_{p=0}^{\infty}\frac{(2p-1)!!}{(2p)!}\left(-\frac{G(0)}{\beta J}\right)^p = \sum_{p=0}^{\infty}\frac{1}{p!}\left(-\frac{G(0)}{2\beta J}\right)^p = \exp\left(-\frac{G(0)}{2\beta J}\right).$$

For a $2d$ square lattice, one can compute the value of $G(0)$ to leading order, yielding

$$G(0) = \frac{\ln(2N)}{4\pi} + o\left(\frac{1}{N}\right),$$

leading to the exact expression of the spin-wave magnetisation at leading order in N, here expressed as a function of the temperature T again,

$$m = \exp\left(-\frac{T}{8\pi J}\ln(2N)\right). \tag{II.39}$$

This magnetisation decreases smoothly as N increases, and features an exponential decay of the magnetisation versus the temperature at any fixed N. Its typical shape is plotted in Fig. II.7(a).

Note that, when considering slightly different shapes of the lattice, one expects to find a similar result but with a geometric correction that affects the precise prefactor in $G(0)$. In this thesis, I will use the slightly different expression

$$m = \exp\left(-\frac{T}{8\pi J}\ln(aN)\right), \tag{II.40}$$

with a a factor that reflects the shape of the lattice. Furthermore, note that this expansion is only valid at very low temperatures, and that higher-order terms in the expansion that led to Eq. (II.37) should *a priori* be taken into account as the temperature increases. In practice, these effects can be described by an effective interaction J_{eff}, that replaces J in the predictions of m and takes into account the interactions between spin waves [117]. One can also explicitly study the susceptibility of this system, as defined in Sec. a).

$$\chi_{m,T} = \frac{\beta}{N}\left(\langle \boldsymbol{M}^2\rangle - \langle \boldsymbol{M}\rangle^2\right),$$

with $\boldsymbol{M}$ the instantaneous extensive magnetisation. However, in the context of the study of the $T \to 0$ limit, and in the following, it is more convenient to define the "reduced" susceptibility

$$\chi_m = T\chi_{m,T} = \frac{1}{N}\left(\langle \boldsymbol{M}^2\rangle - \langle \boldsymbol{M}\rangle^2\right),$$

which simply measures the width of the distribution of magnetisations. In the context of the XY model, on expects $\langle \boldsymbol{M}\rangle = \boldsymbol{0}$ at low temperatures even with a vanishingly small external field. As a result, this function simply behaves like

$$\chi_m = Nm^2 \sim N^{1-\frac{T}{4\pi J}} \tag{II.41}$$

at low temperatures, where I used the scaling of the magnetisation obtained in Eq. (II.39). This susceptibility is plotted in Fig. II.7(b). It is extensive as $T \to 0$, which is a sign that at very low temperatures the system approaches the zero-temperature critical point at which the system orders ferromagnetically. This critical point at $T = 0$ is described by a Gaussian theory, just like a mean-field-level theory, so that it displays the same "apparent" exponent $\eta = 0$.

At intermediate temperatures, the finite-size BKT transition is crossed. As a result, the magnetisation is suddenly suppressed at a higher rate than it would be with spin waves alone, as vortices and antivortices unbind and further destroy the uniform magnetisation state [118, 119]. Consequently, the spin-wave scaling of the magnetisation and susceptibility are no longer well-verified in this regime, even with effective interactions. In order

to pinpoint the finite-size transition temperature, it is useful to define a modified susceptibility that, instead of being extensive in the whole low-temperature regime, is peaked at the BKT transition. Hence, one often defines the reduced susceptibility associated to the fluctuations of the modulus of the magnetisation [116],

$$\chi_{|m|} = \frac{1}{N}\left(\langle \boldsymbol{M}^2\rangle - \langle|\boldsymbol{M}|\rangle^2\right),$$

which goes to zero both as $T \to 0$, and as $T \to \infty$. The reason why this function is peaked at the BKT transition is that this transition is associated with an abnormally large distribution of moduli of the magnetisation [116]. Furthermore, one can use the spin-wave calculations above to predict the behaviour of $\chi_{|m|}$. In order to do so, I introduce the full spin-spin spatial correlation,

$$g(r) = \langle \boldsymbol{s}_0 \boldsymbol{s}_r\rangle = \langle \cos\psi_0 \cos\psi_r\rangle + \langle \sin\psi_0 \sin\psi_r\rangle .$$

I start by focusing on the first term, in which the cosines can be written as full Taylor expansions,

$$\langle \cos\psi_0 \cos\psi_r\rangle = \sum_{p=0}^{\infty}\sum_{q=0}^{\infty} \frac{(-1)^{p+q}}{(2p)!(2q)!}\left\langle \psi_0^{2p}\psi_r^{2q}\right\rangle .$$

Wick's theorem can be applied again, leading, after some algebra (that is reported at length in the appendix of Ref. [116]), to

$$\langle \cos\psi_0 \cos\psi_r\rangle = m^2 \cosh\left(\frac{G(r)}{\beta J}\right).$$

The second term of g can be treated in a similar way, leading to

$$\langle \sin\psi_0 \sin\psi_r\rangle = m^2 \sinh\left(\frac{G(r)}{\beta J}\right).$$

Therefore, one gets

$$g(r) = \langle \boldsymbol{s}_0 \boldsymbol{s}_r\rangle = m^2 \exp\left(\frac{G(r)}{\beta J}\right).$$

This pair correlation function, when summed over all sites, yields the second moment of the magnetisation (this is a standard result: summing a connected 2-point functions over all possible distances yields a response function [2]),

$$\frac{1}{N}\langle \boldsymbol{M}^2\rangle = \sum_r g(r).$$

Therefore, using the definition of $\chi_{|m|}$, I find

$$\chi_{|m|} = m^2 \sum_r \left[\exp\left(\frac{G(r)}{\beta J}\right) - 1\right],$$

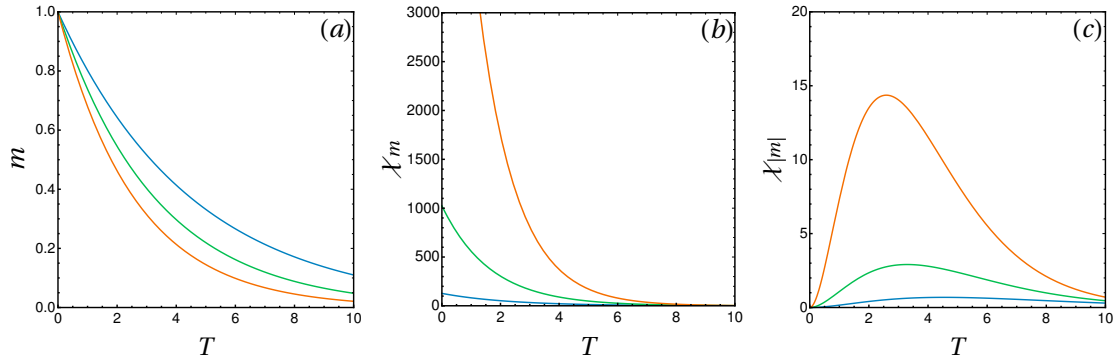

Fig. II.7 **Finite-size spin-wave description.** (*a*) Magnetisation versus the temperature, as obtained from Eq. (II.39) for $J = 1$ and $N = 128$ (blue), 1024 (green), and 8192 (orange). (*b*) Corresponding susceptibility, as given by Eq. (II.41). (*c*) Corresponding modified susceptibility, as given by Eq. (II.42).

in which the exponential can be expanded to leading order (noticing that the sum of $G(r)$ over all positions is zero),

$$\chi_{|m|} \approx \frac{m^2}{2\beta^2 J^2} \sum_r G(r)^2.$$

The expression (II.38) can then be written explicitly,

$$\chi_{|m|} \approx \frac{m^2}{2\beta^2 J^2 N^2} \sum_r \sum_{q\neq 0} \sum_{q'\neq 0} \frac{e^{i(q+q')r}}{\gamma_q \gamma_{q'}},$$

and one can notice that the only non-zero terms in the last sum are obtained for $q+q' = 0$, and that $\gamma_{-q} = \gamma_q$ so that

$$\chi_{|m|} \approx \frac{m^2}{2\beta^2 J^2 N} \sum_{q\neq 0} \left(\frac{1}{\gamma_q}\right)^2.$$

The sum over the q's in the finite-size Brillouin zone can be computed numerically, leading to

$$\chi_{|m|} \approx \frac{N m^2}{2a_{2D}\beta^2 J^2}, \tag{II.42}$$

with $a_{2D} \approx 258.89$ [116], which is plotted in Fig. II.7(*c*). Using the scaling of m against the number of spins obtained in Eq. (II.39), this equation leads to $\chi_{|m|} \sim N^{1-\frac{T}{4\pi J}}$. This shape shows explicitly that this susceptibility scales like the usual one against the size of the system, with the convenient addition of its maximum at the finite-size BKT temperature, $T^\star$. Note that the spin-wave description of $\chi_{|m|}$ can be made better by explicitly defining it as a piece-wise function that takes into account renormalized interactions and an exponential scaling at high temperatures [116].

Near $T^\star$, the susceptibilities (both the usual one and the reduced one) scale according to the BKT value of the ratio of exponents $\gamma/\nu = 2 - \eta$ [112, 116],

$$\chi_m(T^\star) \sim \chi_{|m|}(T^\star) \sim L^{\frac{\gamma}{\nu}} = L^{\frac{7}{8}}.$$

Similarly, at T_{KT}, the magnetisation scales according to the BKT value of the ratio of exponents β/ν,

$$m \sim L^{-\frac{\beta}{\nu}} = L^{-\frac{1}{8}},$$

Note that these scalings are compatible with the spin-wave-level approximations of m and $\chi_{|m|}$, provided that the critical temperature is of the order of $T_{KT}/J \approx \pi/2$. In practice, using $\chi_{|m|}(T^\star)$ instead of $\chi_m(T^\star)$, the finite-size scalings associated to the BKT transition can therefore be studied almost like a usual critical transition. Indeed, one can plot $\chi_{|m|}(T^\star)$, extract $T^\star$ and γ/ν from the position of its maximum, and measure m at that temperature. The difference with a usual critical transition, however, is that the correlation length scales exponentially against the temperature. Therefore, extracting the ν exponent from finite-size scalings requires several decades of $\ln L$, which is numerically (or experimentally) challenging. Furthermore, the right rescaling of the temperature axis to collapse, say, magnetisation curves corresponding to several sizes is $t \to t(\ln L)^{1/\nu}$, where $t = T/T_{KT} - 1$ is the reduced temperature. As a result, arguing in favour of a value of T_{KT} or of a ratio of exponents is also rather difficult, since convincing rescalings also require several decades of $\ln L$.

II.4 Theory of Liquids

The most natural question to ask regarding a model of a liquid is: if I consider the system at a given density, and put it in contact with a heat bath at a given temperature, what will it look like? The answers usually correspond to the so-called "canonical" phases of matter, fluid or solid, depending on the degree of spatial ordering. Furthermore, in many cases, one observes phase separations, for instance between low- and high-density fluids, that are respectively called a gas and a liquid. This picture is a good description of the physics of so-called "simple" liquids, that is to say, liquids made of particles that do not possess any internal degree of freedom. Simple liquids are therefore opposed to "molecular" liquids, which can have elongated shapes and, therefore, anisotropic steric interactions. These molecular liquids can display a large variety of different phases, like in the well-known example of liquid crystals. In extreme cases, like polymers, molecular liquids are even called "complex" liquids, to highlight the opposition to simple liquids. In this thesis, the models I consider are not simple liquids *stricto sensu*, since particles carry spins. However, as further discussed in Chapter III, I only consider simple isotropic interactions, both in the ferromagnetic coupling and in the repulsive potential. Because of this very simple choice, the models considered here constitute a simple extension of simple liquids: all of the anisotropy of the model is contained in the spin degree of freedom, but is not encoded explicitly in the interactions. That is why, in this section, I describe the standard phenomenology and description of simple liquids, so that it may be extended to my model further in the thesis. First, in Sec. II.4.1, I briefly present what one usually

expects in the phase diagram of a liquid, both in the case of passive liquids, and of active liquids. Then, in Sec. II.4.2, I present the most usual methods that are used to predict the aspect of these phase diagrams. These methods are applied to particles carrying spins in Chapter III. Finally, in Sec. II.4.3, I present the main dynamical properties that one expects in both passive and active fluids, which are useful for the comparison to active systems presented in Chapter V.

II.4.1 Phase Diagrams of Liquids

a) Passive Liquids: the Role of Attraction

In the standard case of simple liquids, one usually considers a system described by a Hamiltonian

$$\mathcal{H} = \sum_{i=1}^{N} \left[\frac{p_i^2}{2} + \sum_{i<j} U(r_{ij}) \right],$$

where U is a short-ranged, isotropic, pairwise interaction. This potential is here assumed to be the same one for all particles, meaning that the system is monodisperse. Just like any other Hamiltonian system, it can be described using the statistical mechanics formalism introduced in Sec. II.2. In particular, theoretical calculations are usually performed in the canonical ensemble, meaning that one studies a system of N particles, confined in a volume V, in contact with a bath at a temperature T, and described by the canonical distribution of configurations

$$\mathcal{P}\left[\mathcal{C}\right] = \frac{1}{Z} e^{-\beta \mathcal{H}}$$

One therefore predicts the properties of the system at a given density ρ and temperature T, so that the natural plane to predict a phase diagram is the (ρ, T) plane.

At high temperatures and low densities, the system is expected to behave like a system of independent particles, since the particles are either too far from each other on average to interact, or have very large kinetic energies, so that the potential is almost irrelevant. This regime is therefore well-described by the kinetic part of the Hamiltonian only, leading to a collection of Gaussian independent velocities drawn according to the Maxwell-Boltzmann distribution

$$\mathcal{P}\left[\mathcal{C}\right] \approx \frac{1}{Z} \prod_{i=1}^{N} e^{-\beta p_i^2/2}.$$

A fluid described by these statistics is called an ideal fluid: it is a homogeneous fluid with independent Gaussian-distributed velocities and independent, uniformly distributed positions.

At low temperatures and high densities, the exact opposite picture holds: the physics is dominated by the interactions. Therefore, each particle essentially sits at the minimum of the potential imposed by neighbouring particles. In this situation, applying a force to one particle changes the potential energy landscape of its neighbours, which all strongly respond to the change since they have little kinetic energy: the system is rigid, or "solid".

The most common examples of solid phases are crystalline phases, phases such that particles sit on a regular lattice. Using the vocabulary of critical transitions used in Sec. II.3, going from an isotropic fluid to a crystal, the system spontaneously breaks a symmetry: the fluid-solid crossover is a phase transition. The mechanism is however different from the one described in ferromagnets: instead of developing a Mexican hat feature at low temperatures, a metastable basin of the free energy corresponding to the crystal becomes the global minimum below a finite temperature. This is a first-order transition.

At intermediate values of the temperature and density, the phenomenology depends on the nature of U: if and only if U is attractive, a phase separation domain between a low- and a high-density fluid takes place [1]. This phase-separation is usually called the liquid-gas phase separation, where the low-density fluid is called a gas and the high-density fluid is called a liquid. Any system with a temperature and an average density such that it lies inside of the phase-separating domain is in fact composed of a gas and a liquid, the densities of which are represented by coexistence lines in the (ρ, T) plane. The typical aspect of this coexistence line, as well as the crystallisation line, are sketched in Fig. II.8. When observed, it extends up to a finite temperature, at which it reaches the liquid-gas critical point, and above which the fluid is said to be supercritical. It is called "critical" since, just like a magnetic transition, it is associated to a susceptibility that diverges at the transition, both at the critical point and below the coexistence lines. In the context of fluids, however, this susceptibility is called the compressibility, χ_c, which is usually defined from the variation of volume of a system as a response to a change in pressure at a constant temperature,

$$\chi_c = -\frac{1}{V}\left.\frac{\partial V}{\partial P}\right|_T .$$

Above the critical point, the fluid does not phase separate anymore. This indicates the fact that there is no fundamental difference between a liquid and a gas: they are both isotropic fluids, with the same symmetry. Therefore, they are allowed to be connected over the phase-separation domain.

The liquid-gas critical point can be shown to belong to the same universality class as the Ising model [9], where the "up" and "down" spins are here replaced by "high" and "low" density areas. The only addition to the usual setting of the Ising model is that one should consider the ensemble in which the total magnetisation is conserved, which is tantamount to imposing conservation of mass in the fluid. In this Ising picture, attraction plays the role of ferromagnetic interactions, so that the absence of a phase-separation becomes obvious in the case of a purely repulsive potential: there can be no ferromagnetic ordering without a ferromagnetic interaction.

An interesting special case is that of liquids in $d = 2$ [114]. In that special case, Mermin and Wagner showed that crystalline order is, similarly to the magnetisation of an XY model, destroyed by spin-waves (here called phonons) in the thermodynamic limit [54, 55]. In fact, melting in $d = 2$ is observed to be accompanied by the creation of crystalline defects, so that a scenario similar to that of the BKT transition was proposed by Nelson-Halperin [120] and Young [121] to describe the transition. This scenario, called the KTHNY scenario, hypothesises that melting happens in two steps. At a first temperature T_m, pairs of defects (dislocations) unbind, turning the low-temperature, phonon-rich solid

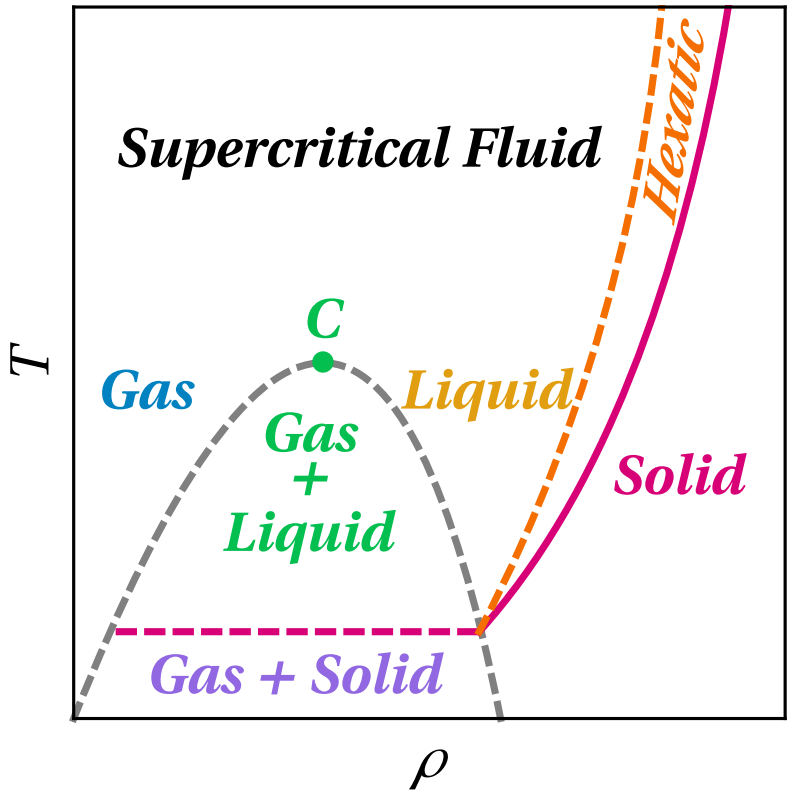

Fig. II.8 **Sketch of the phases of a simple liquid.** For all kinds of monodisperse potentials and in all dimensions $d \geq 2$, a fluid-solid transition is observed at low temperatures or high densities (solid red line). If the potential contains an attractive part, a phase separation between a gas and a liquid appears (dashed grey line), ending in a critical point C (green dot). In the special case $d = 2$, the transition between liquid and solid is mediated by an anisotropic "hexatic" phase, so that there is a liquid-hexatic transition line (dashed orange line).

into a phase with six-fold bond-orientational order, called the hexatic phase. Then, at a second temperature T_h, the defects that appeared at T_m each turn into pairs of defects (disclinations), thus breaking up orientational order and leading to an isotropic liquid. Through renormalisation calculations, the KTHNY scenario predicts that both transitions are of the BKT kind. This result can be seen as a violation of the Mermin-Wagner argument (see Sec. a)). Indeed, the hexatic order can be characterised by a local spin-like variable that can be associated to any particle i, called $\psi_{6,i}$ [122], and defined through

$$\psi_{6,i} = \frac{1}{6} \sum_{j \in \partial i} e^{i \frac{\phi_{ij}}{6}},$$

where $\phi_{ij} = \arctan(r_{ij,y}/r_{ij,x})$ is the angle formed between the horizontal and the line that links particles i and j. This complex variable is equivalent to a vector with a modulus smaller than 1. When particles tend to have 6 neighbours organised with a regular six-fold rotational symmetry, $\psi_{6,i}$ is close to a unit vector. Furthermore, if all particles have a locally hexagonal environment, all the $\psi_{6,i}$ are like unit vectors, and if the hexagonal

domains are oriented in the same direction, the average value

$$\Psi_6 = \frac{1}{N}\sum_{i=1}^{N}\psi_{6,i}$$

is also a unit vector. Therefore, Ψ_6 is the equivalent of an intensive magnetisation for hexatic order, that spontaneously breaks rotational symmetry in $d = 2$. This violation of the Mermin-Wagner argument is mentioned, for instance, in Refs. [114, 115]. Additionally, note that the nature of the hexatic transition at T_h seems to be non-universal. Indeed, while the KTHNY scenario has been observed experimentally in soft colloids [123], a standard first-order-transition scenario has recently been reported numerically [124–126] in the case of hard disks ($U \to \infty$ up to a finite range σ, then $U = 0$), and later observed experimentally in colloidal hard disks [127].

In summary, in a passive simple liquid, one can expect: an isotropic fluid phase at low densities and high temperatures, a solid phase at low temperatures and high densities, a liquid-gas phase separation *if and only if* U has an attractive part, and possibly, in $2d$, a non-universal liquid-hexatic-solid pattern at high densities and low temperatures, as sketched in Fig. II.8. Molecular liquids, due to the presence of additional degrees of freedom, generally have additional phases corresponding to the ordering of these degrees of freedom. In particular, even very simple molecules like the water molecule are known to present so-called "liquid-liquid transitions", between isotropic phases and polar phases in which the internal orientation of the molecule order [128]. The most famous example of such phase diagrams is that of liquid crystals, molecules with strong anisotropies that can arrange into a variety of anisotropic fluid phases [3, 4, 115]. These anisotropic fluid phases typically lie in the low-temperature and high-density portion of the phase diagram, to the right of the liquid-gas phase separation.

b) Active Liquids: Motility-Induced Phase Separations

For the sake of the comparison between the models studied in this thesis and usual models of self-propelled particles, it is useful to briefly summarise the structural phases in active liquids. The issue with active systems is that, since they are not conservative, statistical mechanics cannot be defined on the same grounds of energy and momentum conservation that were used for Hamiltonian systems in Sec. II.2. As a result, the dynamics of active systems in phase space do not rely on the usual statistical ensembles, so that the precise shape of the interactions influences a lot the nature of the observed phases. One should therefore be careful that there is *a priori* no reason to believe that active systems can be classified into classes similar to the universality classes introduced in Sec. II.3, however close two active models might look. A typical example of this fact is illustrated by the comparison between self-propelled hard dumbbells [64] and self-propelled hard-disks [65] in $d = 2$, that exhibit very different phase diagrams.

That being said, the examples of Refs. [64, 65] show that, at low activity, the phase diagram of an active system is not modified dramatically: it is essentially a smooth deformation of the passive phase diagram. Therefore, although the shape of interactions might alter it, it is reasonable to expect, in an active system, the phenomenology of the corresponding passive liquid, at least up to a given value of the activity. However, novel

phenomena also happen at high activities. Some of these phenomena are of particular interest in this thesis and are listed below.

First, many systems of self-propelled particles feature a phase separation, akin to a liquid-gas phase separation, even though they interact through purely repulsive potentials. This kind of phase-separation, which was coined Motility-Induced Phase Separation (MIPS), is commonly explained by an effective slowing down of particles in denser regions, that effectively plays the same role as an attractive interaction [61–63]. It is also recovered in richer models with velocity-velocity alignment and self-propulsion [66].

A second property of interest is that, when considering systems of self-propelled particles that align their velocities together, such as the celebrated Vicsek model [52], a true phase transition to a "magnetised" state for the velocities can be observed at a finite temperature even in $2d$ [58, 129]. This result is a clear reminder that neither the Mermin-Wagner argument nor the BKT scenario have any reason to apply in non-equilibrium systems, *e.g.* when considering spins that are also velocities and move in continuous space. As a result, parts of the phase diagram contains collectively moving liquid states that survive in the thermodynamic limit.

In summary, active systems can generally feature solid phases, ideal fluid phases, hexatic phases in $2d$, and phase-separated states with or without attraction. Furthermore, any of those phases can also be accompanied by a macroscopic alignment of the velocities, that survives in the thermodynamic limit.

II.4.2 Analytical Predictions of Equations of State

In order to discuss the phases displayed by the models I study in this thesis, I need to introduce the usual strategies used to predict the phase diagram of a passive liquid from the shape of its Hamiltonian. I start by presenting, in Sec. a), the so-called virial expansion, which consists in computing an exact, low-density expansion of the pressure. I here follow a textbook strategy [1, 83, 130–132], mostly inspired by Hansen and McDonald [1], and Mayer and Goeppert-Mayer [132] to write the expansion. Then, in Sec. b), I present the so-called Percus-Yevick route, which consists in finding a self-consistent closure of the equation that is verified by the 2-point correlation of a liquid. Finally, in Sec. c), I present a mean-field approach for lattice models, relying on the cavity method, which consists in approximating the hypercubic lattice by a tree-like graph so that the partition function can be written recursively.

a) The Virial Route

In order to predict the phase diagram of a liquid, it is useful to cast the problem into a form such that the thermodynamic functions (pressure, density, temperature, etc.) explicitly intervene. Consider the canonical partition function of a simple liquid of N particles in dimension d,

$$Z_N = \frac{1}{N!}\int d^{dN}\boldsymbol{R} d^{dN}\boldsymbol{P} \prod_{i=1}^{N} \left[e^{-\beta\left(\frac{p_i^2}{2}+\sum_{j<i} U(r_{ij})\right)} \right].$$

The integrals over momenta can easily be computed,

$$\begin{aligned} Z_N &= \frac{1}{N!}\left(\frac{2\pi}{\beta}\right)^{\frac{dN}{2}} \int d^{dN}\boldsymbol{R} \prod_{i=1}^{N} \left[e^{-\beta \sum\limits_{j<i} U(r_{ij})} \right], \\ &\equiv \frac{1}{N!}\left(\frac{2\pi}{\beta}\right)^{\frac{dN}{2}} Z_{N,r} \end{aligned}$$

and only the partial partition function Z_r given by the integral of the interaction factors is non-trivial to compute. A way to cast this partition function into a more tractable shape is to perform a so-called Mayer expansion [1, 132] of the partition function. In order to do so, I define the Mayer functions

$$f_{ij} = e^{-\beta U(r_{ij})} - 1,$$

that count by how much the partition function is modified by a non-zero interaction between particles i and j, compared to the case in which these particles do not interact. Using these functions, the partial partition function can be rewritten

$$Z_{N,r} = \int d^{dN}\boldsymbol{R} \prod_{j<i} \left(1 + f_{ij}(r_{ij})\right).$$

I then expand the product over pairs of particles, and regroup the terms depending on the number of Mayer functions that they contain

$$Z_{N,r} = \sum_{n=0}^{N(N-1)/2} \int d^{2N}\boldsymbol{R} z_n(\boldsymbol{R}),$$

where I defined z_n such that

$$\begin{aligned} z_0 &= 1, \\ z_1 &= \sum_{j<i} f_{ij}(r_{ij}), \\ z_2 &= \sum_{\substack{j_2<i_2 \\ \{(i_2,j_2)\neq(i_1,j_1)\}}} \sum_{j_1<i_1} f_{i_1 j_1}(r_{i_1 j_1}) f_{i_2 j_2}(r_{i_2 j_2}), \\ &\dots \end{aligned}$$

where the subscript of the sum indicates that it contains terms such that $i_1 = i_2$ or $j_1 = j_2$, but not the term with $i_1 = i_2$ *and* $j_1 = j_2$. Using the same notation, the z_n can be written in a more compact way,

$$z_n = \delta_{n,0} + \sum_{\substack{\{j_l<i_l\} \\ \{(i_l,j_l)\neq(i_{l'},j_{l'})\} \\ 1\leq l\leq n}} \left(\prod_{p=1}^{n} f_{i_p j_p} \right).$$

One thus gets a rewriting of the partial partition function as a sum of terms that each contain n-body interactions: in z_0, I count all configurations such that particles are all

independent, in z_1 all the configurations such that only 2 particles interact together, in z_2 all the configurations such that either 2 pairs or a triplet interact together, etc.

In order to relate this Mayer expansion to thermodynamic properties, it is common to switch to the grand-canonical ensemble (see Sec. II.2) at this point. In that ensemble, the considered system is allowed to exchange particles with a reservoir, and the intensive parameter that controls the fluctuations of the number of particles N is the chemical potential, which is defined from a derivative of the canonical free energy

$$\mu \equiv \left.\frac{\partial F_N}{\partial N}\right|_{T,V}.$$

In particular, for an ideal gas, the free energy verifies

$$\beta\frac{F^{id}}{N} = \ln\left(\frac{Z_N}{N!}\right),$$

where $Z_N = (2\pi/\beta)^{dN/2}V^N$. Using Stirling's approximation, one finds

$$\beta\frac{F^{id}}{N} = \ln \Lambda^d\rho - 1,$$

with

$$\Lambda \equiv \left(\frac{2\pi}{\beta}\right)^{\frac{1}{2}},$$

a typical length scale of the microscopic dynamics, the de Broglie thermal length. This expression leads to

$$\mu^{id} = k_B T \ln \Lambda^d\rho. \tag{II.43}$$

The grand-canonical partition function is then a weighted sum of canonical partition functions [1, 81],

$$\Xi = \sum_{N=0}^{\infty} \frac{\hat{z}^N}{N!} Z_N,$$

where $\hat{z}$ is called the fugacity, and is defined through

$$\hat{z} = \frac{e^{\beta\mu}}{\Lambda^d}.$$

Using the Mayer expansion expression of the canonical partition function, the grand-canonical partition function can be rewritten as

$$\Xi = \sum_{N=0}^{\infty} \frac{z^N}{N!} \sum_{n=0}^{N(N-1)/2} \int d^{2N}\boldsymbol{R} z_n(\boldsymbol{R}), \tag{II.44}$$

where the factors obtained by integrating the momentum part of the partition function were absorbed into the definition of the effective fugacity z,

$$z = \frac{e^{\beta\mu}}{\Lambda^d}\left(\frac{2\pi}{\beta}\right)^{\frac{d}{2}} = e^{\beta\mu}.$$

The expression (II.44) is a sum over all possible numbers of particles of the sum over all possible combinations of the Mayer functions described in the canonical ensemble. It is often written using graphical notations, where a Mayer function acting on 2 particles is noted as

$$f(r_{12}) \equiv$$.

In these notations, products of several Mayer functions acting on different particles are simply several of those patterns side by side, meaning that they can be factorized. If two Mayer functions add on a common particle, however, the graphs are linked at the vertex corresponding to that particles,

$$f(r_{12})f(r_{23}) \equiv$$  .

In these notations, I furthermore represent an integral over the position of a particle as a black dot,

$$\int d^d\boldsymbol{r_1} \equiv \bullet,$$

and the integral over two positions linked by a Mayer function is noted as two black dots joined by a line,

$$\int d^d\boldsymbol{r}_1 d^d\boldsymbol{r}_2 f(r_{12}) \equiv$$  .

Using these graphical notations, and absorbing the $z^N/N!$ factors into the graphs, the grand-canonical partition function can be written as

$\Xi =$ 

$=$ 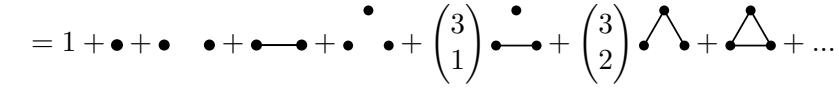

where I used the fact that dummy variables can be interchanged in the integrals. An interesting quantity to represent graphically is the logarithm of this partition function, which gives the grand potential. In order to do so, it is useful to focus on the rules that govern products of graphs. Recalling that each graph contains a $z^N/N!$ factor, the product of two graphs with numbers of vertices m and n is simply given by the juxtaposition of these graphs, multiplied by a factor $(m+n)!/m!n!$. For instance,

$$\bullet^2 = 2!$$

$$\bullet \times$$ $= \frac{3!}{2!1!}$.

Using this property, it is easy to express the exponential of a graph, for instance:

$$\exp\left[\bullet\right] \equiv \sum_{p=0}^{\infty} \frac{1}{p!}\bullet^p$$

$=$ 

In other words, the exponential of a graph consists of the sum of all the graphs made up from products of it. Conversely, the logarithm of an infinite sum of graphs is (up to combinatorial factors) the sum of the connected components that make up the graphs in the sum. Using this result, one can check that the partition function is the exponential of the sum of all connected graphs only,

$\ln \Xi =$ 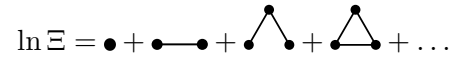 $+ \ldots$

Since each black dot contains a power of the fugacity, this representation is useful to compute derivatives of the grand-canonical free energy, $\Omega = -\ln \Xi/\beta$, with respect to the fugacity. In particular, the density of a homogeneous fluid can be defined through the thermodynamic relation [1, 132]

$$\begin{aligned} \rho &= z\frac{\partial \ln \Xi}{\partial z}, \\ &= \bullet + 2\,\bullet\!\!-\!\!\bullet + 3 \; \text{ 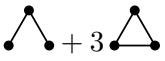 } + \ldots \end{aligned} \tag{II.45}$$

which is an expression of ρ as a power series of the fugacity. I now seek to deduce an equation of state, that is to say an equation that links thermodynamic properties of the system together, from this relation. A formal way to do so is to write down the logarithm of this last equation,

$$\log \frac{\rho}{z} = \ln \frac{\partial \ln \Xi}{\partial z}. \tag{II.46}$$

The left-hand side of Eq. (II.46) can be rewritten in terms of chemical potentials, using the value of μ^{id} obtained in Eq. (II.43), yielding

$$\beta\mu = \beta\mu^{id} - \ln \frac{\partial \ln \Xi}{\partial z}. \tag{II.47}$$

This expression can be injected into the thermodynamic equation that links the pressure, the chemical potential and the density of a system [1, 132],

$$\left.\frac{\partial P}{\partial \rho}\right|_T = \rho \left.\frac{\partial \mu}{\partial \rho}\right|_T,$$

then integrated over densities yielding:

$$\beta P = \rho - \int_0^\rho d\rho' \ln \frac{\partial \ln \Xi}{\partial z}(\rho'), \tag{II.48}$$

where I also used the expression of the pressure of an ideal gas, $\beta P^{id} = \rho$. The last task is therefore to express the right-most term, which was expressed as a power series of the fugacity until now, as a function of the density. This task is exactly equivalent to inverting the series $\rho(z)$ found in Eq. (II.45), which is invertible since all coefficients are positive. In order to invert the series, one can use the fact that the considered fluid is homogeneous, so that the origin can be chosen arbitrarily among the points of each

graph. The effect of choosing the origin is to replace a black dot (position that needs to be integrated over) by a white dot (position that is not integrated over). A special case is that of "reducible" graphs, i.e. graphs that would no longer be connected if one of their vertices were removed. For instance, the graph

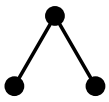

is no longer connected if the top vertex is removed: the top vertex is called an articulation point. For such graphs, if one chooses an articulation point as the origin, the graph becomes a factorisable product of lower-order integrals, for instance

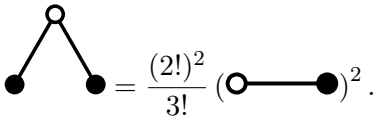

Graphs that present no such articulation point are called star-irreducible. Therefore, ρ can be written as a sum of all the products of graphs that have one white dot, placed anywhere except on an articulation point,

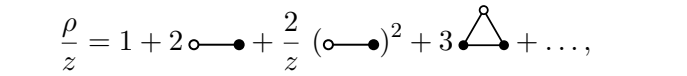

where white dots do not contain a factor of z due to the factorisation of z on the left-hand side. This series can be inverted by brute force iteratively,

$$\begin{aligned} z &= \rho - \sum_{p=2}^{\infty} \alpha_p z^p \\ &= \rho - \alpha_2 \left(\rho - \sum_{p=2}^{\infty} \alpha_p z^p \right)^2 - \sum_{p=3}^{\infty} \alpha_p z^p \\ &= \rho - \alpha_2 \rho^2 - 2\rho \sum_{p=2}^{\infty} \alpha_p z^p + \left(\sum_{p=2}^{\infty} \alpha_p z^p \right)^2 - \sum_{p=3}^{\infty} \alpha_p z^p \\ &= \rho - \alpha_2 \rho^2 - (\alpha_3 + 2\alpha_2)\, \rho^3 + \dots \end{aligned} \tag{II.49}$$

where I called the coefficients in the series α_p to lighten the equations. The fugacity can therefore be expressed as a sum of diagrams with dots coding for a power of ρ, or ρ-graphs. In order to get the equation of state in its final form, one must now notice that, like the series ρ/z, the series $\ln \rho/z$ is given by a sum of z-graphs , with at least two dots, one of which is a white dot that is not an articulation point. Then, each of the dots coding for a power of z in $\ln \rho/z$ can be replaced by the full series of ρ-graphs contained in Eq. (II.49). When this replacement is performed, all the black dots in the graphs of $\ln \rho/z$ can be replaced by a white dot. As a result, all the graphs that contain an articulation point factorise into smaller graphs, until all that is left is a sum of star-irreducible graphs [1, 132]. Consequently, one finds that $\ln \rho/z$ is the sum of all star-irreducible ρ-graphs (drawn in blue), with a white dot denoting the origin

This expression can be rewritten without using graphs as

$$\ln \frac{\partial \ln \Xi}{\partial z}(\rho) = \sum_{i=0}^{\infty} \beta_i \rho^i,$$

with the coefficients β_i (the "Mayer graphs" [132]) given by the graphs of Eq. (II.50), for instance

$$\begin{aligned} \beta_1 &= \int d\boldsymbol{r} f(r), \\ \beta_2 &= \frac{1}{2} \int d\boldsymbol{r}_1 d\boldsymbol{r}_2 f(r_1) f(r_2) f(r_{12}), \\ &\dots, \end{aligned}$$

where the prefactor is in practice simply given by the inverse of the number of possible permutations of the integration variables $\boldsymbol{r}_i$ [132]. Looking at the definition of these Mayer graphs, one sees that each of those β_i graphs counts the contribution due to simultaneous $i+1$-body interactions. Finally, this expression can be inserted into the equation of state (II.48) to get the virial equation of state,

$$\frac{\beta P}{\rho} = 1 + \sum_{i=2}^{\infty} B_i \rho^{i-1}, \tag{II.51}$$

where the virial coefficients B_i, which are functions of the temperature, are defined through

$$B_{i+1}(T) = -\frac{i}{i+1} \beta_i(T).$$

The interest of writing an equation of state such as Eq. (II.51) is that one can seek explicitly the singularities of the compressibility. Indeed, from the virial expansion, it is easy to compute

$$\left.\frac{\partial P}{\partial \rho}\right|_T = -\frac{V^2}{N} \left.\frac{\partial P}{\partial V}\right|_T = \frac{1}{\rho \chi_c},$$

so that zeros of $\partial P/\partial \rho|_T$ correspond to singularities of χ_c. The B_i's, however, are generally challenging to compute beyond the first few. Even in the simple example of hard disks, these coefficients have only been computed up to the 10^{th} order, roughly 40 years after the first six coefficients [133–136]. Consequently, one generally truncates the series (II.51) at a finite order to make calculations more tractable. Since it is a power series in ρ, doing so restricts the domain of validity of the equation of state to low values of the density. Furthermore, since the B_i's are functions of the temperature through a product of Mayer functions, that themselves decrease exponentially with the temperature, the truncation of the virial expansion is *a priori* also valid only at high enough temperatures. A truncated virial expansion is therefore an efficient tool to describe fluid phases, and to predict liquid-gas phase separations, but not fluid-solid transitions that happen at low temperatures and large densities. In practice, one generally compute B_2 and B_3 only, so that the pressure is described by a degree-3 polynomial of the density. The reason

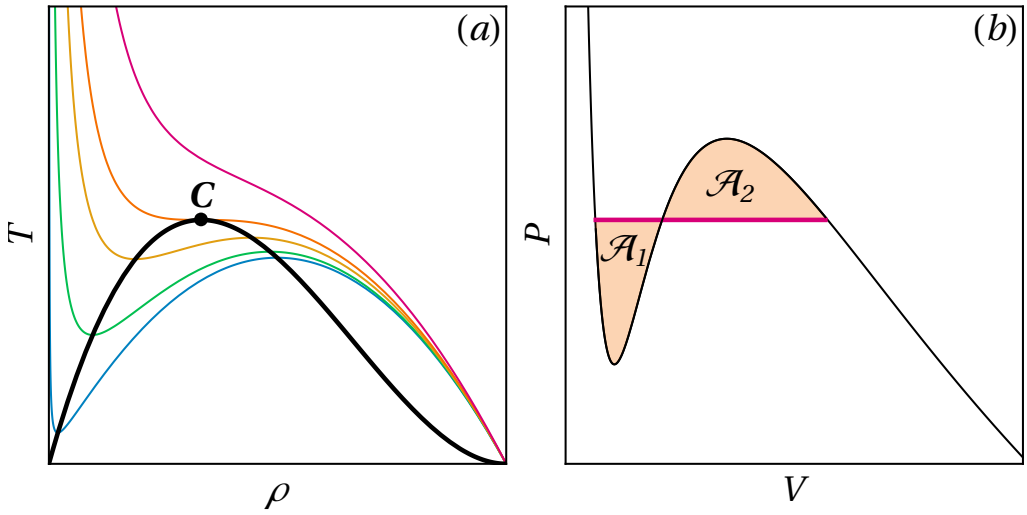

Fig. II.9 **Typical output of a truncated virial expansion.** (a) Isobaric lines in the (ρ, T) plane (coloured lines), obtained for pressures growing from blue to red. The black line is the spinodal, that indicates the location of the extrema of the isobaric lines below the critical value P_c of the pressure. (b) Sketch of the Maxwell construction in the Clapeyron diagram. The homogeneous isothermal line (black) is replaced by a flat line (red) such that the surface areas $\mathcal{A}_1$ and $\mathcal{A}_2$ (light orange) exactly compensate.

for this choice is that it is the minimal number of terms in the expansion that enables the pressure to feature two extrema that merge into an inflexion point, i.e. a structure that could describe a liquid-gas phase separation ending in a critical point like the one described in Sec. II.4.1. To seek the location of this structure, one generally plots curves of constant pressure (isobaric curves) in the (ρ, T) plane. The points of these curves that have a horizontal tangent correspond to points such that the derivative

$$0 = \left.\frac{\partial T}{\partial \rho}\right|_P = \frac{V^2}{N} \left.\frac{\partial T}{\partial V}\right|_P = \frac{1}{\rho \alpha_P},$$

where α_P is the isobaric thermal expansion coefficient. Similarly to the compressibility, this response coefficient features a singularity at liquid-gas phase transitions, as these transitions are characterised by diverging volume fluctuations at a finite value of both the pressure and the temperature. Note that the critical exponents that one finds using a virial expansion are the mean-field ones at all finite orders of the expansion: the virial expansion is therefore equivalent to a mean-field calculation with respect to the critical behaviour [1]. A schematic example of the shape of the isobaric curves obtained from a degree-3 truncated virial expansion is shown in Fig. II.9(a). On this sketch, one indeed sees that below a critical value of the pressure, isobaric lines develop minima and maxima, i.e. points with a diverging compressibility, that indicate a liquid-gas transition. The location of these extrema when varying the pressure in $[0; P_c]$ can be measured, and plotted in the (ρ, T) plane. The resulting line, called the spinodal line, is drawn in Fig. II.9(a) as a black line. At P_c, it ends in a single point, the critical point of the liquid-gas phase separation, that corresponds to the location of an inflexion point of the isobaric lines. Note that, while

the truncated virial expansion method thus predicts the presence of a critical point for the liquid-gas phase separation, the spinodal line is not the same object as the coexistence line presented in Sec. II.4.1. Indeed, the spinodal line is the boundary of the region in which the isobaric lines are growing functions of the density. In terms of the response functions, these correspond to a negative compressibility, which is unphysical. The reason for this unphysical result is that this calculation assumes the fluid to be homogeneous, but that the homogeneous fluid solution is in fact unstable in the region inside the spinodal line. In a real fluid, the growing part of the isobaric lines is well-known to be replaced by an (isothermal) horizontal section [1]. The temperature of this isothermal part is *a priori* free to take any value between the value P_{min} of the local mininum of the pressure, and the value P_{max} of its local maximum. However, there is a geometric argument proposed by Maxwell that allows to find the value of this plateau. This argument was first formulated by Maxwell [137] in the Clapeyron diagram (the (P, V) plane), where isothermal lines are drawn instead of isobaric lines, and states that the mechanical work associated to the transition should be zero. The right choice of the pressure at each temperature and volume is then such that the total oriented area of the regions between the plateau and the original isobaric line is zero (see Fig. II.9(b)), so that a hypothetical cyclic transformation following first the homogeneous isothermal line, then the flat line, does indeed not produce work. The Maxwell construction yields the coexistence line, that delimitates the region where phase separation happens. It is in fact equivalent to requiring that the chemical potential of the two coexisting fluids should be the same [1].[9] Note however that there is no reason to believe that this construction is correct in the (P, V) plane, but not in the (P, ρ) or (T, ρ) planes.

The construction of the virial expansion discussed in this section can be repeated straightforwardly in the case of a molecular liquid carrying a d_i-dimensional vector of internal degrees of freedom $\boldsymbol{\theta}$. In that case, the pair interaction potential U depends on the values of $\boldsymbol{\theta}$ of each particle, so that the Mayer function itself depends on it,

$$f(r_{12}, \boldsymbol{\theta}_1, \boldsymbol{\theta}_2) = e^{-\beta U(r_{12}, \boldsymbol{\theta}_1, \boldsymbol{\theta}_2)} - 1,$$

and the $N-$particle partial canonical partition function associated to the interactions reads

$$Z_{N,r} = \int d^{dN}\boldsymbol{R} d^{d_i N}\boldsymbol{\Theta} \prod_{j<i} (1 + f_{ij}(r_{ij}, \boldsymbol{\theta}_i, \boldsymbol{\theta}_j)) .$$

This partition function can be expanded, and the grand-canonical free energy can be deduced from it, then integrated over the spatial density to yield the pressure in the exact same way as in the case of simple liquids. The only difference is that the Mayer graphs now contain integrals over the internal degrees of freedom as well [1],

$$\beta_1 = \int d\boldsymbol{r}_1 d\boldsymbol{r}_2 d^{d_i}\boldsymbol{\theta}_1 d^{d_i}\boldsymbol{\theta}_2 f(r_{12}, \boldsymbol{\theta}_1, \boldsymbol{\theta}_2)\delta(\boldsymbol{r}_1),$$
$$\beta_2 = \frac{1}{2}\int d\boldsymbol{r}_1 d\boldsymbol{r}_2 d\boldsymbol{r}_3 d^{d_i}\boldsymbol{\theta}_1 d^{d_i}\boldsymbol{\theta}_2 d^{d_i}\boldsymbol{\theta}_3 f(r_{12}, \boldsymbol{\theta}_1, \boldsymbol{\theta}_2) f(r_{23}, \boldsymbol{\theta}_2, \boldsymbol{\theta}_3) f(r_{31}, \boldsymbol{\theta}_3, \boldsymbol{\theta}_1))\delta(\boldsymbol{r}_3),$$
$$\dots,$$

[9] A consequence is that it is also equivalent to the so-called *double tangent construction*, a graphical construction on plots of the free energy against the volume that enforces the equality of pressures and chemical potentials in the two phases.

where I reintroduced an integral over the position of the origin and a Dirac delta in each integral to highlight the symmetry between the $\boldsymbol{\theta}$ and $\boldsymbol{r}$ dependencies. Therefore, although the integrals over internal degrees of freedom can prove to be more challenging in the general case, a truncated virial expansion is still an efficient way to search liquid-gas phase separations in polar liquids.

b) The Percus-Yevick Route

Another common way to find the phase diagram starting from the microscopic model of a liquid is the so-called Percus-Yevick route, following its introduction by Percus *et al.* [138]. This time, instead of computing a thermodynamic property directly, one focuses on correlation functions in the liquid. In order to do so, following textbook methods [1, 4, 83], I consider the broader case of a liquid that is put into an external field $\phi(\boldsymbol{r})$ (for instance, a gravitational field), and is therefore allowed to be inhomogeneous, so that it is described by a density profile $n(\boldsymbol{r})$. In that setting, the grand-canonical free energy Ω becomes a functional of the local density $n(\boldsymbol{r})$, that can be decomposed as

$$\Omega[n(\boldsymbol{r})] = \mathcal{F}[n(\boldsymbol{r})] + \int d^d\boldsymbol{r} n(\boldsymbol{r})\phi(\boldsymbol{r}) - \mu \int d^d\boldsymbol{r} n(\boldsymbol{r}),$$

where I simply separated the energetic contributions of the chemical potential and of the external field from the "intrinsic" free energy term $\mathcal{F}$. This term can itself be decomposed into a term that corresponds to the ideal gas value, and an excess term that is given by the interactions,

$$\mathcal{F}[n(\boldsymbol{r})] = \mathcal{F}^{id}[n(\boldsymbol{r})] + \mathcal{F}^{ex}[n(\boldsymbol{r})].$$

At the equilibrium value of the density profile, $\rho(\boldsymbol{r})$, the functional derivative of the grand potential Ω has to be zero, leading to

$$\left.\frac{\delta\Omega}{\delta n(\boldsymbol{r})}\right|_{\rho(\boldsymbol{r})} = \left.\frac{\delta\mathcal{F}}{\delta n(\boldsymbol{r})}\right|_{\rho(\boldsymbol{r})} - \mu + \phi(\boldsymbol{r}) = 0. \tag{II.52}$$

The expression above is often rewritten after distinguishing the ideal and excess parts of $\mathcal{F}$: evaluating Eq. (II.52) for an ideal gas with no external potential yields

$$\left.\frac{\delta\mathcal{F}^{id}}{\delta n(\boldsymbol{r})}\right|_{\rho(\boldsymbol{r})} = \mu^{id},$$

and I define the direct correlation functions $c^{(n)}(\boldsymbol{r})$ (the name of which will become clearer in the following) through

$$c^{(n)}(\boldsymbol{r}_1, \boldsymbol{r}_2, \ldots, \boldsymbol{r}_n) \equiv -\beta \frac{\delta^n \mathcal{F}^{ex}}{\delta\rho(\boldsymbol{r}_1)\delta\rho(\boldsymbol{r}_2)\ldots\delta\rho(\boldsymbol{r}_n)}.$$

This function is the equivalent, for a liquid, of the n-point correlation defined in the case of spin magnetism by derivating the free energy functional by a coarse-grained magnetisation. Using this definition, Eq. (II.52) becomes

$$c^{(1)}(\boldsymbol{r}) = \beta(\mu^{id} - \mu + \phi(\boldsymbol{r})), \tag{II.53}$$

which is just a rewriting of Eq. (II.47) in the presence of an external field. This identification yields an explicit diagrammatic expression for $c^{(1)}(\boldsymbol{r})$: it is the sum of the density diagrams of Eq. (II.50), but where the white dot now indicates position $\boldsymbol{r}$ instead of an arbitrary origin,

$c^{(1)}(\boldsymbol{r}) =$ 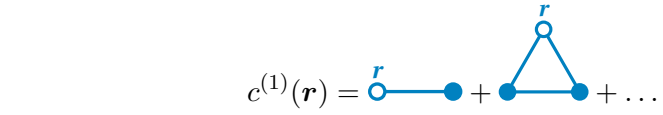

$+ \ldots$ (II.54)

This function is *a priori* just as hard to compute explicitly as the full virial calculation, and a truncated version of the series in $c^{(1)}$ is strictly equivalent to the truncation of the virial expansion. However, it is possible to relate $c^{(1)}$ to other correlation functions of interest. In order to show it, I interpret the density $\rho(\boldsymbol{r})$ as the probability density function that tells me how likely it is to find a particle in a small volume around position $\boldsymbol{r}$, and I introduce the joint probability $\rho^{(2)}$ to find one particle near $\boldsymbol{r}_1$, and another near $\boldsymbol{r}_2$, which can be computed through a generalization of Eq. (II.45),

$$\rho^{(2)}(\boldsymbol{r}_1, \boldsymbol{r}_2) = z^\star(\boldsymbol{r}_1) z^\star(\boldsymbol{r}_2) \frac{\delta^2 \ln \Xi}{\delta z^\star(\boldsymbol{r}_1) \delta z^\star(\boldsymbol{r}_2)},$$

where $z^\star(\boldsymbol{r}) = \exp(\beta\mu - \beta\phi(\boldsymbol{r}))$. To lighten the notations, I define the "intrinsic chemical potential", $\psi(\boldsymbol{r}) = \mu - \phi(\boldsymbol{r})$, that appears in the effective fugacity $z^\star$. This intrinsic chemical potential verifies

$$\frac{\delta \Omega[\rho]}{\delta \psi(\boldsymbol{r})} = -\rho(\boldsymbol{r}), \tag{II.55}$$

prompting me to look at the corresponding second-order derivative,

$$\frac{\delta^2 \Omega[\rho]}{\delta \psi(\boldsymbol{r}_1) \delta \psi(\boldsymbol{r}_2)} = -\beta z^\star(\boldsymbol{r}_2) \frac{\delta}{\delta z^\star(\boldsymbol{r}_2)} \left[z^\star(\boldsymbol{r}_1) \frac{\delta \ln \Xi}{\delta z^\star(\boldsymbol{r}_1)} \right],$$

where I simply used the definition of the density as a derivative of the free energy. The derivative in that last expression can be applied term by term, yielding the relation

$$\begin{aligned} \frac{\delta^2 \Omega[\rho]}{\delta \psi(\boldsymbol{r}_1) \delta \psi(\boldsymbol{r}_2)} &= -\beta \left(\rho^{(2)}(\boldsymbol{r}_1, \boldsymbol{r}_2) - \rho(\boldsymbol{r}_1)\rho(\boldsymbol{r}_2) + \rho(\boldsymbol{r}_1)\delta(\boldsymbol{r}_1 - \boldsymbol{r}_2) \right), \\ &\equiv -\beta H(\boldsymbol{r}_1, \boldsymbol{r}_2), \end{aligned} \tag{II.56}$$

with H a density-density correlation function. Generally, one introduces a normalized version of H, called the reduced pair correlation function h, through the definition

$$H(\boldsymbol{r}, \boldsymbol{r}') = \rho(\boldsymbol{r})\rho(\boldsymbol{r}')h(\boldsymbol{r}, \boldsymbol{r}') + \rho(\boldsymbol{r})\delta(\boldsymbol{r} - \boldsymbol{r}'). \tag{II.57}$$

Having thus defined $H^{(2)}$, I notice that Eqs. (II.55) and (II.56), when put together, yield

$$H(\boldsymbol{r}, \boldsymbol{r}') = k_B T \frac{\delta \rho(\boldsymbol{r})}{\delta \psi(\boldsymbol{r}')}.$$

This equation can be used to write that the functional inverse H^{-1} of H, defined through

$$\int d^d\boldsymbol{r}'' H(\boldsymbol{r},\boldsymbol{r}'')H^{-1}(\boldsymbol{r}'',\boldsymbol{r}') = \delta(\boldsymbol{r}-\boldsymbol{r}'), \tag{II.58}$$

can be expressed as

$$H^{-1}(\boldsymbol{r},\boldsymbol{r}') = \beta\frac{\delta\psi(\boldsymbol{r})}{\delta\rho(\boldsymbol{r}')}.$$

Finally, using Eq. (II.53) and the expression (II.43) of the ideal chemical potential μ^{id} as a function of ρ, the functional derivative of ψ with respect to ρ can be expressed in terms of $c^{(2)}$, so that

$$H^{-1}(\boldsymbol{r},\boldsymbol{r}') = \frac{1}{\rho(\boldsymbol{r})}\delta(\boldsymbol{r}-\boldsymbol{r}') - c^{(2)}(\boldsymbol{r},\boldsymbol{r}').$$

This equation can be inserted into Eq. (II.58), then integrated over $\boldsymbol{r}''$, and expressed in terms of the reduced pair correlation function h using Eq. (II.57), yielding

$$h(\boldsymbol{r},\boldsymbol{r}') = c^{(2)}(\boldsymbol{r},\boldsymbol{r}') + \int d^d\boldsymbol{r}'' c^{(2)}(\boldsymbol{r},\boldsymbol{r}'')\rho(\boldsymbol{r}'')h(\boldsymbol{r}'',\boldsymbol{r}'). \tag{II.59}$$

This equation on h is known as the Ornstein-Zernike equation [139]. It is a recursive equation, that can be rewritten as

$$\begin{aligned} h(\boldsymbol{r},\boldsymbol{r}') = {} & c^{(2)}(\boldsymbol{r},\boldsymbol{r}') \\ & + \int d^d\boldsymbol{r}'' c^{(2)}(\boldsymbol{r},\boldsymbol{r}'')\rho(\boldsymbol{r}'')c^{(2)}(\boldsymbol{r}'',\boldsymbol{r}') \\ & + \int\int d^d\boldsymbol{r}'' d^d\boldsymbol{r}''' c^{(2)}(\boldsymbol{r},\boldsymbol{r}'')\rho(\boldsymbol{r}'')c^{(2)}(\boldsymbol{r}'',\boldsymbol{r}''')\rho(\boldsymbol{r}''')c^{(2)}(\boldsymbol{r}''',\boldsymbol{r}') \\ & + \dots \end{aligned}$$

This recursive structure sheds light on the notion of "direct" correlation function: since h is defined through the density-density correlation, it can be thought of as the "total" correlation between any two particles. It is composed of a "direct" part, $c^{(2)}$, that is caused by close-range interactions between the two particles, surrounded by the fluid, and of an "indirect" part, that is propagated to large distances through neighbouring particles in the integrals. For instance, the first integral that corrects the direct correlation represents the correlation between pairs of particles that are separated by one intermediary particle. In the case of a uniform liquid and of isotropic interactions, Eq. (II.59) takes the simpler form

$$\begin{aligned} h(r) &= c(r) + \rho\int d^d\boldsymbol{r}' c(|\boldsymbol{r}-\boldsymbol{r}'|)h(r'), \\ &= c(r) + c\star h(r) \end{aligned}$$

where I dropped the (2) superscript to lighten the notations, and I introduced the convolution product

$$f\star g(\boldsymbol{r}) = \int d^d\boldsymbol{r}' f(\boldsymbol{r}-\boldsymbol{r}')g(\boldsymbol{r}').$$

Because of this convolution product, the Ornstein-Zernike is often written in Fourier space as

$$\hat{h}(k) = \frac{\hat{c}(k)}{1 - \rho\hat{c}(k)},$$

where the hat represents a Fourier transform and $\boldsymbol{k}$ is the Fourier variable. This last equation can be linked to the usual thermodynamic properties by using the so-called compressibility equation of state, that is obtained by noticing that the compressibility is related to the fluctuations of the number of particles in the grand-canonical ensemble [1],

$$\rho k_B T \chi_c = 1 + \rho \int d^d \boldsymbol{r} h(r). \tag{II.60}$$

This equation leads to

$$\rho k_B T \chi_c = 1 + \rho\hat{h}(0),$$

or equivalently to

$$\frac{1}{\rho k_B T \chi_c} = 1 - \rho\hat{c}(0).$$

In order to seek singularities of χ_c, it is therefore sufficient to determine the value of $\hat{c}(0)$.

The issue is that the Ornstein-Zernike equation alone is not sufficient to determine the forms of h and c: one needs a closure relation. A usual closure relation is the Percus-Yevick [138] closure, which consists in assuming that the direct correlation function can be written as

$$c(\boldsymbol{r}) \approx \left(1 - e^{\beta U(\boldsymbol{r})}\right) g(\boldsymbol{r}),$$

which can be found by expanding c up to first order when considering a inhomogeneous perturbation to a homogeneous fluid [1]. This closure ensures that c is zero when v is zero, that it reflects the density-density correlation at short range, and that the pair correlation function $g = h + 1$ decays exponentially at low densities. It can be injected into the Ornstein-Zernike equation, leading to an equation on g only,

$$e^{\beta U(r)} g(r) = 1 + \rho \int d\boldsymbol{r}' \left[g(\boldsymbol{r} - \boldsymbol{r}') - 1\right] g(\boldsymbol{r}') \left(1 - e^{\beta U(r')}\right),$$

which is known as the Percus-Yevick equation. With this closure, it is in particular easy to study the case of hard-core repulsion of diameter σ,

$$U(r) = \begin{cases} \infty & \text{if } r < \sigma \\ 0 & \text{if } r > \sigma \end{cases}$$

Furthermore, due to this potential, the pair correlation function verifies

$$g(r) = 0 \text{ if } r < \sigma.$$

In that case, one needs to define the cavity distribution function $y(r) = e^{\beta U} g(r)$, so that the Percus-Yevick closure reduces to

$$c(r) = \begin{cases} -y(r) & \text{if } r < \sigma \\ 0 & \text{if } r > \sigma \end{cases}$$

and the Percus-Yevick equation reads

$$y(r) = 1 + \rho \int\limits_{r'<\sigma} d\boldsymbol{r}' y(r') - \rho \int\limits_{\substack{r'<\sigma \\ |\boldsymbol{r}-\boldsymbol{r}'|>d}} d\boldsymbol{r}' y(r') y(|\boldsymbol{r}-\boldsymbol{r}'|).$$

This equation can be solved exactly in $d = 3$ using Laplace transform methods [140–142], leading to an expression of c and g for hard spheres. It is worth noting, however, that these expressions do not yield an unequivocal equation of state for hard spheres: injecting the Percus-Yevick g into the compressibility equation of state or in the virial equation of state lead to two different expressions of the pressure, that become increasingly different as the density increases [1]. This discrepancy is usually treated by using the weighted average of these two expressions of the pressure that best fits numerical observations, called the Carnahan-Starling formula [143]. Furthermore, the same methods cannot be applied in even dimensions of space, and in particular in $d = 2$, so that only approximate expressions of c are found [144].

In the case of a soft interaction potential U, it is in general impossible to solve the Percus-Yevick equation exactly. Furthermore, numerical resolutions of the Percus-Yevick equation showed that it was a good approximation in the case of potentials that are strongly repulsive and short-ranged [1]. One therefore should restrict oneself to such potentials, and seek suitable approximations to add to the Percus-Yevick equation. The most common setting is that of potentials with a hard-core repulsion and a short attractive tail with range λ,

$$U(r) = \begin{cases} \infty & \text{if } r < \sigma \\ u(r) & \text{if } \sigma < r < \lambda \\ 0 & \text{if } r > \lambda \end{cases}$$

where $u(r) \leq 0$. In that setting, a usual approximation is the so-called Mean-Spherical Approximation (MSA), also called the Random-Phase Approximation (RPA), which assumes that

$$\begin{aligned} g(r) &= 0 && \text{if } r < \sigma \\ c(r) &\approx -\beta u(r) && \text{if } r > \sigma. \end{aligned}$$

The approximation for c is in fact obtained by considering only the lowest order in density of the expansion of $c^{(2)}$ analogous to Eq. (II.54), $c(r) \approx f(r)$, then by Taylor-expanding the Mayer function f up to first order. This approximation is therefore valid at low values of the densities (so that only the first graph is kept), and at low values of β, or high temperatures. Using the RPA, the Percus-Yevick closure relation reduces to

$$c(r) = \begin{cases} -y(r) & \text{if } r < \sigma \\ -\beta u(r) & \text{if } r > \sigma, \end{cases}$$

where the cavity distribution function y in the hardcore region is obtained in the same way as in the purely hard case. Like the virial expansion, this approach yields mean-field exponents for the liquid-gas transition [1]. In summary, the Percus-Yevick closure, with the Random-Phase Approximation (PY-RPA for short) is suitable to treat systems with a hardcore repulsion, a short attractive tail, at low densities, and high temperatures. It therefore leads to phase diagrams similar to those obtained by a virial expansion, with the difference that the pressure is not unequivocally defined in the Percus-Yevick framework.

Finally, in the case of a molecular liquid carrying internal degrees of freedom, the derivation above can be repeated, only now the Mayer f function as well as the direct correlation function c and the pair correlation functions h and g all depend on both the distance between two particles, $\boldsymbol{r}$, but also the values of the internal degrees of freedom $\boldsymbol{\theta}$. Assuming that the interactions are still isotropic, this leads to a slightly modified Ornstein-Zernike equation,

$$h(r,\boldsymbol{\theta}) = c(r,\boldsymbol{\theta}) + \rho \int d^d\boldsymbol{r}' d^{d_i}\boldsymbol{\theta}' c(|\boldsymbol{r}-\boldsymbol{r}'|,\boldsymbol{\theta},\boldsymbol{\theta}')h(r',\boldsymbol{\theta}'),$$

where h is a measure of the correlation of the probability density $\rho(\boldsymbol{r},\boldsymbol{\theta})$ of finding a particle in the neighbourhood of $\boldsymbol{r}$, with internal degrees of freedom in the neighbourhood of $\boldsymbol{\theta}$. If the potential only depends on the difference $\boldsymbol{\theta}-\boldsymbol{\theta}'$, one recovers a convolution product over both positions and internal degrees of freedom

$$h(r,\boldsymbol{\theta}) = c(r,\boldsymbol{\theta}) + c \star h(r,\boldsymbol{\theta}).$$

In order to recover the usual spatial pair correlation function, $h(r)$, one needs to compute the mean value of that h using the statistics of $\boldsymbol{\theta}$, that are described by a probability distribution p, so that

$$h(r) = \int d^{d_i}\boldsymbol{\theta} p(\boldsymbol{\theta}) h(r,\boldsymbol{\theta}).$$

This function can then be injected in the usual equations of state to obtain the pressure and compressibility of the considered liquid.

c) The Bethe Approximation

The last method to obtain the mean-field phase diagram of a liquid that I am concerned with in this thesis is the so-called Bethe approximation. This method was developed as a generic mean-field approximation by Bethe [145] and Peierls [146] in the 1930s in the context of fluids, then first applied in the 1940s to ferromagnetism by Weiss [105, 147]. It was more recently generalized to systems with replica-symmetry breaking, such as spin glasses [148, 149], optimization problems [5, 150], and glass-forming liquids [151–153], where it is generally known as the cavity method. In order to illustrate the principle of this method, consider a $2d$ liquid with particles placed on a lattice. A microscopic state of this liquid is defined by a set of occupation numbers, n_i, that each indicate the number of particles sitting on the site indexed by $0 \leq i \leq N$. I here assume that $n_i \in \{0;1\}$, meaning that there is a hardcore repulsion interaction between particles. Furthermore, I assume that the particles interact through a nearest-neighbour attractive interaction, so

that they are described by the Ising-like Hamiltonian

$$\mathcal{H} = -\frac{U}{2}\sum_i \sum_{j\in\partial i} n_i n_j.$$

The originality of the problem compared to an Ising model is that one is here interested in the behaviour in the density-temperature plane. It is therefore useful to define the grand-canonical partition function at the inverse temperature β and for a chemical potential μ

$$\Xi = \sum_{\mathcal{C}} e^{\beta\mu\sum_i n_i + \beta U/2 \sum_i \sum_{j\in\partial i} n_i n_j}, \tag{II.61}$$

where the first sum is over all the allowed configurations of the occupancies. The principle of the Bethe approximation is to write Ξ recursively on the successive neighbours of a given site. In order to do so, one approximates the hypercubic lattice by a "Bethe lattice". This kind of lattice contains only a subextensive number of very large loops (typically $\ln N$ loops with length $\ln N$ for a lattice with N sites [151]), so that loops can be neglected in the thermodynamic limit $N \to \infty$. A Bethe lattice is therefore said to be "locally tree-like", using the fact that graphs without any loops have the structure of a tree. Furthermore, a Bethe lattice has a fixed connectivity: each site has exactly l neighbours. Note that there are still several possible definitions of a Bethe lattice with these constraints: one can choose to work on so-called Random Regular Graphs [154], Erdős-Rényi graphs [155], or Cayley trees [105], for instance. Note that tree-like lattices are good approximations of high-dimensional lattices, so that one can already expect a $d \to \infty$, or mean-field, level of description.

The Bethe approximation consists in removing a site, noted c, from the Bethe lattice; an action called "digging a cavity". In the $N \to \infty$ limit, doing so breaks up the Bethe lattice into l "rooted" trees, i.e. trees that stem from a site with a lower connectivity, the root (see Fig. II.10). In each of the l rooted trees, because of the tree-like structure of the Bethe lattice, it is possible to write the (cavity) conditional probability for the root to be empty or occupied depending on the state of the neighbouring states, in the absence of the root itself. To do so, I call $Z^E_{i\to c}$ and $Z^O_{i\to c}$ the conditional partition functions defined on site i in the absence of c, restricted to the case of an empty (E), and of an occupied (O) root, respectively. The recursion rules for these quantities and a given cavity site c are

$$\begin{aligned} Z^O_{i\to c} &= e^{\beta\mu}\prod_{j=1}^{l-1}\left[Z^E_{i_j\to i} + Z^O_{i_j\to i}e^{\beta U}\right], \\ Z^E_{i\to c} &= \prod_{j=1}^{l-1}\left[Z^E_{i_j\to i} + Z^O_{i_j\to i}\right], \end{aligned} \tag{II.62}$$

where i_j is the j-th neighbour of site i. While they are a bit formal, these equations are quite intuitive to read. The first equation, for instance, states that if site i is occupied, the particle adds an energy μ to the branches, and is connected to sites that are either empty, or occupied, in which case an interaction energy U is added. Using these two

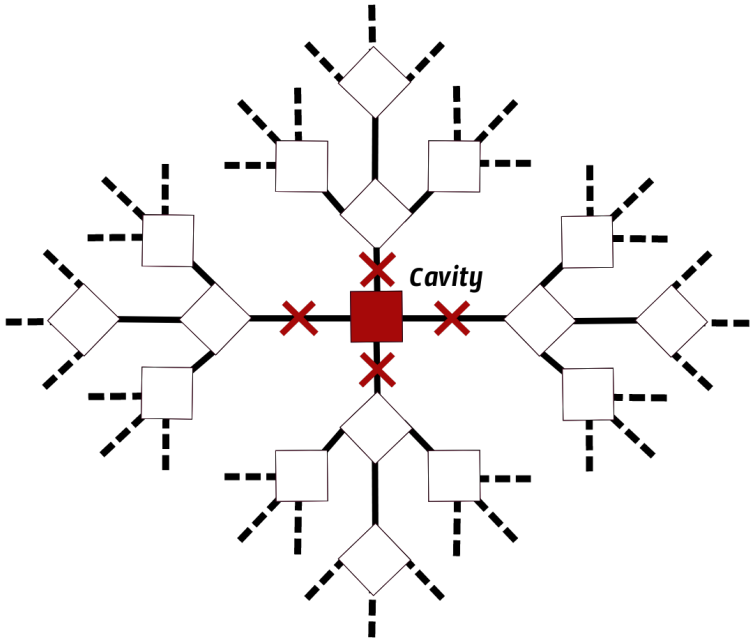

Fig. II.10 **Principle of the Bethe approximation.** A site, the cavity (here, in red) is removed at random in a large treelike graph, thus creating l (here 4) rooted trees.

partition functions, I define the total partition function of site i, $Z^T_{i\to c} = Z^O_{i\to c} + Z^E_{i\to c}$, then the normalized probabilities for site i to be empty, $\psi^E_{i\to c}$ or occupied, $\psi^O_{i\to c}$, defined through

$$\psi^{O,E}_{i\to c} = \frac{Z^{O,E}_{i\to c}}{Z^T_{i\to c}}.$$

From these probabilities, one can recover the full free energy F_c of the fluid on the Bethe lattice. In order to do so, I first define F_0 the free energy associated to the $N-$vertex graph $\mathcal{G}$ obtained after digging a cavity. From this graph, there are two ways to recover a full Bethe lattice [151, 156]. First, one can put back the cavity, thus undoing the operation that was sketched in Fig. II.10. This yields the free energy $F_c(N+1)$ of an $(N+1)-$site Bethe lattice, which can then be expressed as $F_0 + \Delta F^{site}_c$, where

$$\beta\Delta F^{site}_c = -\ln\left[\prod_{i=1}^{l}\left(\psi^E_{i\to c}+\psi^O_{i\to c}\right) + e^{\beta\mu}\sum_{p=1}^{l}\psi^E_{p\to c}\prod_{i\neq p}\left(\psi^E_{i\to c}+e^{\beta U}\psi^O_{i\to c}\right)\right]$$

is the free energy shift associated to adding back the cavity. Second, one could also reconnect the l roots of $\mathcal{G}$ two by two together, without adding back the cavity. This yields the free energy $F_c(N)$, which can be expressed as $F_0 + l\Delta F^{bond}_c/2$ (for an even value of l), with

$$\beta\Delta F^{bond}_c = +\sum_{j\in\partial c}\ln\left[\psi^E_{j\to c}\psi^E_{c\to j} + \psi^E_{c\to j}\psi^O_{j\to c} + \psi^O_{c\to j}\psi^E_{j\to c} + e^{\beta U}\psi^O_{c\to j}\psi^O_{j\to c}\right].$$

the free energy shift associated to connecting two of the rooted trees back together. With these equations, one gets an exact expression for $\Delta F_c = F_c(N+1) - F_c(N)$, thus yielding a recursive expression for the full free energy of an $N-$site Bethe lattice. From this point of view, one can view this method as a recursive construction in which one progressively adds sites to a tree-like graph, one site (noted c) at a time. The final expression for the free energy is

$$\beta F(N) = -\sum_{c=1}^{N} \ln \left[\prod_{i=1}^{l} \left(\psi^E_{i\to c} + \psi^O_{i\to c} \right) + e^{\beta\mu} \sum_{p=1}^{l} \psi^E_{p\to c} \prod_{i\neq p} \left(\psi^E_{i\to c} + e^{\beta U} \psi^O_{i\to c} \right) \right] + \sum_{c=1}^{N} \sum_{j\in\partial c} \ln \left[\psi^E_{j\to c}\psi^E_{c\to j} + \psi^E_{c\to j}\psi^O_{j\to c} + \psi^O_{c\to j}\psi^E_{j\to c} + e^{\beta U}\psi^O_{c\to j}\psi^O_{j\to c} \right]. \quad \text{(II.63)}$$

This expression is here written in a very general setting, in which the density is allowed to be spatially inhomogeneous.

In homogeneous fluid phases, the probability to find a particle does not depend on the position, so that the recursive equations (II.62) reduce to a system of self-consistent algebraic equations,

$$Z^O = e^{\beta\mu} \left(Z^E + Z^O e^{\beta U} \right)^{l-1},$$
$$Z^E = \left(Z^E + Z^O \right)^{l-1}.$$

These equations can be solved (numerically, or even analytically for some choices of l), yielding several branches of possible values, typically only one of which is real-valued. These solutions can then be injected into Eq. (II.63), and one can compute the proportion of occupied sites, that I here call the density,

$$\rho(\mu) = -\frac{1}{N}\frac{\partial F}{\partial \mu},$$

and associated susceptibility

$$\chi_\rho(\mu) = \frac{\partial \rho}{\partial \mu}.$$

One can check from the definition of the partition function (II.61) that

$$\chi_\rho = \frac{1}{N} \sum_{i,j} \left(\langle n_i n_j \rangle - \langle n_i \rangle \langle n_j \rangle \right),$$

which is the on-lattice version of the integral over all space of the pair-correlation function: using Eq. (II.60), one finds that χ_ρ is the compressibility. Therefore, one can find the liquid-gas phase separation by computing the free energy for various values of μ and T, then computing ρ and χ_ρ to report singularities of the free energy in the (ρ, T) plane. In the case of the example used to write the cavity equations, since it is simply an Ising model with spins taking values $0, 1$, the phase separation is similar to the phase diagram of the Ising model in the (m, T) plane. A critical point is observed at $\rho = 0.5$ and

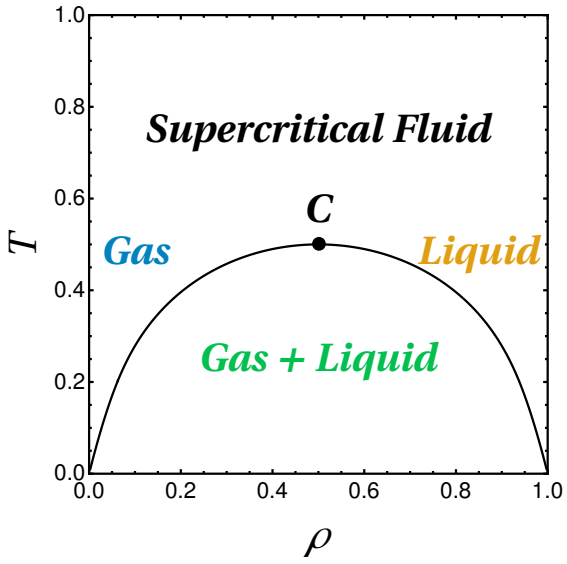

Fig. II.11 **Mean-field Phase Diagram of an Ising-like Lattice Fluid.** The black line is the spinodal line, that is symmetric around half-filling ($\rho = 0.5$).

a symmetrical phase separation domain originates from it at lower temperatures (See Fig. II.11). The left-right symmetry of this separation domain stems from the symmetry under the transformation $n_i \to 1-n_i$, or particle-hole symmetry. Notice that the obtained phase diagram is the mean-field one, as anticipated when introducing the Bethe lattice. Here, it is further justified by the fact that density fluctuations are neglected when seeking fixed points of the recursive equations.

Additionally, one can seek transitions to crystalline phases with this approach. In order to do so, one this time explicitly allows a breaking of translational invariance in the Bethe lattice by dividing it into several sublattices [152]. Typically, one can consider, in the case $l = 4$, 3 sublattices, the sites of which are labeled as a-, b-, and c- sites. In either one of those sublattices, one still seeks homogeneous solutions of the partial partition functions $Z^O_{a,b,c}$ and $Z^E_{a,b,c}$. Furthermore, one assumes that the sublattices are organised in such a way that the sought crystalline order is reproduced [152]. Doing so, one can find branches of solutions such that the densities $\rho_{a,b,c}$ of each sublattice are different, betraying a crystalline structure. These solutions are typically stable at high enough densities, beyond the melting spinodal, that marks the liquid-crystal transition [151]. Note however that all models do not display a liquid-crystal transition and, in particular, it is absent of the simple model used to obtain the cavity equations in the homogeneous case above. For instance, the model described by Eq. (II.61), because of its full particle-hole symmetry, cannot crystallize for $U > 0$.

In a nutshell, the Bethe approximation constitutes a powerful way to find the full mean-field phase diagram of a liquid, including crystal and glassy phases when they exist. This method can also be applied to complex liquids, at the cost of having to write more cumbersome cavity relations on the partial partition functions, as I will discuss in details in Chapter III.

II.4.3 Dynamical Properties

Finally, in order to discuss the common points and differences between the kind of motion created by the models of this thesis, and that observed in active matter, it is useful to briefly review the usual dynamical properties of passive fluids, as well as those of self-propelled particles.

a) Dynamics of Passive Fluids

In a passive fluid at equilibrium, rather than determining the nature of the phase (fluid or solid) by looking at static structural properties like the pair correlation function, it can be interesting to study observables associated to the motion of individual particles at various time scales. In particular, it is often more convenient in experiments, since it is often easier to obtain a long dataset rather than a large system. The most natural microscopic variable associated to the motion of particles is the displacement $\boldsymbol{u}_i(t) = \boldsymbol{r}_i(t) - \boldsymbol{r}_i(0)$, measured between times 0 and t for particle i, that also happens to be much easier to measure experimentally that instantaneous velocities. The mean value (over initial times and particles) of this displacement corresponds to macroscopic flows of particles, and is zero in fluids at rest,

$$\langle \boldsymbol{u}_i \rangle = \boldsymbol{0}.$$

It is however interesting to compute the mean value of the squared modulus of displacements, usually called the Mean-Square Displacement (MSD), and defined through

$$\Delta r^2(t) = \langle u_i^2(t) \rangle.$$

This function is expected to behave like a power law of time, $\Delta r^2(t) \propto t^a$, with $a(t)$ an exponent that depends on t. Notable values of a are $a = 2$, and $a = 1$. In the case $a = 2$ particles typically move of a distance that grows linearly with time, i.e. with a constant velocity v. This kind of motion is called ballistic motion. In the case $a = 1$, particles typically move of a distance that grows like the square-root of time: this kind of motion is called diffusive motion, and one usually defines the diffusion constant D such that $\Delta r^2(t) = 2dDt^{1/2}$, where d is the dimension of space. By extension, if $a < 1$, one says that the motion is subdiffusive, if $1 < a < 2$, it is said to be superdiffusive, and if $a > 2$, it is said to be superballistic. Furthermore, in the case $a = 0$, *i.e.* the case of a plateau, one says that the dynamics are frozen.

In a high-temperature fluid, the MSD is usually ballistic at short times, and becomes diffusive at long times (see Fig. II.12). This crossover is due to the fact that, on sufficiently short time and length scales, particles do not interact with each other and simply move like free particles. However, after the typical time that separates two interaction events (or, equivalently, the distance corresponding to the "mean-free path"), particles interact, which reorients their velocities and causes the diffusive behaviour. As the temperature is cooled down, both the typical velocity of particles and the diffusion coefficient decrease. This is simply explained by the fact that the distribution of velocities in a fluid is essentially a Gaussian with a variance k_BT [1, 80–83, 130]. Then, as the system becomes a solid, this behaviour changes. In $3d$ crystalline solids, and on reasonable time scales, the MSD saturates to a plateau Δr^2_∞, with a value that is typically a fraction of the lattice

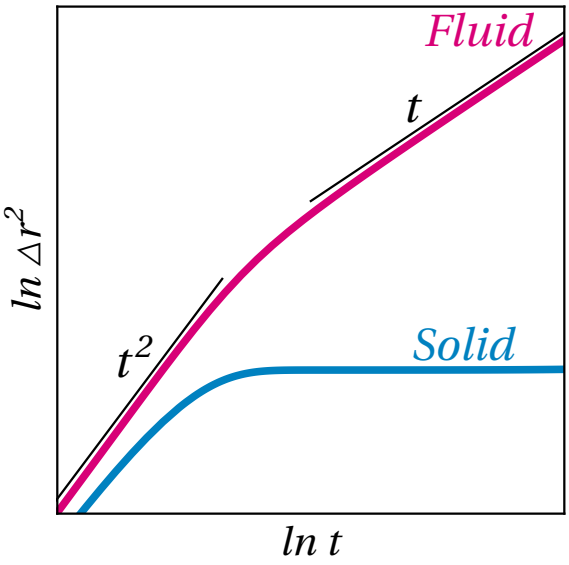

Fig. II.12 **Typical MSDs in a $3d$ passive fluid.**

spacing a. This plateau is at the root of a well-known phenomenological criterion for melting to happen in a crystal, the Lindemann criterion, which states that a crystal melts when $\Delta r^2_\infty \approx 0.01 a^2$ (see for instance Mantisi *et al.* [157] for an example of melting in $3d$ molecular dynamics simulations, and Van-Megen *et al.* [158] for experimental measurements, both in the crystallized and the supercooled regimes of colloidal particles.). The plateau is caused by the formation of a regular arrangement of neighbours around each particle, that plays the same role as a "cage" of potential energy, and the Lindemann criterion simply states that a solid melts when particles start disturbing their neighbours. Note however, that this plateau does not extend to infinite times: there is a typical time after which the MSD resumes its growth due to a finite rate of creation of defects [159], but this time scales like the size of the system and is therefore in general not attained in experiments or simulations.

In $2d$, the melting transition is highly peculiar, as already discussed in Sec. II.4.1. In particular, Mermin [160] showed that Lennard-Jones fluids in $2d$ cannot have bounded MSDs: they cannot feature an infinitely long plateau in the thermodynamic limit. In practice, it means that one expects $2d$ solids to display a much shorter plateau in their MSD than $3d$ systems do, due to the excitation of spin waves and of point-defects. This is another signature that these $2d$ systems do not have a thermodynamic crystallization transition. One therefore generically expect a ballistic-frozen pattern at short times, and an increase (in this thesis, typically, a diffusive increase) of the MSDs at long times, see for instance Ref. [161].[10]

A phenomenological description of the dynamics of a fluid can be obtained by stochastic equations called Langevin equations [165]. They describe the motion of a tagged particle, typically a colloid, that is immersed in a set of typically much lighter, and smaller

[10]Note that a Lindemann criterion can also be defined in $2d$, not directly on the MSDs, but on the relative displacements between pairs of neighbouring particles, which is bounded in solid phases [162–164].

particles: the solvent. For the tagged particle, the Langevin equation on its position $\boldsymbol{r}$ reads

$$m\ddot{\boldsymbol{r}} + \gamma\dot{\boldsymbol{r}} = \boldsymbol{\eta}(t),$$

where m is the mass of the particle, γ is an effective friction coefficient caused by the presence of the solvent, and η_i is a vector of random numbers that describe the forces exerted by the solvent on the particle, and is called the noise. In the context of the Langevin equation, mean values of observables should be understood as averages over the probability distribution of $\boldsymbol{\eta}$, $P(\boldsymbol{\eta})$. This noise is typically assumed to have zero mean, and to have zero memory, so that

$$\begin{aligned}\langle\boldsymbol{\eta}(t)\rangle &= \mathbf{0},\\ \langle\eta_a(t)\eta_b(t')\rangle &= 2\gamma k_B T\delta_{ab}\delta\left(t-t'\right),\end{aligned}$$

where a and b are components of $\boldsymbol{\eta}$, and the factor of $2\gamma k_B T$ ensures that $\langle mv^2(t)\rangle = dk_B T$, as prescribed by the equipartition theorem [81, 82]. The noise $\boldsymbol{\eta}$ is therefore described by a Gaussian white noise. In the case of a pure passive liquid, one can write a Langevin equation for any one of the N particles, and consider that the other particles play the same role as a solvent. The behaviour of the MSD of a fluid can then be recovered as follows.

I first rewrite the Langevin equation in the more usual form

$$\tau\dot{\boldsymbol{v}} + \boldsymbol{v} = \boldsymbol{\eta}(t),$$

where I defined $\tau = m/\gamma$, the inertial time, and I absorbed a factor of $1/\gamma$ in the definition of the noise. For a Gaussian white noise, this stochastic equation on the velocity is called an Ornstein-Uhlenbeck process [166]. It can be integrated over time to yield the time evolution of the velocities,

$$\boldsymbol{v}(t) = \boldsymbol{v}(0)e^{-t/\tau} + \frac{1}{\tau}\int_{t'=0}^{t} dt'\boldsymbol{\eta}(t')e^{-(t-t')/\tau},$$

then integrated a second time to obtain the time evolution of positions,

$$\boldsymbol{r}(t) - \boldsymbol{r}(0) = \boldsymbol{v}(0)\tau\left(1-e^{-t/\tau}\right) + \int_{t'=0}^{t} dt'\boldsymbol{\eta}(t')\left[1-e^{-(t-t')/\tau}\right].$$

From this equation, I compute the MSD,

$$\begin{aligned}\Delta r^2(t) &= \left\langle\left(\boldsymbol{r}(t)-\boldsymbol{r}(0)\right)^2\right\rangle\\ &= \boldsymbol{v}(0)^2\tau^2\left(1-e^{-t/\tau}\right)^2 - \frac{dk_BT}{\gamma}\left(1-e^{-t/\tau}\right)\left(3-e^{-t/\tau}\right) + \frac{2dk_BT}{\gamma}t,\end{aligned}$$

from which I extract the short- and long-time limit behaviours

$$\Delta r^2(t) \approx \begin{cases}\boldsymbol{v}(0)^2t^2 & \text{if } t \ll \tau,\\ \frac{2dk_BT}{\gamma}t & \text{if } t \gg \tau.\end{cases} \tag{II.64}$$

This simple reasoning therefore captures the short-time ballistic behaviour, and the long-time diffusive behaviour. Furthermore, I get an estimate of the value of the diffusion constant,

$$D = \frac{k_B T}{\gamma},$$

which follows the so-called Einstein [167]-Smoluchowski [168]-Sutherland [169] relation. Finally, the ballistic speed is given by the initial speed. Using the fact that the velocities of usual models are Gaussian-distributed in equilibrium with a variance $k_B T/m$, one finds that the ballistic speed is in fact

$$v = \sqrt{k_B T/m}.$$

These expressions also capture the decrease of the ballistic speed and of the diffusion constant when the temperature decreases. The crossover time between the two regimes, t_c, is found by equating the two regimes of Eq. (II.64),

$$t_c = 2d\tau.$$

From it, one can compute the typical length of each ballistic segment, the mean-free path λ_{mf}, given by the value of the ballistic displacement after t_c,

$$\lambda_{mf} = 2d\tau\sqrt{\frac{k_B T}{m}}.$$

These values show that the crossover between the ballistic and diffusive regimes typically happen at the same time regardless of the temperature, but that the associated displacement decreases when the temperature is lowered. Note that, at this level of description, MSDs similar to those of a $3d$ solid are recovered in the $T \to 0$ limit. This Langevin equation does not, however, capture the dynamics in the solid phase at finite temperatures, as it does not include any term encoding the buildup of correlations between the particles at the melting transition.

b) Dynamics of Fluids of Self-Propelled Particles

In the context of self-propelled particles, it is also usual to work with Langevin equations to predict the MSDs. This time, although the precise phenomenology depends on the considered system, one expects particles to display superdiffusion (or, even, ballistic motion) associated to self-propulsion in some regimes. The simplest model that one can use to model assemblies of self-propelled particle at the Langevin level is that of Active Brownian Particles, or ABPs [60], the most general definition of which is given, in $2d$, by the equations of motion

$$\begin{aligned}
\tau_v \ddot{\boldsymbol{r}}_i + \dot{\boldsymbol{r}}_i &= v_0 \hat{\boldsymbol{e}}(\theta_i) - \mu \sum_{j \neq i} \frac{\partial V}{\partial \boldsymbol{r}_i}(r_{ij}) + \boldsymbol{\eta}_i, \\
\tau \ddot{\theta}_i + \dot{\theta}_i &= \mu_r \sum_{j \neq i} \Gamma_{ij} + \xi_i.
\end{aligned}$$

In these equations, μ and μ_r are respectively translational and rotational mobilities, θ_i is the direction of the self-propulsion of particle i, that obeys its own Langevin equation that contains a noise ξ_i and interactions with other particles encoded by the torques Γ_{ij}. These equations are typically considered in the so-called overdamped case, $\tau_v \to 0$ and $\tau \to 0$, as inertial times are typically small for small particles. Furthermore, for simplicity, I only present in this section the case of a single such particle immersed in a solvent, so that the equations of motion reduce to

$$\begin{aligned} \dot{\boldsymbol{r}} &= v_0 \hat{\boldsymbol{e}}(\theta) + \boldsymbol{\eta}, \\ \dot{\theta} &= \xi. \end{aligned}$$

Assuming that the particle is put into a solvent at equilibrium, one usually considers that

$$\begin{aligned} \langle \boldsymbol{\eta}(t) \rangle &= \mathbf{0}, & \langle \eta_a(t) \eta_b(t') \rangle &= \frac{2k_B T}{\gamma_v} \delta_{a,b} \delta(t - t'), \\ \langle \xi(t) \rangle &= 0, & \langle \xi(t) \xi(t') \rangle &= \frac{2k_B T}{\gamma} \delta(t - t'), \end{aligned}$$

and cross-correlations between the two sources of noise are assumed to be zero. The equation on the velocity can be integrated over, yielding

$$\boldsymbol{r}(t) = \boldsymbol{r}(0) + \int_{t'=0}^{t} dt' v_0 \hat{\boldsymbol{e}}(\theta(t')) + \int_{t'=0}^{t} dt' \boldsymbol{\eta}(t'),$$

so that one can write the expression of the mean-square displacement

$$\Delta r^2(t) = v_0^2 \int_{t'=0}^{t} dt' \int_{t''=0}^{t} dt'' \left\langle \hat{\boldsymbol{e}}(\theta(t')) \cdot \hat{\boldsymbol{e}}(\theta(t'')) \right\rangle + 4D_0 t,$$

where I defined the diffusion constant $D_0 = k_B T / \gamma_v$. The task at hand is then to compute the mean value of the dot product $\langle \hat{\boldsymbol{e}}(\theta(t')) \cdot \hat{\boldsymbol{e}}(\theta(t'')) \rangle$.

To do so, it is useful to use Itō's lemma [166, 170] to write the stochastic evolution of the unit vector $\hat{\boldsymbol{e}}(\theta(t)$,

$$d\hat{\boldsymbol{e}}(t) = \hat{\boldsymbol{e}}(t + dt) - \hat{\boldsymbol{e}}(t) = \xi dt \hat{\boldsymbol{e}}_\perp(t) - D_r dt \hat{\boldsymbol{e}}(t),$$

where I defined the rotational diffusion constant $D_r = k_B T / \gamma$, and $\hat{\boldsymbol{e}}_\perp(\theta) = -\sin\theta \hat{\boldsymbol{e}}_x + \cos\theta \hat{\boldsymbol{e}}_y$. This equation can be projected onto $\hat{\boldsymbol{e}}(0)$ then averaged over realisations of the noise,

$$\langle d\hat{\boldsymbol{e}} \cdot \hat{\boldsymbol{e}}(0) \rangle = \langle (\xi dt \hat{\boldsymbol{e}}_\perp(t)) \cdot \hat{\boldsymbol{e}}(0) \rangle - D_r \langle \hat{\boldsymbol{e}}(t) \cdot \hat{\boldsymbol{e}}(0) \rangle dt.$$

The first term on the right-hand side averages to zero, as the stochastic process ξ is not correlated with the value of the vector $\hat{\boldsymbol{e}}$ (it is a non-anticipating function [166]). The equation then simply becomes a first-order ordinary differential equation,

$$\langle d\hat{\boldsymbol{e}} \cdot \hat{\boldsymbol{e}}(0) \rangle = -D_r \langle \hat{\boldsymbol{e}} \cdot \hat{\boldsymbol{e}}(0) \rangle dt,$$

so that one finds,

$$\langle \hat{\boldsymbol{e}}(t) \cdot \hat{\boldsymbol{e}}(0) \rangle = e^{-D_r t}.$$

Noticing that the process is invariant under time translations, for two values of time, one gets

$$\langle \hat{\boldsymbol{e}}(t') \cdot \hat{\boldsymbol{e}}(t'') \rangle = e^{-D_r |t'-t''|}.$$

Finally, the MSD can be written as

$$\Delta r^2(t) = \frac{2v_0^2}{D_r} \left(\frac{1}{D_r} \left(e^{-Drt} - 1 \right) + t \right) + 4D_0 t.$$

Its asymptotic values for short and long times read

$$\Delta r^2(t) \approx \begin{cases} 4D_0 t & \text{if } t \ll 1/D_r \text{ and } t \ll \tau_0, \\ v_0^2 t^2 & \text{if } t \ll 1/D_r \text{ and } t \gg \tau_0, \\ 4D_{eff} t & \text{if } t \gg 1/D_r, \end{cases}$$

where I defined the diffusive-ballistic crossover time τ_0 and the effective diffusion constant D_{eff},

$$\tau_0 = \frac{4D_0}{v_0^2}$$

$$D_{eff} = D_0 + \frac{v_0^2}{2D_r}.$$

This simple model therefore predicts a MSD that is diffusive at short times, with a diffusion constant imposed by the solvent, a ballistic regime caused by self-propulsion at intermediary times, then a final diffusive regime with an effective diffusion constant related to the rotational diffusion at long times. Furthermore, note that if inertia is considered again in the dynamics of the position ($\tau_v > 0$), one also expects the first ballistic regime described in the passive Langevin equation, corresponding to free dynamics between collisions with the solvent. Note that, in Chapter V, a variant of interest is the one with inertia in the angular dynamics only ($\tau_v = 0$, $\tau > 0$), the final diffusion coefficient corresponding of which was predicted analytically in Ref. [171].

Chapter III

Without Spin-Velocity Coupling: a 2d Ideal Spin Fluid

> What in water did Bloom, waterlover,
> drawer of water, watercarrier,
> returning to the range, admire?
>
> James Joyce, *Ulysses*

III.1 Model and Methods

III.1.1 The Model: a Hamiltonian Spin Fluid

In this chapter, that essentially presents the results published in Ref. [75], I will describe the physics of the system defined by the Hamiltonian I.3, but in the case $K = 0$,

$$\mathcal{H}_0 = \sum_{i=1}^{N} \frac{1}{2}\boldsymbol{p}_i^2 + \sum_{i=1}^{N} \frac{1}{2}{\omega_i}^2 + \frac{1}{2}\sum_{k\neq i} U(r_{ik}) - \frac{1}{2}\sum_{k\neq i} J(r_{ik})\cos\theta_{ik} \ , \tag{III.1}$$

with U a purely repulsive short-ranged potential and J a ferromagnetic short-ranged coupling. The model described by this Hamiltonian, which is meant to serve as a reference case for the case $K \neq 0$, is an off-lattice version of an interacting spin systems, in which (anti)ferromagnetically coupled spins are carried by particles, and interact through (usually short-ranged) distance-dependent interactions. As such, it belongs to a family of models called *spin fluids*, introduced by Weis and coworkers [172, 173]. They were first introduced as simplified models of magnetic colloids or alloys, with the (continuous) spin representing the magnetic momentum of particles. More recently, Ising-spin spin fluids were used to study binary fluids [174–176], with the spin representing the species of each particle.

Previous works on continuous-spin spin fluids only considered the case of a three-dimensional space, first with Heisenberg spins [172, 173], and later with planar spins [177]. The aim of these studies was to determine the phase diagram of these unusual systems, that can display both isotropic-(anti)ferromagnetic and gas-liquid-solid phase transitions.

The phase diagrams, with the magnetic and gas-liquid transitions, were found by solving the Ornstein-Zernike equation under various closure hypotheses (namely Born-Green-like and Hypernetted-chain-like relations), in the same spirit as the usual Percus-Yevick approximation (see II.4). The crystal, when predicted [173], was found through density-functional theory, following standard (albeit rather heavy) textbook methods [1], and well-established literature on the matter [178].

In two-dimensional space, as discussed in Sec. II.3, the magnetisation transition of the on-lattice XY model is known to be highly peculiar. The Mermin-Wagner theorem [54, 55] prohibits spontaneous symmetry breaking at any finite temperature. However, a static phase transition occurs at a finite critical temperature, T_{KT} between a high-temperature disordered paramagnet and a low-temperature ferromagnetic phase with quasi-long-range order. This phase transition obeys the Berezinskii-Kosterlitz-Thouless (BKT) scenario, [71, 73, 78] according to which the magnetisation is suppressed by spin waves for $T < T_{KT}$ and by isolated vortices for $T > T_{KT}$. The validity of this scenario as well as its possible influence on the properties of two-dimensional XY spin fluids was, to my knowledge, an open question before this work.[1] This matter is relevant for several physical systems, from ultracold polar atoms, [180] to certain ionic liquids [181].

III.1.2 Choice of Potentials

In order to study the Hamiltonian III.1, I must first set the shape of the interaction potentials U and J. To understand their respective roles, it is useful to write the Hamiltonian equations of motion,

$$\dot{\boldsymbol{p}}_{\boldsymbol{i}} = \sum_{k(\neq i)} \left(\frac{\partial J(r_{ik})}{\partial \boldsymbol{r}_i} \cos\theta_{ik} - \frac{\partial U(r_{ik})}{\partial \boldsymbol{r}_i} \right) , \tag{III.2}$$

$$\dot{\omega}_i = \sum_{k(\neq i)} J(r_{ik}) \sin\theta_{ik} , \tag{III.3}$$

that are used in the Molecular Dynamics simulations (see Sec. II.2.3). The first of these equations displays quite clearly why the physics of liquids of this kind could be interesting from a fundamental viewpoint: a ferromagnetic coupling ($J > 0$) that decays with distance ($J'(r) < 0$) implies that particles with spins lying in the same half-plane ($\boldsymbol{s}_i \cdot \boldsymbol{s}_j > 0$) are attracted to each other, while particles with spins lying in opposite half-planes ($\boldsymbol{s}_i \cdot \boldsymbol{s}_j < 0$) are purely repulsive. Therefore, even for a purely repulsive U coupling, spin-carrying particles feature a spin-mediated effective attraction, that could allow for a liquid-gas phase separation. However, these equations also show that the choice of potentials is constrained, both at the fundamental and numerical levels. At the fundamental level, one should choose U and J in such a way that $U > J$ at short range, so that all particles have a repulsive core and do not simply collapse onto one point. At the numerical level, since I directly integrate Eqs. (III.2) and (III.3) to simulate the Hamiltonian dynamics, U and J should be relatively smooth for the dynamics to be well-behaved without having to resort to a ridiculously small time step.

[1] Note that the spins here simply represent an internal anisotropy and follow *precessional* dynamics with an associated rotational kinetic energy, making the present model a planar rotor model [119, 179] and not a ferromagnet model *stricto sensu*.

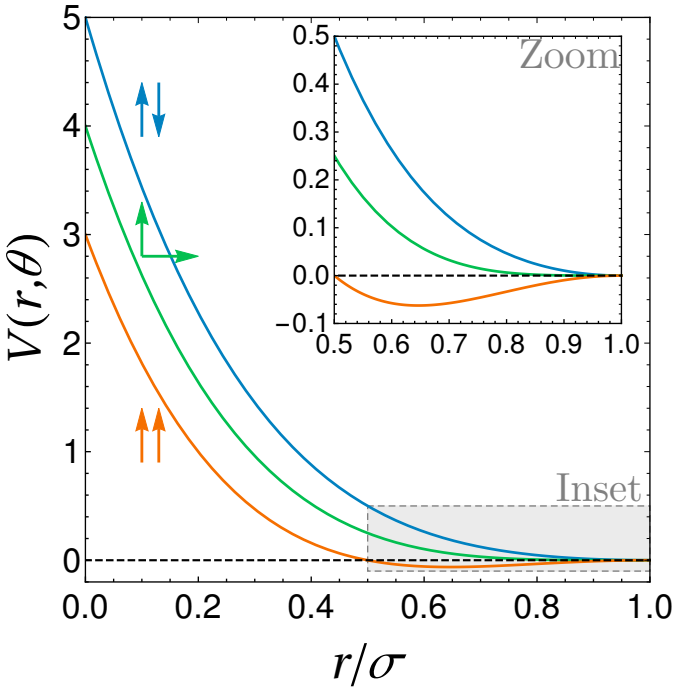

Fig. III.1 **Effective pairwise interaction.** Total pairwise interaction potential $U(r) - J(r)\cos\theta$ used in simulations for aligned (orange), orthogonal (green) and anti-aligned (blue) spins. I highlight the $V(r,\theta) = 0$ line, which separates the repulsive ($V > 0$) and attractive ($V < 0$) parts of the potential, with a dashed black line. In the inset, I show a zoom on the region indicated by a grey rectangle, in order to emphasise the attractive part in the case of aligned spins.

In order to comply with both these constraints, I will use (in this chapter and in all subsequent simulations) soft interaction potentials defined by

$$\begin{aligned} J(r) &= (\sigma - r)^2 \Theta(\sigma - r) \,, \\ U(r) &= U_0 (\sigma - r)^4 \Theta(\sigma - r) \,, \end{aligned} \tag{III.4}$$

where Θ is a Heaviside step function, σ is a range that was fixed to 1, and $U_0 = 4$ was chosen so that both potentials are equal at half-range. I show the associated effective pairwise interaction $V(r,\theta) \equiv U(r) - J(r)\cos\theta$ in the cases of aligned, anti-aligned and orthogonal spins in Fig. III.1. With this choice of potentials, it is useful to define the particle radius $r_0 = \sigma/2$, the zero-temperature exclusion radius for fully-aligned spins. Throughout this thesis, I will use this radius to define the packing fraction,

$$\phi \equiv \frac{\pi r_0^2 N}{L^2}.$$

In two dimensions, this dimensionless density can reasonably take values in the interval $[0; \phi_{CP}]$, where $\phi_{CP} = \pi\sqrt{3}/6 \approx 0.907$ is the fraction at which disks are arranged in a close-packed hexagonal lattice [182].[2]

[2]Note that since we consider soft repulsive potentials, higher packing fractions are not unphysical, but

III.1.3 Simulation Strategy

In the following, I present simulation results obtained by starting from random states with uniformly distributed $\{\boldsymbol{r}_i, \theta_i\}_{i=1..N}$ and $\{\boldsymbol{p}_i, \omega_i\}_{i=1..N}$ drawn from centred, reduced Gaussian distributions. Such initial states are placed into a square box with periodic boundary conditions and, after giving some time for the dynamics to settle in, are subjected either to a numerical annealing or to a high-rate quench. These procedures are implemented as follows.

Numerical annealings are performed by multiplying all rotational velocities by $\lambda_A = 0.9999$ every 100 time units in our adimensionalized variable, with an integration time step equal to $\delta t = 10^{-3}$ in the same units. This method enables us to reach low-energy states which, if the cooling is slow enough, should be equilibrium states of the system.

Quenches are carried out by multiplying all rotational velocities and momentum components by $\lambda_Q = 0.10$ once, at some initial time. This method violently takes the system away from equilibrium, thereby enabling us to study the subsequent equilibration dynamics.

III.1.4 Outline of the Chapter

In the following, using the numerical methods described above, I will focus on a $2d$ ferromagnetic ideal spin fluid, constituted of repulsive disks dressed with short-range ferromagnetic pair interactions. First, in Sec. III.2.1, I discuss the magnetic properties of spatially homogeneous phases in finite size, using Molecular Dynamics simulations. Then, in Sec. III.2.2, I describe a ferromagnetism-induced phase separation (FIPS) that takes place in finite-size simulations, and propose original ways to recover the phase diagram at the mean-field level. I show that, as in the $3d$ case, a ferromagnetism-induced phase separation (FIPS) develops, and provides this system with a non-trivial phase diagram. My main goal is to obtain this phase diagram, and in particular to characterize the interplay between the magnetisation crossover and the liquid-gas separation. In so doing, I recover a phase diagram qualitatively very similar to those obtained for planar spins in $3d$. [177] Schematically, I find a phase separation between a paramagnetic gas and a ferromagnetic liquid. The coexistence curve ends in a tricritical point, from which stems a magnetisation Curie-like line which extends in the region of the phase diagram where the temperature is too high for liquid-gas phase separation to occur, also called the supercritical fluid region in the standard theory of simple liquids. [1] However, a finite-size scaling analysis suggests that the ferromagnetic phase escapes the BKT scenario. This result is confirmed by the numerical study of the equilibration dynamics using equilibrated initial conditions in which the particles are positioned on the vertices of a regular triangular lattice with a few free vortices, or rapid quenches from random high temperature initial conditions into the magnetised phase. No vortices survive either way. The magnetically ordered phases of finite-size systems are characterised by an extremely large correlation length, as expected for a critical system at its lower critical dimension: in the thermodynamic limit (i.e. when the system size becomes larger than the correlation volume), the ferromagnetic order is destroyed by low-energy spin wave excitations, and the Curie line becomes a crossover. Regarding the phase separation, equilibration dynamics following quenches

should not lead to new phenomenology either and are therefore not considered here.

into the coexistence region show that the growth of the order parameter associated to the liquid-vapour phase separation does not follow standard algebraic scalings. Instead, its growth rate is forced to synchronise to that of the magnetisation, suggesting that the gas-side spinodal line coincides with the Curie (crossover) line.

On the theoretical side, I adapt standard methods from the liquid-state theory to describe spin fluids, which carry an internal degree of freedom. I thereby obtain the mean-field equation of state and phase diagram. The latter qualitatively reproduces the phenomenology observed in the simulations. In particular, the magnetisation sets in along a Curie line, which is also the gas-side spinodal line. Finally, these methods allow for a characterisation of the role played by the magnetic interaction range and the softness of the repulsive interaction.

III.2 Numerical Phenomenology

III.2.1 Magnetic Properties of Homogeneous States

As discussed in Sec. II.3, in $d = 2$, the Mermin-Wagner theorem prohibits the critical transition from a hot paramagnet to a cold ferromagnet for on-lattice XY spins [54, 55]. Therefore, while a finite magnetisation is observed at low temperatures in finite-size systems, it is suppressed as the size increases, and the thermodynamic limit is approached [116, 183]. On top of this, the on-lattice XY model features a BKT transition at a finite temperature, at which the mechanism that is behind the suppression of the magnetisation changes, going from low-temperature spin-wave excitations to high-temperature vortex-antivortex proliferation.

In this section, I show that the low-temperature spin-wave behaviour is recovered, as expected from field-theoretical considerations, while vortex unbinding and the BKT scenario disappear off-lattice for our choice of interactions. In order to decouple the discussion of the behaviour of the magnetisation from the one of the structural properties as much as possible, I select a number density such that very little local density fluctuations can take place, namely $\rho = N/L^2 \approx 2.81$ where L is the size of the system. Equivalently, this density corresponds to a packing fraction $\phi = 0.55$. The reason for this particular choice of density will be made clearer when I disclose the full finite-size density-temperature phase diagram in Sec. III.2.2.

a) Low-Temperature Behaviour: Spin-Wave Scaling

Using MD simulations, I cool down systems with a number of particles ranging from 128 to 16384 with a slow simulated annealing (i.e., slow enough to ensure that equilibrium is reached), and measure their magnetisation, and rotational and translational temperatures,

defined as

$$\begin{aligned}
\boldsymbol{M} &= \sum_{i=1}^{N} \boldsymbol{s}_i, \\
T_R &= \frac{1}{N}\sum_{i=1}^{N} {\omega_i}^2 - \left(\frac{1}{N}\sum_{i=1}^{N}\omega_i\right)^2, \\
T_T &= \frac{1}{N}\sum_{i=1}^{N} p_{a,i}^2 - \left(\frac{1}{N}\sum_{i=1}^{N} p_{a,i}\right)^2,
\end{aligned}$$

where $a = x$ or y. I then compute the averages of the modulus of the intensive magnetisation, the temperature T and the usual magnetic susceptibility defined as

$$\begin{aligned}
m &= \frac{1}{N}\langle|\boldsymbol{M}|\rangle, \\
T &= \langle T_R\rangle = \langle T_T\rangle, \\
\chi_m &= \frac{1}{N}\left(\langle \boldsymbol{M}^2\rangle - \langle\boldsymbol{M}\rangle^2\right),
\end{aligned}$$

where $\langle\cdot\rangle$ denotes an average over independent configurations, here obtained by letting the dynamics run for sufficiently long times and using different initial conditions. Note that, having checked that $T_R = T_T$, I henceforth use the symbol T for temperature, without further specification. Curves obtained for $N = 8192$ particles are showcased in Fig. III.2, which displays $m(E)$ and $T(E)$ curves obtained by MD simulations after averaging over 10^2-10^3 configurations for each point in panel (a) and its inset. At low energies and temperatures, I observe a non-zero magnetisation, that crosses over to values close to zero at a finite energy and temperature. In panel (b), I show a typical snapshot of the configuration of spins in the high-magnetisation regime for $N = 8192$ particles. In this snapshots as well as all the others in this section, spins are colour-coded depending on their direction, using the hue variable of the HSL colour code [184], meaning that $\theta = 0$ is coded by pure red, $\theta = 2\pi/3$ by pure green, and $\theta = 4\pi/3$ by pure blue, and that every intermediate colour is a linear interpolation between the nearest two primary colours. This pictures shows that in the low-temperature regime $T \to 0$, the magnetisation is suppressed by harmonic spin waves. This is similar to the very low-temperature regime of the on-lattice XY model [118], described by a massless theory [113, 185].

In panel (c), I show the $m(T)$ curves obtained by combining $m(E)$ and $T(E)$ curves such as those shown panel (a), this time varying the size of the system between $N = 128$ and $N = 16384$ at fixed packing fraction. The magnetisation is suppressed at all temperatures, and the finite-size crossover from high- to low-magnetisation is pushed to lower values of the temperature when increasing the system size, as expected from a model at its lower critical dimension. In the inset of (c), I check that the low-temperature part of the magnetisation curves follows the spin-wave scaling given in Eq. II.40,

$$m = \exp\left(-\frac{T}{8\pi J}\ln(aN)\right).$$

In panel (d), I show the corresponding $\chi_m(T)$ curves, with a logarithmic vertical scale. At low temperatures, this susceptibility grows as the system size increases, and seems to

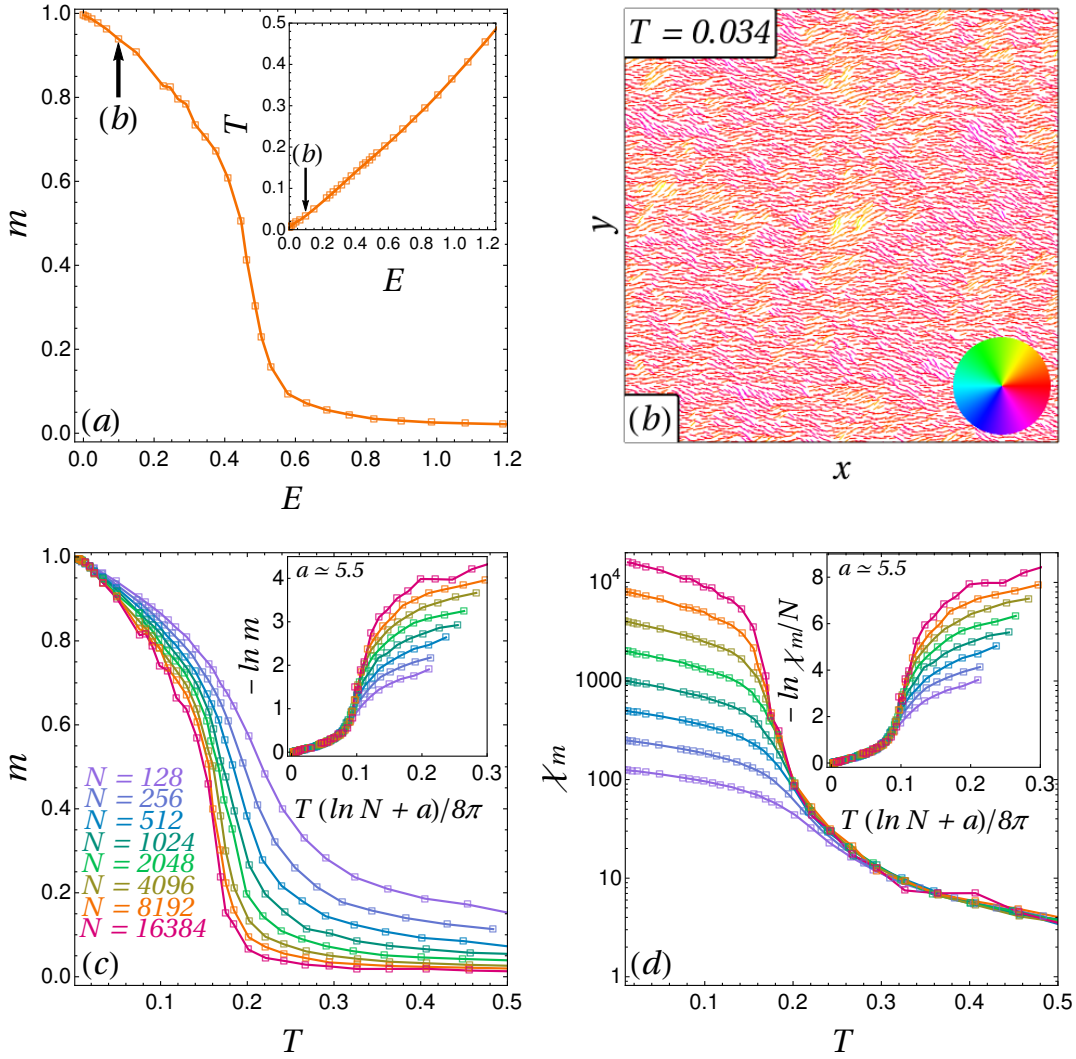

Fig. III.2 **Magnetic Properties at Low Temperatures.** (a) Magnetisation modulus and temperature against the energy per particle for $N = 8192$, (b) typical snapshot of a system of $N = 8192$ particles in the spin-wave regime (c) magnetisation modulus against temperature for growing system sizes, and (d) magnetic susceptibility (in log scale) against temperature for growing system sizes, all at $\phi = 0.55$. In the inset of (a), I report the measured mean temperature against the energy per particle. Black arrows indicate where the snapshot shown in (b) lies in phase space. In the inset of (b), I show the colour-code used for spins to represent their orientation. In the insets of (c) and (d), I report the best collapses of m and χ_m, respectively, near $T = 0$ using the spin-wave scaling described in the main text.

saturate, as expected in the spin-wave regime where the system is smaller than its correlation length. In the inset of (d), I plot χ_m/N against the same rescaled temperature as in the inset of (c), and thereby show that the zero-temperature susceptibility is extensive. This is a check that, as predicted by spin-wave calculations [183], the magnetic properties of the system at low temperature are controlled by a Gaussian fixed point at $T = 0$, so that $\eta \to 0$ as $T \to 0$.

b) Finite-Size Crossover: Is This BKT?

I now discuss the nature of the finite-size crossover between the low- and high-magnetisation regimes. In order to do so, I define a modified susceptibility that features a maximum at a finite temperature, [116] through the fluctuations of the modulus of the magnetisation,

$$\chi_{|m|} = \frac{1}{N}\left(\langle|\boldsymbol{M}|^2\rangle - \langle|\boldsymbol{M}|\rangle^2\right).$$

This modified susceptibility is plotted against the temperature for different system sizes in Fig. III.3(a). As expected, it features a maximum at a finite temperature that decreases with the system size, reflecting the crossover that m undergoes. This maximum, χ_{max}, grows higher and sharper as the system size grows. As shown in the inset of Fig. III.3(a), where Iplot χ_{max}/N against the system size in log-log scale, I measure $\chi_{max} \propto L^{2-\eta}$ with $\eta \approx 0.26 \pm 0.01$. This value is reminiscent of the BKT exponent $\eta = 0.25$, although it is no proof of BKT behaviour alone.

To investigate further, in Fig. III.3(b), I plot the exponent β/ν obtained at each temperature by using the scaling law $m(L,T) \propto L^{-\beta/\nu}$. The corresponding log-log plot of m against the system size is shown in the inset of this panel. I find that β/ν smoothly goes from 0 at zero-temperature (where $m = 1$ regardless of the system size) to 1 at high temperatures (where the magnetisation is simply a sum of independent random variables). The value $\eta \approx 0.26$, if it corresponds to a BKT-like critical point, can be associated to the critical value of β/ν using the hyperscaling law $2\beta/\nu = \eta$. I can therefore evaluate a candidate value for T_{KT} from Fig. III.3(b). Following this strategy, I find $T^\star_{KT} \approx 0.14$, and I define the reduced temperature $t = t/T^\star_{KT} - 1$. Moreover, recalling the on-lattice spin-wave scaling given in Eq. (II.39), at low temperatures, I expect $\beta/\nu = T/(4\pi J_{sw})$. As a result, the initial slope of $\beta/\nu(T)$ enables me to estimate the effective coupling felt by the low-temperature spin waves. I find $J_{sw} \approx 0.13$. Interestingly, in the BKT scenario, the critical temperature seems to follow the RG prediction $T_{KT} \approx 1.35J$. [116, 186] Here, however, I find that $T^\star_{KT} \approx 0.14$ is significantly smaller than $1.35 * J_{sw} \approx 0.19$, which is a first clue that the present system might not follow the BKT scenario.

Having determined the candidate values of the temperature $T^\star_{KT}$, and of the exponents η and β/ν, I still have to check whether the observed value of ν is compatible with BKT physics. In order to do so, I try three different strategies to rescale the magnetisation and susceptibility curves.

(i) Recalling the BKT scaling of the correlation length, $\ln \xi \sim t^{-1/2}$, I rescale the reduced temperature by multiplying it by $(\ln L)^2$, and plot the rescaled magnetisation $mL^{1/8}$ and susceptibility $\chi_{|m|}/L^{7/4}$ in Fig. III.3$(c) - (d)$.

(ii) Assuming that the system does not follow BKT scalings but another similar scaling $\ln \xi \sim t^{-\nu}$, I determine the value of ν such that the curves of $mL^{1/8}$ and $\chi_{|m|}/L^{7/4}$

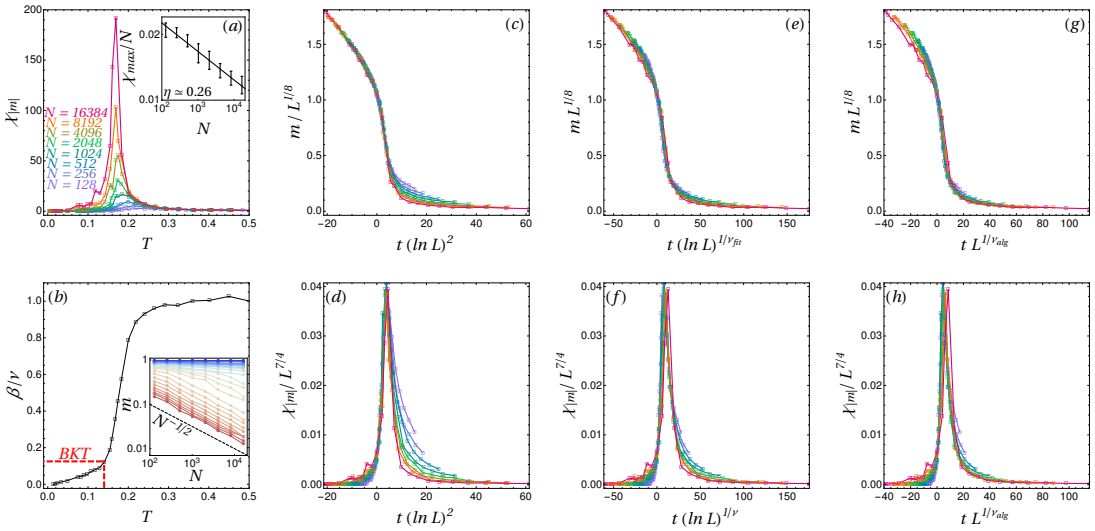

Fig. III.3 **Finite-Size Scalings Near the Crossover.** (a) Susceptibilities of the modulus of the magnetisation for different system sizes, (b) algebraic scaling exponent of the modulus of the magnetisation with size, $(c)-(d)$ logarithmic rescaling of the magnetisation and modulus susceptibility curves with BKT exponents, $(e)-(f)$ best logarithmic rescaling of the magnetisation and modulus susceptibility with a non-BKT $\nu \approx 0.372$, $(g)-(h)$ best algebraic rescaling of the magnetisation and modulus susceptibility with $\nu_{alg} \approx 1.3$. In the inset of (a), I report the measured maxima of $\chi_{|m|}/N$ versus N in log-log representation, with error bars showing a 5% confidence interval around each value, and the best power law fit of it, corresponding to an exponent $\eta \approx 0.26$. The red line in (b) indicates the location of the expected BKT value of $\beta/\nu = 1/8$ at T_{BKT}, which is here very close to the apparent transition temperature. In the inset of (b), I report $m(N)$ in log-log scales at various temperatures, going from blue (low temperatures) to red (high temperatures). The dashed black line shows the $N^{-1/2}$ limit observed at high temperatures. In $(c)-(h)$, $t = T/T^{\star}_{KT} - 1$ is the reduced temperature, where $T^{\star}_{KT}$ is the putative BKT temperature found in (b).

against $t(\ln L)^{1/\nu}$ collapse best near the crossover. The resulting curves, obtained for $\nu = 0.37$ (below the BKT value $\nu = 1/2$), are shown in Fig. III.3$(e) - (f)$.

(iii) Assuming that, for the range of sizes explored in this paper, the crossover can be described by an effective algebraic rescaling of the reduced temperature, I seek the value ν_{alg} that leads to the best collapse of $mL^{1/8}$ and $\chi_{|m|}/L^{7/4}$ against $tL^{1/\nu_{alg}}$ near the crossover. The resulting curves, shown in Fig. III.3$(g) - (h)$, are obtained for $\nu_{alg} = 1.3$.

I find that out of these three strategies, the BKT rescaling yields the poorest collapse at temperatures near, but above the crossover. As in the case of an on-lattice XY model the susceptibility is known to be very close to the exact RG predictions [116], this is a sign that the finite-size crossover of the magnetisation might, in fact not follow the BKT scenario here. However, a thorough proof of this result using only finite size scalings would be numerically very tedious, as several decades of $\log N$ would be required for a precise determination of the value of ν in the hypothesis $\ln \xi \sim t^{-\nu}$. A recent example of these difficulties is the study of the closely related problem of melting of hard disks in $2d$, which was only recently shown (after a 50-year long controversy) to follow a two-step melting scenario [124].

That is why I now focus on another aspect of the on-lattice BKT phenomenology, the unbinding of pairs of topological defects at the crossover. In order to do so, I simulate a system of $N = 8192$ particles, interacting through the same $J(r)$ and placed in a box with the same linear length as heretofore, but with particles pinned on the nodes of a regular triangular lattice. I then cool it down using MD simulations, and taking the same annealing rate as before, but without updating the particles' positions. As expected in an on-lattice setting because the BKT scenario holds there, at temperatures close to but above the finite-size crossover temperature, we observe free vortices and antivortices in the system. A typical example is shown in Fig.III.4(a), which was obtained at a temperature $T \approx 0.15$, and where I highlight with black crosses and letters an unbound vortex (V) - antivortex (A) pair. In order to check the stability of this structure in the off-lattice setting, we use this configuration as an initial condition for particle positions, spins and rotational velocities, draw their velocity components from Gaussian distributions with variance T, and let the dynamics run. As shown in Fig.III.4$(b) - (d)$, in which I show snapshots separated from the initial condition by a time τ each time indicated in the top left corner, this leads to the annihilation of the topological defects when they meet.

The annihilation of free topological defects suggests that this kind of defects is made unstable by the coupling to fluid motion and attracto-repulsion, so that this system does not follow the usual BKT scenario of vortex unbinding at finite temperatures. This suggestion is made stronger by the fact that free vortices similar to those shown in Fig.III.4(a) are *never* clearly observed at any step during the annealing, even for sizes and temperatures at which they have been reported [183] and should be expected if the BKT scenario were realized. Instead, the suppression of magnetisation is seemingly still caused by (anharmonic) spin waves.

All in all, the behaviour observed here is reminiscent of the finite size 1d Ising model [103], which features an exponentially growing correlation length at low temperatures analogous to spin waves and a finite-size crossover to low magnetisation at higher temperatures. If the analogy holds, the crossover happens because, at the lower

critical dimension, the correlation length ξ grows exponentially with temperature and diverges [113]. As a consequence, finite size systems are in practice always smaller than ξ at a finite temperature, and therefore behave in a mean-field-like way at small enough temperatures.

A final confirmation of the absence of vortices at equilibrium is provided by following the non-equilibrium relaxation after a fast quench to a very low temperature (see Fig. III.5). At short times, rather inhomogeneous states with a lot of vortices develop.

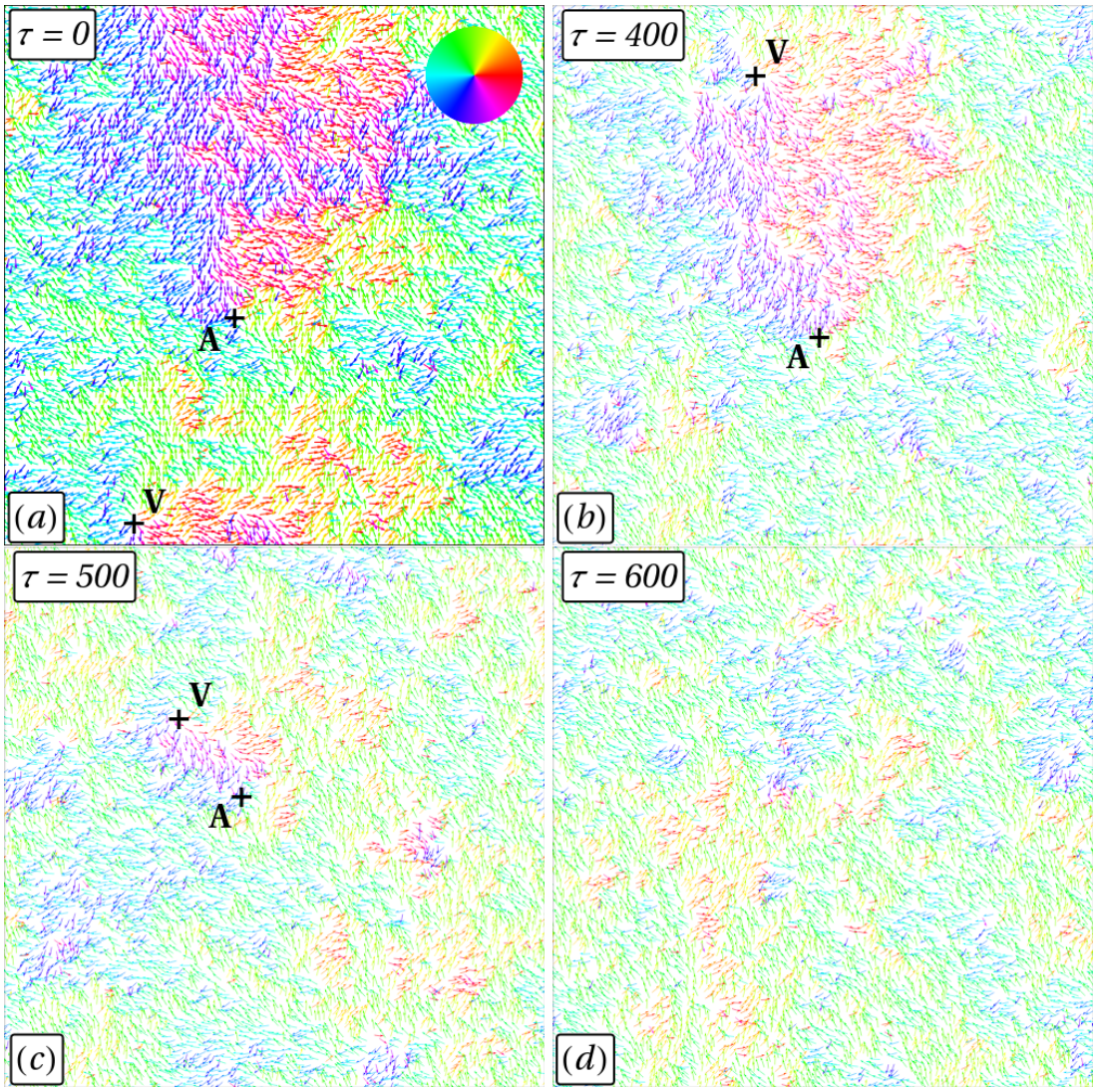

Fig. III.4 **Dynamics starting with free vortices in the initial condition.** I run the dynamics of the spin fluid, starting from the initial condition (a), that was prepared by equilibrating 8192 spins pinned on a triangular lattice at $T \approx 0.15$. In $(b) - (d)$, we show snapshots taken at times $\tau = 400$, 500 and 600. The position of the two free point defects is indicated by a cross, as well as a letter reflecting its nature: V for vortex and A for antivortex.

These vortices rapidly annihilate, leading at longer times to the emergence of large domains with homogeneous magnetisations. The short lifetime of the vortices, is coherent with the equilibrium results: in the absence of a BKT transition, the vortices created by the non-equilibrium dynamics die out during equilibration. This contrasts with the quench dynamics of the square-lattice XY model [93] at very low temperatures, where exceeding vortex-antivortex pairs annihilate rather slowly and a finite density of paired vortices survives.

Altogether I have obtained evidence that our $2d$ XY spin fluids might not belong to the BKT universality class [74]. This important feature is another manifestation of the fragility of the BKT behaviour against changes in the underlying lattice [187], the interaction symmetry [188], the addition of quenched non-magnetic impurities [119], or the form of the potential [189, 190]. In the present case, the coupling between the spin alignment and the attraction-repulsion between particles makes point defects even costlier than usual, which could account for the suppression of BKT physics. Indeed, since aligned spins are attractive and anti-aligned spins repulsive, creating a vortex-antivortex pair entails creating a strong repulsion at the core of each defect, within a group of otherwise attractive particles. The creation of such a local repulsion would then lead to local density fluctuations, that are increasingly discouraged as the system becomes denser, and the compressibility of the fluid goes down.

III.2.2 Phase Separation

I now concentrate on the stability properties of the fluid phases at different packing fractions and temperatures. Like previously done for the magnetic properties, one can study them either after a slow annealing or a fast quench, thus focusing on the static equilibrium properties or the equilibration dynamics. Note that I choose not to discuss the solid phases of the system here, although they play a role in Chapter V.

a) Equilibrium properties

A liquid-gas phase separation is expected in systems such that interactions have an attractive part, and is rather robust against the precise shape of the potential. [1, 191] It is associated to a line of first-order phase transitions terminating in a critical point that belongs to the Ising universality class, both on-lattice and in continuous space. [9] The symmetry associated to the transition is the discrete $\mathbb{Z}_2$ symmetry, and the liquid-gas critical point is thus also expected in $2d$.

A slow annealing, just like the one described in the previous section, can be repeated for other densities, which allow for larger local density fluctuations. I anneal systems with packing fractions $\phi \in [0.10; 0.55]$ and $N = 2048$ particles. I do observe phase-separated states (Fig III.6(g)), meaning that a spin-mediated effective attraction is sufficient for the separation to occur, without an explicit attractive part in the interaction potential. This phase separation takes place between an isotropic gas and a ferromagnetic liquid, as described in previous works for Heisenberg and planar spins in three dimensions. [172, 173, 177] As a result, the liquid-gas critical point lies exactly on the finite-size Curie line, where the crossover to finite magnetisation takes place in the supercritical fluid. This is reminiscent of the tricritical point, observed in higher dimension of space [172, 173, 177]. Such tricritical points are always accompanied by a cusp of the coexistence lines [192].

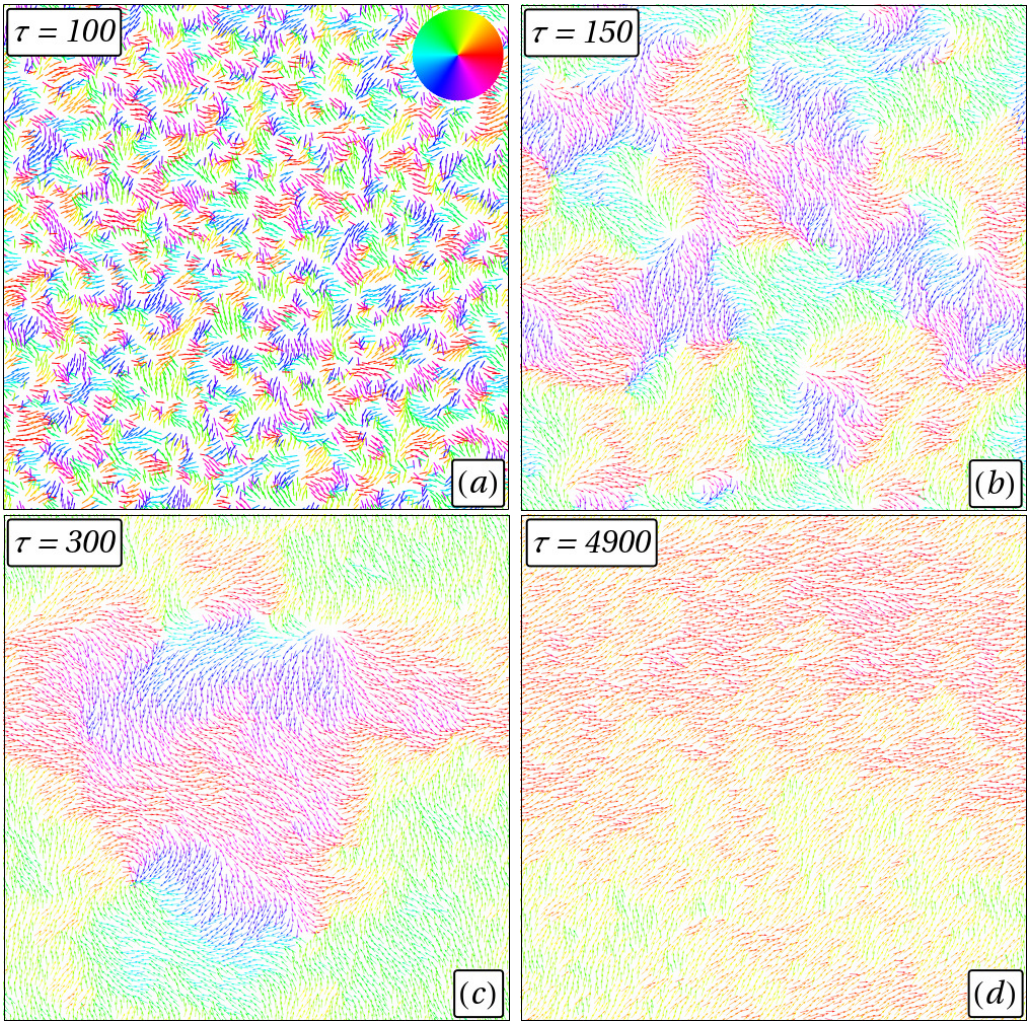

Fig. III.5 **Magnetic equilibration after a quench.** Snapshots of a system composed of 8192 particles, in a square box with periodic boundary conditions, after a quench from an average temperature $T_0/T^\star_{KT} \approx 15$ to an average temperature $T_Q/T^\star_{KT} \approx 1.7\,10^{-1}$, at 4 different times τ after the quench, (a) $\tau = 100$ (b) $\tau = 150$ (c) $\tau = 300$ (d) $\tau = 4900$. Spins are colour-coded on a circle, which is reminded in panel (a).

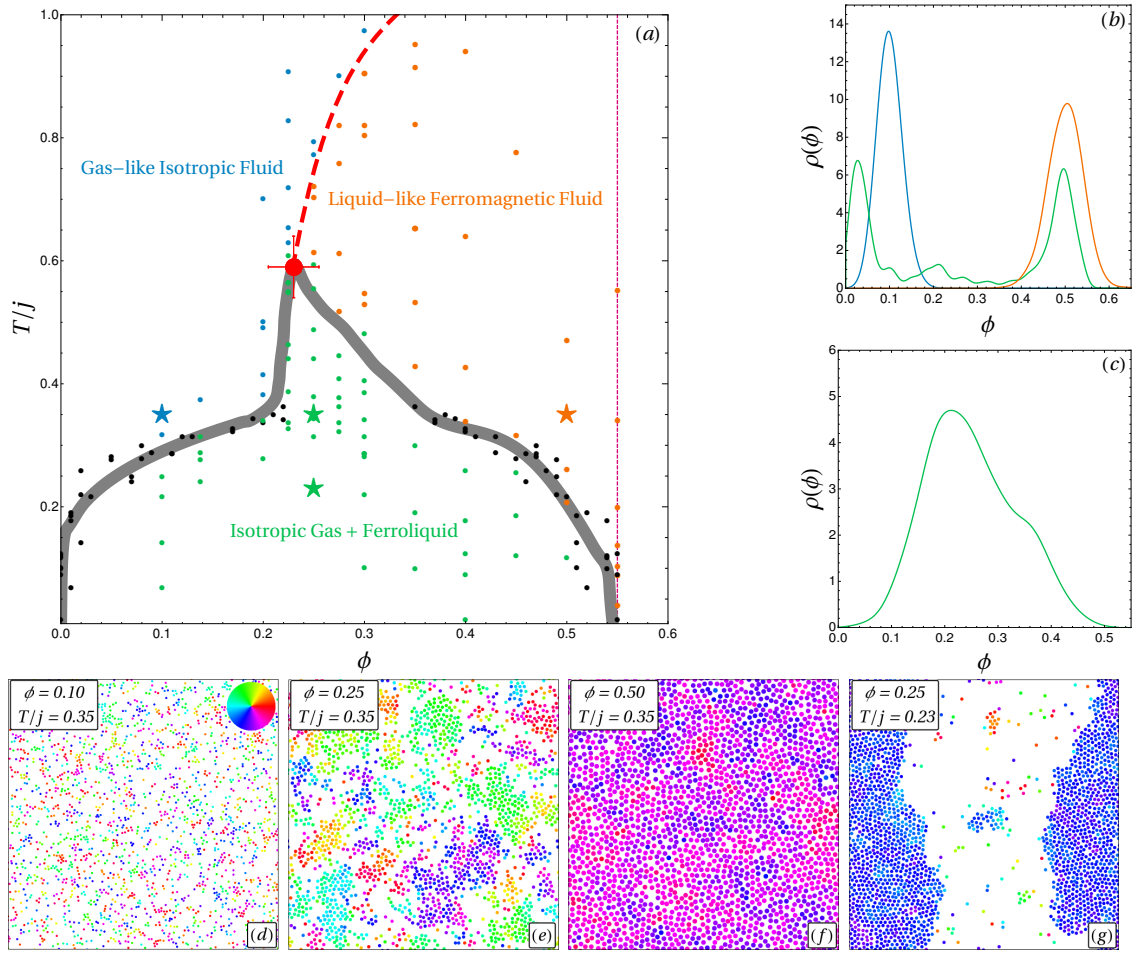

Fig. III.6 **Numerical phase diagram.** (*a*) Points on the phase diagram close to the putative finite-size Curie line (dashed red) and coexistence curve (gray) below the liquid-gas critical point (red dot). I use orange disks for homogeneous magnetised states, blue disks for homogeneous isotropic states, and green disks for phase separated states. Whenever possible, I determined the densities of the two fluids in equilibrium: the corresponding liquid and gas densities are plotted as black disks. I indicate by a magenta dashed line the packing fraction $\phi = 0.55$ that was used throughout Figs. III.2-III.5. Stars are points for which we show density distributions in (*b*) and (*c*). (*b*): well-resolved density peaks corresponding to each part of the phase diagram, that correspond to the snapshots (*d*), (*f*) and (*g*). (*c*) is an example of the density distribution of a phase-separated state, illustrated in the snapshot (*e*), for which peaks cannot be resolved with the system size we used. It seems that the Curie line meets the coexistence curve exactly at the liquid-gas critical point, here found at $\phi \approx 0.23$ and $T/j \approx 0.6$, meaning that it is a tricritical point. A sharp feature of the coexistence line, that looks like a cusp, is visible on this line. Error bars for the tricritical point were roughly determined by visual inspection of density inhomogeneities in that region of the phase diagram.

This is clearly observed in Fig. III.6(a) where the phase diagram indicates the domains of stability for the magnetically isotropic and ferromagnetic homogeneous fluids, together with the coexistence region between the two. Note that the temperature has been rescaled by an averaged value of the ferromagnetic coupling,

$$j = \frac{2}{\sigma}\int_{\sigma/2}^{\sigma} dr J(r) = 1/12,$$

in order to make the comparison between these results and the predictions of Sec. III.3 easier. In this phase diagram, the coexistence line is obtained by computing the coarse-grained density probability distribution. The typical aspect of these distributions is shown in Fig. III.6(b) and (c), along with the corresponding snapshots in panels (d) through (g). The homogeneous phases are clearly identified by a single peak in the distribution. Deep in the coexistence regime, two well-identified peaks enable us to pinpoint the densities of the two coexisting phases. Closer to the top of the coexistence region, the peaks are less separated but the distribution is still clearly not unimodal (Fig. III.6(c)). This, together with the visual inspection of the system, enable me to infer the shape of the coexistence region closer to the critical point.

b) Dynamics after a quench

When quenching the system deep into the coexistence region, one expects both magnetic domain and liquid droplet growths. I here investigate the joint dynamical evolution of these growth processes when the system relaxes to equilibrium. More specifically, it is interesting to see how the droplet growth, associated to a correlation length ξ_l, is linked to the growth of magnetised domains, associated to an *a priori* different correlation length ξ_m.

I define the spatial magnetic correlation function at time τ,

$$C(r,\tau) = \langle \boldsymbol{s}_i(\tau)\cdot\boldsymbol{s}_{\boldsymbol{j}}(\tau)\rangle_{r_{ij}=r},$$

where the average is computed over all particle pairs separated by a distance r and random initial conditions. Similarly, I define the density-density correlation function at time τ,

$$h(r,\tau) = \langle \delta\rho(0,\tau)\delta\rho(r,\tau)\rangle,$$

related to the standard radial distribution function $g(r,\tau)$ through $h = g - 1$. At short range, h typically features exponentially damped oscillations that correspond to the microscopic structure of the liquid, [193] while longer-range structures code for the typical size of liquid domains in phase-separated states. [194, 195]

Concerning the magnetic ordering, when the BKT scenario holds, the spatial correlation following a quench into the critical phase obeys the scaling law [93]

$$C_{BKT}(r,\tau) \sim r^{-\eta(T)} f_{BKT}\left(\frac{r}{\xi_m(\tau)}\right),$$

where τ is the time after the quench, f_{BKT} is a scaling function, and $\eta(T)$ is the static XY exponent. The temperature dependence of $\eta(T)$ reflects the fact that the whole low temperature phase is critical in the $2d$ XY model. In the present system, I have provided

evidence that the BKT scenario does not hold, so that I actually expect a non-critical scaling of the correlation function

$$C(r,\tau) \sim f\left(\frac{r}{\xi_m(\tau)}\right),$$

typical of conventional coarsening systems. Likewise, after a quench into a phase-separated region, the density-density correlation function h is expected to follow the scaling law [194, 195]

$$h(r,\tau) \sim f_h\left(\frac{r}{\xi_l(\tau)}\right),$$

where f_h is another scaling function.

The correlation lengths ξ_m and ξ_l typically grow algebraically on short time scales,

$$\xi \sim \tau^{1/z},$$

where z, the dynamical exponent, defines the universality class of the dynamics. Following the nomenclature introduced by Hohenberg and Halperin, [196] well-known examples are that of model A with $z = 2$, when the order parameter is locally non-conserved, and that of model B with $z = 3$, when the order parameter is locally conserved. [197]

Here, I compute the correlation functions $C(r,\tau)$ and $h(r,\tau)$ for $\tau \in [5; 5000]$ for systems of $N = 8192$ particles, and average over 10 to 20 independent quenches. Regarding the magnetisation, the correlation length $\xi_m(\tau)$ is extracted through the definition $C(\xi_m(\tau),\tau) = 0.5$. As can be seen on Fig. III.7(a), $\xi_m(\tau) \sim \tau^{1/2}$, that is $z_m = 2$. The inset of the figure confirms the scaling for the correlation function. As for the density fluctuations, it is convenient to define the correlation length $\xi_l(\tau)$ as the first value beyond the oscillatory regime such that $h(\xi_l(\tau),\tau) = 0$. It also features a power-law dependence on τ (Fig. III.7(b)), although with a different exponent: $\xi_l(\tau) \sim \tau^{1/3}$, so that $z_l = 3$. Here also, the inset confirms the scaling property of the correlation function.

I conclude that the local conservation laws associated with the order parameters (density is conserved while magnetisation is not) govern the dynamical scalings: the magnetisation (respectively density) fluctuations follow the prescriptions of model A (respectively model B).

However, the order parameters themselves are expected to grow concomitantly since the effective attraction is mediated by the local magnetisation. I shall investigate this focusing on three different quench protocols, as sketched on Fig. III.8:

(i) a quench at a density lower than that of the tricritical point (or critical density for short), starting from the high-temperature isotropic gas, and across the liquid-gas coexistence line,

(ii) a quench at a density higher than the critical density, starting from an isotropic supercritical fluid, and across *both* the Curie line and the liquid-gas coexistence line, and

(iii) a quench at a density higher than the critical density, starting from a magnetised supercritical fluid and crossing only the liquid-gas coexistence curve.

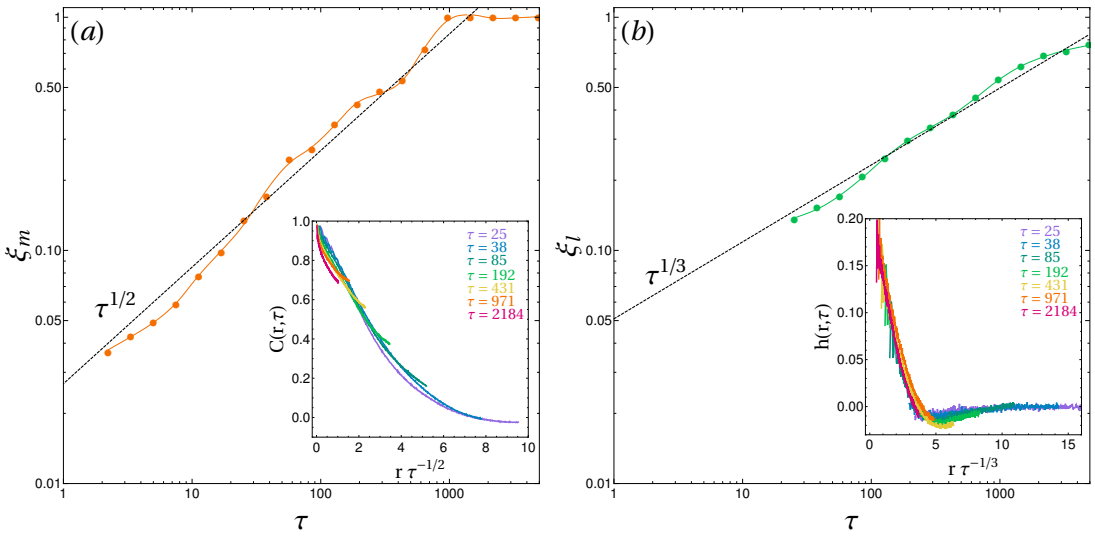

Fig. III.7 **Correlation lengths growth after a quench.** (*a*) Magnetic correlation length ξ_m, here obtained from $C(\xi_m(\tau),\tau) = 0.5$, which is in good agreement with a $\tau^{1/2}$ growth (dashed black line). In the inset of (*a*), I plot C against the rescaled distance $r\tau^{-1/2}$, which leads to a rather good collapse. (*b*) Liquid correlation length ξ_l, obtained from the correlation function $h = g - 1$ using $h(\xi_l(\tau),\tau) = 0$, follows a $\tau^{1/3}$ growth (dashed black line). In the inset of (*b*), I plot h against the rescaled distance $r\tau^{-1/3}$ after taking out the short distance oscillations, thus collapsing the curves. Both correlation lengths are normalized by $L/2$, the upper bound of measurable correlation lengths in a periodic square box of linear length L. All the curves presented here were obtained for $N = 8192$ particles, for $\phi = 0.35$ and each g or C was averaged over 10 to 20 realizations.

Figure III.9 displays four successive snapshots illustrating the coarsening dynamics for each of the above cases. In case (*i*) (first column), the system is initially in a paramagnetic gas phase. After the quench, magnetised liquid domains grow by attracting nearby particles whose spins are aligned with the magnetisation of the domain. In case (*ii*) (second column), the system starts from a paramagnetic supercritical fluid. Crossing the Curie line, the magnetisation should set in. However, crossing the coexistence line at a density larger than the critical one, density inhomogeneities develop in the form of gas pockets across which the ferromagnetic alignment cannot carry over. In case (*iii*) (third column), the system is initially in a ferromagnetic supercritical fluid with a finite magnetisation. Accordingly, the crossing of the coexistence curve leads to the coarsening of gas pockets, but within a magnetisation pattern that is already established.

To be more quantitative, one needs to introduce proper order parameters measured within spatial scales dictated by the coarsening process. The simulation box is divided into $(l/L)^2$ boxes $\mathcal{B}_a$ with linear size l. We first introduce a local magnetisation:

$$m_a = \frac{1}{n_a}\left|\sum_{\boldsymbol{r}_i\in\mathcal{B}_a} \boldsymbol{s}_i\right|,$$

where n_a is the number of particles in box $\mathcal{B}_a$. Since I am interested in the magnetisation

inside liquid droplets, I define a mean local magnetisation modulus weighted by the local density so as to give less statistical weight to empty regions,

$$m_l = \frac{\overline{n_a m_a}}{\overline{n_a}}, \tag{III.5}$$

where the overline symbolizes an average over all boxes. The analogue of the magnetisation for the liquid-gas transition is the difference $\Delta\phi = \phi_l - \phi_g$ between the average packing fraction of the liquid, ϕ_l, and the one of the gas, ϕ_g. [9] These packing fractions are estimated from the list of local packing fractions $\phi_a = n_a \pi r_0^2/l^2$ in box $\mathcal{B}_a$ by computing

$$\begin{aligned} \phi_l &= \frac{\overline{\phi_a \Theta\left(\phi_a - \overline{\phi_a}\right)}}{\overline{\Theta\left(\phi_a - \overline{\phi_a}\right)}}, \\ \phi_g &= \frac{\overline{\phi_a \Theta\left(\overline{\phi_a} - \phi_a\right)}}{\overline{\Theta\left(\overline{\phi_a} - \phi_a\right)}}, \end{aligned} \tag{III.6}$$

where Θ is the Heaviside step function.

By construction, $\Delta\phi$ is close to 0 if the distribution of densities is unimodal and grows over time to its equilibrium value $\Delta\phi_{eq}(T)$ given by the coexistence curve. I therefore

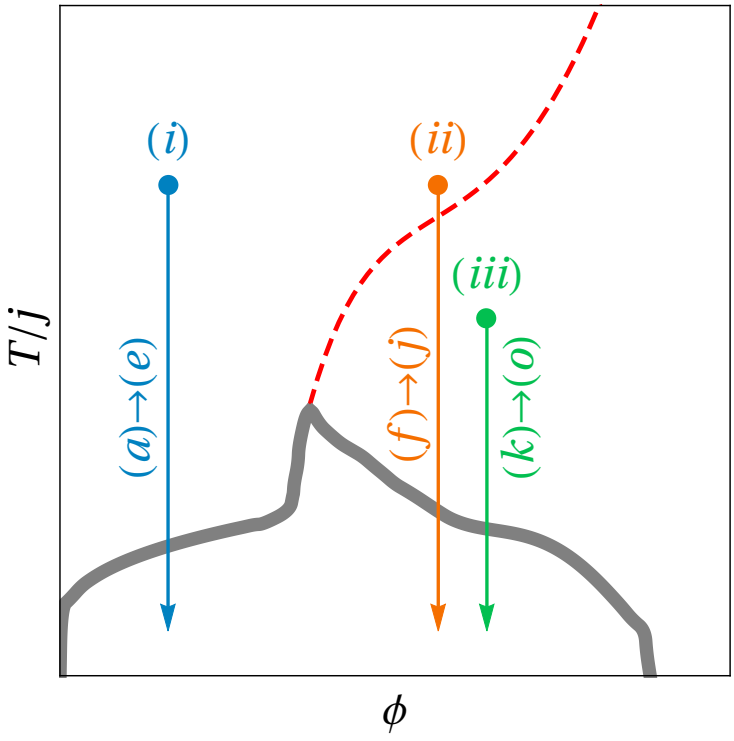

Fig. III.8 **Sketch of the three kinds of considered quenches.** The Roman numbers correspond to the definitions given in the main text. The letters indicate the corresponding panels of Fig. III.9.

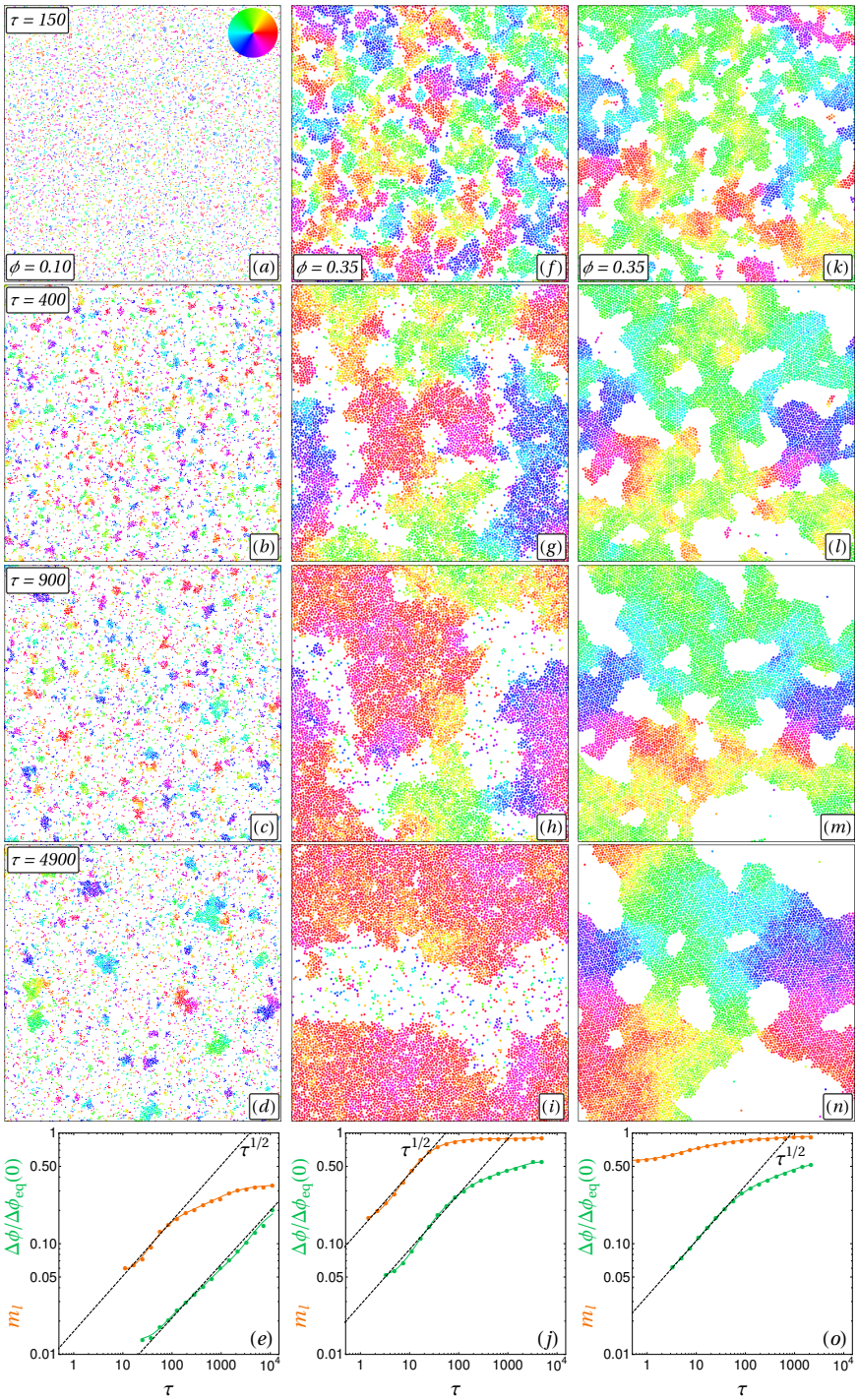

Fig. III.9 **Dynamics after a quench through the liquid-vapour coexistence curve.** Quenches in the three cases discussed in the main text and schematically represented in the phase diagram in Fig III.8. Four snapshots are shown in each case in panels $(a)-(d)$,$(f)-(i)$,$(k)-(n)$. I show the growth of the local order parameters m_l and $\Delta\phi = \phi_l - \phi_g$, defined in Eqs. (III.5) and (III.6), in panels (e), (j) and (o), using the same order as in the snapshots. In order to make the snapshots easier to peruse, the times after the quench are all indicated in the leftmost column, and the packing fractions in the top row. The colour-code used for the spins is reminded in panel (a). For all snapshots, we used $N = 8192$ particles.

normalize $\Delta\phi$ by the zero-temperature width of the numerical phase diagram shown in Fig. III.6(a) to get a quantity that is bounded between 0 (homogeneous phases) and 1 ($T = 0$ phase-separated state at equilibrium).

Just like the correlation length growth, a local order parameter, say $\Delta\phi$, is expected to follow an algebraic scaling $\Delta\phi \sim t^{\lambda_l/z}$ for short times following a quench across a critical transition. The exponent λ_l relates the growth of m to the corresponding correlation length ξ_l: $\Delta\phi \sim \xi_l^{\lambda_l}$. [198, 199] As seen on Fig. III.9(e) and (j) at short times, for both cases (i) and (ii), I observe

$$m_l \sim t^{1/2},$$
$$\Delta\phi \sim t^{1/2}.$$

Their dynamics are synchronized. Note that m_l is not strictly the order parameter associated with the correlation function $C(r, \tau)$, as the modulus in Eq. (III.5) erases long-range correlations between spin orientations. However, assuming that m_l behaves like the local vector magnetisation in the liquid at short times (i.e. when correlations are short-ranged), and together with the values $z_l = 3$ and $z_m = 2$, I respectively find $\lambda_l \simeq 3/2$ and $\lambda_m \simeq 1$ for the liquid and magnetic growths.

The value $\lambda_m \simeq 1$ is the expected analytical value for $O(n)$ vector models in $2d$ with $n \to \infty$, [198] and is therefore coherent from the magnetic point of view. The λ_l we find, however, is more surprising, as the standard liquid-gas separation belongs to the same universality class as the $2d$ Ising model with locally conserved order parameter and should thus exhibit $\lambda = 2$, following general scaling arguments. [200] I attribute this discrepancy to the coupling of the density field to the locally non-conserved magnetisation field via the spin-mediated effective attraction. Coincidentally, the selected growth rate, $\tau^{1/2}$, is the slower of the two *a priori* expected values, namely $\tau^{1/2}$ for a standard $O(n)$ model in $2d$ and $\tau^{2/3}$ for a standard liquid-gas phase separation.

In case (iii), following a quench through the coexistence curve only (i.e. starting from below the Curie line), Fig. III.9(o) shows that $\Delta\phi$ retains the scaling $t^{1/2}$ while the magnetisation has already set in before the quench and does not obey any algebraic scaling.

Altogether, the short-time dynamics of the order parameters following a quench is dominated by the slowest-growing one, namely the magnetisation, thereby altering the standard scalings for the growth of the density order parameter. An intuitive way to think about it is that the liquid-gas phase separation has to wait for the magnetisation to set in in order to induce the effective attraction. This interpretation means that the limit of stability of the gas, or gas-side spinodal line, and the continuation of the Curie line under the coexistence curve are one and the same. If this were the case, both the compressibility and the magnetic susceptibility should diverge at the exact same values of temperature and density. This result is, in fact, consistently recovered in the theoretical approaches developed in the following sections.

III.2.3 Summary of the Numerical Results

Altogether, the above numerical study shows that

1. in spatially homogeneous states, the finite-size magnetisation crossover escapes the BKT scenario as it is not accompanied by vortex unbinding, and is akin to a usual critical system studied at its lower critical dimension.

2. a phase separation between a paramagnetic gas and a ferromagnetic liquid takes place as a result of the spin-mediated effective attraction.

3. the finite-size Curie line hits the liquid-gas coexistence curve exactly at the critical point, and is accompanied by a cusp in the coexistence line.

4. the relaxation dynamics following a quench into the coexistence region suggests that the finite-size Curie line and the gas-side spinodal coincide.

In the following, I shall recover the above observations using different theoretical approaches. Starting with a Bethe-lattice description, I obtain the mean-field phase diagram, which already captures the main aforementioned features. This approach deals with the magnetic and liquid properties at the same mean-field level of approximation. An alternative off-lattice approach would be to follow previous works on $3d$ spin fluids [172, 173, 177] and write down a set of integro-differential equations obtained from the Ornstein-Zernike equation and Born-Green-like closures. Here, I rather develop lighter approaches, taking advantage of the mean-field-like behaviour of the magnetisation, while retaining a finite-dimensional description of the liquid structure. In short, I propose a Curie-Weiss like scheme for the magnetisation, where the number of neighbours is found from the pair correlation function of the liquid. Apart from confirming the general properties of the phase diagram, it enables me to capture the influence of both the softness of the repulsion, and the interaction ranges.

III.3 Mean-Field Predictions

III.3.1 Bethe-lattice description

First, I discuss an on-lattice description of the equilibrium properties of my spin fluid, using a cavity method (see Sec. II.4). In order to model our continuous-space interactions, I take inspiration from the Blume [201]-Capel [202] (BC) model, defined as a lattice model of ferromagnetic Ising spins with vacancies. It is described by the Hamiltonian

$$H_{BC} = -J \sum_{<i,j>} n_i n_j S_i S_j + U \sum_i n_i^2,$$

which contains ferromagnetic alignment of strength J, an on-site repulsion of amplitude U, acting on Ising spins $\{S_i = \pm 1\}$ and occupation numbers $\{n_i = 0, 1\}$. For $U \to \infty$, this model has been shown to feature a tricritical point atop a phase separation region, even though it then only contains hardcore exclusion and nearest-neighbour ferromagnetic interactions. [203] This model has been shown to be closely related to $2d$ Ising-spin fluids, [204] which suggests that an XY-spin extension could be relevant here. However, simply replacing the Ising spins by XY spins would lead to an over-simplistic phase diagram: the full particle-hole symmetry in the $U \to \infty$ limit enforces a symmetric coexistence region around a tricritical point at half-filling [203], just like in the case of the

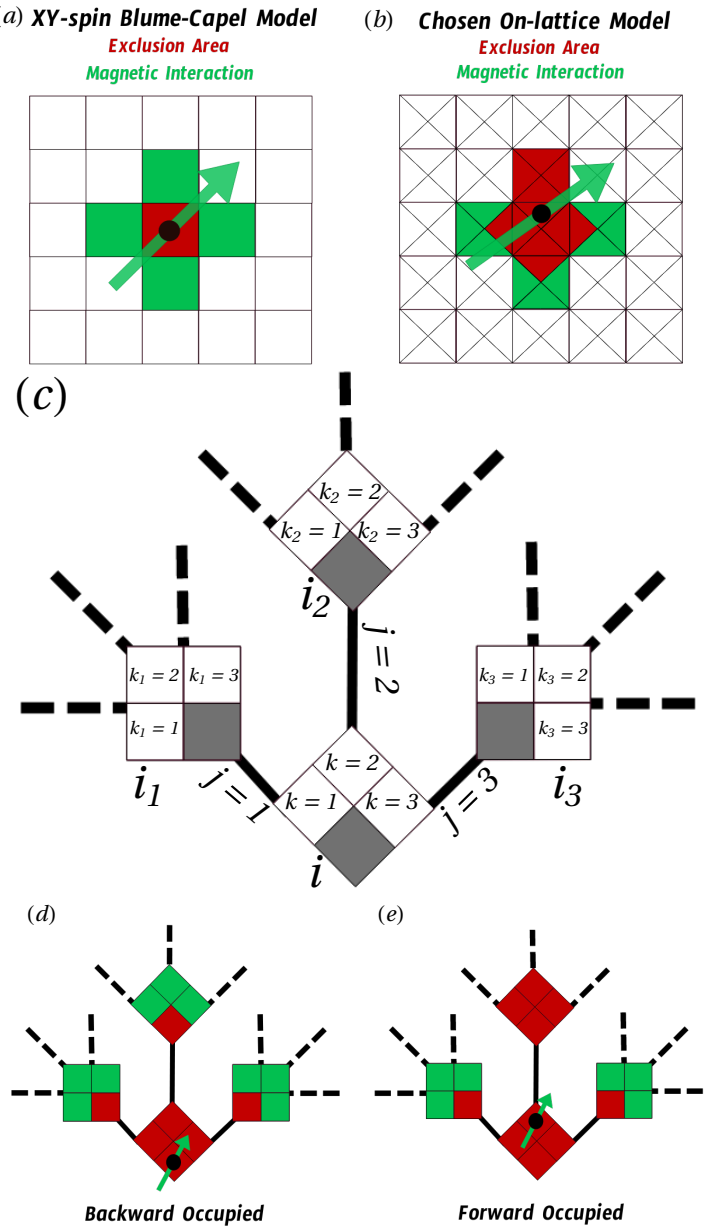

Fig. III.10 **On-lattice interaction rules.** Exclusion and magnetic rules for (a) an XY-spin Blume-Capel model, and (b) the lattice model I use instead. When a square box contains a particle (black bullet), it forbids any other particle from occupying the red area. In case (a), it amounts to the usual exclusion rule. In case (b), the exclusion rule depends on the location of the particle within the square box. All particles carry an XY spin and interact ferromagnetically with their nearest neighbours, as defined by the square lattice (green area). (c) Rooted tree as obtained by digging a cavity in the Bethe lattice which approximates the original lattice. (d) and (e) display the two types of occupied states of a given site that arise due to the anisotropy of the exclusion rules.

Ising-like lattice gas shown in Fig. II.11 of Sec. II.4. To describe richer physics, I define a slightly different Hamiltonian,

$$H = -J \sum_{<i,j>} n_i n_j \boldsymbol{S_i} \cdot \boldsymbol{S_j} + U \sum_{<i,j>} f\left(\sigma_i, \sigma_j\right) n_i n_j,$$

with XY spins, and where I introduce a repulsion that depends on an internal degree of freedom σ_i, here used to make interactions slightly anisotropic in a way inspired by previous works on colloidal gels and glasses. [152, 153, 205] I restrict myself to the case of hardcore exclusion, $U \to \infty$, as it simplifies calculations in the following. To be more specific, for the direct XY-spin extension of the BC model (Fig. III.10(a)), one uses standard exclusion rules, namely one particle per site at most (red area), and nearest-neighbour magnetic interactions (green area). Here, the particle has 4 possible locations within each site of the square lattice (Fig. III.10(b)), thus providing an anisotropy to the exclusion pattern (red area). The magnetic interactions are unchanged.

I obtain a mean-field description of the lattice fluid by approximating the square lattice by a Bethe lattice, which only contains nearest-neighbour couplings. I then compute the free-energy density resorting to the cavity method presented in Sec. c). Any site c in the Bethe lattice is connected to 4 neighbouring sites. Removing site c, each of its neighbours becomes the root of a rooted tree-like graph (Fig. III.10(c)). This is called "digging a cavity". On each of these rooted tree-like graphs, it is then possible to obtain recursively the (cavity) probability of the possible states of the root in terms of the (cavity) probabilities of the states of its nearest neighbours in absence of the root itself. With my choice of interactions, the possible states of the root can be split into three kinds: empty, backward occupied when the particle is located closer to the root, and forward occupied when it is located closer to any of the branches (Fig. III.10(d)-(e)).

I call $Z^B_{i\to c}(\theta_i)$, $Z^{F_k}_{i\to c}(\theta_i)$, and $Z^E_{i\to c}$ the cavity partition functions defined on site i in absence of c and restricted to the backward occupied, forward occupied towards the k-th branch, and empty configurations, respectively. In cases corresponding to an occupied site, there is a dependence on the orientation of the spin of the particle, here noted as θ_i. I finally introduce $Z^F_{i\to c}(\theta_i) = \sum_{k=1}^{3} Z^{F_k}_{i\to c}(\theta_i)$. In the grand-canonical ensemble the recursion rules for these three quantities and a given cavity site c read,

$$\begin{aligned}
Z^{F_k}_{i\to c}(\theta_i) &= e^{\beta\mu} Z^E_{i_k\to i} \\
&\qquad \prod_{j(\neq k)} \left[Z^E_{i_j\to i} + \int d\theta_j Z^F_{i_j\to i}(\theta_j) e^{\beta J \cos\theta_{ij}} \right] \\
Z^B_{i\to c}(\theta_i) &= e^{\beta\mu} \prod_j \left[Z^E_{i_j\to i} + \int d\theta_j Z^F_{i_j\to i}(\theta_j) e^{\beta J \cos\theta_{ij}} \right] \\
Z^E_{i\to c} &= \prod_j \left[Z^E_{i_j\to i} + \int d\theta_j \left(Z^F_{i_j\to i}(\theta_j) + Z^B_{i_j\to i}(\theta_j) \right) \right]
\end{aligned} \tag{III.7}$$

where μ is the chemical potential, and i_k a neighbouring site in the k-th direction (see panel Fig. III.10(c) for notations). These equations look cumbersome, but they are in fact quite simple to understand as enumerations of allowed states of the neighbours of the root, i, depending on its state. The first equation, for instance, means that if the root is forward occupied in a given direction, it forces the nearest neighbour in that direction to be empty ($j \neq k$), but the other two neighbours can be either forward occupied or empty.

From these quantities, I can also define recursions on normalised probabilities by dividing each equation by $Z^T_{i\to c} \equiv Z^E_{i\to c} + \int d\theta_i \left(Z^F_{i\to c}(\theta_i) + Z^B_{i\to c}(\theta_i) \right)$, the sum of all partial partition functions on the removed link between i and c. I denote these probabilities $\psi^S_{i\to c}$, where S is E, B, F_k or F just like for their partial partition function counterparts. I furthermore introduce $\psi^O_{i\to c}(\theta_i) = \psi^B_{i\to c}(\theta_i) + \psi^F_{i\to c}(\theta_i)$, the probability that site i is occupied (in any way) in the absence of the cavity and carries a spin parametrized by θ_i. From these probabilities, the free energy F and, therefore, the thermodynamic properties can be reconstructed by considering all the processes that allow to reconnect four cavity sites to obtain a well-defined Bethe lattice where all the sites have connectivity equal to four (see Sec. c), and Refs. [5, 150, 152, 153] for more details). This free energy verifies

$$\beta F = -\sum_{c=1}^{N} \ln \left[\prod_{i=1}^{4} \left(\psi^E_{i\to c} + \Psi^O_{i\to c} \right) + e^{\beta\mu} \sum_{p=1}^{4} \psi^E_{p\to c} \int d\theta_j \prod_{i\neq p} \left(\psi^E_{i\to c} + \int d\theta_i e^{\beta J \cos(\theta_i - \theta_j)} \psi^F_{i\to c}(\theta_i) \right) \right]$$

$$+ \sum_{\langle i,j \rangle} \ln \left[\psi^E_{i\to j}\psi^E_{j\to i} + \psi^E_{i\to j}\Psi^O_{j\to i} + \psi^E_{j\to i}\Psi^O_{i\to j} + \int d\theta_i d\theta_i e^{\beta J \cos(\theta_i - \theta_j)} \psi^F_{i\to j}(\theta_i)\psi^F_{i\to j}(\theta_i) \right],$$

where I introduced

$$\Psi^O_{i\to j} = \int d\theta_i \psi^O_{i\to c}(\theta_i)$$

to make the equation somewhat lighter. Looking for homogeneous solutions, in which all ψ's are site-independent, the recursive equations (III.7) become a system of self-consistent algebraic equations, and they can be easily solved numerically once the spin orientation has been discretized (here, I use 16 values). For some values of the temperature and chemical potential, there are two branches of solutions for the free energy thus obtained, corresponding to two different homogeneous phases, and the observed phase is that with the lowest value of the free energy. When these branches cross, it indicates a coexistence between the two fluids. Phase separations are then visible as singularities of the free energy: a discontinuity of $\partial F/\partial\mu$ corresponds to a density jump (see Sec. II.4.1). The onset of the magnetisation, on the other hand, is computed directly using the statistical weights corresponding to each angle on the branch of solutions. For completeness, I also seek the liquid-crystal coexistence curves using the technique described in Sec. c), which is inspired from Ref. [152]. Recall that the liquid-crystal transition is absent in the case of the usual BC model, [203] and is here a result of the anisotropic exclusion rules.

Figure III.11 displays the so obtained phase diagram in the $(\phi, T/J)$ plane. The packing fraction is calculated from the ratio of filled sites on the lattice (that can go up to 1) by rescaling it so that for a completely filled lattice it takes the value of the $2d$ close-packing packing fraction, $\phi_{CP} = \pi\sqrt{3}/6 \simeq 0.9069$.

The mean-field phase diagram in Fig. III.11 captures the phenomenology observed in the simulations: liquid-gas phase coexistence takes place, even for hard-core exclusion; it terminates at a tricritical point, located within this approximation at $\phi_c \approx 0.26$ and $T_c/J \approx 0.24$. These values, especially the packing fraction, are in good agreement with the simulation results considering that it is just a mean-field approximation and that,

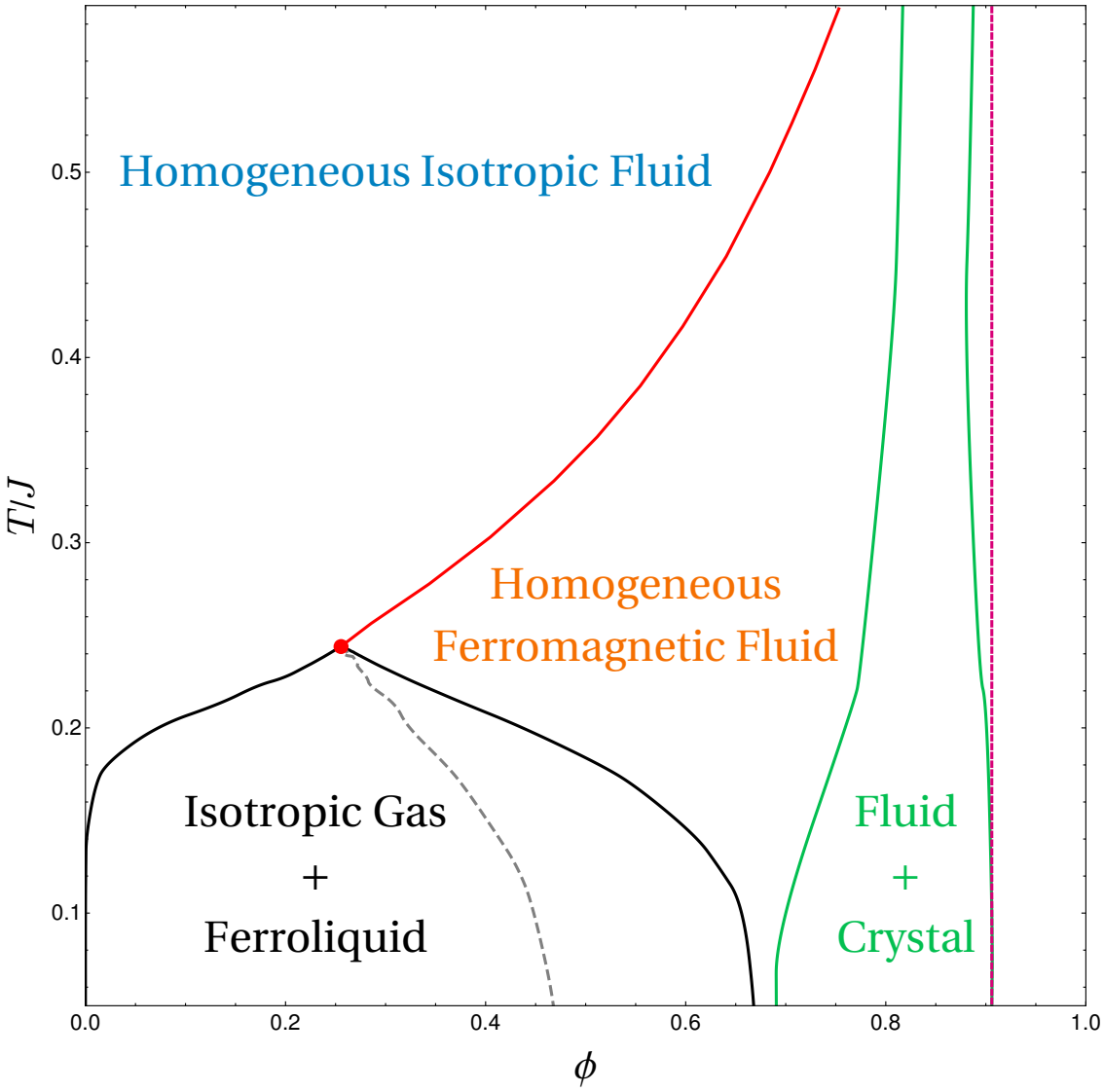

Fig. III.11 **Bethe-lattice phase diagram.** Phase diagram corresponding to a numerical resolution of the coupled equations (III.7) for homogeneous and crystalline solutions, in the $(\phi, T/J)$ plane, using 16 discrete values for spin orientations. I plot the coexistence line between the paramagnetic gas and the ferromagnetic liquid (black), the Curie line (red), the spinodal line associated to the liquid-gas separation (dashed gray), and the fluid-crystal coexistence region (green lines). I also spot the close-packing density (magenta line). The left-most branch of the spinodal is practically superimposed with the coexistence curve. The tricritical point is found at $\phi_c \approx 0.26$ and $T_c/J \approx 0.24$.

moreover, it approximates the soft potential of the simulations by a hard one. Note that within mean field, the Curie line is a true critical line, which becomes a crossover in $2d$, as already stressed in Sec. III.2.1. This combined analysis of magnetic and density degrees of freedom gives access to the spinodal lines. On the gas-side, I observe that the spinodal is essentially superimposed with the coexistence curve. This corroborates the numerical observations. Finally, I reckon that within the range of explored temperatures, the fluid-crystal coexistence region and the liquid-gas coexistence one are well-separated. This ensures that not taking into account the solid phases when discussing the fluid ones is justified.

III.3.2 Curie-Weiss-like approximation

I now discuss an alternative off-lattice approach to describe a $2d$ spin fluid at the mean-field level while keeping some information about the liquid structure. The idea is to introduce an equivalent of the Weiss molecular field [100, 206] in continuous space, in order to get a self-consistent Curie-Weiss-like mean-field resolution (see Sec. II.3). To do so, I first consider, much like in Langevin's theory of paramagnetism, a single spin placed in a thermal bath at inverse temperature β, and in a magnetic field with amplitude h. Let θ be the angle between the spin and the magnetic field. The thermodynamic average magnetisation of this spin, $m = \langle \cos\theta \rangle$, can be written as

$$m = \frac{1}{Z_0} \int_0^{2\pi} d\theta \cos\theta \, e^{\beta h \cos\theta},$$

with Z_0 the partition function. The integral in the right-hand side can be rewritten in a more compact form by introducing I_n, the modified Bessel function of the first kind with parameter n, [101]

$$m = \frac{I_1(\beta h)}{I_0(\beta h)}.$$

Like in the usual Curie-Weiss approximation for lattice models, I now want to describe the spin fluid by a collection of spins that are only coupled through an effective field, defined through

$$h_{\text{eff}}(\beta, \phi, m) = \frac{1}{2} N_n(\langle \cos\theta \rangle = m) J m, \tag{III.8}$$

where N_n is the number of magnetic neighbours of a particle in the spin fluid, J is an effective amplitude of the ferromagnetic coupling over the interaction range, and m is the magnetisation. The self-consistent equation for the magnetisation in this Ansatz is then

$$m = \frac{I_1(\beta h_{\text{eff}}(\beta, \phi, m))}{I_0(\beta h_{\text{eff}}(\beta, \phi, m))}. \tag{III.9}$$

Computing the magnetisation from this equation requires the knowledge of the number of neighbours N_n at a given temperature and packing fraction in the spin fluid. The latter is closely related to the radial distribution function $g(r)$ introduced in Sec. III.2.1. Indeed, recalling that the range of magnetic interaction is denoted σ, the number of magnetic

neighbours reads

$$N_n = 2\pi\rho \int_{r=0}^{\sigma} dr\, r\, g(r).$$

I therefore need to estimate $g(r)$. Computing $g(r)$ from the microscopic Hamiltonian is a central task of the theory of simple liquids, for which various methods have been devised (see Sec. II.4, and Ref. [1]). In these methods, one generally first computes or chooses an approximate form for the direct correlation function, $c(r)$, the part of $g(r)$ that only contains the correlation between the position of two particles due to their direct interactions, as opposed to longer-range correlations that are mediated by other particles. $c(r)$ and $g(r)$ are related by the Ornstein-Zernike equation [1],

$$h(r_{12}) = c(r_{12}) + \rho \int d^2\boldsymbol{r}_3 c(r_{13}) h(r_{32}),$$

where $h(r) = g(r) - 1$ and $r_{ij} = |\boldsymbol{r}_i - \boldsymbol{r}_j|$.

The next two subsections correspond to two different methods to approximate $g(r)$ in a spin fluid. In both cases, I consider square-shaped interaction potentials,

$$U(r) = u\Theta(\sigma_{\text{rep}} - r),$$
$$J(r) = j\Theta(\sigma - r),$$

where Θ is a step function, $u > j$, and $\sigma_{\text{rep}} \leq \sigma$. I use σ_{rep} as the unit length scale, and $f = (\sigma/\sigma_{\text{rep}})^{-1}$ parametrises range ratio between repulsion and magnetic interactions. As before, j is used as a unit energy scale. The first one is inspired by the standard Percus-Yevick approach for hard spheres. It applies in the hard-disk limit, corresponding to $u/j \to \infty$, with finite j and f fixed. In this context, $f \in [0; 1]$ with $f = 0$ corresponding to infinite-range magnetic coupling, and $f = 1$ corresponding to vanishing-range magnetic interactions. The second one, inspired by the virial expansion methods. It provides results which are more analytically tractable. In the third subsection, I discuss the respective advantages of these methods in the context of hard disk exclusion. In a last subsection, I finally discuss the role played by f and u/j in the virial method, taking advantage of the tractability of this scheme.

a) Percus-Yevick-Random-Phase-Approximation-Curie-Weiss (PY-RPA-CW)

An approach that is rather usual in studies focussing on hard disks with an attractive tail consists in using a Percus-Yevick Ansatz for the core exclusion part of the potential, and a simple treatment of the attractive part, like for instance a Random-Phase Approximation (RPA), also called Mean-Spherical Approximation (MSA) (see Sec. II.4). The Percus-Yevick Ansatz, applied to a liquid of hard disks, consists in approximating $c(r)$ by $g(r)(1-\exp\beta U(r))$, which leads to a nice closure of the Ornstein-Zernike equation. In so doing, the Percus-Yevick approach leads to an analytic form of the direct correlation function for a hard-sphere liquid in $3d$. This advantage is lost in even dimensions, but some efficient quasi-exact analytic form can be found by an extrapolation of their low density values. Here, I use a form proposed in the literature, [144] that reproduces the exact numerical values up to packing fractions that are very close to crystallization. The RPA, on the other hand, consists in a linearization of the attractive part of the potential. Since the

present particles carry spins, the attractive part of the potential not only depends on the distance between two particles, r, but also on their relative spin orientation θ. In this context, the direct correlation function reads

$$c(r,\theta) = c_{\mathrm{PY}}(r) + c_{\mathrm{RPA}}(r,\theta),$$

where

$$\begin{aligned} c_{\mathrm{RPA}}(r,\theta) &= \beta\frac{j}{2}\cos\theta\,\Theta(\sigma - r)\Theta(r - \sigma_{\mathrm{rep}}),\\ c_{\mathrm{PY}}(r) &= \Theta\left(1 - \frac{r}{\sigma_{\mathrm{rep}}}\right) c_0(\phi)\\ &\quad\times\left(1 - 4\phi + 4\phi\omega_2(\frac{r}{2\sigma_{\mathrm{rep}}}) + s_2(\phi)\frac{r}{\sigma_{\mathrm{rep}}}\right), \end{aligned}$$

and

$$\begin{aligned} c_0(\phi) &= -\frac{1+\phi+3p\phi^2-p\phi^3}{(1-\phi)^3},\\ s_2(\phi) &= \frac{3}{8}\phi^2\frac{8(1-2p)+(25-9p)p\phi-(7-3p)p\phi^2}{1+\phi+3p\phi^2-p\phi^3},\\ \omega_2(x) &= \frac{2}{\pi}\left(\arccos x - x\sqrt{1-x^2}\right),\\ p &= \frac{7}{3} - \frac{4\sqrt{3}}{\pi}. \end{aligned}$$

The Ornstein-Zernike equation is usually solved in Fourier space to deal with the otherwise cumbersome convolution. Here, I resort to both a Fourier transform over space and a Fourier series over the angles. Because of the linearization of attractive interactions in the context of the RPA, c depends on θ only through $\cos n\theta$ with $n = 0, 1$, so that the series contains only two terms,

$$c(r,\theta) = \frac{1}{(2\pi)^2}\int d^2\boldsymbol{k}e^{-i\boldsymbol{k}\cdot\boldsymbol{r}}\sum_{n=0}^{1}\hat{c}_n(\boldsymbol{k})\cos n\theta.$$

The pair correlation function then reads

$$\begin{aligned} g(r,\cos\theta) =&\\ &1+\frac{1}{(2\pi)^2}\int d^2\boldsymbol{k}e^{-i\boldsymbol{k}\cdot\boldsymbol{r}}\sum_{n=0}^{1}\frac{\hat{c}_n(k)\cos n\theta}{1-\rho\hat{c}_n(k)}. \end{aligned}$$

Finally, the number of neighbours N_n, the spins of which have a given orientation θ relative to that of a central particle is

$$N_n(\cos\theta) = 2\pi\rho\int_{\sigma_{\mathrm{rep}}}^{\sigma} dr\, r\, g(r,\cos\theta). \tag{III.10}$$

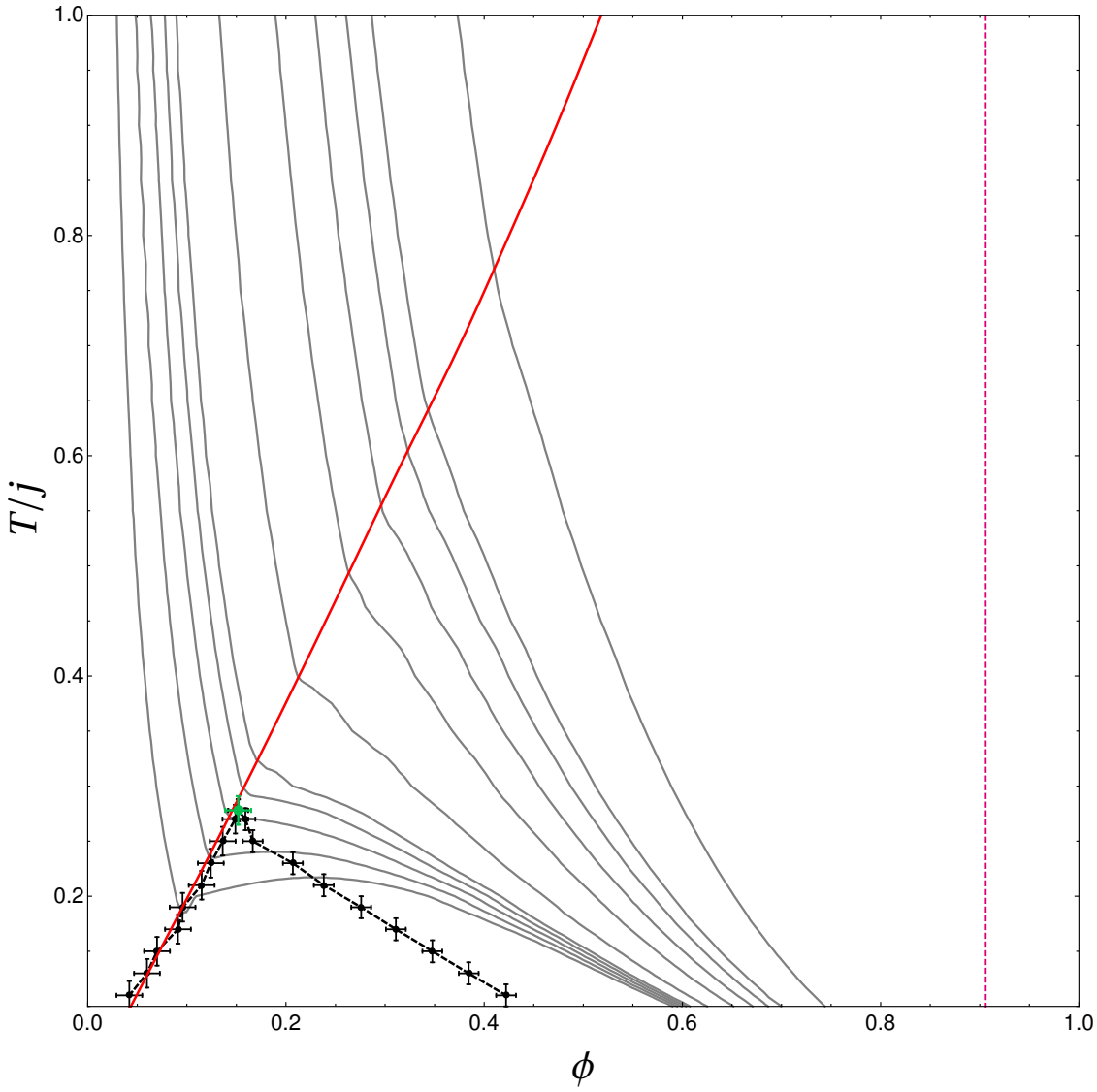

Fig. III.12 **Isobaric curves and Curie line in the PY-RPA-CW description.** I show the Curie line (solid red), spinodal curves (solid black) and a few isobaric curves (solid gray), for the same magnetic range-core size ratio as in the on-lattice calculation ($f = (\sigma/\sigma_{\rm rep})^{-1} \approx 0.72$), close to the critical point. I added the close-packing line in magenta. Error bars are shown on the spinodal curve, corresponding to a rough evaluation of the stability of our algorithm searching for a vanishing of the inverse compressibility. I find a phase separation between an isotropic gas and a ferroliquid, with a tricritical point located at $\phi_c \approx 0.1518$, $T_c \approx 0.278$, plotted above as a green dot. Also notice that the Curie line seems to be playing the role of a left-most spinodal under the critical point, and isobaric curves display a cusp when they cross it rather than a smooth minimum.

Within the context of the present Curie-Weiss approximation, $\cos\theta = m$, so that Eq. (III.8), Eq. (III.9) and Eq. (III.10) form a self-consistent set of equations from which the magnetisation $m_{\rm SC}(\phi, T)$ and, therefore, the Curie line can be computed. Correspondingly, once the self-consistent magnetisation is known, we obtain the liquid properties, and in particular the compressibility χ_c through the thermodynamic relation: [1]

$$\frac{1}{\rho k_B T \chi_c} = 1 - \rho \hat{c}(k = 0, m_{\rm SC}).$$

The zeros of the inverse compressibility define the spinodal curve. Finally, integrating this equation over the density yields the compressibility state equation for the pressure [1]

$$P = \rho k_B T - k_B T \int_{\rho'=0}^{\rho} d\rho' \, \rho' \, \hat{c}(k = 0, m_{\rm SC}).$$

Figure III.12 displays the phase diagram obtained following the method explained above, together with a few isobaric curves. The method predicts a liquid-gas phase separation at low temperature, which ends at a tricritical point on the Curie line. Just like in the Bethe-lattice approach, the Curie line is here a true critical line as the Curie-Weiss self-consistent approach is mean-field-like, but it becomes a crossover in $2d$. I also recover that the left-most spinodal curve seems to be exactly located on the Curie line. Interestingly enough, the isobaric curves, when crossing the spinodal line, show a cusp instead of a flat minimum, indicating a sudden jump of compressibility associated to the nucleation of the liquid.

b) Virial Expansion - Curie-Weiss (VE-CW)

In order to complement the PY-RPA-CW description and to discuss the role played by the amplitude of the repulsive potential and interaction ranges, I analyze the system in the low-density limit. In this context, I write the direct correlation function up to first order in density using the Mayer expansion of the partition function described in Sec. II.4,

$$c(r, \theta) \simeq f(r, \theta) + \rho f(r, \theta) \, (f \star f) \, (r, \theta),$$

where f is the Mayer function associated to the pairwise interaction potential

$$\begin{aligned} f(r, \theta) = \Theta(\sigma - r) \left(e^{\beta j \cos\theta} - 1 \right) \\ + \Theta(\sigma - r) \Theta(\sigma_{\rm rep} - r) e^{\beta j \cos\theta} \left(e^{-\beta u} - 1 \right), \end{aligned}$$

and $\star$ is a convolution product computed over both positions and angles,

$$f \star g(r_{12}, \theta_{12}) \equiv \int d^2 \boldsymbol{r_3} d\theta_3 f(r_{13}, \theta_{13}) g(r_{32}, \theta_{32}).$$

I then use the Ornstein-Zernike equation in real space, cut it off at order ρ, and thence get the angle-dependent version of the pair correlation function,

$$g_\theta(r, \theta) = g_\theta^{(0)}(r, \theta) + \rho g_\theta^{(1)}(r, \theta),$$

with

$$g_\theta^{(0)}(r,\theta) = 1 + f(r,\theta),$$
$$g_\theta^{(1)}(r,\theta) = (1 + f(r,\theta))\,(f \star f)\,(r,\theta).$$

The usual pair correlation function g is obtained by averaging g_θ over the spin angles,

$$g(r) = \int d\theta p(\theta) g_\theta(r,\theta),$$

where $p(\theta)$ is the angle distribution of spins in the spin fluid at the considered density and temperature. The actual angle distribution is a priori a complicated function to compute. In the context of my self-consistent scheme, I choose a Von Mises distribution parametrized by temperature and an effective field h that mimics the distribution observed for an isolated spin coupled to h:

$$\Upsilon(\theta;\beta h) \equiv \frac{e^{\beta h \cos\theta}}{2\pi I_0(\beta h)}. \tag{III.11}$$

This distribution provides a natural way to define the analogue of a Gaussian law wrapped on a circle, [207] whose two notable limits are the low- and high-variance regimes

$$\Upsilon(\theta;\beta h) \underset{\beta h \to 0}{\sim} \frac{1}{2\pi} + O\left(\beta h\right),$$
$$\Upsilon(\theta;\beta h) \underset{\beta h \gg 1}{\sim} \sqrt{\frac{\beta h}{2\pi}} e^{-\frac{\beta h}{2}\theta^2} \underset{\beta h \to \infty}{\to} \delta(\theta).$$

The number of magnetic neighbours reads

$$N_n = 2\pi\rho \int_{r=0}^{\sigma} dr\, r \int d\theta \Upsilon(\theta;\beta h) g_\theta(r,\theta). \tag{III.12}$$

By setting $h = h_{\text{eff}}$, the effective field introduced in Eq. (III.8), Eq. (III.9) and Eq. (III.12) form a self-consistent set of equations from which I compute the magnetisation and Curie line in the low-density limit.

Regarding the liquid properties of the fluid, notice that the low-density expansion of the correlation functions is equivalent to a cut-off virial expansion, which is usually written as an equation of state for the pressure, [1]

$$\frac{\beta P}{\rho} = 1 + B_2(T)\rho + B_3(T)\rho^2 + \dots \tag{III.13}$$

where B_2 and B_3 are the first two virial coefficients,

$$B_2(T) = -\frac{1}{2}\int d\boldsymbol{r} d\theta_1 d\theta_2 p(\theta_1) p(\theta_2) f(r,\theta_{12}),$$
$$B_3(T) = -\frac{1}{3}\int d\boldsymbol{r_1} d\boldsymbol{r_2} d\theta_1 d\theta_2 d\theta_3 p(\theta_1) p(\theta_2) p(\theta_3) \times f(r_{12},\theta_{12}) f(r_2,\theta_{23}) f(r_1,\theta_{31}).$$

These coefficients are averages over spin orientations and particle positions of the zero-th and first terms of the density expansion of $c(r)$, assuming an homogeneous spatial density ρ and a spin orientation distribution $p(\theta)$.

Inserting the Von Mises distribution (III.11) into the definitions of B_2 and B_3, we then obtain exact expressions for these virial coefficients. Details on the computation and their precise shapes are given in App. B. The first one, that is not too cumbersome, reads

$$B_2(h,T) = \frac{\pi}{2}\sigma^2 \left\{ [1 - I_0(\beta j)] - 2\sum_{n=1}^{\infty} I_n(\beta j)\frac{I_n(\beta h)^2}{I_0(\beta h)^2} \right\} + \frac{\pi}{2}{\sigma_{\text{rep}}}^2 \left[I_0(\beta j) + 2\sum_{n=1}^{\infty} I_n(\beta j)\frac{I_n(\beta h)^2}{I_0(\beta h)^2} - e^{-\beta u} \right]. \tag{III.14}$$

$B_3(h,T)$ is given by a similar expression: both coefficients contain a series of Bessel functions $I_n(\beta j)$ and $I_n(\beta h)$ with $n \in \mathbb{N}$, which is the equivalent of a high-temperature expansion [2] of an XY model. I give in Eq. (III.14) the full n expansion, but the terms happen to be quickly decreasing with order n at any value of βj and βh. [101] This allows me to cut off the series making negligible errors in the ensuing computations. We also check that these expressions, in the zero-field, standard hard-disks limit ($h \to 0, j \to 0, u \to \infty$) do yield the usual hard disks coefficients (see App. B for more details). [133]

I then write the virial equation of state for the pressure as given by Eq. (III.13) using the first two virial coefficients and the effective field h_{eff} found from our self-consistent scheme. I finally locate the spinodal curves as the points where the derivative of P with respect to ρ vanishes, which correspond to local extrema of isobaric curves in the (ϕ, T) plane.

The main panel of Fig. III.13 displays the phase diagram obtained using this method, together with a few isobaric curves in the hardcore exclusion limit ($u \to \infty$) and for an interaction range ratio $f = (\sigma/\sigma_{\text{rep}})^{-1} = 1/2$. I recover a liquid-gas phase separation between a paramagnetic gas and a ferromagnetic liquid, ending at a tricritical point. I find that, like in the on-lattice and PY-RPA-CW description, the Curie line plays the role of the left-most spinodal, where isobaric curves develop a cusp: this feature is thus a robust property of this system. The coexistence curve is also found close to the critical point using a standard Maxwell construction. It starts off extremely close to the Curie line, as in the on-lattice approach, and has a similar shape as the one obtained in simulations. The supercritical part of the obtained diagram is also interesting, as isobaric curves feature an inversion of curvature. This feature is equivalent to the presence of a local maximum in the isobaric thermal dilatancy (or expansion coefficient),

$$\alpha_P = -\frac{1}{\rho}\left(\frac{\partial \rho}{\partial T}\right)_P.$$

Such maxima define the so-called Widom line, which separates gas-like and liquid-like regimes of the supercritical fluid. [208] While here this might very well be a high-density artifact of the low-order cut-off in the virial expansion, it is also observed in real polar liquids. [128, 208] More in-depth studies of spin fluids would be required to confirm this feature.

Finally, I study the role played by the magnetisation in this model by setting the effective field in the Von Mises angle distribution $\Upsilon(\theta; \beta h)$ to zero, so that $p(\theta) = 1/2\pi$. I

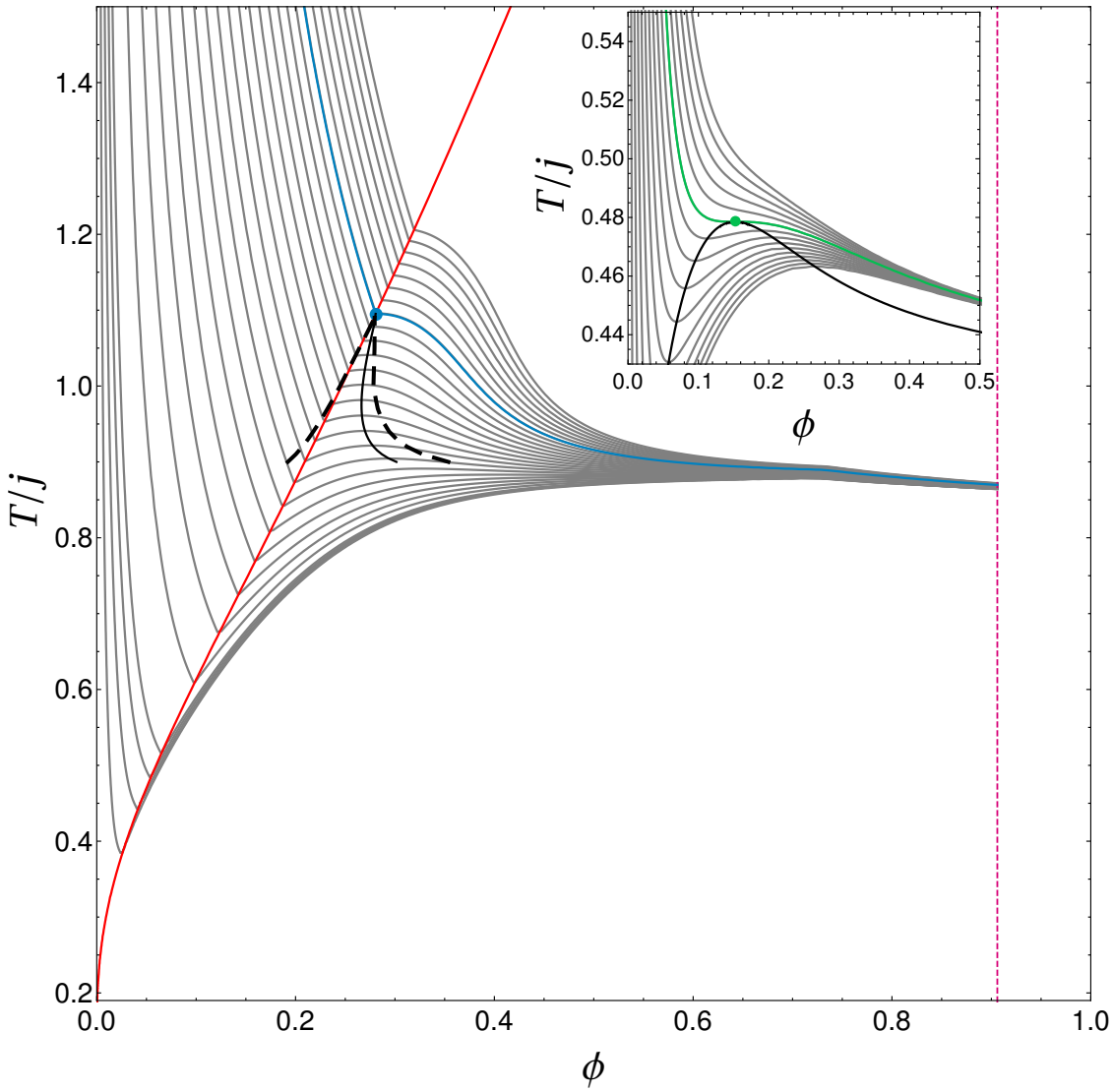

Fig. III.13 **Isobaric curves and magnetisation in the VE-CW description.** The isobaric curves (gray) and Curie line (red) were obtained with the VE-CW description of the spin fluid, in the $(\phi, T/j)$ plane, for $f = (\sigma/\sigma_{\rm rep})^{-1} = 1/2$. I find a tricritical point at $\phi_c \approx 0.28$, $T_c \approx 1.10j$, here plotted in blue along with the critical isobaric curve. The solid black line indicates the right-hand branch of the spinodal line, and the dashed black line is the coexistence curve found from a Maxwell construction. [1] In the inset, I plot the same quantities for a uniform distribution of spin angles (zero magnetisation). A critical point is still observed, at $\phi_c \approx .15$ and $T_c/j \approx .48$, plotted in green along with its critical isobaric curve. The solid black line is the spinodal line.

show the corresponding phase diagram in the inset of Fig. III.13. Interestingly, I observe a liquid-gas transition caused solely by the spin-mediated attraction, although this system does not get magnetised as I assumed a flat angle distribution. In this case, the isobaric curves feature smooth minima in the phase separation region, and do not change curvature in the supercritical fluid regime, indicating that both cusps on the isobars and local maxima of α_P are linked to the onset of the magnetisation.

c) Comparison between PY-RPA-CW and VE-CW

In order to understand the qualitative difference between the outcome of the PY-RPA-CW and VE-CW approaches and how they compare to simulations, it is interesting to compare the pair correlation functions $g(r)$ and the magnetisation they predict around the magnetisation transition. Figure III.14 displays the pair correlation functions at a packing fraction $\phi = 0.55$ around the Curie temperature in simulations of $N = 8192$ particles (panel (a)), in the VE-CW scheme (panel (b)) and in the PY-RPA-CW approach (panel (c)). The last two panels, are computed in the hardcore limit ($u \to \infty$) and for an interaction range ratio $f = 1/2$. Recall that in simulations, the interaction potentials are instead those defined in Eq. (III.4). The pair correlation functions obtained in the simulations show that the onset of magnetisation is accompanied by an increase of structure, with the appearance of a second and third peak. At the order I consider in this thesis, the VE-CW predicts unrealistically sharp features in the pair correlation function, and no structure beyond twice the magnetic interaction range. This is due to the very nature of the cut-off in the virial expansion: I neglected any event other than two- and three-body interactions, so that the sharpness of hardcore exclusions remains apparent in $g(r)$. Still, the VE-CW approach captures the structuration of the liquid at the onset of the magneti-

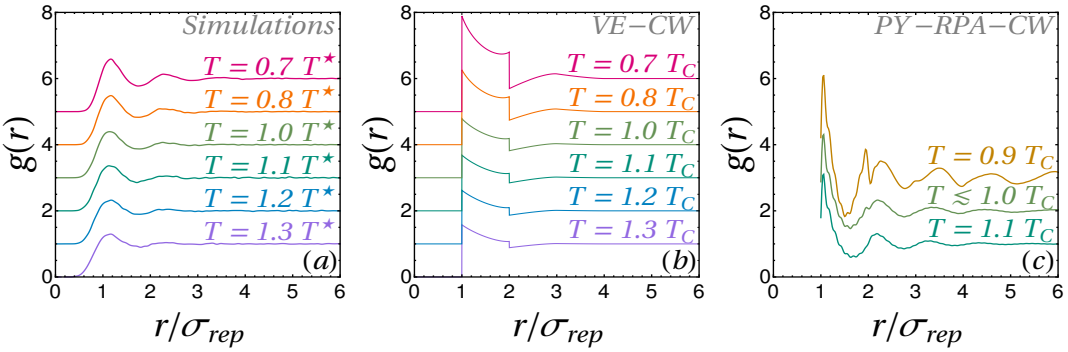

Fig. III.14 **Comparison of analytical and numerical radial distribution functions.** I show the Radial Distribution Functions measured at $\phi = 0.55$ (a) in equilibrated simulations with $N = 8192$ particles, (b) computed using the VE-CW approximation, and (c) computed using the PY-RPA-CW approximation. The curves in (b) and (c) are computed in the hardcore limit $u \to \infty$ and for $f = 1/2$. The simulation curves are measured around the finite-size crossover temperature $T^\star$ (see Sec. III.2.1). The theoretical curves are plotted around the Curie temperature T_C found in each approach. In all three subplots, curves are shifted by a constant for better comparison.

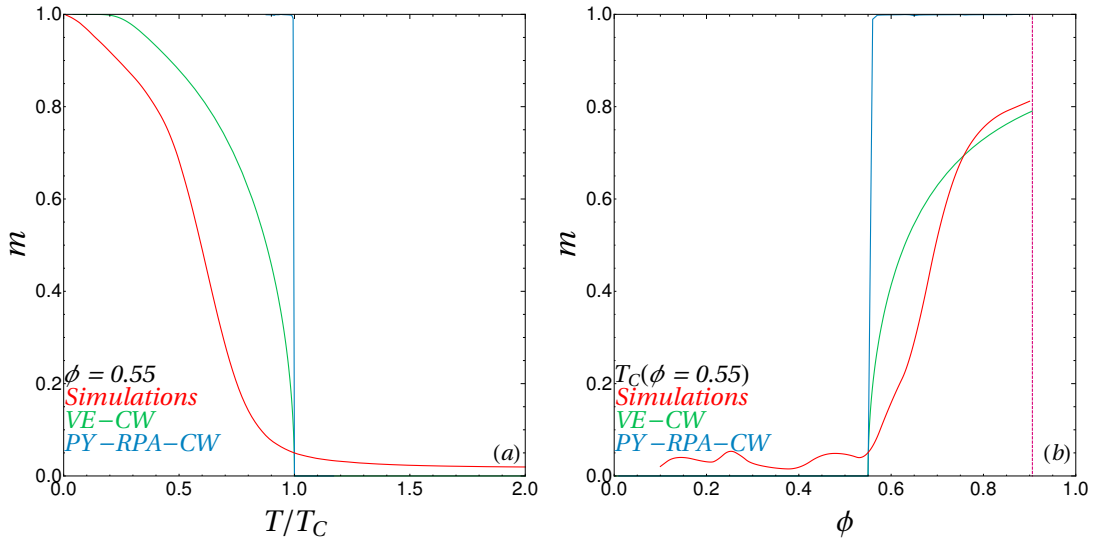

Fig. III.15 **Comparison of the numerical and analytical predictions for the magnetisation.** (a) Magnetisation versus temperature rescaled by $T_C(\phi = 0.55)$, the corresponding Curie temperature at $\phi = 0.55$. (b) Magnetisation against the packing fraction at $T_C(\phi = 0.55)$. In both panels, simulations of $N = 8192$ particles are shown in red, VE-CW calculations are shown in green, and PY-RPA-CW calculations are shown in blue. In both theoretical approaches, $u \to \infty$ and $f = 1/2$.

sation, despite the strength of the approximations. By construction, the PY-RPA-CW route very well describes the hardcore repulsion and avoids the sharp discontinuities in $g(r)$ reported above. However, long-ranged oscillations develop for temperatures as close as $0.9T_C$. This suggests that the effective attraction is very much overestimated.

This is further confirmed when looking at the magnetisation curves. Figure III.15 shows the magnetisations observed in simulations and predicted in both approaches against the temperature (panel (a)) and the packing fraction (panel (b)). In panel (a), I choose $\phi = 0.55$, and the temperature is normalized by the Curie temperature $T_C(\phi = 0.55)$ observed or predicted in each case. Although the two analytical approaches are mean-field and therefore display mean-field critical exponents (e.g. $\beta = 1/2$), they predict very different behaviours away from the transition. Indeed, the PY-RPA-CW approach predicts a very sharp increase to unit magnetisation, while the VE-CW approach features a smoother variation, that compares better with simulation data. In panel (b), the temperature is set to $T_C(\phi = 0.55)$. Again, the PY-RPA-CW approach predicts a sharp increase to unit magnetisation, while the VE-CW grows smoothly and qualitatively reproduces numerical results.

These curves can be used to understand qualitatively the shapes of the isobaric curves in both cases. In the PY-RPA-CW description, the sharp onset of the magnetisation induces a transition across the Curie line from a purely repulsive fluid to an attractive fluid whose attraction is essentially fixed. This explains the sudden change of slope at the Curie line, which connects the isobaric lines corresponding to these two fluids. In the VE-CW description, the effective attraction grows smoothly, and the slope of the isobaric

curves is governed by the rate of change of the magnetisation with both the temperature and packing fraction. In particular, close to the Curie line, the magnetisation increases sharply, and favours a rapid compaction with very little cooling.

d) Role of the Interaction Parameters using the VE-CW scheme

Magnetic Interaction Range – Using the virial approach, that proved to yield a good qualitative representation of the system in fluid phases, it is also easy to tune the shape of the interaction potentials. First, let us keep hard disks and change the interaction range ratio $0 < f < 1$. Regardless of this value, I always observe a liquid-gas phase separation and a Curie line that is also the left-most spinodal and the locus of cusps on the isobaric curves, as illustrated in the example of Fig. III.16(a) ($f = 0.9$).

Figure III.16(b) shows how the tricritical point moves in the (ϕ, T) plane as f is varied. As magnetic interactions are made increasingly short-ranged (f increases), the Curie line is sent to lower temperature, and the critical point follows. The reason is that as each particle gets fewer magnetic neighbours, magnetic order becomes harder to establish. The behaviour of the tricritical density is more intriguing. It essentially decreases as f increases, suggesting that in the $f \to 1$ limit, the coexistence region shrinks towards the origin of the (ϕ, T) plane. Also, a local minimum of the tricritical density sits close to $f = 1/2$. As shown in the inset, it is also present in the absence of magnetisation, as

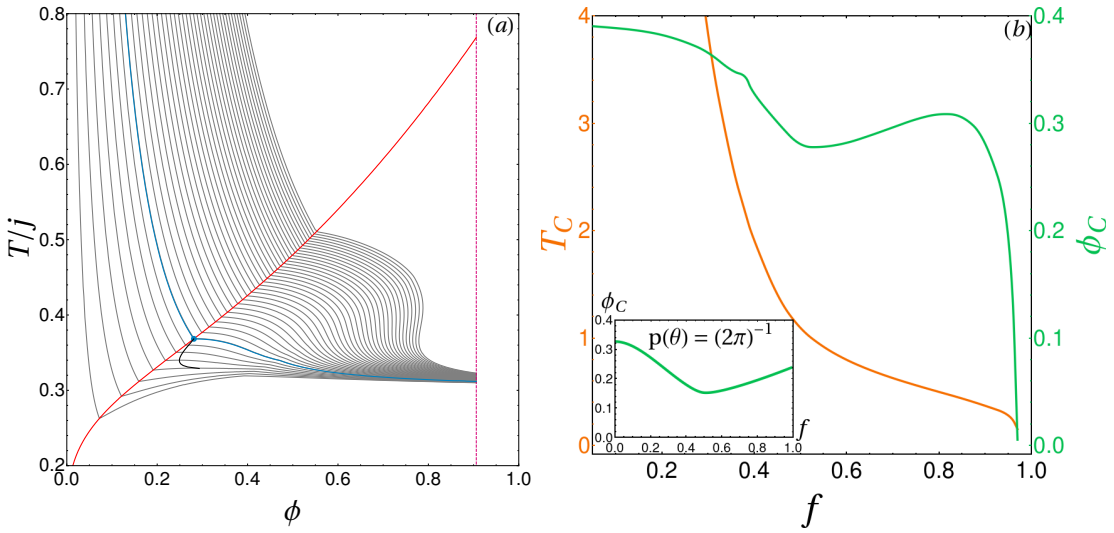

Fig. III.16 **Effects of the interaction range.** (a) Phase diagram in the (ϕ, T) plane found in the VE-CW approach diagram for hard disks and $f = 0.9$. I plot the Curie line (red), the right-most spinodal line (black), some isobaric lines (gray) and I highlight the critical isobaric line as well as the tricritical point (blue). I also spot the close-packing density (magenta). (b) Displacement of the tricritical temperature (orange) and packing fraction (green) in the VE-CW description when varying f for hardcore exclusion. In the inset, I plot the critical packing fraction found from the virial approach with a flat distribution of spins (no magnetisation).

obtained for a uniform distribution of spins ($p(\theta) = 1/2\pi$). It is seemingly related to the fact that for $f = 1/2$, one cell of the regular hexagonal packing of the hard disks perfectly matches the attraction range.

Coming back to Fig. III.16(a), it is interesting to note that for high values of f such as $f = 0.9$, the isobaric curves present an s-shaped feature at high density. Notwithstanding that this feature can be an artifact of the low order cut-off of the virial expansion, if real, it would correspond to a region with a negative expansion coefficient. Interestingly, this kind of behaviour has also been reported in realistic polar liquids. Water, for instance, displays a similar anomaly of its expansion coefficient associated to a liquid-liquid transition caused by the ordering of molecules due to H bonds. [209] Models of single-component systems with isotropic interactions have successfully reproduced such anomalies using specifically devised attractive potentials. [210] My observation that spin fluids present similar features suggests that they could be useful alternative models in which an effective attraction with the appropriate shape sets in spontaneously. Following another line of thought, it could be interesting to make the connection with the gelation of hard disks with very short attractive interactions, where unusual thermodynamic features are associated to the formation of long ramified chains, [211] and unusual glassy behaviour has been reported for polar "patchy" colloids. [212] Indeed, the here reported anomalous behaviour takes place close to the sticky disk limit. [213]

Softness of the Repulsion – Finally, I briefly discuss the role of having a soft square-potential repulsion (finite u) instead of a hardcore exclusion. The corresponding shapes of the effective potential $V(r, \theta) = U(r) - J(r)\cos\theta$ are plotted in Fig. III.17(a), and compared to the potentials used in simulations. To set the comparison, the amplitude of the square repulsion potential u corresponding to the simulations potential $U(r)$ is taken to be:

$$u_{\text{sim}} \equiv \frac{2}{\sigma}\int_0^{\sigma/2} dr\, U(r) = \frac{31}{20}.$$

When varying j/u, the softness parameter, with $j \neq 0$ and $u \neq 0$, I still observe the same features on the phase diagram, but with a shifted tricritical point. Figure III.17(b), displays the evolution of the coordinates of the tricritical point against j/u. Starting from the hard disk limit ($j/u = 0$), when the particles become softer, the tricritical point goes up in temperature and in packing fraction. Being softer allows for more neighbours and therefore makes both magnetisation and compaction easier, hence the shift to higher temperatures. The shift to higher packing fractions, follows from the fact that the tricritical point has to remain on the Curie line. For values corresponding to my simulations ($j/u_{\text{sim}} = 5/93$), the repulsion is hard enough that the displacement is barely noticeable.

III.4 Summary

In this chapter, I discussed several equilibrium and non-equilibrium properties of XY spin fluids in $2d$, with a variety of theoretical approaches and simulations.

I numerically showed that these systems do not follow the Berezinskii-Kosterlitz-Thouless scenario of vortex unbinding in homogeneous phases. The zero-temperature

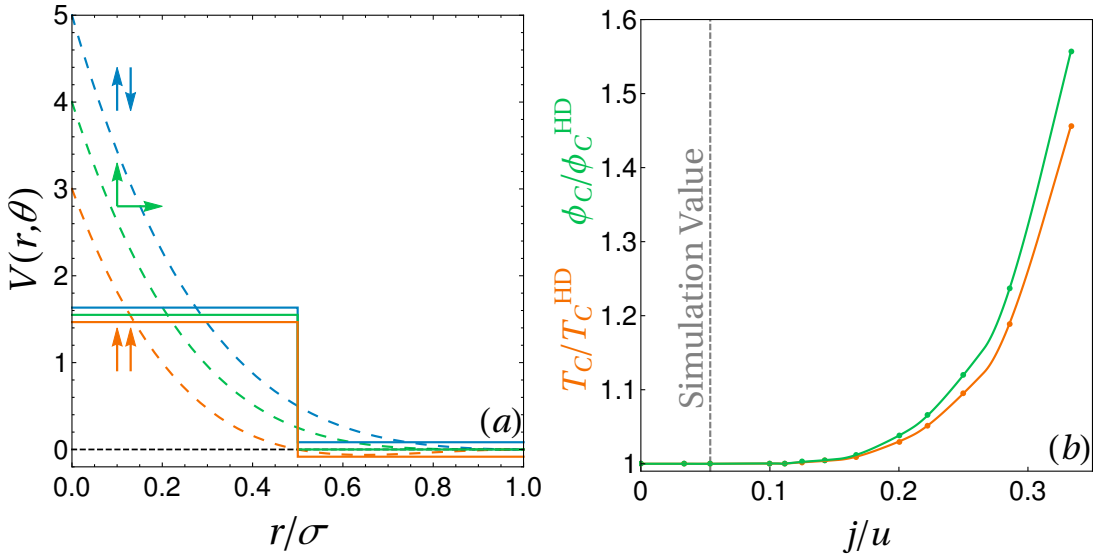

Fig. III.17 **Effects of the repulsion amplitude.** (a) Typical aspect of the square-shaped interaction potential used in the soft VE-CW approach (full lines), compared to the potentials used in simulations (dashed lines). The $V = 0$ line, corresponding to the separation between attractive and repulsive parts, is highlighted by a dashed black line. (b) Effect of j/u on the coordinates of the tricritical point for $f = 1/2$. I plot the critical temperature (orange) and packing fraction (green), normalized by the hard-disk value found at the same f.

ferromagnetic order is instead destroyed solely by low-energy spin-wave excitations. Accordingly the magnetic correlation length diverges exponentially at $T = 0$. Hence, finite-size systems are in practice also smaller than the correlation length and appear to behave in a mean-field-like fashion. It would be interesting to see if this feature breaks down in high-density solid phases, in which the quasi-long-range positional order of the particles constrains them to be near the vertices of a lattice, and the magnetic behaviour should resemble the one of the conventional $2d$ XY model. In the same line of thought, it would be interesting to see whether BKT phenomenology would be recovered by tuning the interaction potentials we used here, for instance by making $J(r)$ deeper, thereby favouring crystalline phases. As a last note on the presence or absence of BKT physics, a more recent work [214] found that the BKT scenario might be present in a variant of our spin fluid, where the spin-spin interaction was chosen such that spins are always repulsive, regardless of their relative alignments. Their result relied on the detection of vortex-antivortex pairs in a system at a lower density, using the fact that without the spin-mediated attraction, there can be no phase separation such as the one described in Sec. III.2.2. It would be interesting to understand whether the obscuration of BKT physics that I described is due to the difference in the studied density, or in the chosen potentials.

I also showed the presence of a phase separation between a paramagnetic gas and a ferromagnetic liquid at low temperatures due to the effective spin-mediated attraction between the particles. This last finding, which is quite similar to previous results in $3d$ for Heisenberg and planar spins, is recovered with various analytical mean-field approxi-

mations, and is found to be robust against the shape of interaction potentials.

The out-of-equilibrium relaxation after a quench into the phase-separated region indicates that, even though the correlation lengths associated to magnetic and liquid properties grow in standard way, the order parameter associated to the liquid-vapour phase separation grows with an unusual exponent. The liquid droplet growth thus escapes the locally non-conserved order parameter dynamic universality class exemplified by Model B, and is instead synchronised with the growth of the magnetisation. This synchronisation suggests that the Curie line plays a special role in the phase-separating regime, the one of the left-most branch of the spinodal curve, as also shown with analytical mean-field-level calculations. Physically, the coincidence of the Curie line and gas-side spinodal means that the development of magnetisation destabilises the gas and stabilises the liquid. This could have interesting implications on the precise clustering dynamics going beyond my study of domain growth, including in the long time regime and after quenches of varying speed that could lead to nucleation-dominated dynamics. [215]

The study of spin fluids of the kind I used in this chapter could be relevant in a variety of fields beyond collective motion, ranging from the study of ferromagnetic gases [180] and liquids [181] to more general occurrences of polar fluids in physics. Those occurrences include usual liquids, in which polarity seem to be responsible for still not-well-understood properties, as in the case of water [209]. Finally, polarity and polarity-mediated interactions are ubiquitous ingredients of systems of self-propelled particles (see Sec. I.1). For instance, a phenomenon similar to a FIPS has recently been reported in a model of swarming, in which polarity was introduced in the guise of synchronisation [216]. A better understanding of the properties induced by polarity in equilibrium can therefore shed light on the unusual properties of polar active systems.

Chapter IV

Static Properties of a Spin-Velocity Coupled Spin Fluid

> Spinoza says that if a stone which has been projected through the air, had consciousness, it would believe that it was moving of its own free will. I add this only, that the stone would be right.
>
> Arthur Schopenhauer, *The World as Will and Representation*

IV.1 Outline

Having studied the reference case of an XY spin fluid in a $2d$ space in Chapter III, I now turn my attention back to the full model of Bore *et al.* [69]. As discussed in Chapter I.2.2, it describes the dynamics of N particles that carry continuous planar spins of norm equal to 1. The particles are confined to move in $2d$, in a periodic square box of linear size L. Their motion is described by the Lagrangian

$$\mathcal{L} = \sum_{i=1}^{N} \frac{1}{2}\dot{\boldsymbol{r}}_i^2 + \sum_{i=1}^{N} \frac{1}{2}\dot{\boldsymbol{s}}_i^2 + \sum_{i=1}^{N} K\dot{\boldsymbol{r}}_i \cdot \boldsymbol{s}_i - \frac{1}{2}\sum_{k\neq i} U(r_{ik}) + \frac{1}{2}\sum_{k\neq i} J(r_{ik})\cos\theta_{ik} \ .$$

In the following, I will consider the same couplings U and J as in Sec. III.1,

$$J(r) = (\sigma - r)^2\Theta(\sigma - r) \ ,$$
$$U(r) = U_0(\sigma - r)^4\Theta(\sigma - r) \ ,$$

where Θ is a Heaviside step function, σ is the range of the interactions (fixed to 1), and $U_0 = 4$, so as to make the comparison with Chapter III and Ref. [69] easier. Furthermore, I will only consider the case $K \geq 0$ as the case $K \leq 0$ can be recovered by simply flipping

all the spins. In the Hamiltonian formalism the Lagrangian (I.2) transforms into the Hamiltonian

$$\mathcal{H} = \sum_{i=1}^{N} \frac{1}{2}\boldsymbol{p}_i^2 + \sum_{i=1}^{N} \frac{1}{2}\omega_i^2 - \sum_{i=1}^{N} K\boldsymbol{p}_i \cdot \boldsymbol{s}_i + \frac{1}{2}\sum_{k\neq i} U(r_{ik}) - \frac{1}{2}\sum_{k\neq i} J(r_{ik})\cos\theta_{ik} \ , \quad \text{(IV.1)}$$

with the canonical momenta $\omega_i = \dot{\theta}_i$ and $\boldsymbol{p}_i = \dot{\boldsymbol{r}} + K\boldsymbol{s}_i$. As already stressed in Sec. II.2, since the model described by this Hamiltonian is not invariant under a Galilean transformation, the statistical mechanics description of this model requires that one sets not just one, but two control parameters. In the microcanonical ensemble, these parameters are the energy E and the total momentum $\boldsymbol{P}$. In this thesis, I restrict myself to the case $\boldsymbol{P} = \boldsymbol{0}$, so that the velocity of the centre of mass $\boldsymbol{v}_G$ and the intensive magnetisation $\boldsymbol{m}$, defined through

$$\boldsymbol{m} = \frac{1}{N}\sum_{i=1}^{N} \boldsymbol{s}_i \ , \qquad \text{and} \qquad \boldsymbol{v}_G = \frac{1}{N}\sum_{i=1}^{N} \dot{\boldsymbol{r}}_i \ ,$$

satisfy $\boldsymbol{v}_G + K\boldsymbol{m} = 0$. This choice ensures that the high-energy states, in which spins are completely disordered, are also still, so that collective motion can only emerge at low energies or temperatures.[1]. However, it also leads to a frustration when minimising the energy: the ferromagnetic coupling leads to spin alignment but, as the magnetization grows, so must the velocity of the center of mass, which comes at a high cost in kinetic energy. In practice, as the velocity of a magnetised state grows linearly with K, one expects this cost to increase as K grows.

Bore *et al.* [69] showed that there exist moving magnetised states at very low temperatures, that satisfy $\boldsymbol{P} = \boldsymbol{0}$, and consequently anti-align the particle velocities with their spins. At higher values of K, non-magnetised states featuring topological defects such as vortices and antivortices were suggested as candidate ground states [69]. In light of the results of Chapter III, it seems that the presence of these defects is entirely due to the addition of a spin-velocity coupling, since vortices are not thermodynamically stable for $K = 0$. However, quite a few questions were left unanswered: if they are not generated by a BKT-like transition, what is the origin of these defects? Can their nature and number be tuned by changing K or N appropriately? Do they proliferate, or die out as the temperature is increased? In polar states, how well do the velocities order? Furthermore, Bore *et al.* only considered states with a homogeneous density. Since, in the $K = 0$ case, a FIPS is observed at low enough densities and temperatures, even more questions arise: is this phase separation preserved with the addition of K? And if so, can one observe polar, moving droplets? And what replaces topological defects at low densities?

In this Chapter, that reproduces the results published in Ref. [76], using molecular dynamics simulations and analytic calculations, I characterize the $2d$ behaviour of this model when varying the size, dimensionality, temperature, density, and spin-velocity coupling intensity. I report a finite-size magnetisation crossover that is accompanied by a collective ordering of the velocities at low enough temperatures and low enough values

[1] It is however by no mean the only interesting regime of this system: for $\boldsymbol{P} \neq \boldsymbol{0}$, corresponding to cases in which even the hot gas phase is moving, the system might look more like true non-equilibrium systems that feature collective motion.

of the spin-velocity coupling constant K. This ordering breaks down at a finite value of K, that depends on the size of the system, as accurately predicted using simple energetic arguments. As suggested in Ref. [69], the resulting non-magnetised ground states feature topological defects that, by suppressing the magnetisation, enable the system to avoid a high kinetic energy cost. The crossover between magnetised and non-magnetised states resembles a first-order phase transition, as both families of states are metastable close to the critical value of the spin-velocity coupling. When heated up, systems prepared in a non-magnetised ground state display a maximum of the modulus of their magnetisation at a finite temperature. This feature is reminiscent of an "Order by Disorder" [217, 218] (ObD) transition, in which a system develops a spontaneous magnetisation upon heating, and can be explained by the examination of the free energies of the metastable states of the system.[2] When exploring lower values of the density, a phase separation domain between a paramagnetic gas and a ferromagnetic moving liquid is also observed at low enough values of K. However, as K is tuned up, non-moving states progressively invade the ferromagnetic domain, leading to a large zoology of still, phase-separated states as well. Finally, the magnetised states are characterized by a collective ordering of the instantaneous velocities, which is however rapidly destroyed by thermal fluctuations. The above results are rather general. On one hand the choice of the spin-velocity coupling is highly constrained by the structure of the Hamiltonian dynamics. On the other hand neither the geometry nor the dimensionality seem to play a major role in these observations.

The rest of the Chapter is organized as follows. First, in Sec. IV.2, I describe in details the simulation strategy used in this chapter. In Sec. IV.3 I characterise the low-temperature equilibrium states and predict their location in parameter space with simple energetic arguments, as well as their nature, resorting to a coarse-grained continuous theory. In Sec. IV.4 I consider the finite temperature regimes and describe an order-by-disorder phenomenon for a subset of values of the parameters. The crossover towards order is studied, and proved to behave much like a first-order phase transition. In Sec. IV.5 I discuss the alignment of velocities in collectively moving phases. Then, in Sec. IV.6, I discuss the generality of these results against changes in various parameters. First, I show that the Ferromagnetism-Induced Phase Separation (FIPS) that I described in Chapter III in the $K = 0$ case is recovered, leading to both moving droplets and many variants of non-moving states. Then I discuss the roles of the geometry, the dimensionality, and the nature of the spin-velocity coupling. Finally, I summarize and comment the results of this section in Sec IV.7.

IV.2 Simulation strategy

As described in Sec. II.2.3, the numerical analysis of the present model is carried out using "microcanonical" Molecular Dynamics (MD) simulations of the dynamics defined by the Hamiltonian in Eq. (IV.1), which conserves energy and momentum, and I restrict myself to initial conditions such that $\boldsymbol{P} = \boldsymbol{0}$. This is the same method as in Chapter III, so that the results for $K > 0$ can easily be compared to the results for $K = 0$. In this chapter, I use random initial states with uniformly distributed $\{\boldsymbol{r}_i, \theta_i\}_{i=1,\dots,N}$ and $\{\boldsymbol{p}_i, \omega_i\}_{i=1,\dots,N}$ drawn from centered reduced Gaussian distributions. Such configurations are placed in a square

[2] Equivalently, ObD can be seen as a re-entrance of the ordered phase between two disordered regions.

box with periodic boundary conditions and, after giving some time for the dynamics to settle in, they are subjected to a numerical annealing, the precise implementation of which is described in Sec. II.2.3. In most of the chapter, like in Sec. III.2.1, I focus on the physics of homogeneous phases, and therefore set the density to $\rho = N/L^2 \approx 2.81$ (or, equivalently, $\phi \approx 0.55$ in terms of the packing fraction defined as $\phi = \rho\pi\sigma^2/16$). Whenever curves represent observable mean values, it mean that I averaged the results over $10^2 - 10^3$ independent configurations obtained by sampling initial conditions and recording states at times that are far enough from each other that the corresponding configurations can be considered to be independent.

IV.3 Finite-Size Ground States

IV.3.1 The parameter space

In order to fully understand the conditions for the observation of moving states or topological defects, I start by focusing on equilibrium states in the lowest attainable energy configuration, which I interpret as states at very low temperatures and therefore call "ground states". As shown in Fig. IV.1, I find three kinds of ground states depending on the values of K and N:

(i) *Polar states:* These are fully magnetised states with $m = 1$, with collective motion taking place in the direction opposite to the magnetisation as imposed by the momentum conservation, $\boldsymbol{v_G} = -K\boldsymbol{m}$.

(ii) *Solitonic states:* These are non-moving states with $m \approx 0$, characterized by a continuous rotation of spins in one direction.

(iii) *Vortex states:* These are non-moving states with $m \approx 0$, characterized by 4 topological point defects, 2 vortices and 2 anti-vortices.

Importantly enough, neither local nor global ordering of velocities is observed in the solitonic and vortex states. The reason for this is the high kinetic energy cost of the magnetised states, which increases with K and N like NK^2. As these parameters are increased starting from a polar state, the system produces topological defects as a way of setting the global magnetisation to zero and therefore escape the collective motion imposed by momentum conservation. The strong frustration induced by the high kinetic energy cost associated to magnetised states with a finite velocity of the centre of mass has thus the effect of *generating* topological defects in the equilibrium ground states. Note that these defects are not thermal excitations and should not be confused with the vortices observed at the BKT transition in lattice models of XY spins [72, 183], that I describe in Sec. II.3. In fact, as discussed at length in Sec. III.2.1, no BKT transition occurs in the $K = 0$ limit of the model (IV.1).

IV.3.2 Continuum theory

The nature of the observed ground states, can be further confirmed by considering the solutions of a coarse-grained continuum theory for the magnetic properties of the model.

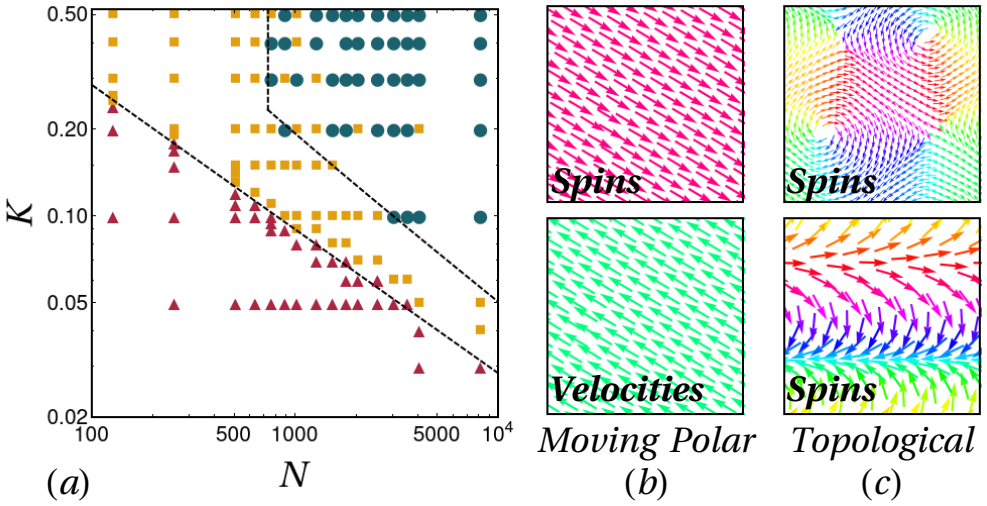

Fig. IV.1 **Zero-temperature homogeneous states.** (a) Nature of the ground states found numerically in the K-N plane: polar states (red triangles), solitonic state (yellow squares), vortex states (blue disks). Only the polar state is a collectively moving state. The nature of each point was determined using a majority rule over 1 to 10 different realisations of the annealing procedure, which was left running down to temperatures of the order of 10^{-3}. The crossover lines correspond to Eqs. (IV.6), (IV.7) and (IV.9).(b) Snapshots of a polar state obtained for $N = 128$, and $K = 0.2$, showing both the spins (top) and the corresponding velocities (bottom). The unit length for spin arrows is $K = 0.2$ times the one used for the velocities.(c) Snapshot of a vortex state (top), obtained for $N = 768$, and $K = 0.4$, and of a solitonic state (bottom), obtained for $N = 128$, and $K = 0.5$.

I define $\mathcal{L}_{kin}$, $\mathcal{L}_{sv}$ and $\mathcal{L}_{int}$, the kinetic, spin-velocity and interaction contributions to the Lagrangian. They read

$$\mathcal{L}_{kin} = \sum_{i=1}^{N} \left(\frac{1}{2} v_i^2 + \frac{1}{2} \omega_i^2 \right) ,$$
$$\mathcal{L}_{sv} = K \sum_{i=1}^{N} \boldsymbol{v}_i \cdot \boldsymbol{s}_i ,$$
$$\mathcal{L}_{int} = -\frac{1}{2} \sum_{k \neq i} U(r_{ik}) + \frac{1}{2} \sum_{k \neq i} J(r_{ik}) \boldsymbol{s_i} \cdot \boldsymbol{s_k} ,$$

respectively, with $\boldsymbol{v}_i = \dot{\boldsymbol{r}}_i$ and $\omega_i = \dot{\theta}_i$. The symbol $\sum_{k \neq i}$ indicates a double sum over i and k from 1 to N with no repeated indices included. Focusing first on the interaction term $\mathcal{L}_{int}$, I assume that the spins are locally well aligned, so that $\boldsymbol{s}_i \cdot \boldsymbol{s}_k \approx 1 - \theta_{ik}^2/2$, where $\theta_{ik} = \theta_i - \theta_k$, in the neighbourhood defined by the range of $J(r)$. Therefore,

$$\mathcal{L}_{int} \approx -\frac{1}{2} \sum_{k \neq i} U(r_{ik}) + \frac{1}{2} \sum_{k \neq i} J(r_{ik}) - \frac{1}{4} \sum_{k \neq i} J(r_{ik}) \theta_{ik}^2 ,$$

The main effect of the first two terms is to ensure the uniformity of the density profile $\rho(\mathbf{r}) \approx \rho_0$. Accordingly, I will discard them in the following and concentrate on the last term, that I henceforth call $\mathcal{V}$, and want to approximate using a continuum description. To do so, I assume that there exists a discrete mesh of allowed positions for the particles [219], with arbitrarily small spacing, so that I may define coarse-grained fields on this mesh as:

$$\mathcal{V} \equiv \sum_{k\neq i} J(r_{ik})\theta_{ik}^2 = \sum_{\boldsymbol{r}}\sum_{\boldsymbol{r'}}\sum_{k\neq i} J(\boldsymbol{r},\boldsymbol{r'})(\theta(\boldsymbol{r'})-\theta(\boldsymbol{r}))^2\delta(\boldsymbol{r}-\boldsymbol{r_i})\delta(\boldsymbol{r'}-\boldsymbol{r_k}) \ .$$

with δ being Kronecker symbols. First, rewriting the sum over $\boldsymbol{r'}$ after the transformation $\boldsymbol{r'} \to \boldsymbol{r}+\boldsymbol{d}$, and using the rotational and translation invariances of J; second expanding the difference of θ to the first order, I obtain

$$\mathcal{V} \approx \sum_{\boldsymbol{r}}\sum_{\boldsymbol{r}+\boldsymbol{d}}\sum_{k\neq i} J(d)\left(\boldsymbol{\nabla}\theta(\boldsymbol{r})\cdot\boldsymbol{d}\right)^2\delta(\boldsymbol{r}-\boldsymbol{r_i})\delta(\boldsymbol{r}+\boldsymbol{d}-\boldsymbol{r_k}) \ .$$

I now take the continuum limit by taking the mesh size to zero and find that in the absence of singular values of $\boldsymbol{\nabla}\theta$:

$$\mathcal{V} \xrightarrow{a\to 0} \int d^2\boldsymbol{r}\,\rho(\boldsymbol{r})\int d^2\boldsymbol{x}\,\rho(\boldsymbol{r}+\boldsymbol{x})J(x)(\boldsymbol{\nabla}\theta(\boldsymbol{r})\cdot\boldsymbol{x})^2 \ .$$

For $J(r) = J_0\Theta(\lambda - r)$, with Θ a step function and λ the range of the ferromagnetic interaction, and recalling that $\rho(\mathbf{r}) \approx \rho_0$, I finally obtain, after integration of the second integral:

$$\mathcal{V} \approx \int d^2\boldsymbol{r}\,\rho_0^2\pi J_0\frac{\lambda^4}{4}(\boldsymbol{\nabla}\theta(\boldsymbol{r}))^2 \ .$$

The two other contributions to the Lagrangian, namely, $\mathcal{L}_{kin}$ and $\mathcal{L}_{sv}$ are local, so that the same procedure as above can be trivially applied. Finally, I can write a continuum Lagrangian theory of the form

$$\mathcal{L}_c = \int d^2\boldsymbol{r}\ \rho_0\left[\frac{1}{2}\dot{\theta}^2(\boldsymbol{r}) - \frac{c^2}{2}(\boldsymbol{\nabla}\theta(\boldsymbol{r}))^2 + \frac{1}{2}v^2(\boldsymbol{r}) + K\boldsymbol{v}\cdot\hat{\boldsymbol{e}}(\theta(\boldsymbol{r}))\right] ,$$

where $c^2 \equiv J_0N_\lambda\lambda^2/16$ with $N_\lambda \equiv \rho_0\pi\lambda^2$ the number of particles in one interaction volume, and $\hat{\boldsymbol{e}}(\theta(\boldsymbol{r}))$ is a unit vector pointing in the direction given by θ. This form of the Lagrangian clearly shows that $K\boldsymbol{v}$ plays the role of a field, and creates a non-perturbative term even in the low-temperature expansion which otherwise gives a free theory for the XY model at low temperatures [72].

I can now write the Euler-Lagrange equations for θ and $\boldsymbol{v}$ to describe the low-energy regime of this theory,

$$\begin{aligned} \boldsymbol{v} &= -K\hat{\boldsymbol{e}}(\theta(\boldsymbol{r})) \ , \\ \left(\frac{\partial^2}{\partial t^2} - c^2\triangle\right)\theta &= K\boldsymbol{v}\cdot\hat{\boldsymbol{e}}\left(\theta(\boldsymbol{r})+\frac{\pi}{2}\right) \ , \end{aligned} \tag{IV.2}$$

where the additional $\pi/2$ comes from the derivative of $\hat{\boldsymbol{e}}(\theta(\boldsymbol{r}))$ with respect to θ. Interestingly, at this level of description, Eq. (IV.2) selects solutions such that the local momentum is zero. When injecting this zero-momentum condition into the equation on

θ, I simply recover a wave equation on θ: this is the usual spin-wave regime [72] at low temperatures, that describes magnetised low-temperature states in finite size (see Sec. II.3). To describe states that are close in energy to a finite-size polar moving state, I set $\theta(\boldsymbol{r}) = \theta_0 + \delta\theta(\boldsymbol{r})$, and $\boldsymbol{v} = -K\hat{\boldsymbol{e}}(\theta_0) + \boldsymbol{\delta v}(\boldsymbol{r})$ corresponding to a small perturbation around a polar state aligned along θ_0, say $\theta_0 = 0$. The Lagrangian evaluated for such states reads,

$$\mathcal{L}_c = \int d^2\boldsymbol{r}\ \rho_0 \left[\frac{1}{2}\dot{\delta\theta}^2(\boldsymbol{r}) - \frac{c^2}{2}(\boldsymbol{\nabla}\delta\theta(\boldsymbol{r}))^2 + \frac{1}{2}v^2(\boldsymbol{r}) - K^2\cos\delta\theta(\boldsymbol{r}) + K\boldsymbol{\delta v}(\boldsymbol{r})\cdot\hat{\boldsymbol{e}}(\delta\theta(\boldsymbol{r}))\right],$$

and contains a field term $K^2\cos\delta\theta$ that is independent of the amplitude of the velocity perturbation. In particular, it yields a term of order one, contrary to the other terms in the Lagrangian that are vanishingly small for $\delta v \sim \delta\theta \ll 1$. Therefore, close to low-temperature polar ground states, the effective theory describing spin alignment is essentially a sine-Gordon theory with a field of amplitude K^2.

The sine-Gordon theory is known to feature solitonic solutions and vortex patterns, as reported in previous numerical works[220, 221]. I shall here briefly discuss both families of states. Solitons are propagative solutions of the sine-Gordon theory whose functional form can be shown to be [220]

$$\vartheta(\xi) = 4\chi\arctan\exp\left(\gamma\sqrt{h_{sG}}(\xi - \xi_0)\right) - \chi\pi,$$

where ϑ is the orientation of the local magnetisation field, $\xi = x - ct$ is the usual variable of propagative solutions, with a propagation velocity c, ξ_0 is an offset for this variable that sets the position of the centre of the soliton, $\chi = \pm 1$ is the so-called polarity of the soliton, $\gamma = 1/\sqrt{1-c^2}$ is a Lorentz factor associated to the propagation velocity, and h_{sG} is the in-plane magnetic field of the sine-Gordon theory. This function represents a localized rotation of 2π of the magnetisation field along the x direction. Noticing that in simulations I only ever see one such rotation over the size of the whole box, I plot in Fig. IV.2(a) the magnetic field with a constant amplitude and an orientation defined by the following function of position $\boldsymbol{r} = (x, y)$,

$$\vartheta_\Lambda(x,y) = \tag{IV.3}$$
$$\pi - 4\arctan\exp\left(x - x_0\right) - 4\arctan\exp\left[x - (x_0 - 2\Lambda)\right] - 4\arctan\exp\left[x - (x_0 + 2\Lambda)\right],$$

where 2Λ is the range of the box in which I plot the field, that is centered on $(0,0)$. This field is a perfect reproduction of the arched states that I observe at low temperatures in the numerical simulations, as shown in Fig. IV.2(b), thus justifying the name "solitons" that I give them. As there is neither damping nor forcing in the present model, the soliton propagation velocity is a priori free to select any value [222]. In practice, this velocity is found to be very low in simulations, but non-zero.

The sine-Gordon equation also features vortex solutions, but their exact functional shape is in general hard to derive. It is customary to consider vortex structures that are solutions of the Laplace equation, and to assume that they are little deformed by the addition of the non-linear term in the sine-Gordon equation [223, 224]. One-defect solutions can then be written as

$$\vartheta_\pm(x,y) = \pm\arctan\left(\frac{y-y_0}{x-x_0}\right) + \frac{R}{2}\log\left[(y-y_0)^2 + (x-x_0)^2\right], \tag{IV.4}$$

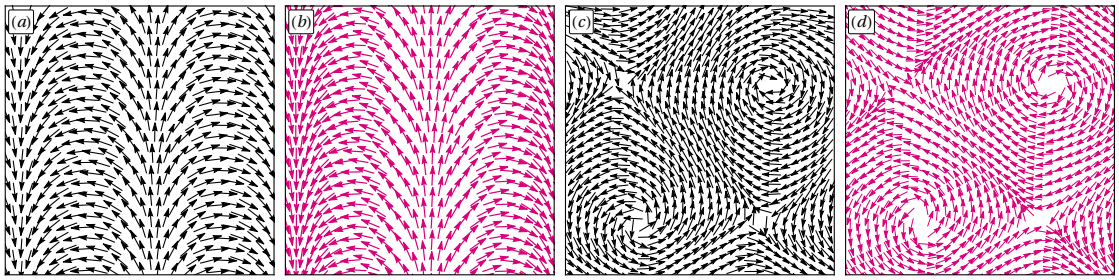

Fig. IV.2 **sine-Gordon solitons and vortices.** (a) sine-Gordon soliton found in the continuum theory, Eq. (IV.3), with $\Lambda = 1$, $x_0 = 0.5$, plotted in $[-1;1]^2$. (b) Ground state for $N = 512, K = 0.3$ found in numerical simulations. (c) Laplace vortex-antivortex state in the continuum theory, Eq. (IV.4), with $R = 0.295$, repeated over periodic boundary conditions and centered on the same points as in panel (d). (d) Ground state for $N = 768, K = 0.4$ found in numerical simulations.

where (x_0, y_0) are the coordinates of the centre of the defect, R is a parameter that tunes the twist of the spiral surrounding the defect, and the sign in front of the arctan determines whether the defect is a vortex $(+)$ or an antivortex $(-)$. An example of a 4-vortex configuration obtained with this functional form is shown in Fig. IV.2(c), and compared to a 4-vortex numerical ground state shown in Fig. IV.2(d). In this example, I chose the positions of the centers of the defects as well as the value of R to best fit the numerical observations.

Altogether the low energy magnetic excitations of the continuous theory perfectly match the very low temperature magnetic states obtained numerically, confirming the intuition of the mechanism whereby the system escapes the kinetic energy cost of the moving polar state, when K or N are too large. Note, however, that this description fails to capture the velocity configuration. Indeed, in the continuum theory, I assume that velocities are essentially all aligned, whereas in simulations soliton and vortex patterns do not display any velocity alignment, as I further discuss in Sec. IV.5.

IV.3.3 Energetic arguments

One can further estimate the energy of these states and thereby obtain the range of parameters in which each state is observed. The total kinetic and magnetic energy per particle in a moving polar state is

$$E_{pol} = \frac{1}{2}K^2 - \frac{1}{2}z\bar{J} + E_U$$

where the velocity is everywhere assumed to be $-K\boldsymbol{m}$, z is the number of neighbours of each particle, and $\overline{J}$ is the mean value of the ferromagnetic coupling for the inter-particle distances $\bar{r}$ in the considered configuration. The energy contribution due to the repulsive interaction E_U is likely to be very similar in the three different states of interest and therefore does not need to be evaluated.

The energy of a zero-temperature solitonic state can be approximated as follows. I consider that the rotation is smooth, so that two neighbours along the direction of the

rotation (on average half the neighbours) are misaligned by an angle $2\pi\bar{r}/L$, while spins are perfectly aligned along the other direction. Then, since all the velocities in a soliton at $T = 0$ are exactly zero, the total energy of a solitonic state can be approximated by

$$E_{sol} \approx -\frac{z\bar{J}}{2}\left[\frac{1}{2}\cos\left(\frac{2\pi\bar{r}}{L}\right)+\frac{1}{2}\right]+E_U\ . \tag{IV.5}$$

In both cases, I set the number of magnetic neighbours to 6 (in agreement with the numerical observations at the density used in the simulations), and compute the typical value of the ferromagnetic coupling by taking $\bar{J} = J(\bar{r})$. For a triangular lattice one has that $\bar{r} = \sigma/2\sqrt{\phi}$.

Equating now the two energies E_{pol} and E_{sol} yields an equation for the line separating polar and soliton ground states,

$$K_c^{pol-sol} = \sqrt{\frac{z\bar{J}}{2}\left(1-\cos\frac{2\pi\bar{r}}{L_c}\right)} = \sqrt{\frac{z\bar{J}}{2}\left(1-\cos\left[2\pi\bar{r}\sqrt{\frac{\rho}{N_c}}\right]\right)}\ , \tag{IV.6}$$

which is the lower dashed black line reported in Fig. IV.1. It captures remarkably well the crossover between the two kinds of states. Note that approximating the cosine by its Taylor expansion up to second order, yields $K_c^{pol-sol}L_c \approx \sqrt{\pi^2 z\bar{J}\bar{r}^2}$, and stresses that K and L play a similar role in breaking the magnetic order.

To predict the curve that separates the solitonic and vortex states, I use an exact expressions for the excess energy of a vortex-antivortex pair compared to a fully magnetised configuration in an on-lattice XY model [72]. Taking into account only nearest-neighbour pairs of defects, this excess energy can be written as

$$\Delta E_{4D-pol}^{2dXY} = E_{4D}^{2dXY} - E_{pol}^{2dXY} \approx 8\pi\bar{J}\ln\frac{d}{a}\ ,$$

where d is the distance between the two defects and a is the size of the centre of the defect. Here $d = L/2$ and the vortex core diameter is of the order of the particle-particle spacing $a \simeq \bar{r}$. I then equate ΔE_{4D-pol}^{2dXY} to $E_{sol} - E_{pol}$ in its Taylor-expanded form and find a critical value for the number of particles above which four vortices states are more favorable than the solitonic ones:

$$N_c^{sol-vor} = \exp\left(2\phi z\right)\ . \tag{IV.7}$$

This corresponds to the vertical line in Fig. IV.1. While it does correspond to the size above which I mostly observe vortices, note that K also plays a role in the change between soliton and vortex states that is not explained by this crude estimate of the energy. A way to take into account the effect of K on the vortex state energy is to reckon that K plays the same role as an in-plane field in the magnetic model analog, and to use the expression for the energy of a vortex-antivortex pair in a field: [221]

$$\Delta E_{4D-pol}^{h} \approx E_{4D}^{2dXY}(h) - E_{pol}(h) = \Delta E_{4D-pol}^{2dXY} + 8\pi^2\sqrt{h}\left(\sqrt{\frac{d}{a}}-1\right)\ . \tag{IV.8}$$

In the magnetic analogue h is the amplitude of an external in-plane field, while here it is an effective field due to the spin-velocity coupling K. According to the effective sine-Gordon theory (see Sec. IV.3.2), $h = K^2$. An alternative and more intuitive manner

to obtain the quadratic dependence on K is to recall that Eq. (IV.8) gives the excess energy of vortex-antivortex pairs with respect to a magnetised configuration under the same field. As a consequence, both energies should in principle be written in the same frame. In the present case, however, I am comparing the energy of a non moving vortex configuration to that of a moving polar phase. I should therefore translate all velocities by $\boldsymbol{v_G} = -K\boldsymbol{m}$. This change of reference frame creates, however a new K-dependent term in the Lagrangian $\mathcal{L}_{Gal} = -K^2\boldsymbol{m} \cdot \sum_{i=1}^{N} \boldsymbol{s}_i$, which contains an effective field on spins of magnitude K^2. Finally, replacing the field in the expression of the in-field excess energy of vortices and equating E_{4D}^{2dXY} to E_{sol} yields the following equation with a K dependence:

$$K_c^{4D-pol} = \frac{2\phi z - \ln\sqrt{N_c}}{\pi\left(\sqrt{N_c} - 1\right)}. \tag{IV.9}$$

The resulting line is shown, when it is higher than the zero-field one, in Fig. IV.1. It fits numerical observations well, even though the crossover between solitons and vortices is rather broad as I am working with finite and moderately small system sizes. Note that Eqs. (IV.6) and (IV.9) predict that the soliton states disappear at a finite value of N: this is expected as solitons carry a non-zero topological charge (the vector field winds once around one direction of the Euclidean torus), and should not survive in the thermodynamic limit, unlike pairs of vortices and antivortices (the total winding number of which is 0). Furthermore, the number of vortices or solitons, is *a priori* independent of the size of the system. Indeed, while defects usually appear in equilibrium due to local frustration, such structures here develop only because the *total* magnetisation should be zero for the kinetic energy to be low, resulting in a global frustration between the conservation of the momentum and the one of the energy. As a result, there is no typical length scale associated to frustration smaller than the size of the system itself, and the $m = 0$ patterns are scale-free. One can also reason from the point of view of energetic costs: additional vortices or solitons would only create more local curvature, leading to an increased magnetic cost, but no kinetic energy gain. Finally, one could *a priori* circumvent defect formation by scaling K with N, in the same way that one usually rescales interaction constants in mean-field couplings. Here, the right choice would be $K\ N^{-1/2}$ so that the kinetic energy of a magnetised state remains unchanged when increasing N. However, I choose not to discuss such scalings at length in this thesis, since such rescaled interactions, while they are used in fully-connected descriptions for instance, are rather artificial.

IV.4 Effects of the temperature

IV.4.1 Magnetisation as a function of Temperature

Since I am performing microcanonical simulations, statistics can only be obtained at one value of the energy by sampling initial conditions. Rather than using the energy as a control parameter, I assume ergodicity and treat the system as one of statistical mechanics, as explained in Sec. IV.1. In particular, I introduce the statistical temperature T, which is usually measured using velocity fluctuations. In the present case the coupling between the velocities and the spins modifies, however, the usual equipartition relations [69], as

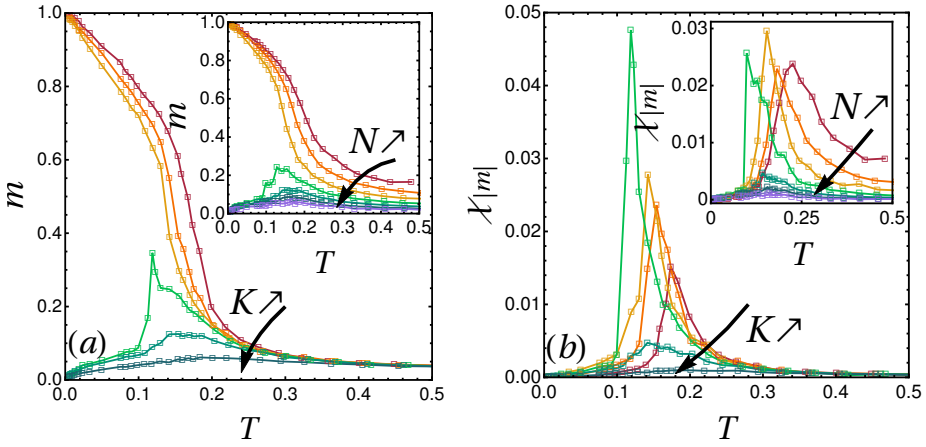

Fig. IV.3 **Finite-temperature behaviour and Order by Disorder.** (a) Magnetisation modulus versus temperature for $K = 0, 0.05, 0.06, 0.07, 0.1, 0.2$ at $N = 2048$ (main plot), and for $N = 128, 256, 512, 1024, 2048, 4096, 8192$ at $K = 0.1$ (inset). (b) The reduced susceptibility per particle versus temperature for the same parameters as in panel (a).

discussed in Sec. II.2:

$$T = \frac{1}{N}\sum_{i=1}^{N}\omega_i^2 - \left(\frac{1}{N}\sum_{i=1}^{N}\omega_i\right)^2 , \tag{IV.10}$$
$$2T = \frac{1}{N}\sum_{i=1}^{N}\boldsymbol{p}_i^2 - \left(\frac{1}{N}\sum_{i=1}^{N}\boldsymbol{p}_i\right)^2 - K^2\left(\frac{1}{N}\sum_{i=1}^{N}\boldsymbol{s}_i^2 - \left(\frac{1}{N}\sum_{i=1}^{N}\boldsymbol{s}_i\right)^2\right) .$$

The latter expression shows that the fluctuations of momenta and spins are coupled as long as $K \neq 0$, in such a manner that the temperature is not directly proportional to the translational kinetic energy. The former, on the other hand, shows that the temperature is proportional to the rotational kinetic energy, which is thus the most natural thermometer. Having checked that both definitions yielded the same mean value of the temperature, I heretofore only refer to the mean temperature over independent configurations at the same energy, $\langle T \rangle$, as T.

I start by studying the effects of the finite temperature on the magnetic properties of the homogeneous phases of the system using the (intensive) magnetisation modulus $m = \langle |\mathbf{m}| \rangle$, which is the order parameter of the polar phase. Fig. IV.3(a), displays the equilibrium value of m against T for increasing values of K at fixed N (main panel) or increasing values of N at fixed K (inset). When varying K, I observe three types of behaviours.

(i) For small K, when the ground state is the moving polar state, I observe a finite-size crossover between a (moving) ferromagnetic state at low temperatures and a non moving paramagnetic state at high temperatures (red-to-orange curves of Fig. IV.3(a)). This is the same crossover as the one reported in the case $K = 0$ between the magnetised ground state and the paramagnetic high temperature phase

(see Sec. III.2.1): the polar state does not survive in the thermodynamic limit in $2d$ due to low energy spin waves excitations [75]. The effect of K is to decrease the value of the magnetisation modulus at finite temperatures with respect to the $K = 0$ case. This can be understood by analyzing the spin waves excitations at low temperature within the framework of the continuum-limit theory described in Sec. IV.3.2. Indeed, close to $T = 0$ these spin-waves are described by a free Gaussian theory, that comes from the Taylor expansion of the spin-spin interaction terms in the Hamiltonian at second order [73]. Spin waves suppress global magnetisation as the the temperature increases. Furthermore, the effective spin-spin coupling decreases with temperature when taking into account higher-order terms in the Taylor expansion. In the $K \neq 0$ case, an effective field is generated on top of the spin-spin interaction term. The direction of this effective field is opposite to the one of global magnetisation, and its amplitude grows with K. As a result, the effective spin-spin coupling is further decreased by the addition of K, leading to stronger spin-wave suppression of the magnetisation as K increases. In short K favors the bending of the magnetisation field.

(ii) For large K, when the ground state has zero magnetisation modulus because of its topological structure, the magnetisation modulus crosses over from $m \simeq 0$, to a high-temperature paramagnetic regime where $m \sim 1/\sqrt{N}$.

(iii) When K takes moderately large values, although the ground state remains non polar ($m(T = 0) = 0$), the magnetisation grows to a maximum at a finite temperature, before it crosses over to the paramagnetic regime at high temperatures. I shall focus on this intriguing phenomena in the next section IV.4.2.

When increasing N at a fixed K, as shown in the inset of Fig. IV.3(a), the same three scenarii are observed. This is another sign of the qualitative similarity between the roles played by K and N, that was already pointed out in Sec. IV.3.

Inspired by the literature on the XY model [75, 116, 183], I also introduce a "reduced" susceptibility associated to m, like in Chapter III,

$$X_{|m|} = N\left(\langle m^2\rangle - \langle |m|\rangle^2\right).$$

While it is not the usual response function of a magnetic system to an external field, this quantity captures the broadening of the distribution of $|m|$ that occurs at the finite-size paramagnetic-ferromagnetic crossover with a peak that grows and narrows with the system size [116]. In Fig. IV.3(b), I plot the "reduced" susceptibility per particle, $\chi_{|m|} = X_{|m|}/N$ against the temperature T defined in Eq. (IV.10), corresponding to the magnetisation curves shown in Fig. IV.3(a). Upon increasing K at a fixed N (main panel), the susceptibility peak observed in the case of a polar ground state grows with K and is shifted towards lower temperatures. Recall that the same behaviour is observed upon increasing N at $K = 0$ [75], as described in Sec. III.2.1. A peak is also observed in cases in which the magnetisation features a local maximum [green curve in Fig. IV.3(b)], and it is even higher and shifted to lower temperatures compared to the peak observed for polar states. Finally, the peak is suppressed at K large enough, when the magnetisation simply

crosses over from the one of a topological ground state to that of a paramagnet. Likewise, when varying N at a fixed value of K (inset), the same scenario is observed: the peak of the extensive susceptibility $X_{|m|} = N\chi_{|m|}$ grows, is shifted to lower temperatures, and is then suppressed. This behaviour is in sharp contrast with the smooth, algebraic evolution of the height of the peak reported in the case $K = 0$ [75], that is shown in Sec. III.2.1.

IV.4.2 Unusual Order-by-Disorder Scenario

As described in Sec. IV.4.1, a surprising feature of the model is that, for some finite value of K or N, the magnetisation exhibits a local maximum at a finite temperature. In other words, the order parameter *grows* when thermal fluctuations are switched on. This behaviour is akin to Order-by-Disorder transitions [217, 218, 225] observed in frustrated magnets, whereby a system with a non-trivially degenerate ground states develops long-range order by the effect of classical or quantum fluctuations. In such geometrically frustrated spin models, the ObD phenomenon is due to a huge disproportion in the density of low-energy excitations associated with a specific ground state. Typically, in most ObD systems, the ground state has a zero magnetisation, but at a finite temperature it has the same free energy as a large number of states with a non-zero magnetisation, so that the mean magnetisation becomes extensive. Here the mechanism must be of a different nature.

In fact, in the present case the growth of a spontaneous magnetisation upon increasing the temperature is essentially due to the fact that the kinetic energy cost associated to collective motion in polar states decreases with T. The reason is that, as already discussed in Sec. IV.3, the magnetisation modulus decreases as the temperature is increased due to spin waves fluctuations, and so does the kinetic energy cost induced by momentum conservation. Hence, at moderately large K magnetised states become less and less costly compared to the soliton or vortex ones upon increasing the temperature, until a point where the free energy of the (moving) polar states crosses the one of the (non moving) soliton or vortex states and become the preferred minimum, in a way similar to a first-order phase transition. When the temperature is further increased, the topological states become unstable, and the polar minima continuously merge into a single paramagnetic minimum, as in the $K = 0$ case [75]. This scenario is pictorially sketched in Fig. IV.4$(a)-(b)$ in terms of a Landau-like free energy representation (see Sec. II.3 for more context on such representations). The fact that the system develops a spontaneous magnetisation and exhibits collective motion with a finite velocity of the centre of mass, upon increasing the temperature starting from a topological ground state with zero magnetisation, is thus due to the re-entrant shape of the surface separating the polar states from the solitonic ones in the extended phase diagram of Fig. IV.1, when a vertical axis corresponding to temperature is added.

Note that this interpretation relies on the existence of metastable states, corresponding to local stable minima of the free energy at finite temperature. In the thermodynamic limit, metastablity is forbidden in finite dimensional systems due to the convexity of the free energy. The ObD-like transition described here is in fact only a smooth crossover, and is continuously suppressed as the system size is increased. Yet, at finite N one can explicitly check in numerical simulations that both the topological and polar states are indeed locally stable at low enough temperature, as explained below. First, I fine-tune

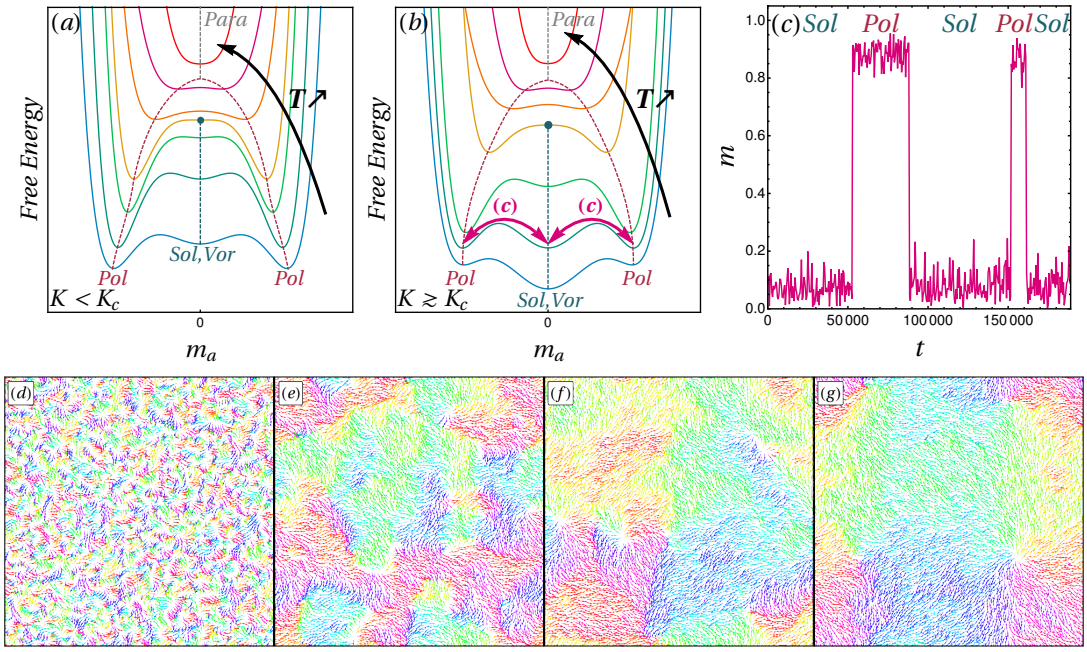

Fig. IV.4 **Coexistence and metastability.** (a) Sketch of the evolution of the free energy as a function of the magnetisation (along a particular direction) with increasing temperature (bottom to top) for low values of K: the low-temperature global minima are polar (Pol) and simply follow a Mexican hat scenario until they merge into a paramagnetic $(Para)$ state, while soliton and vortex (Sol, Vor) states are only metastable at low temperatures. (b) Free energy for $K \geq K_c$: the topological states are now global minima of the free energy until they cross the locally stable polar states at a finite temperature. At an intermediate temperature, when the Pol and Sol, Vor states have about the same free energy, switches between the two minima are observed in the Hamiltonian dynamics, as shown in (c). (c) Switches between low- and high- magnetisation regimes in the course of time for $N = 128, K = 0.25, T = 0.03$. $(d) - (g)$ snapshots after a quench of $N = 8192$ particles at $K = 0.03$ from $T \approx 2$ to $T \approx 0.04$, at times $t = 50, 150, 250, 4000$ after the quench, respectively. The different colours represent different local magnetic orientations.

K and N to get a system very close to the polar-soliton ground-state crossover, and I choose N to be rather small (here $N = 128, K = 0.25$). I then let the dynamics run at a finite but low temperature, $T = 0.03$. As shown in Fig. IV.4(c), switches between low- and high-magnetisation states can be observed, proving that both states are indeed local minima of the free energy. However, even for such small systems, one must wait very long times for switches to happen: this is an indication that the energy barrier between the two states is rather high compared to thermal fluctuations. One indeed expects that the energy barrier between a solitionic pattern and a polar state should scale linearly with the system size, since a collective reorganization of the spin degrees of freedom is necessary to switch between them.

Another indication of the existence of topological non-magnetised states beyond the range of parameters for which they are the equilibrium configurations is provided by the following observation. Consider a system with K and N such that at zero temperature the ground state is the polar one, and quench it from a high-temperature to a very low temperature. The result, shown in Fig. IV.4(d)$-$(g), shows that because non-equilibrium vortices appear during such quenches (as already observed for $K = 0$ [75], see Sec. III.2.1), the system often ends up in a 4-vortex state (whose centers being located at the equidistant points where red, yellow, green and blue regions meet).

IV.4.3 Qualitative Free Energy Expression

To go beyond the sketchy description of the free energy used in Fig. IV.4, I introduce simple expressions for the free energy densities of both families of states at low temperatures and in spatially homogeneous states, in the same spirit as the discussion of the energy of the different ground states (Sec. IV.3). First, the energy per particle of a soliton will be considered to be unaltered by temperature, and to remain of the same form E_{sol} as in Eq. (IV.5), with the addition of a kinetic energy term E_{fluc} associated to the fluctuations of the velocities around their mean values. Then, I approximate the associated entropy per particle, S_{sol}, by considering that it is only associated to the number of ways in which one can draw a soliton pattern of size L with N particles, separated from their nearest neighbours by a typical distance $\bar{r}$,

$$S_{sol} = \frac{1}{N} \ln\left(\frac{L}{\bar{r}}\right) .$$

The energy of a polar moving state at finite temperature should depend on the total magnetisation of the system to reflect the momentum conservation constraint, and on the kinetic energy E_{fluc} associated to the fluctuations of the velocities, which I assume takes the same value as in the solitonic case. Therefore, I modify the expression of E_{pol} introduced in Sec. IV.3 to include this effect,

$$E_{pol} = -\frac{1}{2} z \bar{J} + \frac{1}{2} K^2 m(K, N; T)^2 + E_{fluc} ,$$

where $m(K, N; T)$ is the intensive magnetisation modulus. The exact form of m at all temperatures and for all values of K below K_c is not known exactly. I thus choose to drop the K dependence and to approximate m by the exact expression obtained within

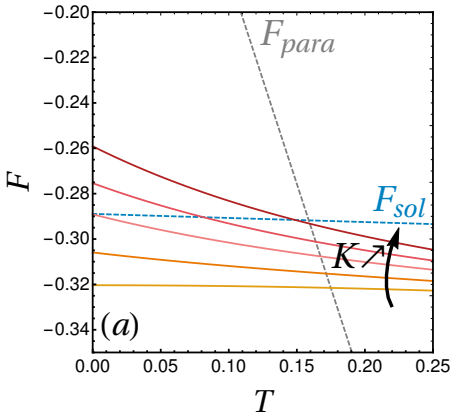

Fig. IV.5 **Low-temperature free energies of magnetic and solitonic branches.** Free energies F_{sol} (dashed blue line) and F_{para} (dashed gray line) and F_{pol} (full lines with different values of K between 0 (yellow) and 0.35 (red)) defined in the text versus temperature, for $N = 128$.

a spin-wave approximation [116, 183],

$$m(N;T) = \exp\left(-\frac{T}{8\pi\bar{J}}\ln(bN)\right) ,$$

where b is a constant that was evaluated from finite-size scaling [75] in the case $K = 0$, yielding the value $b \approx 5.5$ (see Sec. III.2.1). Finally, assuming that the system is well described by the spin-wave approximation in the considered domain of temperatures, I approximate the entropy per particle of magnetised states by counting how many ways there are to fit waves with a typical wave-length in an $L \times L$ box,

$$S_{pol} = \frac{1}{N}\ln\left(\frac{L}{\xi_{sw}(N;T)}\right)^2 ,$$

where I took the typical wave-length to be the spin-wave correlation length ξ_{sw}, that itself is well approximated, at low temperatures, by [183]

$$\xi_{sw} = Lm(N;T) .$$

I then have simple approximations for the free energies per particle F_{pol} and F_{sol} associated to polar and soliton states at low temperatures:

$$F_{pol} = E_{fluc} - \frac{1}{2}z\bar{J} + \frac{1}{2}K^2 m(K,N;T)^2 + \frac{2T}{N}\ln m(N;T) , \tag{IV.11}$$

$$F_{sol} = E_{fluc} - \frac{1}{2}z\bar{J}\left[\frac{1}{2}\cos\left(\frac{2\pi\bar{r}}{L}\right) + \frac{1}{2}\right] - \frac{T}{N}\ln\left(\frac{L}{\bar{r}}\right) . \tag{IV.12}$$

I can also approximate the free energy per particle of paramagnetic states by assuming that their magnetic energy averages to 0, and that their entropy is simply given by the choice of random angles for all particles, so that

$$F_{para} = E_{fluc} - T\ln 2\pi . \tag{IV.13}$$

Assuming that the energy associated to thermal fluctuations of the velocities is the same in all three states, E_{fluc} can be omitted in all expressions hereafter[3]. The expressions (IV.11), (IV.12) and (IV.13) for the different branches of interest of the free energy density can be used to estimate which state is favoured at a given temperature for a given value of K and N. In particular, I can determine parameters such that $F_{sol} = F_{pol}$ for $K \geq K_c$. Indeed, at the temperature such that these two branches cross, the system goes from a low-magnetisation soliton to a magnetised state. The crossing between F_{sol} and F_{pol} therefore corresponds to the temperature T_{max} at which a maximum of the magnetisation is reached, with height m_{max}. The results obtained when varying K for $N = 128$, as in Fig. IV.3, are shown in Fig. IV.5. As discussed in Sec. IV.4, the main effect of K is to bring magnetic states higher up in energy at very low temperatures, so that they cross the solitonic branch at a finite temperature below the one at which it crosses the paramagnetic branch. From these simple arguments, one also predicts that the soliton branch directly crosses the paramagnetic branch for all values of K larger than the value K_{max} for which F_{sol}, F_{pol} and F_{para} meet at a single point (here, $K_{max} \approx 0.36$). These simple arguments thus allow me to rationalise the finite temperature results presented above.

Note, however, that they are formulated in the special case $\boldsymbol{P} = \boldsymbol{0}$. Presumably, as the modulus of the total momentum is tuned up, I would expect the ObD scenario to still hold at small enough values, but to be progressively pushed down to lower temperatures, as well as higher values of K and N. Indeed, since the total momentum plays the same role as an external field, increasing its modulus should progressively raise the value of the magnetisation at high temperatures and relax the frustration at low temperatures, by favoring the magnetised state more and more.

IV.5 Ordering of the Velocities

I am yet to describe how velocities order in polar moving states. Because of the conservation of the total momentum, any state with a macroscopic magnetisation also moves with a collective velocity $\boldsymbol{v}_G = -K\boldsymbol{m}$. Therefore, one expects velocity vectors to align together (and to select the same speed) as the temperature is lowered. It is thus interesting to define an order parameter that reflects the alignment properties of the velocities,

$$\mu = \left\langle \left| \frac{1}{N} \sum_{i=1}^{N} \hat{\boldsymbol{v}}_i \right| \right\rangle ,$$

which reflects the alignment of unit velocities regardless of the velocity moduli, and is often called the polarity in the context of active matter [11]. I furthermore define an observable that measures the alignment of unit velocities onto the spins,

$$\nu = \left\langle \frac{1}{N} \sum_{i=1}^{N} \hat{\boldsymbol{v}}_i \cdot \boldsymbol{s}_i \right\rangle .$$

The variations of μ and ν with temperature, obtained for increasing K at fixed N or increasing N at fixed K are shown in Fig. IV.6$(a) - (d)$.

[3]This omission is justified by the fact that the fluctuations of the velocities are essentially Gaussian in all cases such that the system is either well-magnetised (polar moving and paramagnetic), or such that the velocities are essentially independent from the spins (vortex and soliton states), see IV.5

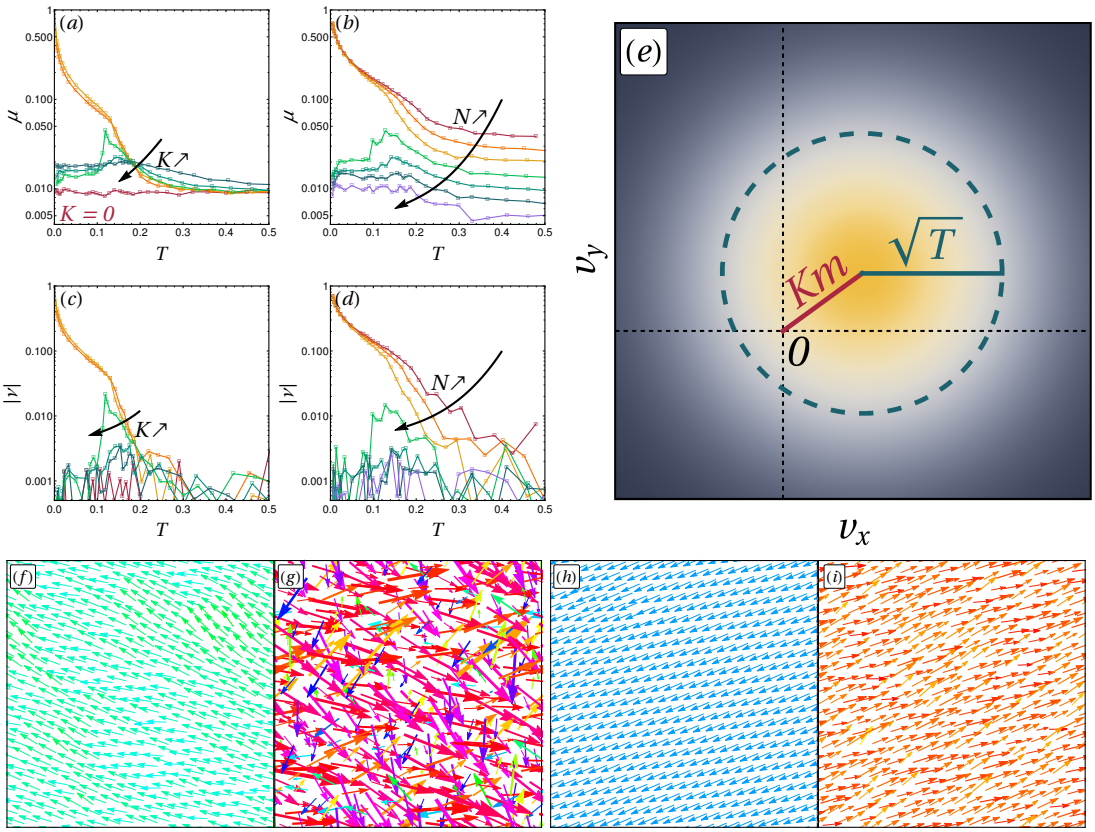

Fig. IV.6 **Ordering of velocities.** (a) Polarity of the velocities versus temperature, in log scale, for $N = 2048$ and varying $K = 0, 0.05, 0.06, 0.07, 0.1, 0.2$. (b) Polarity versus temperature, this time fixing $K = 0.1$ and taking $N = 128, 256, 512, 1024, 2048, 4096, 8192$. (c) Spin-velocity alignment versus temperature, in log scale, corresponding to (a). (d) Spin-velocity alignment versus temperature, in log scale, corresponding to (b). The colours are the same as in Fig. IV.3. (e) Sketch of the distribution of velocity vectors in magnetised phases, shown as a density plot, with values growing from grey to yellow. The distribution is centered on $\boldsymbol{v}_G$, at a distance Km from the origin (red line), and has a standard deviation of the order of $\sqrt{T}$ (blue circle). $(f) - (i)$ Snapshots of the magnetisations and velocities, respectively, for $N = 512$ and $K = 0.1$ at $T \approx 7 \cdot 10^{-3}$. The colour of each vector represents its orientation, while its thickness is proportional to its length. $(g) - (h)$ Snapshots of the same system at $T \approx 3 \cdot 10^{-6}$.

For low values of K and N, such that the system has a polar ground state, both μ and ν grow to 1 at low temperatures. However, these curves do not behave like the magnetisation: μ and ν become significantly larger than zero only at very low temperatures (note the logarithmic scale of the μ and ν axis). This is even more striking when comparing the magnetisation and velocity fields at low temperatures, as illustrated by the snapshots in Fig. IV.6$(f)-(i)$. In particular, in the snapshots IV.6$(f)-(g)$, I observe that even deep in the magnetised phase, where the system moves with a collective velocity, both the orientations (colours) and moduli (lengths and thicknesses) of the velocity arrows seem to vary a lot across the system. This comparatively weak ordering of the velocities compared to that of the spins can be explained by focusing on the distribution of velocity vectors. Rewriting the equipartition equation (II.12) associated to momenta in terms of the velocities, one finds that

$$2T = \left\langle v_i^2 \right\rangle - \langle v_i \rangle^2 + 2K \left(\langle \boldsymbol{v}_i \cdot \boldsymbol{s}_i \rangle - \langle \boldsymbol{v}_i \rangle \cdot \langle \boldsymbol{s}_i \rangle \right). \tag{IV.14}$$

In particular, deep in the magnetised phase, one can assume that all spins are essentially aligned and equal to the (unit) magnetisation vector, $\boldsymbol{s}_i \approx \boldsymbol{m}$. In this simple case, the spin-velocity terms in Eq. (IV.14) cancel out, so that the usual equipartition relation, $2T = \langle v_i^2 \rangle - \langle v_i \rangle^2$, is recovered. Consequently, at very low temperatures, the velocity vectors are essentially drawn from a Gaussian distribution centred at $\boldsymbol{v}_G = -K\boldsymbol{m}$, and with an isotropic variance T. This distribution is sketched as a density plot in Fig. IV.6(e), with values growing from grey to yellow. From this sketch, it is immediately visible that, as long as the standard deviation of the velocity distribution is larger than K, meaning that $T \geq K^2$, there is a significant probability for velocities to be pointing in any direction other than that of $\boldsymbol{v}_G$. Their moduli, however, are skewed towards larger values. Hence the aspect of the snapshot in Fig. IV.6(g), in which velocities display a low polar order, but are biased towards larger, red arrows. In practice, for polar order to be visible, like in snapshot IV.6(i), one needs to reach temperatures such that $T \ll K^2$, thus ensuring that the Gaussian distribution of the velocities does not take significant values close to $\boldsymbol{v} = \boldsymbol{0}$. This constraint on the value of the temperature to observe polar order of the velocities is highly unusual compared to other models that feature collective motion. The reason for this is two-fold. First, in abstract models of self-propelled particles like the Vicsek model [52], the speed of particles is often fixed to a nominal value, so that the distribution of the velocities is naturally off-centred and very sharp. In that sense, a conservative setting makes it harder to observe a polar order of the velocities, since it imposes constraints on the width of the speed distribution. Second, in order to stabilise the polar state, K needs to be small enough, so that the velocity of the centre of mass is never that large and μ can only grow at very low temperatures.

For very large values of K or N, such that the ground state is not polar and no ObD is observed at finite temperatures, μ remains low at all temperatures. This is expected, since no collective velocity develops in this case. Furthermore, ν also remains small, thus indicating that the velocities do not locally align on the spins either. In other words, in vortex and soliton structures, the velocities do not draw solitons or vortices themselves, but simply remain disordered at low temperatures: velocity alignment is destroyed. This is proof that there is no true microscopic source of velocity alignment. At first sight, one would have expected the introduction of the self-alignment of the velocity on the spin in the Lagrangian to be responsible for a transfer of the ferromagnetic alignment of the

spins to the velocities, even in vortex or soliton states[4]. This is not the case because the alignment of the velocities is actually entirely driven by the constraint imposed by the momentum conservation: $\boldsymbol{v}_G = -K\boldsymbol{m} = 0$. This constraint is only global and promotes local alignment between the velocities in a very indirect way.

Finally, for intermediate values of K or N, however, a macroscopic magnetisation is observed at finite temperatures, following the ObD scenario described in Sec. IV.4.2. As a consequence, a collective velocity is also observed at finite temperatures, and it is accompanied by a local maximum of both μ and ν. In other words, the ObD phenomenon saves collective motion from a total extinction caused by topological defects at finite temperatures in a finite range of the parameters. Furthermore, in the range of K and N such that we observe switches between polar and soliton states, such as those described in Fig. IV.4, the collective velocity itself also switches between low and high values. This spontaneous intermittent motion is highly unusual in a conservative setting, as such behaviours are usually expected in systems with friction, like granulars [226], or activity, such as *E. Coli* bacteria that alternate between "runs", i.e. ballistic motion along straight lines, and "tumbles", i.e. pauses in the motion during which they re-orient themselves [227].

IV.6 Possible extensions

In this section, I discuss the generality of the observations of this chapter when changing various aspects of the model. First, I consider a different shape for the spin-velocity coupling in Sec. IV.6.1. Then, in Sec. IV.6.2, I consider the effect of a simple change of the geometry of the box. In Sec. IV.6.3, I discuss the effect of switching from a $2d$ space and XY spins to a $3d$ space and Heisenberg spins. Finally, in Sec. IV.6.4, I discuss the effect of varying the density in a $2d$ space, and extend the discussion of this chapter to phase-separated states.

IV.6.1 Quadratic Spin-Velocity Coupling

As discussed in Sec. II.2.2, the shape of spin-velocity couplings that lead to well-behaved physics and to an analytically tractable Lagrangian-Hamiltonian inversion is very constrained. Essentially, the only reasonable shape for such couplings is a degree-two polynomial. In order to study the effect of this more general coupling, I derive the mean-field description of the corresponding Hamiltonian, resorting to the same method I used in Sec. II.3.2. Just like in the case of the linear coupling only, I discard the repulsive interactions and consider fully-connected interactions, leading to the Hamiltonian

$$\mathcal{H} = \sum_{i=1}^{N} \left[\frac{{\omega_i}^2}{2} + \frac{{p_i}^2}{2} - \tilde{K}_1 \left(\boldsymbol{p_i} \cdot \boldsymbol{s_i} \right) + \tilde{K}_2 \left(\boldsymbol{p_i} \cdot \boldsymbol{s_i} \right)^2 - \frac{J}{2} \boldsymbol{s_i} \cdot \overline{\boldsymbol{m}} \right] .$$

The associated partition function is defined by

$$Z \equiv \int d^{2N}\boldsymbol{R}\, d^{2N}\boldsymbol{\mathcal{P}}\, d^{N}\boldsymbol{\Theta}\, d^{N}\boldsymbol{\Omega}\, \exp\left[-\beta \left(\mathcal{H} - \boldsymbol{\alpha} \cdot \boldsymbol{P} \right)\right] ,$$

[4] I also checked this briefly in the case of integrated displacements such as those described in Chapter V: the displacements of particles in a cold soliton or vortex state only go from an inertial ballistic regime to a diffusive regime, without any sign of an active-like superdiffusion or higher effective diffusion due to the spin-velocity coupling.

with a parameter $\boldsymbol{\alpha}$ to be determined. Like in the linear case, the integrals over the positions and angular velocities factorize and can be easily computed, yielding

$$Z = \left(\frac{2\pi}{\beta}\right)^{N/2} V^N \int d^N\boldsymbol{\Theta} \prod_{i=1}^{N} Z_{p_i}(\theta_i) \exp\left(\frac{\beta J}{2}\boldsymbol{s_i}\cdot\overline{\boldsymbol{m}}\right) ,$$
$$Z_{p_i}(\theta_i) \equiv \int d^2\boldsymbol{p_i} \exp\left[-\beta\left(\frac{{p_i}^2}{2} - \boldsymbol{p_i}\cdot\left(\boldsymbol{\alpha}+\tilde{K}_1\boldsymbol{s_i}\right) + \tilde{K}_2\left(\boldsymbol{p_i}\cdot\boldsymbol{s_i}\right)^2\right)\right] .$$

Calling $s_{i_{x,y}}$ the projections of spins onto the x, y direction, the exponent in the last expression can be rewritten in a more compact form by using a vector notation:

$$Z_{p_i}(\theta_i) \equiv \int d^2\boldsymbol{p_i} \exp\left(-\frac{1}{2}{}^t\boldsymbol{p}A\boldsymbol{p} + {}^t\boldsymbol{B}\cdot\boldsymbol{p}\right)$$

with

$$A \equiv 2\beta \begin{pmatrix} \frac{1}{2}+\tilde{K}_2{s_{i_x}}^2 & s_{i_x}s_{i_y}\tilde{K}_2 \\ s_{i_x}s_{i_y}\tilde{K}_2 & \frac{1}{2}+\tilde{K}_2{s_{i_y}}^2 \end{pmatrix} \qquad \text{and} \qquad {}^t\boldsymbol{B} \equiv \beta\left(\boldsymbol{\alpha}+\tilde{K}_1\boldsymbol{s_i}\right) ,$$

and the integration over $\boldsymbol{p}_i$ readily calculated to obtain

$$Z_{p_i}(\theta_i) = \sqrt{\frac{4\pi^2}{\det A}} \exp\left(\frac{1}{2}{}^t\boldsymbol{B}A^{-1}\boldsymbol{B}\right) .$$

Moreover, using the fact that $\boldsymbol{s_i}$ is a unit vector, one finds

$$\begin{aligned} \det A &= \beta^2\left(1+2\tilde{K}_2\right), \\ \frac{1}{2}{}^t\boldsymbol{B}A^{-1}\boldsymbol{B} &= \frac{1}{2\det A}\left(B_1^2A_{22}+B_2^2A_{11}-2A_{21}B_1B_2\right) , \\ &= \frac{\beta}{1+2\tilde{K}_2}\left[\frac{\tilde{K}_1^2+\alpha^2}{2} + \tilde{K}_1\boldsymbol{\alpha}\cdot\boldsymbol{s_i} - 2\tilde{K}_2 v_{G,x}s_x\alpha_y s_y + \tilde{K}_2\left(s_x^2\alpha_y^2+s_y^2\alpha_x^2\right)\right] . \end{aligned}$$

Note that in the case $K_2 > 1/2$, that was already flagged as non-physical right from the definition of the quadratic term, one finds that $\det A$ becomes negative; and in the limit $K_2 \to 1/2$, this determinant goes through an infinite value. The last results can be used to write

$$Z_{p_i}(\theta_i) = \frac{2\pi}{\beta\sqrt{1+2\tilde{K}_2}} \exp\left\{\frac{\beta}{1+2\tilde{K}_2}\left[\frac{\tilde{K}_1^2+\alpha^2}{2} + \tilde{K}_1\boldsymbol{\alpha}\cdot\boldsymbol{s_i} - 2\tilde{K}_2\alpha_x s_x\alpha_y s_y + \tilde{K}_2\left(s_x^2\alpha_y^2+s_y^2\alpha_x^2\right)\right]\right\} .$$

Then, I notice a number of identities:

$$2\alpha_x\alpha_y s_x s_y - s_x^2\alpha_y^2 - \alpha_x^2 s_y^2 = (\boldsymbol{\alpha}\cdot\boldsymbol{s})^2 - \alpha^2 ,$$
$$\frac{1}{1+2\tilde{K}_2} = 1-2K_2 , \qquad \frac{\tilde{K}_1}{1+2\tilde{K}_2} = K_1 , \qquad \frac{\tilde{K}_2}{1+2\tilde{K}_2} = K_2 ,$$

and I define Z_θ through

$$Z_\theta \equiv \int d^N\boldsymbol{\Theta} \prod_{i=1}^{N} Z_{p_i}(\theta_i) \exp\left(\frac{\beta J}{2}\boldsymbol{s_i}\cdot\overline{\boldsymbol{m}}\right),$$

so that I can rewrite

$$Z_\theta = \left(\frac{2\pi\sqrt{1-2K_2}}{\beta}\right)^N \exp\left[\frac{\beta N}{2}\left(\frac{K_1^2}{1-2K_2}+\alpha^2(1-2K_2)\right)\right]\mathcal{I}$$

with

$$\mathcal{I} \equiv \int d^N\boldsymbol{\Theta}\exp\left[\beta N\overline{\boldsymbol{m}}\left(\boldsymbol{h}+\frac{JN}{2}\overline{\boldsymbol{m}}+K_1\boldsymbol{\alpha}\right)-\beta NK_2\alpha^2 g(\boldsymbol{\Theta})\right] ,$$
$$g(\boldsymbol{\Theta}) \equiv \frac{1}{N}\sum_{i=1}^{N}\cos^2(\theta_i-\theta_\alpha)-1 .$$

It is now useful to apply a Hubbard-Stratonovich transformation,

$$\exp\left(\frac{\beta J}{2}N^2m^2\right) = \frac{\beta N}{2\pi}\int d^2\boldsymbol{u}\ \exp\left[-\beta N\left(\frac{u^2}{2}-JN\boldsymbol{u}\cdot\boldsymbol{m}\right)\right] ,$$

and the definition $\boldsymbol{\gamma}(\boldsymbol{u}) \equiv jN\boldsymbol{u}+\boldsymbol{h}+K_1\boldsymbol{v}_G$, to derive a more convenient expression for $\mathcal{I}$

$$\mathcal{I} = \frac{\beta N}{2\pi}\exp\left[\beta NK_2\alpha^2\right]\int d^2\boldsymbol{u}\exp\left[-\beta N\frac{u^2}{2}\right][J(\boldsymbol{u})]^N$$

with

$$J(\boldsymbol{u}) \equiv \int_0^{2\pi} d\theta\exp\left[-\beta K_2v_G^2\cos^2(\theta-\theta_\alpha)+\beta\gamma\cos(\theta-\theta_\gamma)\right] .$$

Therefore, the full partition function reads

$$Z = V^N\left(\frac{2\pi}{\beta}\right)^{N/2}\frac{\beta N}{2\pi}\left(\frac{2\pi\sqrt{1-2K_2}}{\beta}\right)^N\exp\left[\beta N\left(\frac{K_1^2}{2(1-2K_2)}+\frac{\alpha^2}{2}\right)\right]\int d^2\boldsymbol{u}\ e^{-\beta N\frac{u^2}{2}}J(\boldsymbol{u})^N$$

$$= \left(V\sqrt{1-2K_2}\right)^N\left(\frac{2\pi}{\beta}\right)^{\frac{3N}{2}-1}N\exp\left[\frac{\beta N}{2}\left(\frac{K_1^2}{1-2K_2}+\alpha^2\right)\right]\int d^2\boldsymbol{u}\ e^{-\beta N\frac{u^2}{2}}J(\boldsymbol{u})^N .$$

In order to compute $J(\boldsymbol{u})$, I need to evaluate the integral

$$f(\boldsymbol{a},b) = \int_{-\pi}^{\pi} d\theta\exp[a\cos\theta+b\cos^2(\theta+\theta_a)] .$$

With this aim, I use the identities [101]:

$$\exp\left[b\cos^2(\theta+\theta_a)\right] = \sum_{n=0}^{\infty}\frac{(b/4)^n}{n!}\left[\binom{2n}{n}+2\sum_{k=0}^{n-1}\binom{2n}{k}\cos\left(2(n-k)(\theta+\theta_a)\right)\right] ,$$
$$\cos\left(2(n-k)(\theta+\theta_a)\right) = \cos\left(2(n-k)\theta\right)\cos\left(2(n-k)\theta_a\right)-\sin\left(2(n-k)\theta\right)\sin\left(2(n-k)\theta_a\right) .$$

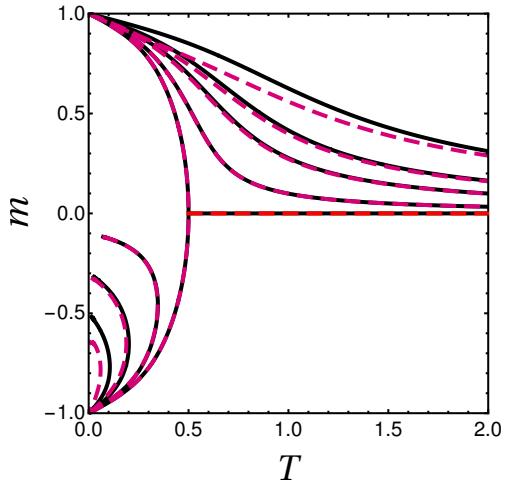

Fig. IV.7 The possible magnetisation densities at the saddle point. K_1 is taken equal to 1 and I plotted several values of the modulus of the velocity of the centre of mass $\alpha = 0, 0.1, 0.3, 0.5, 1$. The red curves are obtained for $K_2 = 0.49$. The black curves are a reference, and represent the magnetisation in the case $K_2 = 0$.

Then, integrating out odd terms that involve sines, and after some algebra, I find an exact expression for f:

$$f(\boldsymbol{a}, b) = 2\pi e^{\frac{b}{2}} \left(I_0(a) I_0(\frac{b}{2}) + 2 \sum_{j=1}^{\infty} \cos(2j\theta_a) I_j(\frac{b}{2}) I_{2j}(a) \right) .$$

Taking advantage of the fact that $J(\boldsymbol{u}) = \left[f(\beta\boldsymbol{\gamma}, -\beta K_2 \alpha^2) \right]^N$, I can now move on to the computation of the integral over $\boldsymbol{u}$:

$$\mathcal{J} = \int_{\mathbb{R}^2} d^2\boldsymbol{u} \, \exp\left[-\beta N \left(\frac{u^2}{2} - \frac{1}{\beta} \log\left[f(\beta\boldsymbol{\gamma}, -\beta K_2 \alpha^2) \right] \right) \right] .$$

There is no easy way to compute this integral so that I have to resort to a saddle point approximation, by minimizing the expression in the exponential with respect to $\boldsymbol{u}$. After some replacements the expression to optimize reads

$$\mathcal{F}(\boldsymbol{u}) = \frac{u^2}{2} - \frac{1}{\beta} \log \left(I_0(\beta\gamma) I_0(-\beta K_2 \frac{\alpha^2}{2}) + 2 \sum_{j=1}^{\infty} \cos(2j\theta_\gamma)(-1)^j I_j(\beta K_2 \frac{\alpha^2}{2}) I_{2j}(\beta\gamma) \right) .$$

Seeking zeros of the gradient of $\mathcal{F}$, first noticing that the $2d$ minimizer is attained for $\boldsymbol{u}$ aligned with $\boldsymbol{v_G}$, which fixes $\theta_\gamma = \arccos(\hat{\boldsymbol{\gamma}} \cdot \hat{\boldsymbol{v}}_G) \equiv 0[\pi]$, I obtain an implicit equation for the optimum $\boldsymbol{u}^\star$:

$$\boldsymbol{u}^\star = \pm \mathrm{sign}(K_1) \hat{\boldsymbol{\alpha}} \frac{I_1(\beta\gamma) I_0(\beta |K_2| \frac{\alpha^2}{2}) + \sum_{j=1}^{\infty} (-1)^j I_j(\beta K_2 \frac{\alpha^2}{2}) \left(I_{2j-1}(\beta\gamma) + I_{2j+1}(\beta\gamma) \right)}{I_0(\beta\gamma) I_0(\beta |K_2| \frac{\alpha^2}{2}) + 2 \sum_{j=1}^{\infty} (-1)^j I_j(\beta K_2 \frac{\alpha^2}{2}) I_{2j}(\beta\gamma)} .$$

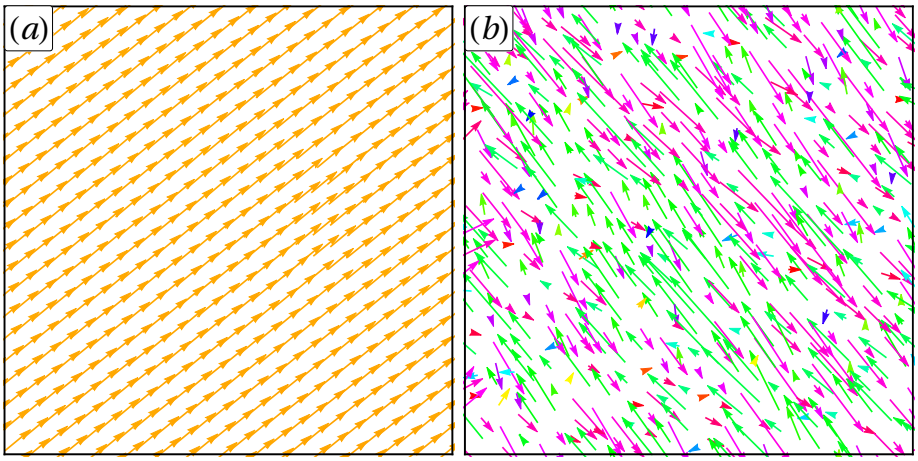

Fig. IV.8 **Low-energy state with a nematic spin-velocity coupling.** (*a*) Spin configuration. (*b*) Velocity configuration. Both spins and velocities are colour-coded according to the direction in which they are pointing. Simulation performed with $N = 512$ particles, $K_1 = 0$ and $K_2 = 0.49$, down to a temperature $T \approx 10^{-5}$.

Under a critical temperature, this equation has two branches of minimizing solutions, corresponding to two minima of $\mathcal{F}$ that are not at the same height due to the presence of K_1 [69]. One can solve this equation numerically and compare the result to the case in which $K_2 = 0$. The results are essentially the same, except that K_2 makes the magnetisation more impervious to $\beta K_1 \alpha$, as shown in Fig. IV.7, where, unlike in Fig. II.5, I do not distinguish explicitly the stable and unstable solutions. This similarity can be explained from the equation itself, as the sums over Bessel functions are naturally perturbative because of properties of Bessel functions of growing parameter [101], with larger corrections when $\beta K_1 \alpha$ increases. Finally, I write the mean value of the momentum per particle with $K_2 \neq 0$,

$$\langle \boldsymbol{p} \rangle = \boldsymbol{\alpha} + K_1 \boldsymbol{m} - 2K_2 \langle (\boldsymbol{v}_i \cdot \boldsymbol{s}_i)\, \boldsymbol{s}_i \rangle,$$

which leads, by identification with the definition of the canonical momentum, to $\boldsymbol{\alpha} = \boldsymbol{v}_G$ just like in the case $K_2 = 0$.

In the end, adding a quadratic coupling leads to the same qualitative behaviour at the mean-field level. Therefore, I do not expect any new physics as long as $K_1 \neq 0$, although the domains of stability of polar and topological states are probably shifted by the addition of K_2. An interesting special case, however, is $K_1 = 0$ and $0 < K_2 < 1/2$. In that situation, the spin-velocity coupling does not favor a polar alignment of the velocity onto the spin, but only a nematic alignment. As a result, one does not expect any collective motion to arise in that case. However, a similar nematic ordering of the velocities onto the direction of an internal spin was considered in a recent model of Vicsek-like particles with velocity reversals [87], so that this model could be of interest for future research. An example of a numerical low-energy state obtained for $K_1 = 0$ and $K_2 = 0.49$, with $N = 512$ particles and $\phi = 0.55$, is showcased in Fig. IV.8$(a) - (b)$, where I show the spin configuration and the velocity configuration, respectively. These snapshots show that, for

this choice of K_1 and K_2, the spins order at low temperatures, and that while the velocities do not order into a collectively moving state, they favour orientations orthogonal to the spins and display nematic order.

IV.6.2 Effect of the geometry

In the rest of the chapter, every simulation was performed in a periodic square box. Topologically, this box is homotopic to a Euclidean (flat) torus [228]. This geometry imposes some constraints. For example, the total number of vortices has to be compensated by the total number of antivortices. Changing the topology of the simulation box could be interesting, as it would lead to different proportions of vortices and antivortices, and perhaps to whole new defects. The role of geometry in finite size is less clear: one could wonder whether the configurations of 2 vortices and 2 antivortices simply come from the square shape of the box, for instance. To address this question in a minimal way, I simulate the system in a periodic hexagon (which is also equivalent to a Euclidean torus [228]) and in a periodic rectangle. Examples of a few ground states obtained under these conditions are shown in Fig. IV.9. I observe the same phenomenology in hexagonal boxes as in square

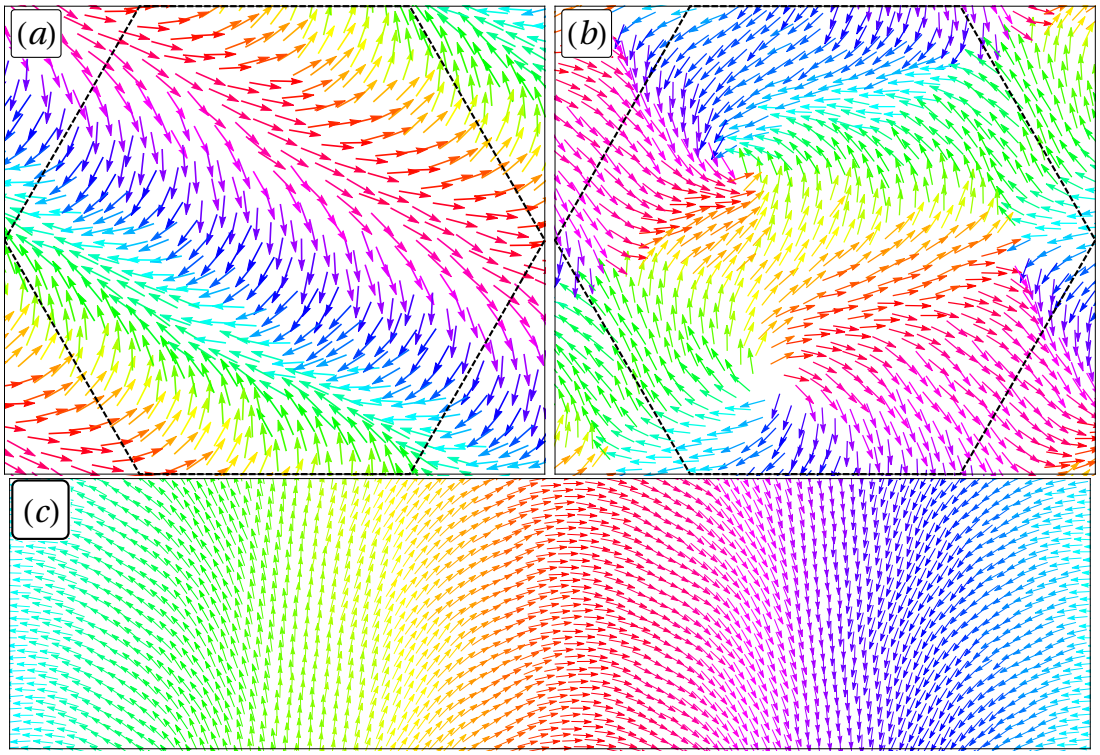

Fig. IV.9 **Effect of Boundary Conditions.** Numerical ground state with hexagonal periodic boundary conditions for (a) $N = 512$, $K = 1.0$ and (b) $N = 800$, $K = 1.0$. (c) Numerical Ground State in a periodic rectangle for $N = 2048$, $K = 0.5$. In (a) and (b), the simulation box is showed as a dashed black line.

ones: at low (K, N), the observed non-magnetic states are solitons, and when K or N

increase, 2 vortices and 2 antivortices develop. In rectangular boxes, the more slender the box becomes, the more solitons are favoured. Indeed, using the argument given in the main text for the energy of a soliton, their cost decreases if the rotation is made smoother. Therefore, in rectangular boxes, the solitons will select the longest side and be favoured with respect to vortex configurations.

In summary, as long as the homotopy class of the simulation box does not change, and using the few examples shown in Fig. IV.9, I expect the same phenomenology as in square boxes, since I only ever observed the same 4-vortex, soliton, and polar phases. Possibly there will be a shift of the crossover lines in the (K, N) plane that can be expected to depend on the precise geometry.

IV.6.3 Effect of dimensionality

In this thesis, I mostly worked with the model defined on a $2d$ space and, consequently, with $2d$ continuous spins. However, the crossover between magnetic and non-magnetic ground states, that is only due to an energetic trade-off, should survive in higher dimensionality of space and with spins of higher dimension. In order to check that dimensionality does not play an important role with respect to this qualitative feature, I now focus on the case $d = 3$.

First, I revisit the mean-field calculation in $3d$ and with Heisenberg spins. The main difference with respect to the $2d$ case with planar spins comes from the angular dependence in the momentum associated to the spins. More precisely, the Hamiltonian I want to study now is

$$H \equiv \sum_{i=1}^{N} \left\{ \frac{\boldsymbol{p_i}^2}{2} + \frac{p_{\theta_i}^2}{2} + \frac{p_{\phi_i}^2}{2\sin^2\theta_i} - K_1\, \boldsymbol{p_i}\cdot\boldsymbol{s_i} - \frac{1}{2}\sum_{k(\neq i)} \left[J(r_{ik})\boldsymbol{s_i}\cdot\boldsymbol{s_k} - u(r_{ik}) \right] \right\} .$$

I now focus on the angular part of the partition function: the p_{θ_i} contribution is simply a Gaussian integral that gives a constant. However, the integral over p_{ϕ_i} looks a bit more dangerous for future calculations because of the $\sin\theta_i$ factor. The first (Gaussian) integral reads:

$$\int_{\mathbb{R}} dp_{\phi_i}\ \exp\left(-\beta \frac{p_{\phi_i}^2}{2\sin^2\theta_i} \right) = \sqrt{\frac{2\pi\sin^2\theta_i}{\beta}} .$$

Then, using the fact that $0 \leq \theta_i \leq \pi$, one can simply take the sin out of the square root for all values of i. Therefore, for each particle, I simply obtain a $\sin\theta_i$ factor that should be integrated over θ_i. In fact, this is simply the factor I was missing in the partition function to recover $d\boldsymbol{s_i} = \sin\theta_i d\theta_i d\phi_i$! I thus find that the spins should be integrated over a sphere, and not simply over a cube in angular coordinates. The same trick can be reproduced for any higher dimension. In the end, I will simply recover the hyperspherical infinitesimal surface element. Therefore, in any $d \geq 3$, I get, after some usual algebra, the saddle-point solution

$$\log Z_d \approx N \left[-\left(d - \frac{1}{2} \right) \log\beta + \log V + \frac{\beta}{2}\alpha^2 - \beta\mathcal{F}(\boldsymbol{u}^\star) + cst \right]$$

where, as in the $2d$ case, I have to minimize a function of $\boldsymbol{u}$, an intermediate integration variable, defined through

$$\mathcal{F}(\boldsymbol{u}) \equiv \frac{u^2}{2} - \frac{1}{\beta} \log \left(\frac{I_{\frac{d}{2}-1}(\beta\gamma)}{(\beta\gamma)^{\frac{d}{2}-1}} \right) \qquad \text{with} \qquad \boldsymbol{\gamma} \equiv \boldsymbol{u} + K_1 \boldsymbol{\alpha} \; .$$

The value of the minimizing value, $\boldsymbol{u}^\star$, is given by an implicit equation, and $\boldsymbol{u}^\star$ is still the value of the mean magnetisation in the saddle-point approximation. The results in any dimensionality are essentially similar, except that in the absence of a rescaling of interactions with d, the ferromagnetic transition that I observe is sent to lower temperatures. I show the particular $d = 3$ case in Fig. IV.10.

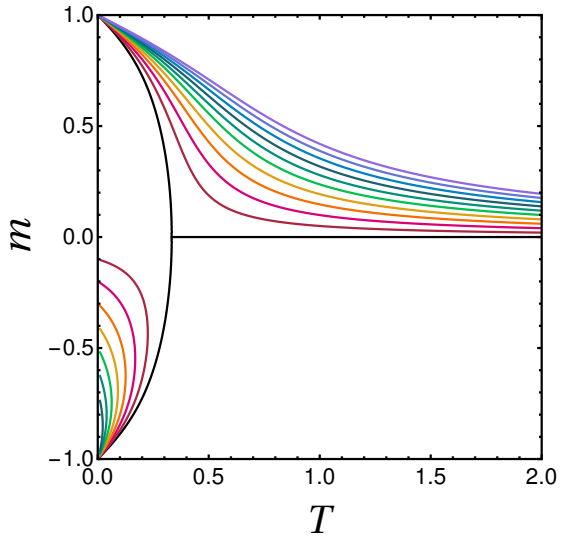

Fig. IV.10 **Mean-field magnetisation versus temperature in $d = 3$.** All the curves shown were obtained with $K_1 = 1$, for growing values of α between 0 and 1 by steps of 0.1. A ferromagnetic state is still observed, but the transition occurs at a temperature lower than 0.5 since we did not rescale the interactions when going from 2 to 3 dimensions.

Having checked that, at the mean-field level, results for $d = 3$ are qualitatively the same as in $d = 2$, I now reproduce the same simulations[5] as in the $2d$ case in $3d$ space, with classical Heisenberg spins instead of XY spins, and obtain ground states for a few values of K and N and a density such that no phase separation is observed. A few snapshots thus obtained in a periodic cubic box, and for a $3d$ packing fraction $\phi_{3d} \equiv \frac{N\pi\sigma^3}{48L^3} \approx 0.32$, are shown in Fig.IV.11, and confirm that polar states and solitons are still observed in that case when varying K and N. In Fig. IV.11(d), which shows a slice of the soliton state shown in Fig. IV.11(b), a $2d$-like vortex-antivortex structure is also seen. A priori, I could expect true $3d$ point defects to arise in $3d$ as well for larger systems and, possibly, larger values of K.

[5] See Sec. II.2.3 for more details on the simulation method in $3d$.

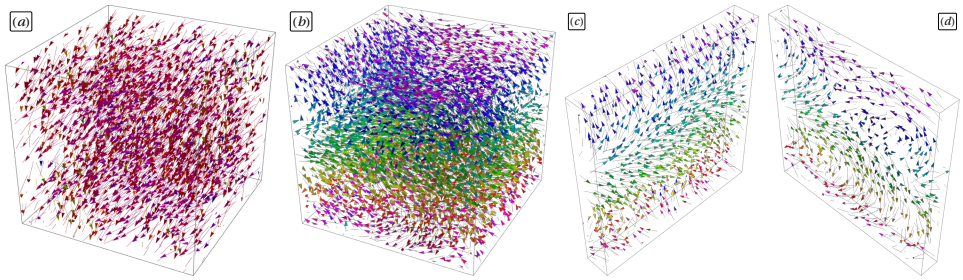

Fig. IV.11 **3d frustrated states.** (a) Low-temperature polar state in a system with $N = 2000$, $K = 0.1$. (b) Low-temperature soliton state in a system with $N = 5000$, $K = 0.5$ (c) and (d) are slices of (b), that make the soliton structure more apparent. In the top part of (d), a structure reminiscent of a vortex-antivortex pair can also be seen.

IV.6.4 Effects of the density

Finally, I briefly discuss the role of the density. I showed in Sec. III.2.2 that, in the case $K = 0$, the model described by the Hamiltonian (IV.1) features a phase separation between a ferromagnetic liquid and a paramagnetic gas at low densities and temperatures. This phase separation, which is observed even when the pairwise potential $U(r)$ is purely repulsive, is induced by the ferromagnetic coupling $J(r)$. Indeed, a $J(r)$ that decreases as r increases creates an effective attraction between aligned spins, that is sufficient to cause a phase separation, that I coined Ferromagnetism-Induced Phase Separation (FIPS). Because J is the only source of attraction in the system, I also showed that the left-most spinodal of the liquid-gas phase separation was the lower part of the finite-size Curie line, so that a tricritical point sits at the top of the coexistence line, which presents a cusp. For $K > 0$, a phase separation between a liquid and a gas is still expected at low densities and temperatures, since the spin-mediated attraction between particle is not affected by the presence of a spin-velocity coupling. Furthermore, one expects that increasing K or N should create still, phase-separated states at low enough temperatures, with patterns in the magnetisation field such that $m = 0$ as $T \to 0$, just like in the homogeneous case. It is *a priori* hard to predict all the possible shapes of such states. However, increasing the density at a constant temperature, and for a given values of K and N, should intuitively increase the mean number of neighbours of each particle. As a result, curving the magnetisation field should become more and more costly as the density increases. Therefore, one expects a domain of still, "patterned" states at low densities and temperatures, that grows as K or N is increased. This picture is schematically drawn atop the coexistence line and Curie line from Sec. III.2.2 in Fig. IV.12(a).

In order to check this picture, I simulate systems at various packing fractions, and for a few sets of values of K and N. At low densities, I do observe a rather large zoology of patterned phase-separated states, two examples of which are shown in Fig. IV.12$(b-c)$. At very low densities (close to the left-most side of the coexistence line), as illustrated by Fig. IV.12(b), the system can organise into two anti-magnetised droplets, and thus replace the energetic cost linked to curving the magnetisation field by a surface tension cost. Note that each of these anti-magnetised droplets have (up to finite size fluctuations) a zero total velocity: they are *not* collectively moving in opposite directions but are both still. At

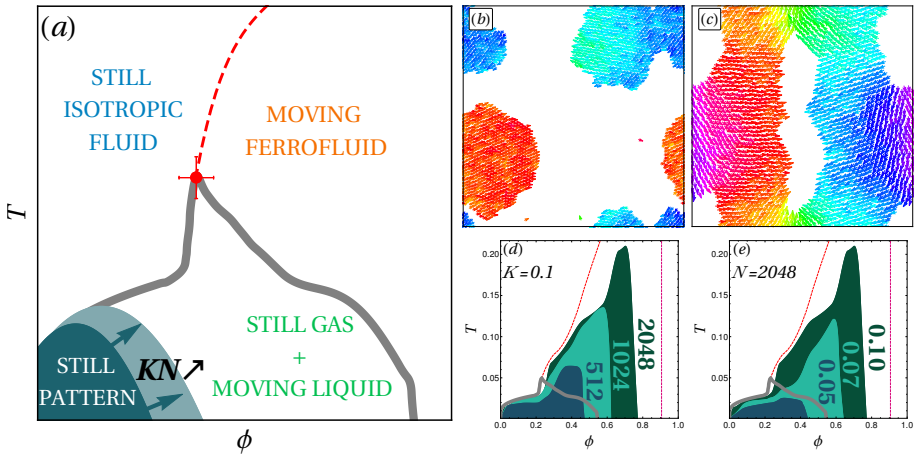

Fig. IV.12 **Density-Temperature phase diagram.** (a) Sketch of the finite-size phase diagram in the packing fraction, temperature plane, for a low value of KN. Increasing the value of KN bloats the patterned region with a small m. $(b)-(c)$ Examples of spin maps of low-temperature ($T \approx 0.01$) patterned phase-separated states: 2 anti-magnetised droplets obtained for $N = 2048, K = 0.05, \phi = 0.20$, and opened up vortices obtained for $N = 2048, K = 0.05, \phi = 0.40$. Spins are coloured depending on their orientation. $(d)-(e)$ Extent of the patterned regions, as obtained from simulations when varying (d) N at a fixed $K = 0.1$, or (e) K at a fixed $N = 2048$. The boundaries of the patterned states are obtained by visual inspection of states obtained by slow annealings, for 16 different values of the packing fraction in the interval $0 < \phi \leq 0.8$.

higher densities, closer to the right-most side of the coexistence line, patterns reminiscent of those observed in the homogeneous case are observed, as illustrated by Fig. IV.12(c). This configuration resembles the vortex configurations I described in the homogeneous case, but where the system decreased the cost of the magnetic pattern by "unzipping" the line between two of the vortices, thereby creating a hole with no topological charge. The holes at the cores of the two remaining topological defects are also enlarged, as ill-aligned spins are more repulsive. These patterned states are reminiscent of some steady-state solutions obtained for ABP-like self-propelled particles with a finite-range alignment interaction [66], suggesting that there might be a deeper link between these structures in the conservative setting and in the active setting. I also report in Fig. IV.12$(d-e)$ the location of such patterned states when varying N at a fixed K (Fig. IV.12(d)), and vice-versa (Fig. IV.12(e)). These results confirm the picture that increasing K or N causes the patterned region to invade the ferromagnetic domains of the phase diagram, starting from the bottom-left corner. Finally, for all considered values of K and N, the patterned domains are clearly below the Curie line at high densities, meaning that the order-by-disorder phenomenon illustrated in Fig. IV.3 is observed for various values of the density. In fact, it can even be observed in the phase-separated region for sufficiently low values of K and N.

IV.7 Summary

In this chapter, I studied the equilibrium properties of a $2d$ Hamiltonian model of a ferromagnetic spin fluid with a spin-velocity coupling. I showed that the homogeneous phases exhibit a rich behaviour, including the existence of frustration-induced topological defect configurations as ground states, ObD-like transition, and collective motion. Topological defects appear as a consequence of a classical spin-orbit coupling, which is reminiscent of the so-called topological phase transitions observed in quantum models when a spin-orbit coupling is added [229], and could have deeper connections with active matter, as parallels between quantum theories with a spin-orbit coupling and flocking have recently been proposed [230]. The same phenomenology is recovered for different values of the density, including in phase-separated regions. It is also recovered when moving from $d = 2$ to $d = 3$, or when changing the geometry of the boundary conditions. These results can therefore be seen as robust.

From the point of view of magnetism, this model can be thought of as an efficient dynamics to prepare topological defect configurations, for instance in dimension $d \geq 3$, in which case observing and describing topological excitations is notoriously challenging [231]. From the point of view of collective motion, the model seems limited in terms of the amplitude of the velocities it gives access to, especially for large systems. A solution would be to choose K such that it scales with the size of the system, at the cost of creating non-physical interactions. One could also in principle think of other coupling scheme between the spins and velocities, and hope for stronger effects. However, I showed in Sec. II.2 that the choice of the spin-velocity coupling is, in fact, very constrained by the requirement of having well-defined Hamiltonian dynamics. In practice, adding coupling terms beyond the quadratic order in velocity, leads to a situation in which the Hamiltonian dynamics can not be obtained from the Legendre transform of the Lagrangian [86]. I have also checked in Sec. IV.6.1 that adding a quadratic coupling to the model with a linear coupling $K \neq 0$ leads to the same phenomenology. The present model is therefore one of the *very few* reasonable conservative models in which a spin-velocity coupling leads to collective motion. Yet, the case of a model with only a quadratic coupling but no linear coupling, $K = 0$, can be of interest to describe a situation in which a nematic ordering of the velocities onto the direction of the spin is favoured. An example of such a nematic coupling was studied in a recent model of Vicsek-like particles with velocity reversals [87]. Finally, in the context of assemblies of self-propelled particles, regular arrangements of vortices [48, 67] and soliton-like structures [232–234] have been described in experiments, simulations, and microscopic models. This could be an indication that such structures are relevant in models of collective motion, regardless of the presence or absence of activity.

Chapter V

Dynamics of Moving Phases

> Il ne voyageait pas, il décrivait une circonférence. C'était un corps grave, parcourant une orbite autour du globe terrestre, suivant les lois de la mécanique rationnelle.
>
> Jules Verne, *Le Tour Du Monde en 80 Jours*

V.1 Overview: Hamiltonian Flocking?

I have shown in Chapter IV that collective motion can be observed as an equilibrium property of a finite-size, $2d$ Hamiltonian polar liquid in which particles carry unit vectors (spins) that are coupled to their velocity, corresponding to the Hamiltonian

$$\mathcal{H} = \sum_{i=1}^{N} \frac{1}{2}\boldsymbol{p}_i^2 + \sum_{i=1}^{N} \frac{1}{2}\omega_i^2 - \sum_{i=1}^{N} K\boldsymbol{p}_i \cdot \boldsymbol{s}_i + \frac{1}{2}\sum_{k\neq i} U(r_{ik}) - \frac{1}{2}\sum_{k\neq i} J(r_{ik})\cos\theta_{ik} \ . \quad \text{(V.1)}$$

However, surprisingly enough, I also showed in Sec. IV.5 that the alignment of instantaneous velocities, as captured by the polarity μ, only develops at very low temperature. This result is intriguing, as one would in general expect a collective velocity to be associated with a polar order of the velocities. The same is, in fact, true of some natural occurrences of collective motion. In flocks of birds, for instance, the "velocities" are in fact measured using pictures taken at two different times [235], and it is mentioned in the literature that if the time interval between pictures is too short (thus yielding a more accurate value of the instantaneous velocities), the measurements are marred by large disordered fluctuations attributed to wing flapping [14]. Likewise, the instantaneous velocities of systems of grains and colloids are likely to be disordered in dense, collectively moving phases, since they are reoriented at every collision with their neighbours. Assuming that wing flapping and collisions play a role similar to that of an equilibrium temperature, it

is therefore natural to introduce the time-integrated displacements of particles,

$$\boldsymbol{u}_i(\tau) = \int_0^\tau dt \boldsymbol{v}_i(t),$$

that smooth out thermal fluctuations of the velocities over a time scale τ.

In this Chapter, which mostly reproduces the results published in Ref. [77], I use these displacements as the observables of interest, and I focus on systems such that K and N are small enough for collective motion to be observed at low temperatures.[1] The selected velocity of the centre of mass is then imposed by the conservation of $\boldsymbol{P}$, which is fixed to zero, so that $\boldsymbol{v}_G + K\boldsymbol{m} = 0$, where $\boldsymbol{m} = \frac{1}{N}\sum_{i=1}^N \boldsymbol{s}_i$ and $\boldsymbol{v}_G = \frac{1}{N}\sum_{i=1}^N \dot{\boldsymbol{r}}_i$ are the intensive magnetisation and the velocity of the centre of mass, respectively. I here use the same interaction potentials as in Chapters III and IV,

$$J(r) = (\sigma - r)^2\Theta(\sigma - r)\ ,$$
$$U(r) = U_0(\sigma - r)^4\Theta(\sigma - r)\ ,$$

where Θ is a Heaviside step function, σ is the range of the interactions, that I fix to 1, and $U_0 = 4$ so that both potentials are equal at half range, resulting in an effective hard radius $r_0 = \sigma/4$ at zero temperature, through which I define the packing fraction $\phi \equiv \pi N r_0^2/L^2$. I then resort to the same "microcanonical" Molecular Dynamics (MD) simulations (described in Sec. II.2.3) to prepare equilibrated configurations at various energies, using a slow annealing procedure. These cold equilibrated configurations are used as initial configurations, from which I run the conservative dynamics defined by the Hamiltonian (V.1), and the statistical sampling is induced by the random choice of initial conditions.

In order to compare this system with examples of flocks from the active matter literature, which are described at rather low mean densities, I first simulate systems at a low average density, $\phi \approx 0.14$, and low temperatures, expecting to see phase-separated moving states. In Fig. V.1$(a)-(d)$, I show successive snapshots of the displacements $\boldsymbol{u}_i(\tau) = \boldsymbol{r}_i(\tau) - \boldsymbol{r}_i(0)$ of particles, integrated over a time $\tau = 100$ to remove thermal fluctuations, for $N = 512$ particles, with $K = 0.03$, and at a temperature $T \approx 1.9 \times 10^{-2}$. The pictures show a gas surrounding a liquid droplet, in which individual particle displacements are well aligned together, an object that I shall henceforth call a *Hamiltonian flock*. Their polarity, as defined in the context of flocks of birds [11], $\Phi \equiv (1/N)\sum_i \boldsymbol{u}_i/|\boldsymbol{u}_i|$ is here typically of the order of $\Phi \approx 0.9$, meaning that the droplet is in fact undergoing collective motion, as visible when comparing panels (a) through (d). However, these snapshots also reveal other aspects of the dynamics of Hamiltonian flocks. First, they show that the velocity of the flock does not move in a straight line, but also turns with time. Furthermore, one can see that the central drop exchanges particles with the surrounding gas, as expected in phase-separated states in equilibrium. Finally, it seems that the flock

[1] Note however that this chapter is a snapshot of my understanding of the dynamics as of September 2019, when the present manuscript was completed. Subsequent discussions with I. Giardina and A. Cavagna about the comparison with flocks have resulted in a greatly improved account of the comparison between Hamiltonian flocks and bird flocks, which was published as Ref. [77], following a comment [236] and a reply to the latter [237].

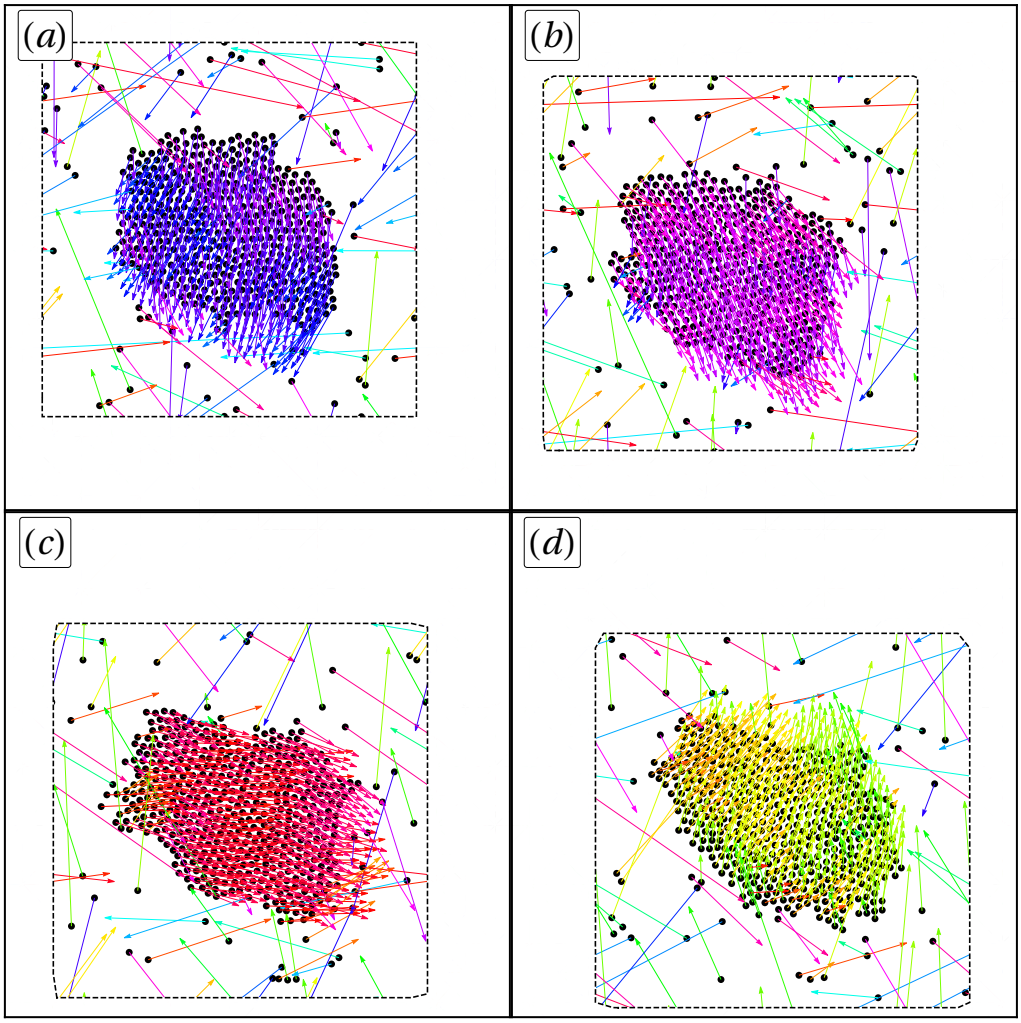

Fig. V.1 **Hamiltonian flocking.** $(a) - (d)$ Successive snapshots of the displacements of $N = 512$ particles, with $K = 0.03$, at a packing fraction $\phi \approx 0.14$, at a temperature $T \approx 1.9 \times 10^{-2}$, with snapshots separated by a time $\tau = 100$. Displacements are colour-coded according to their direction, and the periodic simulation box (dashed gray line) here follows the motion of the centre of mass of the system to "unwrap" the periodic boundaries.

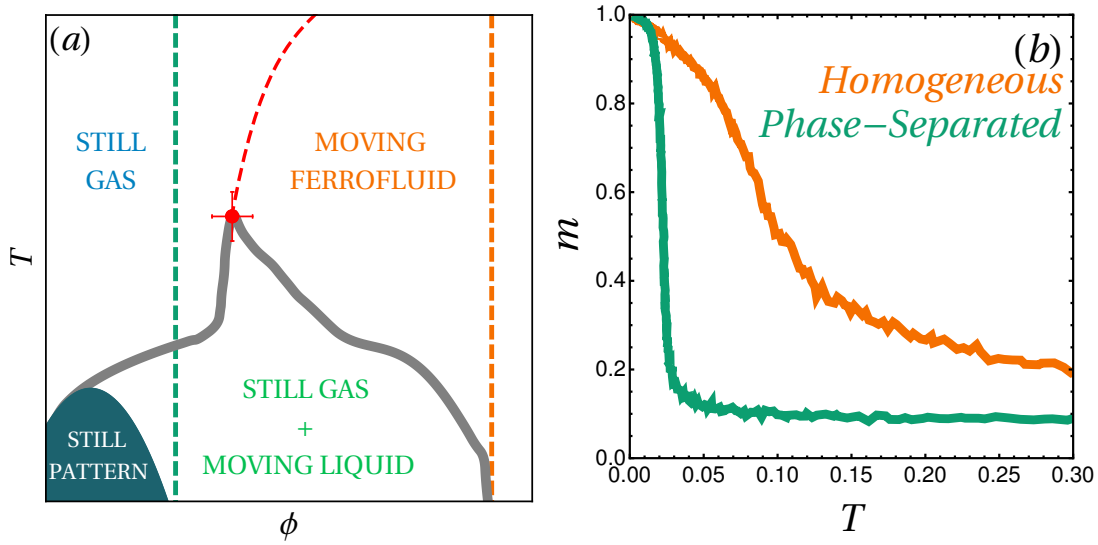

Fig. V.2 **Phase Diagram at finite N and K.** (a) Sketch of the finite-size phase diagram in the packing fraction, temperature plane, for a low value of KN. Increasing the value of KN bloats the patterned region with a small m [76]. The dashed orange and teal lines indicate the densities we chose to study in detail, $\phi = 0.55$ and $\phi \approx 0.14$. (b) Magnetisation modulus m versus the temperature for $N = 128, K = 0.23, \phi = 0.55$ (orange) and $N = 128, K = 0.03, \phi \approx 0.14$ (teal).

deforms, and even rotates a bit between snapshots, revealing that the particles inside the flock are here able to rearrange.

Altogether, it seems that Hamiltonian flocks display a very rich phenomenology, and many questions come to mind in the context of self-propelled systems. For instance: what is the aspect of a typical trajectory of a Hamiltonian flock? Do particles simply diffuse inside the flock, or do they display faster dynamics, like birds for instance [12]? How correlated are the displacements across the flock? And, overall, do Hamiltonian flocks resemble any kind of natural flock? In order to tackle these questions, in Sec. V.2, I start by focusing on spatially homogeneous flocks. The reason for this choice is that homogeneous phases are conceptually much simpler than phase-separated phases. These flocks are much easier to understand when separating the centre-of-mass and relative components of their displacements, which allows me to propose effective model inspired by usual models of self-propelled particles to describe the self-propelled regime. Then, in Sec. V.3, I discuss the main effects of lowering the density, and notably the development of spontaneous rotations of the flocks. I show that these rotations are at the origin of strong, scale-free displacement-displacement correlations reminiscent of those observed in natural flocks. Finally, in Sec. V.4, I sum up and comment on the results of this chapter.

V.2 Homogeneous States: Emergent Self-Propulsion

V.2.1 Strategy

In order to understand the physics that were hinted at in Fig. V.1, one must first recall the main properties of the phase diagram of the present system in finite size, that was established in Chapters III and IV. These important features are sketched, in the context of a small value of KN, in Fig. V.2(a). Due to the presence of a short-ranged ferromagnetic coupling, spins align with each other at low temperatures, resulting, in finite size, in a Curie line that separates a paramagnetic fluid and a ferrofluid. Because of momentum conservation, a magnetised state is always a moving one, so that these phases are here in fact a still fluid and a moving ferrofluid. The ferromagnetic coupling, because it is finite-ranged, also creates an effective attraction between aligned spins, that is sufficient to cause a phase separation (a Ferromagnetism-Induced Phase Separation, or FIPS) at low temperatures, between a still gas and a moving ferrofluid, with a tricritical point at the summit of the separation domain [75]. Finally, I showed in Chapter IV that, for finite values of K and N, the system chooses to kill off its total magnetisation at low temperatures and densities to avoid having to pay a high kinetic energy cost, by creating patterns such as vortices or solitons. As a result, in the limit of infinite sizes, the magnetisation transition is avoided both because the spins are at their lower critical dimension, and because of the cost of kinetic energy: magnetised, moving phases are only observable in finite-size samples. In the context of this chapter, I always tune K and N so that the still, patterned region of the phase diagram is sent to densities lower than the ones I consider. The system in Fig.V.1 was obtained at a density lower than that of the tricritical point, shown as a dashed green line in Fig. V.2(a). When varying the temperature at that density, the system magnetises and, therefore, self-propels, as it crosses the coexistence line, as shown in Fig. V.2(b), where I plot (in green) the magnetisation at the considered density, for $N = 128$, $K = 0.03$.

This phase-separated regime is *a priori* the most interesting one to compare to real-life collective motion. Yet, the numerical study of moving droplets is made more difficult compared to homogeneous phases due to the exchanges with the surrounding gas, deformations, and rotations of the droplets, as shown in the snapshots of Fig. V.1. For these reasons, I here start by characterizing the dynamical properties of the moving homogeneous liquid phase at higher density $\phi = 0.55$ (orange dashed line in Fig. V.2(a), with the corresponding curve $m(T)$ plotted in Fig. V.2(b)). For this study I set $N = 128$ and $K = 0.23$.

V.2.2 Homogeneous Moving States

I prepare equilibrated, homogeneous states at various temperatures, let the conservative Hamiltonian dynamics run and record the displacements $\boldsymbol{u}_i(t)$ of particles after a time t, for various initial times. I first look at the aspect of the trajectories of the centre of mass in the magnetized regime, two examples of which are shown in Fig. V.3(a) – (b). At high enough temperatures, Fig. V.3(a), these trajectories resemble persistent random walks, while at very low temperatures, Fig. V.3(b), they develop loops, that correspond to long coherent turns. To make sense of these trajectories, as described in Sec. II.4.3, it

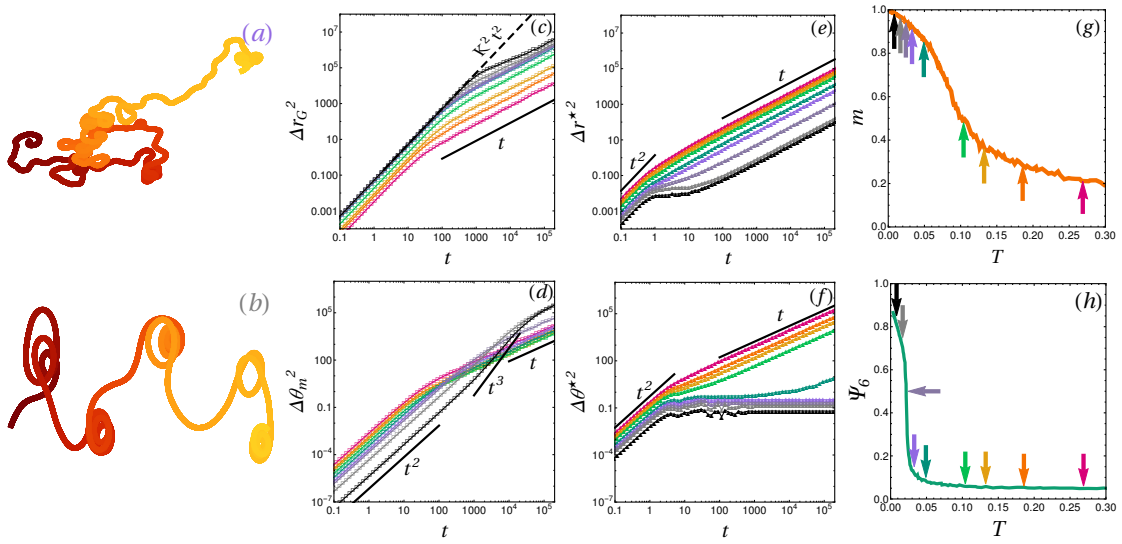

Fig. V.3 **Dynamics and Structure of Homogeneous phases.** $(a)-(b)$ Trajectories of the center of mass after a time $t = 20000$, with time going from red to yellow, for two temperatures corresponding to the (a) mauve, and (b) light gray curves from panels $(c)-(f)$. $(c)-(d)$ Center-of-mass (c) MSDs and (d) MSADs, divided by time, versus time, in log-log scale, for $N = 128, K = 0.23$ and at different temperatures (growing from black to red). The dashed black line in (c) indicates the zero-temperature collective speed $v = K$. $(e)-(f)$ Corresponding curves for the relative displacements. (g) Mean magnetization modulus versus the temperature corresponding to panels $(c)-(f)$. Arrows indicate temperatures of the MSD curves. (h) Mean hexatic order parameter corresponding to panels $(c)-(f)$.

is interesting to study how the Mean Square Displacement (MSD), $\Delta r^2 = \left\langle \frac{1}{N}\sum_i \boldsymbol{u_i}(t)^2 \right\rangle$ scales with time, as it reflects the type of motion that the particles undergo: for instance, if $\Delta r^2 \propto t^2$ the motion is ballistic, and if $\Delta r^2 \propto t$ the motion is diffusive. Here, I expect the centre of mass of the system itself to display rich dynamical behaviour, so that, rather than computing the full MSD, I define the displacement of the centre of mass,

$$\boldsymbol{u}_G(t) = \frac{1}{N}\sum_{i=1}^{N} \boldsymbol{u}_i(t),$$

and the relative displacements

$$\boldsymbol{u}_i^\star(t) = \boldsymbol{u_i}(t) - \boldsymbol{u}_G(t).$$

I then compute the associated Mean Square Displacements (MSDs) $\Delta r_G^2 = \langle \boldsymbol{u_G}(t)^2 \rangle$ and $\Delta r^{\star 2} = \left\langle \frac{1}{N}\sum_i \boldsymbol{u_i^\star}(t)^2 \right\rangle$, where the average is done over initial conditions. Likewise, I introduce the Mean Square Angular Displacements (MSADs) $\Delta\theta_m^2(t)$, associated to the orientation $\theta_m = \arctan(m_y/m_x)$ of the mean magnetization, and $\Delta\theta^\star(t)^2$, associated to the fluctuations around it. These quantities are plotted against time, in log-log scale, in Fig. V.3$(c)-(f)$.

The position $\boldsymbol{r}_G$ of the center of mass, panel (c), crosses over from a short-time ballistic motion to a long-time diffusive motion. Note that there is no short time diffusive regime, although it is generally expected in systems of self-propelled particles (see for instance Peruani *et al.* [238]), since the system is here not in a solvent, but isolated. Its centre of mass therefore behaves like a free particle at short times. The collective speed $v_G = Km$ grows as the temperature decreases, corresponding to the growth of the magnetisation modulus, which is recalled in panel (g). Since the magnetisation can *at most* be 1, the collective speed saturates to K at very low temperatures, a emphasized by the dashed black line in panel (c). The diffusion constant of the centre of mass, D_G also grows as the self-propulsion speed increases. The crossover time from one regime to the other, which is roughly given by

$$\tau_{r,G} = \frac{4D_G}{K^2 m^2},$$

grows as T decreases, indicating that D_G grows faster than v_G. In particular, D_G grows significantly at very low temperatures, when m is almost a constant. Note that, in very cold cases (mauve to black curves), a subdiffusive regime develops between the ballistic and diffusive regime, as further discussed below.

The direction θ_m of the magnetisation, panel (d), also crosses over from a short-time ballistic regime to a long-time diffusive regime. The ballistic regime indicates that the magnetisation follows inertial dynamics. The Hamiltonian equations of motion lead to $\ddot{\theta}_m = A_{int} - K \sum_i \boldsymbol{v}_i \cdot \boldsymbol{s}_i^{\perp}$, where A_{int} is the sum of all ferromagnetic interactions and $\boldsymbol{s}_i^{\perp} = \partial_{\theta_i} \boldsymbol{s}_i$. On average, we expect the interaction terms to compensate, while the spin-velocity term yields a typical $\dot{\theta}_m$ proportional to the typical speed. Consequently, this term decreases when the temperature is lowered, as velocities align more and more on their spin, as discussed in Chapter IV, and velocity fluctuations decrease like $\sqrt{T}$. The rotational diffusion constant, D_r, does not evolve monotonically with the temperature. In the paramagnetic phase, it decreases slightly as the temperature decreases. As the magnetisation crosses over, this decrease slows down, then turns into an increase. This increase corresponds to a growth of the crossover time from the ballistic to the diffusive regime, suggesting that inertia becomes stronger. This argument is supported by the development, at very low temperatures, of an intermediary superballistic regime that tends to $\Delta\theta_m^2 \propto t^3$, which can be attributed to an inertia so large that θ_m is almost uniformly accelerated, as further discussed in Sec. V.2.3. This superballistic rotation of $\boldsymbol{m}$ corresponds to the subdiffusive motion of $\boldsymbol{r}_G$: in this regime, the system does not explore space efficiently because it undergoes persistent turns.

The relative displacements, panel (e), also crosses over from a short-time ballistic regime to a long-time diffusive regime. In their case, the ballistic speed is set by the width of the thermal distribution of individual velocities around the collective one, that is essentially proportional to $\sqrt{T}$ (see Chapter IV). The diffusive regime simply corresponds to the usual self-diffusion of particles in the fluid. At very low temperatures, an intermediary subdiffusive regime appears: this behaviour is a well-known signature of the liquid-solid transition, as discussed in Sec. II.4. All in all, these relative displacements behave in a completely standard way for a fluid, in contrast with some natural realisations of collective motion like flocks of birds, that display superdiffusion even in the motion relative to the centre of mass [12]. Interestingly, the liquid-solid transition is concomitant

with the sudden increase of inertia that leads to turns, as shown by the increase of the hexatic order parameter [122], Ψ_6, shown in panel (h). The relative angular displacements, panel (f), follow the same general scenario: a ballistic regime with a speed given by $\sqrt{T}$, followed by a diffusive regime at high temperatures, and by a subdiffusive-diffusive pattern at temperatures below that of the magnetization crossover. Since this system is well described, for $K = 0$ and at low temperatures, by the spin-wave approximation [75], I posit that this dependence might be attributed to it as well. Recalling that the correlation length of spin waves is given by $\xi_{sw} \propto \exp(-T/T_0)$ [183], I expect the number of possible spin-wave excitations to go like the number of ways to fit objects of size ξ_{sw} in the simulation box, $N_{sw} \sim (L/\xi_{sw})^2$. Therefore, the number of possible excitations decreases exponentially as the temperature is decreased, so that the dynamics get blocked very violently when the magnetisation becomes large.

Finally, looking at the centre-of-mass and relative displacements (of both angles and positions) side by side, one sees that the former are typically larger than the latter at long times and low temperatures. Consequently, the dynamics of the system is dominated by "collective" displacements at long times and low temperatures, and by "thermal" displacements at short times and high temperatures.

In summary, the displacement data shows that, at low enough temperatures and long enough times, the present conservative system crosses over from a short-time regime in which displacements are dominated by the microscopic dynamics, that can be explained by standard magnetism and theory of liquids, to a long-time collective regime in which particles all follow the centre of mass. The latter seems to change its behaviour around the liquid-solid transition.

V.2.3 Effective Model

Having understood qualitatively the dynamics of the system, I now turn to a more quantitative description. Since, unlike in active systems like live flocks of birds [12], the relative motion here simply reflects the properties of a standard cohesive material, I focus on the dynamics of the centre of mass. Because of the conservation of the total momentum, its dynamics is entirely controlled by that of the magnetization vector $\boldsymbol{m}$. For simplicity, I neglect the fluctuations of the modulus of the magnetisation, so that $\boldsymbol{m} = m(T)\hat{\boldsymbol{e}}(\theta_m)$ with $m(T)$ the mean magnetisation modulus at temperature T and $\hat{\boldsymbol{e}}(\theta_m)$ a unit vector oriented with angle θ_m. I now seek a simple equation to describe the dynamics of θ_m.

In this goal, I write the expression of the intensive angular momentum, $\boldsymbol{\ell} = \boldsymbol{L}/N$, that is conserved due to the invariance under a joint rotation of space and spins (see Sec. II.2),

$$\boldsymbol{\ell} = \dot{\theta}_m \hat{\boldsymbol{e}}_z + \frac{1}{N}\sum_{i=1}^{N} \boldsymbol{r}_i \times \boldsymbol{p}_i,$$

where $\hat{\boldsymbol{e}}_z$ is the out-of-plane unit vector that completes the $3d$ direct basis $(\hat{\boldsymbol{e}}_x, \hat{\boldsymbol{e}}_y, \hat{\boldsymbol{e}}_z)$, and $\times$ is a vector product. I then decompose the positions, velocities, and spins as follows:

$$\begin{aligned}
\boldsymbol{r}_i &= \boldsymbol{r}_G + \boldsymbol{r}_i^\star, \\
\boldsymbol{v}_i &= -K\boldsymbol{m} + r_i^\star \Omega \hat{\boldsymbol{e}}_{\phi,i} + \boldsymbol{\delta v}_i, \\
\boldsymbol{s}_i &= \boldsymbol{m} + \boldsymbol{\delta s}_i,
\end{aligned}$$

where $\boldsymbol{r}_G$ is the position of the center of mass, $\boldsymbol{r}_i^\star$ is the position of particle i relative to the center of mass, $\boldsymbol{m}$ is the mean magnetization, Ω is the mean rotational velocity around the center of mass, $\hat{\boldsymbol{e}}_{\phi,i}$ is the orthoradial unit vector in the local polar basis centered on $\boldsymbol{r}_G$, $\boldsymbol{\delta v}_i$ is the remaining part of the velocity, that essentially contains thermal fluctuations (and potentially deformation modes that I do not explicitly consider here), and $\boldsymbol{\delta s}_i$ is the fluctuation of spin i around its mean value. Note that I here assume that the system has a well-defined centre of mass and is free to rotate around it, which is *a priori* impossible in the case of a homogeneous density in a periodic box. Using these decompositions, the angular momentum reads

$$\begin{aligned}\boldsymbol{\ell} &= \dot{\theta}_m \hat{\boldsymbol{e}}_z + \frac{1}{N}\sum_{i=1}^{N} \boldsymbol{r}_i^\star \times (r_i^\star \Omega \hat{\boldsymbol{e}}_{\phi,i} + \boldsymbol{\delta v}_i) + \frac{K}{N}\sum_{i=1}^{N} \boldsymbol{r}_i^\star \times \boldsymbol{\delta s}_i, \\ &= \dot{\theta}_m \hat{\boldsymbol{e}}_z + \left(\frac{1}{N}\sum_{i=1}^{N} r_i^{\star 2}\right) \Omega \hat{\boldsymbol{e}}_z + \frac{1}{N}\sum_{i=1}^{N} \boldsymbol{r}_i^\star \times (\boldsymbol{\delta v}_i + K \boldsymbol{\delta s}_i), \\ &= \dot{\theta}_m \hat{\boldsymbol{e}}_z + I\Omega \hat{\boldsymbol{e}}_z + \boldsymbol{\delta \ell},\end{aligned}$$

where I introduced the mechanical moment of inertia I and the angular momentum fluctuations $\boldsymbol{\delta \ell}$. Note that $\boldsymbol{\delta \ell}$ has no reason to be small, but that I essentially consider it like a random number that results from the Gaussian distributions of velocity fluctuations and spin fluctuations. Looking at the expression of this conserved angular momentum, one could expect spontaneous rotations or deformations of droplets in response to an angular acceleration of the magnetization: this is further discussed in Sec. V.3. Here, instead, I make the (strong) assumption that $\Omega \propto \dot{\theta}_m$ at all temperatures. I call f a putative constant proportionality factor, such that $\Omega = f\dot{\theta}_m$. Under this assumption, the equation of motion (projected onto the vertical axis) reads

$$0 = \ddot{\theta}_m(1 + fI) + f\dot{I}\dot{\theta}_m + \eta.$$

In this form, assuming that $\dot{I}$ and I can be treated as constants in this discussion, one can identify a characteristic inertial time

$$\tau_m \sim \frac{1 + fI}{f\dot{I}}. \tag{V.2}$$

This time grows as the moment of inertia increases, but also as the deformation dynamics (encoded by $\dot{I}$) are suppressed. In other terms, the characteristic time should here increase as the system becomes rigid.

I therefore posit that the dynamics of the centre of mass can, even in the case of a homogeneous system, be described by the equations

$$\begin{aligned}\boldsymbol{v}_G &= -K\boldsymbol{m}, \\ \tau_m \ddot{\theta}_m + \dot{\theta}_m &= \sqrt{D_r}\tilde{\eta}_G,\end{aligned}$$

where τ_m is an effective memory time, D_r is the rotational diffusion constant, and η_G is a gaussian white noise such that $\langle \eta_G(t) \rangle_\eta = 0$, and $\langle \eta_G(t)\eta_G(t') \rangle_\eta = 2\delta(t - t')$, with the average taken over realization of the noise. Equation V.2.3 states that the total momentum is strictly conserved, so that the dynamics are fully determined by the fluctuations of

the magnetisation vector $\boldsymbol{m}$. Equation V.2.3, on the other hand, states that the angular velocity of the magnetization vector follows an Ornstein-Uhlenbeck process. I therefore call this model one of an Angular Velocity Ornstein-Uhlenbeck Particle (AVOUP). This model was introduced in the context of modelling of experimental living systems, ranging from microtubules to flatworms [30, 48, 67, 239], that display large-scale synchronizations into circular motion, that are reminiscent of Fig. V.3(b). It is also a variant of the Active Brownian Particles (ABPs) model [60], that is recovered for $\tau_m \to 0$. It is possible, for ABPs both without [60, 170] (see Sec. II.4.3) and with memory [171] to write the exact expression of the effective diffusion constant acting on the position, D_G as a function of the self-propulsion speed, of the rotational diffusion constant D_r and, in the case of AVOUPs, of the memory time τ_m. For Eqs. V.2.3 and V.2.3, these predictions are

$$D_G^{ABP} = \frac{K^2 m(T)^2}{2D_r},$$
$$D_G^{AVOUP} = D_G^{ABP}\Gamma(\tau_m D_r)\sum_{n=0}^{\infty}\frac{(\tau_m D_r)^{n+1}}{\Gamma(n+1+\tau_m D_r)},$$

where I introduced the Euler Γ function. The last expression can be approximated by a Borel summation [240] of the series it contains,

$$D_G^{AVOUP} \approx D_G^{ABP}\Gamma(\tau_m D_r)\int_{t=0}^{\infty} ds\, e^{-s}\sum_{n=0}^{\infty}\frac{(\tau_m D_r)^{n+1}}{\Gamma(n+1+\tau_m D_r)}\frac{s^n}{n!},$$

which can be rewritten exactly (at the cost of introducing the incomplete Gamma function $\hat{\Gamma}(a,z)$ [101]) as

$$D_G^{AVOUP} \approx D_G^{ABP} e^{\tau_m D_r}\,(\tau_m D_r)^{1-\tau_m D_r}\left(\Gamma(\tau_m D_r) - \hat{\Gamma}(\tau_m D_r, \tau_m D_r)\right),$$

thus enabling numerical evaluations.

I use the prediction V.2.3 of the diffusion constant to validate that AVOUPs constitute a good effective description of the motion of the centre of mass. In order to do so, I extract D_r from the long-time diffusive behaviour of θ_m, and τ_m from a short-time exponential fit of the two-time autocorrelation $C(t) = \langle\dot{\theta}_m(0)\dot{\theta}_m(t)\rangle_0$, where the average is computed over initial conditions, with a normalization such that $C(0) = 1$. These inputs of the model are plotted against the temperature in Fig. V.4(a). Notice that τ_m rises concomitantly with Ψ_6, confirming that the orientational inertia of the magnetization is linked to the rigidity of the system, as inferred from the development of plateaux in Fig. V.3, and from the naïve estimate of Eq. (V.2). I then plot in Fig. V.4(b) the values of D_G measured using the long-time behaviour of ${\Delta r_G}^2$, as well as estimations using the AVOUP model (blue) and its zero-memory limit, the ABP model (red).

The AVOUP description yields a very good estimation of D_G at all considered temperatures, and the zero-memory limit is essentially only valid at temperatures such that the magnetization is still low. To further confirm that AVOUPs provide a satisfying description, I show in the insets of Fig. V.4(b) a few trajectories obtained by integrating AVOUPs dynamics for various memory times. They are good qualitative reproductions of the trajectories shown in Fig. V.3(a) – (b). The AVOUP description is therefore a

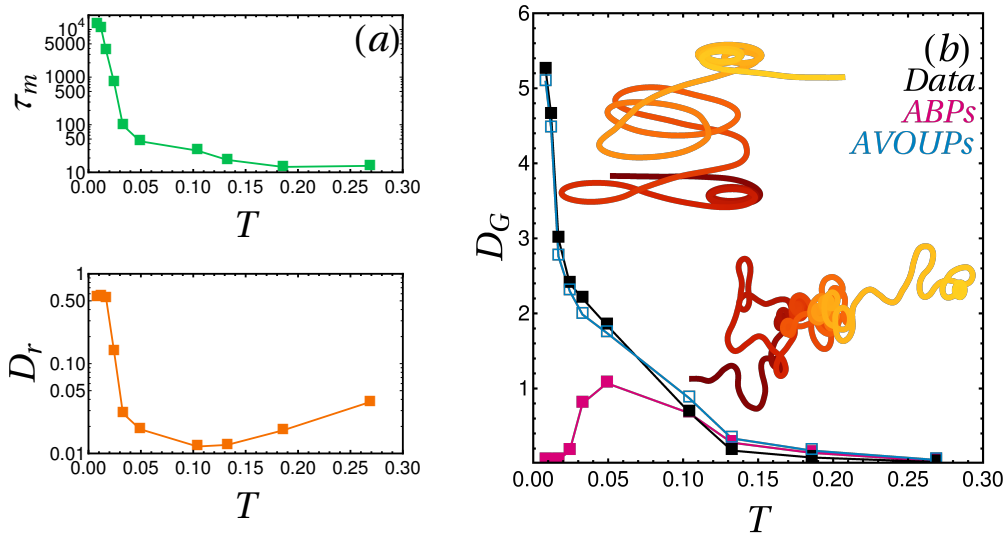

Fig. V.4 **AVOUPs Dynamics.** (a) Autocorrelation time τ_m versus the temperature T (top), and rotational diffusion constant (bottom), versus the temperature, both in lin-log scale. (b) Main panel: Effective diffusion constant of the center of mass against the temperature (black), together with the ABP (red) and AVOUP (blue) estimations. Inset: Trajectories, with time going from red to yellow obtained by integrating the AVOUP equations of motion over a time 10000, with an integration step $dt = 1$, a fixed value of $Km = 0.1$ and of $D_r = 1$. From left to right,setting τ_m is set to 5000, and 500.

good model of the dynamics of the centre of mass, that behaves like a single self-propelled particle. It is important to stress, however, that this description is *not* valid at the scale of individual particles: self-propulsion is here a property that emerges at the scale of the whole system, although the motion of particles relative to the centre of mass is typical of standard, passive dense phases. Finally, note that the superballistic behaviour of the angles is recovered in the large inertia limit $\tau_m \to \infty$, which yields a random-acceleration process (RAP), $\tau_m \ddot{\theta}_m = \sqrt{D_r}\tilde{\eta}_G$, that behaves like $\Delta\theta_m^2 \sim t^3$ at long times [241]. In fact, this regime was recently linked to looping trajectories in the context of self-propulsion with memory [242].

V.3 Phase-Separated States: Spontaneous Rotations

V.3.1 Angular Momentum Conservation

Having understood the main features of the dynamics of homogeneous phases, I now go back to the more complicated issue of phase-separated states. The AVOUP description and the general features of the trajectory of the centre of mass are almost unchanged in the context of a moving droplet. The only major difference occurs at very low temperatures, such that the system is very magnetised, structurally ordered, dynamically frozen, and immersed in a gas with an extremely low density. Under these circumstances, as shown in Fig. V.5(a) – (b), the relative displacements display a second ballistic regime at

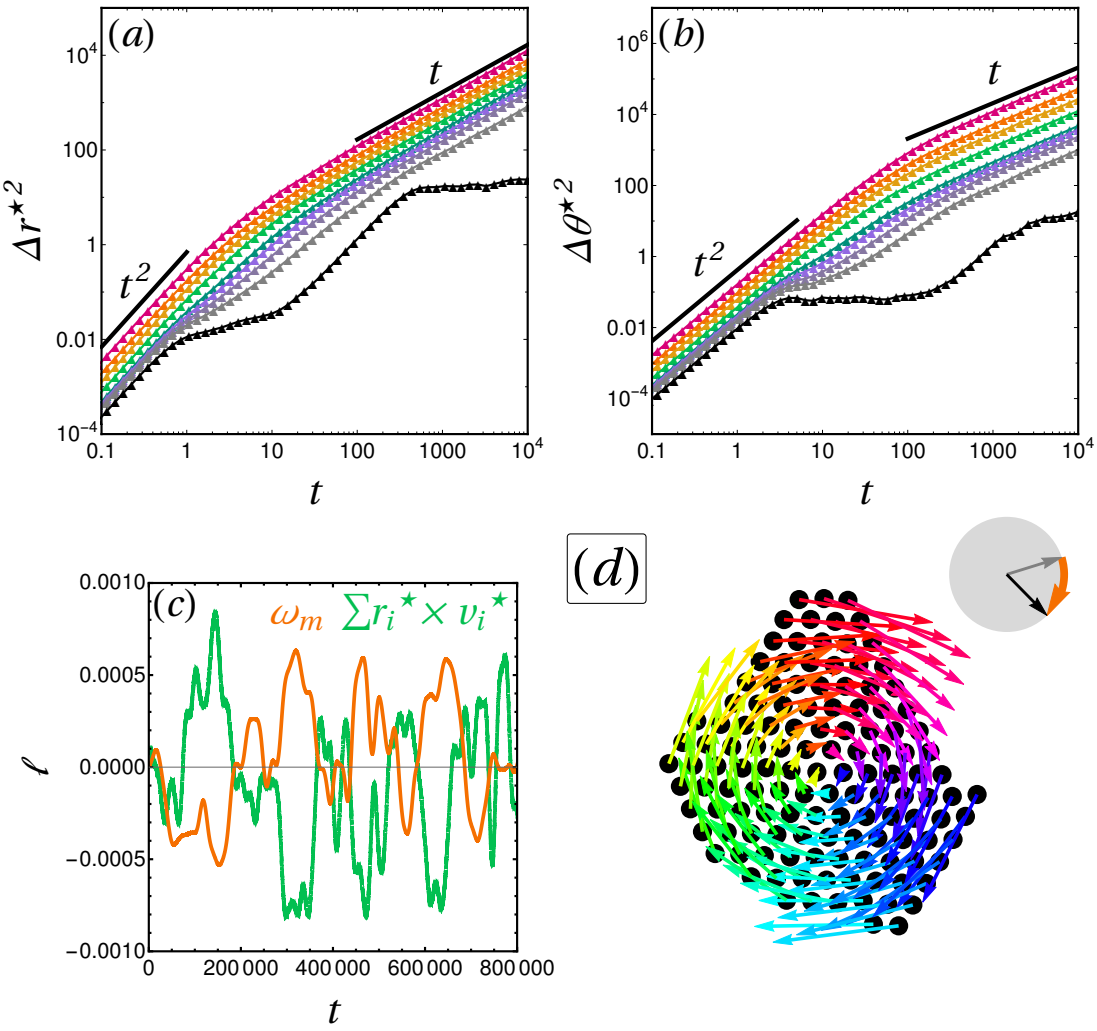

Fig. V.5 **Spontaneous Rigid Rotations.** $(a) - (b)$ Relative (a) MSDs and (b) MSADs obtained for $N = 128, K = 0.03, \phi \approx 0.14$ for various temperatures, growing from black to red. (c) $\omega_m = \dot{\theta}_m$ (orange) and $\sum \boldsymbol{r}_i^\star \times \boldsymbol{v}_i^\star$ (green), time-averaged over a time window with width $\tau = 10^2$, versus time. (d) Snapshot of relative displacements, integrated over a time $\Delta t = 2 \times 10^4$, colour-coded according to their orientation and rescaled by their mean value. In the inset of each panel, we show the initial magnetization vector (grey arrow), the final magnetization (black arrow), and the direction of the magnetization rotation (orange curved arrow).

intermediary times. To understand the origin of this new ballistic regime, I go back to the expression of the conserved angular momentum,

$$\boldsymbol{\ell} = \dot{\theta}_G \hat{\boldsymbol{e}}_z + I\Omega\hat{\boldsymbol{e}}_z + \boldsymbol{\delta\ell}.$$

The time derivative of this quantity should be zero, yielding

$$\mathbf{0} = \ddot{\theta}_G \hat{\boldsymbol{e}}_z + \dot{I}\Omega\hat{\boldsymbol{e}}_z + I\dot{\Omega}\hat{\boldsymbol{e}}_z + \boldsymbol{\eta},$$

where I noted $\boldsymbol{\eta} = \boldsymbol{\delta\dot{\ell}}$. This equation states that, in response to a change of angular velocity of the magnetization, the system can retain a conserved angular momentum by choosing one of the following solutions. First, it can change its moment or inertia, i.e. undergo a radial deformation. Second, it can change the velocity of its rigid rotation. Third, it can absorb the change into thermal fluctuations of the velocities and spins. In the very low-temperature, rigid phases, the most likely compensation is a rigid rotation. Intuitively, one expects the deformation part to be important in cold liquid states, when deformations are possible but thermal fluctuations are relatively small. Likewise, one expects the thermal part to dominate in hot phases. In the case of Fig. V.5$(a)-(b)$, the second ballistic regimes of the coldest curve should therefore correspond to rigid rotations around the centre of mass of the droplet. At very low temperatures, and on the time scales on which the second ballistic regime is observed, these rotations should essentially verify $\dot{\theta}_m = -I\Omega$. This is confirmed when plotting time-averaged versions of $\dot{\theta}_m$ and $\sum \boldsymbol{r}_i^\star \times \boldsymbol{v}_i^\star/N$, like in Fig. V.5$(c)$. The aspect of the associated displacement fields is illustrated in the snapshot shown in Fig. V.5(d). In summary, cold rigid droplets of this system display spontaneous rotations around their centre of mass, that are opposed to rotations of the magnetisation, which themselves control the shape of the trajectory. This phenomenology is sketched in Fig. V.6. These spontaneous rotations are reminiscent of similar phenomena

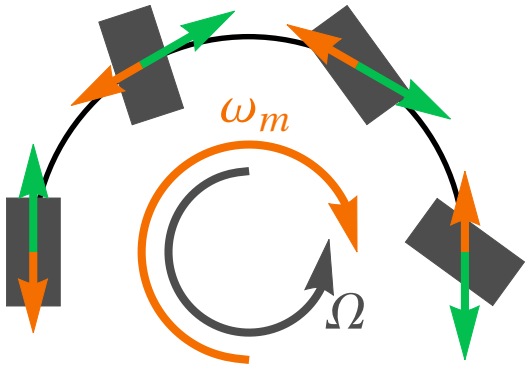

Fig. V.6 **Typical Dynamics of a Cold Droplet.** The magnetization $\boldsymbol{m}$ (orange) imposes the velocity of the centre of mass (green). If $\boldsymbol{m}$ starts turning at a rate ω_m, the trajectory displays a turn, and the droplet rotates around its centre of mass, opposite ω_m, at a rate $\Omega = I\omega_m$.

in biological systems like flocks of birds [11], dense shaken granulars [40], or clusters of cells [243], and in some abstract models of active matter [64, 65, 244]. Interestingly, although they generally violate energy and momentum conservations, systems of polar,

self-propelled particles are often argued to be invariant under rotations of space and polarities, which is exactly the condition for a "generalised" angular momentum, that depends on the polarities of particles, to be conserved. It would therefore be interesting to check in these systems whether such a conservation law could account for the observed spontaneous rotations.

V.3.2 Displacement-displacement Correlations

Finally, inspired by the study of flocks of birds [11], I compute, in the cold droplet regime, the spatial correlation of the relative displacements,

$$C_d(r,\tau) = \frac{1}{c_0} \frac{\sum\limits_{j\neq i} \boldsymbol{u}_i^\star(\tau)\boldsymbol{u}_j^\star(\tau)\delta(r-r_{ij})}{\sum\limits_{j\neq i}\delta(r-r_{ij})},$$

where c_0 is a normalization factor that ensures $C_d(0) = 1$, and δ is a binning function. This function is plotted with $\tau \approx 10^3$ against the distance r, rescaled by the largest distance in the droplet, r_{max}, for three system sizes ($128, 512, 2048$ particles, with $K = 0.03, 0.03, 0.001$ respectively to ensure motion), at $T \approx 10^{-2}$ in Fig. V.7(a). For all considered sizes, I observe the same pattern with strong correlations for $r/r_{max} \leq 0.48$, and strong anticorrelations for $r/r_{max} \geq 0.48$. These correlations do not depend on any length scale other than the size of the flock: they are scale-free. I also plot in Fig. V.7(b) the equivalent function for speed fluctuations,

$$C_{sp}(r,\tau) = \frac{1}{c_0} \frac{\sum\limits_{j\neq i} \delta c_i(\tau)\delta c_j(\tau)\delta(r-r_{ij})}{\sum\limits_{j\neq i}\delta(r-r_{ij})},$$

where

$$\delta c_i(\tau) = |\boldsymbol{u}_i(\tau)| - \frac{1}{N}\sum_{k=1}^{N} |\boldsymbol{u}_k(\tau)|\,.$$

Likewise, I find scale-free correlations, as shown in Fig. V.7(b), this time with a strong correlation at short- and long-range, but a strong anticorrelation around $r/r_{max} \approx 0.5$. These patterns are here simply another representation of a rigid rotation displacement pattern, such as the one shown in Fig. V.5(d): a rigid rotation is exactly a correlation of the relative displacements at the scale of the size of a system. A more quantitative argument is obtained when computing C_d numerically for a homogeneous rigid disk rotating at a constant rate. The result, obtained for 2.10^6 shots of a Monte Carlo integration, yields the dashed black lines of Fig. V.7, and captures the shape obtained in simulations. Note that the shape of C_d can be computed analytically: the calculation is reproduced in App. C.

In other words, the present model captures a non-trivial feature of flocks of birds, the spontaneous build-up scale-free correlations of fluctuations of the velocities and speeds [11], but they are here solely caused by rigid rotations. This result is interesting, since the usual explanation for the correlations of C_d in flocks of birds is that the velocities of birds essentially have a nominal modulus and should behave like continuous, XY-like spins. As a result, Cavagna *et al.* argue that, because of their continuous rotational symmetry, they

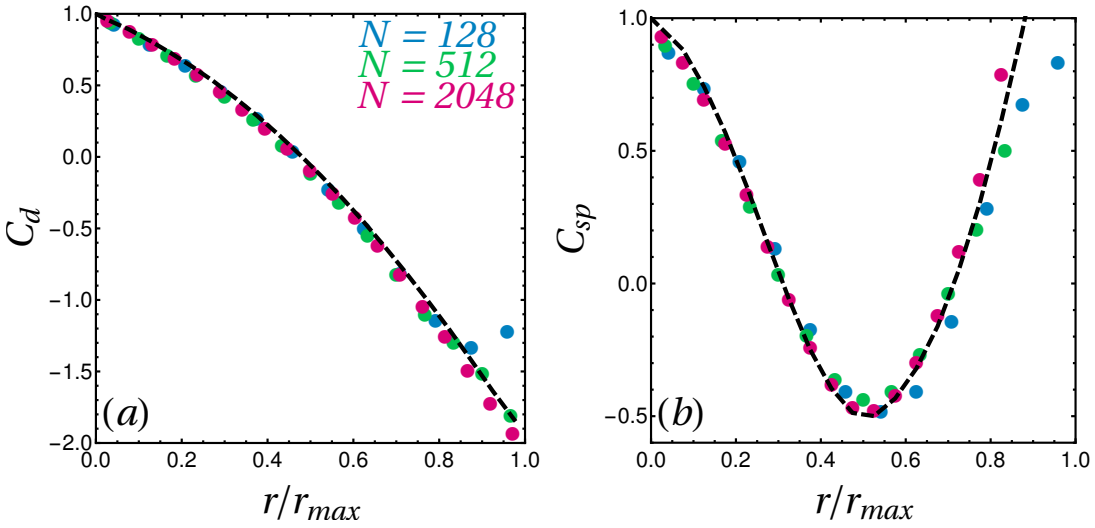

Fig. V.7 **Scale-free, long-ranged correlations.** (*a*) Displacement correlations $C_d(r,\tau)$ against the distance normalised by the largest distance in the droplet, for system sizes growing from blue to red. (*b*) Corresponding curves for C_{sp}. The dashed black lines are numerical estimations for a homogeneous disk rotating at a constant speed. r_{max} roughly goes from 12 particle diameters ($N = 128$) to 48 particle diameters ($N = 2048$).

should be susceptible to Goldstone modes, in the same way as spins. This argument does indeed provide an interpretation for the form of C_d, but not for that of C_{sp}. The result of Fig. V.7 suggests that, seeing the velocities of the flock not as spins, but as displacements in a solid body provides a simple explanation for a scale-free behaviour of both C_d and C_{sp}: any small amount of rigid body rotation in flocks of birds could be responsible for scale-free correlations. This idea is supported by detailed studies of the coherent turns of flocks of birds. These studies have shown that a finite inertia (that dominates at short time scales) is necessary to account for the propagation of turning information across flocks, which is in fact a spin wave, also called "second sound" by analogy with ultracold helium [14, 245]. At this short time scale, the flock structure typically does not rearrange [12, 14]: it is rigid.

An obvious loophole in this explanation is that the shape of the correlation functions described by Cavagna *et al.*, which is reminded in Fig. V.8$(a)-(b)$, is slightly different from the shapes shown in Fig. V.7. This difference can be attributed to either of three reasons: first, the density in flocks is not homogeneous, it is higher at the boundary [10]. Intuitively, this density profile, compared to the homogeneous case, should lead to lower absolute values of the correlation functions at long distances, and shift the curves off-centre. These intuitive consequences are compatible with the shift between the observations and the calculation in the case of a homogeneous disk shown in Fig. V.8$(a)-(b)$. Second, flocks are not perfectly circular, they are generally elliptic in the two directions of large extension, which should mostly off-centre the correlation functions. Finally, and most importantly, the displacement fields can have other components than simple rotations. To measure the importance of this last effect, I use the data in the SI of Ref. [11], that corresponds to

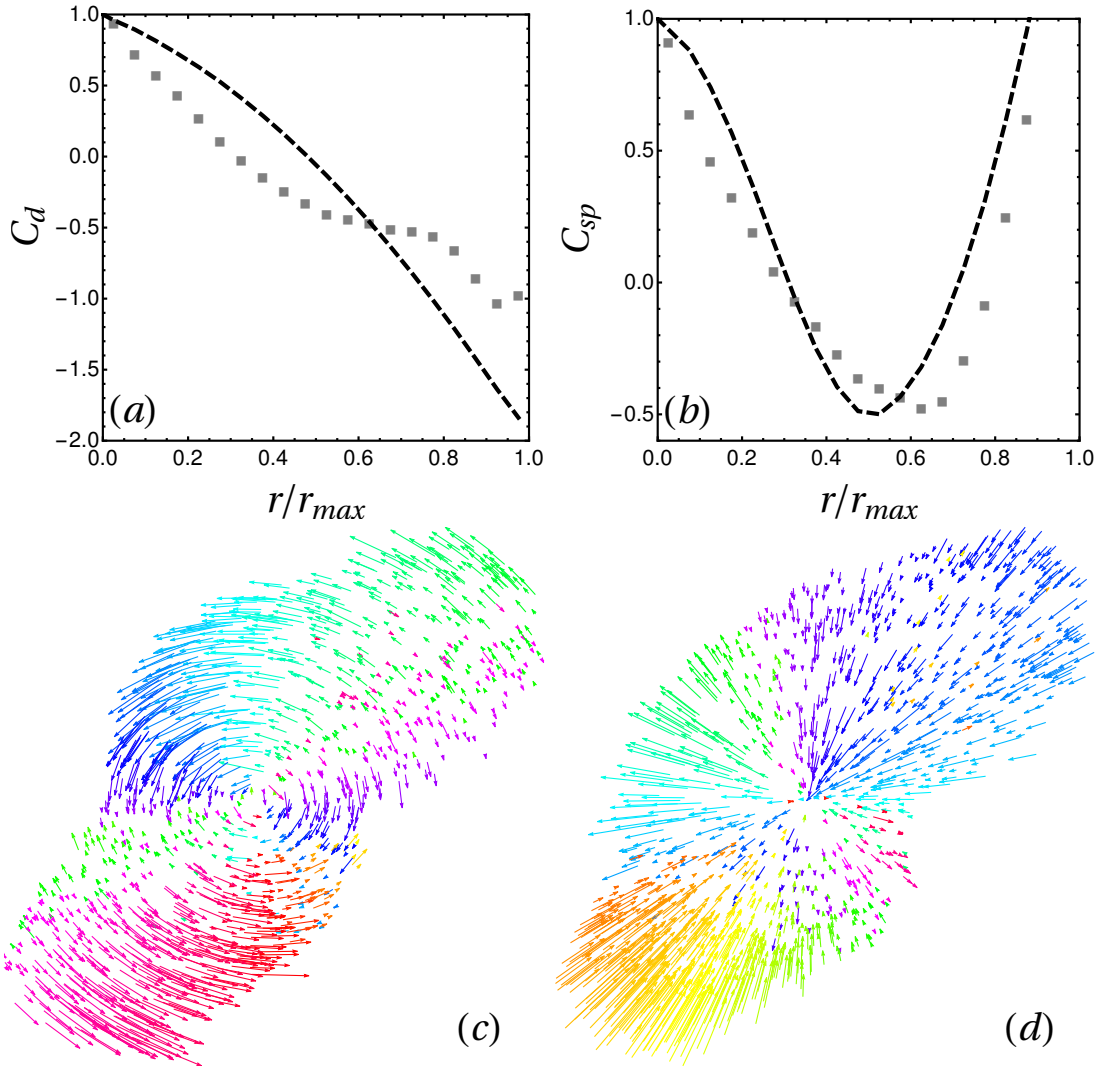

Fig. V.8 **Bird Displacement Fluctuations.** (*a*) Displacement correlations $C_d(r,\tau)$ against the distance normalised by the largest distance in the flock, computed from the SI of Ref. [11]. (*b*) Corresponding curves for C_{sp}. The dashed black lines are numerical estimations for a homogeneous disk rotating at a constant speed. (*c*) Azimuthal displacement fluctuations around the main rotation axis in the flock, colour-coded according to their direction. (*d*) Projected radial displacement fluctuations around the centre of mass of the flock, as seen from above the main rotation axis.

one realisation of a flock. In this flock, I seek the main rotation axis (Δ), by computing the sum $\sum \boldsymbol{r}_i \times \boldsymbol{v}_i$. I then use this axis as the zenith direction of a spherical coordinate system, centered on the centre of mass of the flock, and I decompose the displacement fluctuations into their radial, polar, and azimuthal components. I find that the polar component (carried by the $\hat{\boldsymbol{e}}_\theta$ unit vector in polar coordinates) is typically much smaller than the other two, so that I omit it in this discussion. The azimuthal component (carried by the $\hat{\boldsymbol{e}}_\phi$ unit vector in polar coordinates) contains the rotation part of the displacements around the chosen zenith direction. The measured field, with all birds represented in the plane perpendicular to (Δ) is plotted in Fig. V.8(c), with a rescaling factor such that all displacements are visible. Although it is not a perfect solid rotation, this picture shows that there is indeed some rigid rotation in the flock, which could account for correlations akin to those observed in my system. Finally, the radial component, which contains the dilatation and compression parts of the displacement field, is plotted in Fig. V.8(d), at the same scale as the azimuthal field. This picture shows that the radial component is locally as large as the azimuthal one, so that it could modify the shape of the displacement-displacement correlations. Additionally, it roughly assumes the shape of a quadripolar field: the long direction of the flock is compressed, and the short one expanded. If this shape is a general one across different flocks, it would mean that flocks of birds have a finite Poisson ratio, a property of elastic solids [246]. This finite elasticity could also partly explain the difference between the correlation curves obtained in natural flocks and in the Hamiltonian flocks studied in this thesis. Indeed, while Hamiltonian flocks are defined with finite-range, metric interactions, birds interact with non-metric (typically visual) interactions [15], that intuitively allow for stronger elastic effects, since the distances between birds are not fixed by an underlying potential.

V.4 Summary

In this Chapter, I have shown that my conservative model of collective motion is characterized by a very rich dynamical behaviour compared to standard equilibrium dynamics. Indeed, at low temperatures, displacements develop a strong polar order, that is associated to a long-time, collective ballistic regime, that is reminiscent of systems of active self-propelled particles [60, 65, 244]. At even longer times, an effective diffusion is also found due to spontaneous rotations of the magnetisation at the bottom of its Mexican hat potential with a finite inertia, leading to looped trajectories. This rotation develops a larger and larger inertia as the temperature decreases, with a sharp increase at the rigidity transition associated to the buildup of a large moment of inertia. Due to the conservation of angular momentum, this rotation of the magnetisation is accompanied by a spontaneous rotation of the Hamiltonian flock. These spontaneous rotations are reminiscent of similar phenomena in systems of self-propelled particles, both in experiments [11, 40, 243], and in abstract models of active matter [64, 65, 244, 247]. Since these systems are generally invariant under rotations, it would be interesting to check whether such rotations could be attributed to the conservation of a generalized angular momentum, that would contain terms that depend on the polarities of particles.

In the special case of birds, this idea is also supported by the fact that a finite rotational inertia was shown to be responsible for long coherent turns [14], akin to the loops

of Hamiltonian flocks. While it was shown that bird flocks are not structured liquids in the usual sense (their pair correlation function is that of a disordered liquid [235]), they are often studied at time scales that are short in front of the typical time of neighbour reshuffling. In other words, they are often studied at time scales at which they behave like solids. From this point of view, it might be interesting to see flocks, not as systems of continuous spins, but as elasto-visco-plastic objects undergoing rotations, elastic deformations, and plastic deformations. These rotations and deformations might shed another light on the displacement-displacement correlation functions of these systems.

Finally, birds are known to interact through non-metric interactions [15]. Therefore, pushing the parallel between solids and flocks even further, one could expect that flocks of birds move almost like a solid at the considered time scales because they are, in fact, rigid, although in a non-metric sense. Indeed, recent works on liquids with topological interactions, defined through their Voronoi tessellation, have shown that they can be described like usual liquids, and feature liquid-solid transitions, both to crystals and glasses [248, 249]. Therefore, perhaps a more thorough comparison between the physics of flocks of birds and that of Voronoi liquids would help rationalise the position of flocks of birds in the usual categories of the physics of liquids.

Chapter VI
Conclusion

> Je n'ai fait cette lettre-ci plus longue que parce que je n'ai pas eu le loisir de la faire plus courte.
>
> Blaise Pascal, *Les Provinciales*

VI.1 Summary

In this thesis, I have studied a model of interacting particles carrying spins, that align ferromagnetically at short range, with a spin-velocity coupling. This seemingly simple model was suggested as a candidate to observe collective motion without the addition of any activity, that would be due to the breaking of the Galilean invariance alone. It however inherits the combined complexity of the physics of $2d$ polar liquids, of the $2d$ magnetism of XY spins, and of the unusual conservation laws induced by its non-Galilean nature. As a result, prior to this thesis, the complete phase diagram of this system in finite size was a completely open question. In particular, it was not clear how much the magnetic properties resembled usual spin systems, or what was the mechanism behind the emergence, or suppression, of collective motion. Furthermore, although zero-temperature snapshots had demonstrated that collective motion was observed in some situations, the ordering of the velocities themselves, and the connections with usual self-propelled systems was left undiscussed.

In the absence of a spin-velocity coupling, I have shown that, even for purely repulsive interaction potentials, the aligning interaction can create a spin-mediated attraction. As a result, in $2d$, a fluid of particles carrying aligning XY spins phase separates between an isotropic gas and a ferroliquid. In finite size, the ferroliquid develops a macroscopic magnetisation below a finite crossover temperature, following a scenario that is different from that of an on-lattice XY model. In particular, I showed that the magnetisation crossover was not associated to the unbinding of vortex pairs. Finally, I showed, both numerically and using original mean-field level descriptions, that the finite-size Curie line is also the left-most spinodal of the liquid-gas phase separation. Consequently, a tricritical point sits at the top of the phase separation domain, and the relaxation dynamics of the liquid and magnetic orderings are synchronized on each other.

Adding a spin-velocity coupling, by breaking Galilean invariance, enables the fluid to spontaneously develop a collective velocity in the low-temperature magnetised phase, despite the conservation of energy and momentum. Having shown that the shape of the spin-velocity coupling itself is highly constrained by the requirement that the dynamics remain conservative and that the Lagrangian to Hamiltonian switch is do-able analytically, I have checked that this collective motion is indeed observed at low temperatures, provided that the system size and the spin-velocity couplings are made small enough that the kinetic energy is not too costly compared to the ferromagnetic coupling energy. In large systems and for large spin-velocity couplings, due to a frustration between the energy and momentum conservations, moving polar states are replaced by states in which the total magnetisation is zero while the local magnetisation is high. The states selected by this frustration are, in homogeneous states, solitons and vortex-antivortex pairs that span the periodic box. The shape of these states, as well as their stability domains, are predicted through simple energetic arguments. Switching on the temperature, I have shown that these topological states could develop a finite magnetisation, that reaches a maximum at a finite temperature. This unusual "order-by-disorder" feature can here be explained qualitatively by the lowering of the cost of kinetic energy as the magnetisation decreases. The same phenomenology is recovered in the phase-separated regime, in different geometries, and in a higher-dimensional space. Therefore, spin-velocity couplings in spin fluids lead to the emergence of collective motion at a finite temperature and across a finite interval of densities, at the cost of making either the spin-velocity coupling or the size of the system small enough.

Focusing on the collectively moving phases, I have shown that their dynamics can be decomposed into a centre-of-mass and a relative component. While the relative component simply reflects the equilibrium properties of the fluid, the centre-of-mass component is reminiscent of the dynamics of self-propelled particles. I have shown that the motion of the center of mass can, in fact, be accurately described by a single Active Brownian Particle, with a spin inertia that plays the role of a memory. Interestingly, while the memory time is usually a parameter that is set externally in models of self-propelled particles, it is here a function of the temperature. As a result, the aspect of the trajectory of the centre of mass changes dramatically as the system becomes rigid, and persistent loops appear. In phase-separated systems, due to the conservation of angular momentum, I have shown that these loops were associated to spontaneous rotations of self-propelled droplets. These rotations, as well as the coherent turns in the trajectories, raise the question of the importance of the conservation of angular momentum and of the rigidity in natural flocks.

Altogether, I have shown that conservative models with spin-velocity couplings can display spontaneous collective motion at low temperatures. This collective motion is observed across finite intervals of the control parameters, and can in particular be observed in arbitrarily large systems, at the cost of choosing $K \sim N^{-1/2}$ or, in other words, a collective velocity that decreases with N. It is accompanied by a very rich dynamical behaviour, which is very reminiscent of active systems, and shows that the breaking of Galilean invariance might be at least as important as activity to observe such behaviours. The tool used to break Galilean invariance is the addition of (classical) couplings between an internal spin degree of freedom and the velocity, that remind of the (quantum) spin-orbit couplings observed in atomic physics. Interestingly, other parallels between quantum

models with spin-orbit couplings and stochastic descriptions of flocking have recently been drawn [230], suggesting that further comparisons between conservative models with spin-velocity couplings and flocking are meaningful.

Finally, in spite of the interesting parallels drawn with active, self-propelled systems, one should be aware of the shortcomings of Hamiltonian flocks. The first, and perhaps the most important of these shortcomings is that because the collective velocity described in this thesis has to become vanishingly small as N increases, collective motion *cannot* survive in the $N \to \infty$ limit, unlike in the Vicsek model for instance. Furthermore, since Hamiltonian flocking is a consequence of global conservation laws, it is *a priori* impossible to observe several flocks moving in different directions in this model. Finally, at equilibrium, it seems that a number of properties of active matter cannot be recovered. An example is that of the polar bands observed in the Vicsek model: while they constitute a plausible steady state in a non-equilibrium setting, at equilibrium, such states would cost both a lot of kinetic energy, and a lot of interfacial energy due to surface tension.

VI.2 Perspectives

In this thesis, I have reached a good understanding of the occurrences of collective motion in a conservative model of particles with a spin-velocity coupling, using a microscopic description and using microcanonical simulations.

An interesting direction for future research would be to establish a Navier-Stokes level hydrodynamic description for a conservative self-propelled model. Indeed, doing so would enable one to compare the full hydrodynamic equations to the Toner and Tu equations [250], which are the most general hydrodynamic equations one can write for active, self-propelled systems. These equations on the velocity field $\boldsymbol{u}$ and the density ρ can be written as [28, 250]

$$\begin{aligned} \frac{\partial \rho}{\partial t} + \boldsymbol{\nabla} \cdot (\rho \boldsymbol{u}) &= 0 \\ \frac{\partial \boldsymbol{u}}{\partial t} + \lambda \boldsymbol{u} \cdot \boldsymbol{\nabla} \boldsymbol{u} + \ldots &= \left(a_2(\rho) - a_4(\rho) u^2 \right) \boldsymbol{u} - \boldsymbol{\nabla} P + \nu \boldsymbol{\delta} \boldsymbol{u}, \end{aligned}$$

where the first equation represents the conservation of mass, and the second equation is written phenomenologically, assuming that the velocities behave like a magnetization close to a magnetic-like transition. The latter contains a real factor λ that, unlike in the usual Navier-Stokes equation, can be different from 1 due to the non-Galilean character of the system [250], a_2 and a_4, two parameters that define a Landau-like mean-field potential for the velocity, a pressure P, and a viscosity ν. I also omitted all other possible derivatives of the velocity that are compatible with the symmetries of the system, that are in fact not useful to understand them. These equations are sufficient to predict a number of exotic properties of Vicsek-like models. First, as the density evolves, a_2 and a_4 change, allowing for a mean-field-like transition between an isotropic state $\boldsymbol{u} = \boldsymbol{0}$ to a polar phase. Furthermore, when considering a perturbation around an ordered state in these equations, one finds that the variance of velocity fluctuations, that is akin to the susceptibility of an XY model diverges. Consequently, this variance diverges at large wavelengths, which also leads to a divergence of the density fluctuations [28]: these equations predict Giant Number Fluctuations such as those observed in the Vicsek Model. Similarly, these large

fluctuations lead to transverse superdiffusion [250–252], that are indeed observed in simulations of the Vicsek model [56] or in flocks of birds [12], for instance. Finally, it was shown multiple times (see [57, 59], for instance) that homogeneous polar phases described by such equations are linearly unstable close to the apolar-polar transition, leading to the formation of polar bands. It is *a priori* a hard endeavour to write such equations exactly from the microscopic theory, although first steps towards establishing such equations are described in App. D. However, it is usual to write hydrodynamic equations phenomenologically. The procedure is the following: to each conserved quantity, one can associate an evolution equation that contains advection, and pressure and viscosity terms due to interactions. In my model, the most relevant conserved quantities should be the number of particles, yielding the (unchanged) mass conservation equation, and the momentum, to which is associated the momentum field $\boldsymbol{\pi}$, leading to the equation

$$\frac{\partial \boldsymbol{\pi}}{\partial t} + \lambda \boldsymbol{u} \cdot \boldsymbol{\nabla} \boldsymbol{\pi} = -\boldsymbol{\nabla} P + \nu \boldsymbol{\delta} \boldsymbol{\pi}. \tag{VI.1}$$

In the limit of a zero viscosity, this equation is indeed the one obtained in App. D. Additionally, in the spirit of the Toner and Tu equation, one could write the dynamics of the magnetisation field $\boldsymbol{m}$ close to the magnetisation transition,

$$\frac{\partial \boldsymbol{m}}{\partial t} + \lambda \boldsymbol{u} \cdot \boldsymbol{\nabla} \boldsymbol{m} + \ldots = \left(a_2(\rho) - a_4(\rho) m^2\right) \boldsymbol{m} - \boldsymbol{\nabla} P_m + J \boldsymbol{\delta} \boldsymbol{m}, \tag{VI.2}$$

where P_m is a magnetic "pressure" and J a magnetic viscosity, caused by interactions. Using the definition of the momentum with respect to the velocity and magnetisation, I substract K times Eq. (VI.2) from Eq. (VI.1) to write an equation on the velocity field $\boldsymbol{u}$,

$$\begin{aligned} \frac{\partial \boldsymbol{u}}{\partial t} + \lambda \boldsymbol{u} \cdot \boldsymbol{\nabla} \boldsymbol{u} = & \\ & - K \left(a_2(\rho) - a_4(\rho) m^2\right) \boldsymbol{m} - \boldsymbol{\nabla}(P - K P_m) + \nu \boldsymbol{\delta} \boldsymbol{u} + K(\nu - J) \boldsymbol{\delta} \boldsymbol{m}. \end{aligned} \tag{VI.3}$$

This equation looks similar to Toner and Tu's equations, except that velocities and magnetizations are distinct. In the limit of a homogeneous, zero momentum $\boldsymbol{\pi} = \boldsymbol{0}$, however, I recover one equation only:

$$\frac{\partial \boldsymbol{u}}{\partial t} + \lambda \boldsymbol{u} \cdot \boldsymbol{\nabla} \boldsymbol{u} = \left(a_2(\rho) - a_4(\rho) u^2 / K^2\right) \boldsymbol{u} - \boldsymbol{\nabla}(P - K P_m) + J \boldsymbol{\delta} \boldsymbol{u}, \tag{VI.4}$$

which is very similar to that of Toner and Tu. Consequently, in large ordered systems with total momentum zero, one could expect some properties of Vicsek-like models to be recovered. However, in the results of the main text, I show no sign of transverse superdiffusion, of band formation, or of giant density fluctuations. Why is that? The possible reasons, which are yet to be explored, could be any of the following. First, it could be explained by finite-size effects: hydrodynamic descriptions are generally good in very large systems, here maybe even so large that I did not see active-like properties. This size limitation might in fact also be problematic when attempting to build a hydrodynamic theory for the model studied in this thesis, as spontaneous, collective velocities can only be vanishingly small in infinitely large systems. Second, effects like the transverse superdiffusion could be suppressed by the repulsive interactions I considered, which

are generally absent of Vicsek-like models and naturally reorient velocities and local momenta. Finally, the hypothesis that the momentum field is perfectly homogeneously zero is a very strong one. In practice, it could be that Eq. (VI.4) is never accurate, but that it is replaced by Eq. (VI.3), in which the Landau-like terms act on the magnetisation and not the velocity, so that the Toner and Tu fluctuations of the velocities are lost. All in all, I believe that exploring the commonalities and differences between the equations describing the Hamiltonian model of this thesis and the Toner and Tu equations would be quite interesting, as it would shed light on the physics of self-propelled systems that have a polarity that is not necessarily aligned on their velocity.

Another natural extension of this work would be to consider interactions between these particles and an external object. For instance, one could consider the interactions with a wall. Doing so would would enable one to compare the forces exerted by conservative flocks to those observed in active flocks, which have been of interest in the active matter community for a few years [253–255]. In the case of the precise model studied in this thesis, however, one should heed the fact that a hard wall with infinite mass would simply serve as a momentum reservoir, and set the overall velocity to zero. An interesting experiment would therefore be to consider a soft or mobile wall, possibly surrounded by another, simpler fluid. Another interesting direction could be to place the system not in contact with a wall, but in an oscillating magnetic field. While breaking down conservation laws, this experiment could lead to interesting (steady) oscillating states for both spins and velocities. Finally, in order to observe self-propulsion at a scale smaller than that of a whole system, one could consider a binary system, composed of n particles with a spin-velocity coupling, and $N - n$ particles with $K = 0$. In that situation, at low temperatures, one expects the $K = 0$ particles to order into a ferroliquid, thus exerting a field on the $K > 0$ particles, that should want to move along it with a less stringent conservation condition on the total momentum if $N \gg n$. This "tracer" experiment could be an interesting conservative equivalent of active microrheology, a field in which one considers one active tracer subjected to a propulsion force placed in an assembly of passive objects [29]. In particular, with my aligning interactions, this experiment would be akin to experiments of bacteria placed in nematic liquids, that self-propel in an aligning medium [256].

Linked to the question of coupling this system to an object is the idea of studying it at other values of the total momentum. While I solely focused on the $\boldsymbol{P} = \boldsymbol{0}$ case in this thesis because I was interested in studying the emergence of collective motion from a still hot configuration, the case $P \neq 0$ could be relevant for comparison to active systems. In particular, perhaps other ground states could be found in the case of a non-zero total momentum, and maybe these ground states could bridge the gap between, say, the states I discuss in this thesis, and the steady states found for systems of active particles with alignment interactions [66]. Indeed, these steady states typically feature topological defects reminiscent of those I discussed in Chapter IV.

Finally, variations on this model, including nematic spin-velocity couplings, polar spin-velocity couplings with nematic interactions, or spin-velocity couplings that depend on the values of the particles' spins and positions could shed light on various models that were introduced in the context of active matter, but do not yet have obvious passive equivalents. These models include Vicsek-like models with velocity reversals that mimic a nematic spin-velocity coupling [87], systems of self-propelled particles with (steric) nematic in-

teractions [232, 233], or self-propelled particles that interact through concentrations of solutes [29, 45, 242].

All of these directions have the potential to bring about novel, or at least clearer, ideas about the role of activity itself in a number of exotic properties of self-propelled systems.

Appendix A

Non-Convex Kinetic Energy: A Simple Example

> Two roads diverged in a yellow wood,
> And sorry I could not travel both
> And be one traveler, long I stood
>
> Robert Frost, *The Road Not Taken*

As an illustration of the deep issues that arise when the kinetic energy is not a convex function of the velocity in the Lagrangian formalism, in this section I briefly discuss the properties of the one-particle Lagrangian studied in Chi *et al.* [86]. It is defined by

$$\mathcal{L} = \frac{1}{12}\dot{q}^4 - \frac{1}{2}\dot{q}^2 - \frac{1}{2}q^2, \tag{A.1}$$

where q is the position of a particle on a $1d$ infinite line. The canonical momentum associated to this Lagrangian reads

$$p \equiv \frac{\partial \mathcal{L}}{\partial \dot{q}} = \dot{q}\left(\frac{\dot{q}^3}{3} - 1\right).$$

The issue with this expression is that, in the region $\dot{q} \in \left[-\sqrt{3}; \sqrt{3}\right]$, p becomes a decreasing function of $\dot{q}$ so that there are several possible values of $\dot{q}$ associated to one value of p. This is illustrated in Fig. A.1, where I plot the value of p as a function of $\dot{q}$. A direct consequence is that it is impossible to write an unequivocal inverse map $\dot{q}(p)$, so that no single-valued Hamiltonian can be defined simply through the usual Legendre transform,

$$\mathcal{H} = p\dot{q}(p) - \mathcal{L}(q, \dot{q}(p); t).$$

To better understand what is wrong with the dynamics of this model, it is however possible to write the Euler-Lagrange equation of motion,

$$\ddot{q}\left(\dot{q}^2 - 1\right) + q = 0,$$

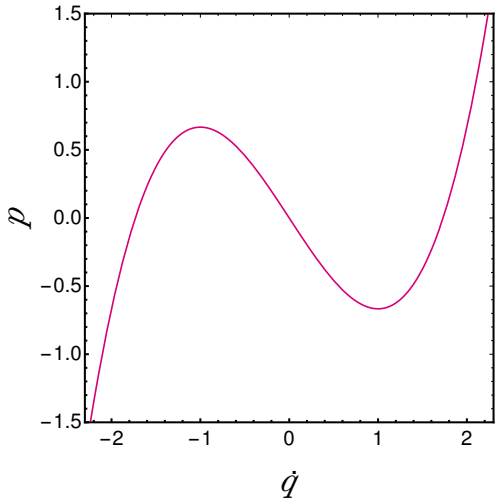

Fig. A.1 **Momentum Versus the Velocity.**

an equation that can be multiplied by q and integrated, thus defining a conserved quantity, that I shall call the energy, that reads

$$E = \frac{q^2}{2} + \frac{1}{4}\left(\dot{q}^2 - 1\right)^2 .$$

This definition of the energy can be used to draw a phase portrait (lines of constant energy in the $(q, \dot{q})$ plane), describing the dynamics of this system. This phase portrait is plotted in A.2, as well as the corresponding trajectories in the (q, p) "phase plane". On the latter, the mapping problem appears quite clearly: trajectories of different energies intersect each other in phase space, indicating that the pair of variables (q, p) does not fully describe the state of the system. The phase portrait in $(q, \dot{q})$, while it might look more standard, is in fact just equally strange. Consider, for example, a pair of closed curves describing the same energy. From any point on the higher of the two closed curves, $\dot{q} > 0$, so that the particle moves to the right. When it reaches the right-most point of the closed curve, it is stuck with no other solution that to jump to the lower curve, with the transformation $\dot{q} \to -\dot{q}$. This implies an infinite spike in $\ddot{q}$, but still satisfies the equation of motion since the right-most point of the ovoid curves is always located at $\dot{q} = 1$, and q can remain a constant. Then, on the lower curve, the same thing happens: the particle moves to the left-most point of the closed curve, then has to jump to the higher curve again. Therefore, the dynamics of such systems are also unphysical, as they allow for infinite accelerations.

Regarding the definition of the Hamiltonian, notwithstanding the weirdness of the dynamics and the impossibility to write an inverse map $\dot{q}(p)$, there has been some effort in the literature to get a single-valued Hamiltonian. Although I do not use these strategies in this thesis, but discard entirely non-convex theories instead, I want to say a few words about them. Essentially, two paths were explored [86]. The first strategy was quantizing the system with a path-integral formalism, which yields a well-behaved quantum action, with the peculiarity that in the classical limit several paths (corresponding to several possible values of the velocity for one momentum) dominate the dynamics so that there

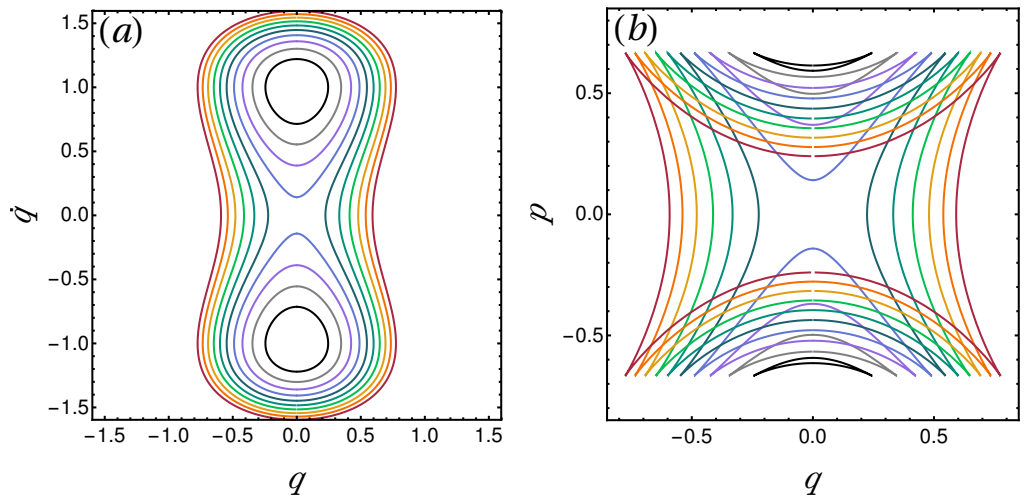

Fig. A.2 **Phase Portraits.** (a) Constant energy trajectories in the $(q, \dot{q})$ plane, with energies going from 0.03 (black) to 0.3 (red) by increments of 0.03, and (b) corresponding trajectories in the (q, p) plane.

is no unequivocal classical trajectory for such systems. The second strategy was to use a generalization of the Legendre transform, called the Lengendre-Fenchel transform, so that the Hamiltonian is defined by

$$\mathcal{H} = \sup_{\dot{q}} \{p\dot{q} - \mathcal{L}\} .$$

This definition yields a single-valued Hamiltonian, regardless of the expression of the Lagrangian, only with non-differentiable points indicating where non-convexities lied (see Fig. A.3(a)). From the point of view of the geometric interpretation of the Legendre transform, this point corresponds to a value of p that matches several tangents of $\mathcal{L}$, seen as a function of $\dot{q}$. Interestingly enough, the Lagrangian obtained by applying the Legendre-Fenchel transform to the obtained Hamiltonian is, however, different from the starting Lagrangian in the non-convex domains (see Fig. A.3(b)). In these domains, the starting Lagrangian is replaced by its convex hull, thus erasing any non-convexity issue. Note that this "convexification" is reminiscent of the Maxwell construction in thermodynamics [1], which consists in replacing non-convexities of a thermodynamic potential by a flat line (this is discussed in more details in Sec. II.4). The Maxwell construction then corresponds to phase-separated states, that are mixtures between the phases at each end of the flat line. Here, the effective Lagrangian of Fig. A.3(b) can be similarly interpreted as a mixed state of the several velocities allowed for one given value of p in the non-convex region.

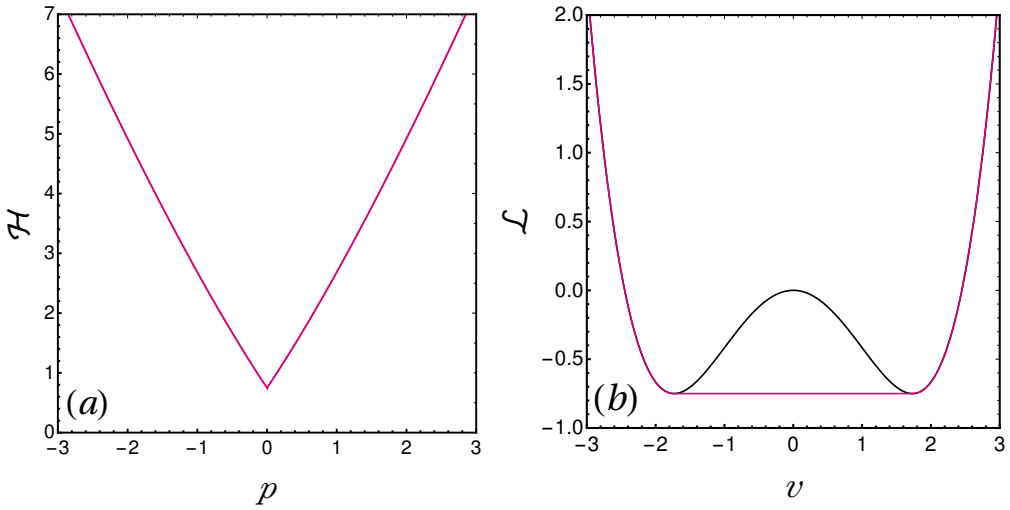

Fig. A.3 **Legendre-Fenchel Hamiltonian and Lagrangian** (a) Hamiltonian obtained from a Legendre-Fenchel transform from Lagrangian (A.1) versus the momentum, at position $q = 0$, (b) original Lagrangian (A.1) (black) and Lagrangian obtained from the Legendre-Fenchel Hamiltonian (red) versus the velocity, at position $q = 0$.

Appendix B
Computation of the Virial Coefficients

One's too few, three too many.

Old English Proverb

In this Appendix, I give more details on the computation of the virial coefficients used in the VE-CW approach of Chapter III, for arbitrary values of β and h in our choice of parametrization of the angle distribution of spins. As mentioned in the main text, the integrals I need to compute are

$$\begin{aligned} B_2(\beta,h) &= -\frac{1}{2}\int d\boldsymbol{r}d\theta_1 d\theta_2 p(\theta_1,\beta h)p(\theta_2,\beta h)f(r,\theta_{12}), \\ B_3(\beta,h) &= -\frac{1}{3}\int d\boldsymbol{r_1}d\boldsymbol{r_2}d\theta_1 d\theta_2 d\theta_3 \\ &\quad \times p(\theta_1,\beta h)p(\theta_2,\beta h)p(\theta_3,\beta h) \\ &\quad \times f(r_{12},\theta_{12})f(r_2,\theta_{23})f(r_1,\theta_{31}), \end{aligned}$$

with

$$\begin{aligned} p(\theta;\beta h) &= \frac{e^{\beta h\cos\theta}}{2\pi I_0(\beta h)}, \\ f(r,\theta) &= \Theta(\sigma-r)\left(e^{\beta j\cos\theta}-1\right) \\ &+ \Theta(\sigma-r)\Theta(\sigma_{\text{rep}}-r)e^{\beta j\cos\theta}\left(e^{-\beta u}-1\right). \end{aligned}$$

A nice feature of these expressions is that in both cases, integrals over space and integrals over angles can be decoupled. Furthermore, as I only used square-shaped potentials for both repulsion and magnetic alignment, the space integrals only amount to disk overlap computations. Finally, I can comment on several limits of the amplitudes of the interactions that can still be taken smoothly at this level. For $j \to 0$, we recover a square-potential liquid, with either hardcore exclusion ($u \to \infty$) or soft square-potential repulsion. Likewise, for $0 < j < \infty$, the hard-disk limit can be taken smoothly, as the $u \to \infty$ limit simply amounts, for a finite value of j, to taking $e^{-\beta u} \to 0$.

I will treat each virial coefficient separately, starting by the lowest-order one as it happens to be easier to compute.

B.1 Computation of B_2

The space integral in B_2 is the one of the surface of a disk, and the only non-trivial integral to compute is the one over the angles. In order to compute it, I write the exponential of the difference between angles as [101]

$$\begin{aligned} e^{\beta j \cos\theta_{12}} &= I_0(\beta j) + 2\sum_{n\geq 1} I_n(\beta j)\cos(n\theta_{12}) \\ &= I_0(\beta j) + 2\sum_{n\geq 1} I_n(\beta j)\left[\cos(n\theta_1)\cos(n\theta_2)\right. \\ &\qquad \left. + \sin(n\theta_1)\sin(n\theta_2)\right]. \end{aligned}$$

It is then rather simple to write the full form of B_2 in terms of Bessel functions

$$\begin{aligned} B_2(h,T) = \frac{\pi}{2}\sigma^2 &\left\{[1 - I_0(\beta j)] - 2\sum_{n=1}^{\infty} I_n(\beta j)\frac{I_n(\beta h)^2}{I_0(\beta h)^2}\right\} \\ + \frac{\pi}{2}f^2\sigma^2 &\left\{I_0(\beta j) + 2\sum_{n=1}^{\infty} I_n(\beta j)\frac{I_n(\beta h)^2}{I_0(\beta h)^2} - e^{-\beta u}\right\}. \end{aligned}$$

In this thesis, I also used the values of B_2 in the hard-disk limit $u \to \infty$, which can be taken smoothly,

$$\begin{aligned} B_2^{HS}(h,T) &= \frac{\pi}{2}\sigma^2 \left\{\left[1 + (f^2-1)I_0(\beta j)\right]\right. \\ &\qquad \left. +2(f^2-1)\sum_{n=1}^{\infty} I_n(\beta j)\frac{I_n(\beta h)^2}{I_0(\beta h)^2}\right\}, \end{aligned}$$

and, in some cases, also in its $h \to 0$ limit, which reads:

$$B_2^{HS}(0,T) = \frac{\pi}{2}\sigma^2\left[1 + (f^2-1)I_0(\beta j)\right].$$

In the limit $j \to 0$, this coefficient simply becomes the well-known hard-disk coefficient, [133]

$$B_2^{HS} = \frac{\pi}{2}f^2\sigma^2.$$

B.2 Computation of B_3

When computing B_3 explicitly, the integrals over the angles are computed by using the same trick as the one used to calculate B_2. The integrals over space, however, are a

bit more complicated to calculate, as they now comprise overlap surface computations between disks of unequal radii

$$\begin{aligned} J_f &\equiv \int d^2\boldsymbol{r_1} d^2\boldsymbol{r_2} \Theta(f\sigma - r_{12})\Theta(\sigma - r_2)\Theta(\sigma - r_1), \\ J_{ff} &\equiv \int d^2\boldsymbol{r_1} d^2\boldsymbol{r_2} \Theta(\sigma - r_{12})\Theta(f\sigma - r_2)\Theta(f\sigma - r_1). \end{aligned}$$

It is useful for the low-density radial distribution function calculation explained in Sec. b) to define the integrals over, say, $\boldsymbol{r}_1$ separately. They can, in fact, be grouped under the definition

$$A_{f_1,f_2}(r_2) \equiv \frac{1}{\sigma^2} \int d^2\boldsymbol{r_1} \Theta(f_1\sigma - r_1)\Theta(f_2\sigma - r_{12}).$$

The trick is then to write this integral in polar coordinates and with the changes of variables $\boldsymbol{r}_{1,2} \to \boldsymbol{r}_{1,2}/\sigma$ (which should be taken into account in the integral over $\boldsymbol{r}_2$ afterwards),

$$\begin{aligned} A_{f_1,f_2}(r_2) &= \int_{r_1=0}^{f_1} r_1 dr_1 \int_{\phi=-\pi}^{\pi} d\phi \\ &\qquad \Theta({f_2}^2 - \left(r_2^2 + r_1^2 - 2r_2 r_1 \cos\phi\right)) \end{aligned}$$

This integration can be carried out by noticing that the geometric domain defined through the Θ function can be cut into two complementary parts that are simple to integrate over ϕ. Geometrically, the domain I am drawing is the overlap between a disk centered on the point located (in polar coodinates) at (r_1, ϕ), and a second disk centered on $(r_2, 0)$, with disk radii f_1 and f_2, respectively. Below a given value of the distance between the two disks and the origin, all values of ϕ belong to the domain defined by the step function, while over this distance there is a finite interval of ϕ, symmetric around zero, that belong to this domain. Using this, the integral can be rewritten in the general form:

$$\begin{aligned} A_{f_1,f_2}(r_2) &= 2\pi \left[\frac{r_1^2}{2}\right]_0^{\min(f_1, f_2 - r_2)} \Theta(f_2 - r_2) \\ &+ \int_0^{f_1\sigma} dr_1 r_1 \left[2 \arccos\left(\frac{r_1^2 + r_2^2 - f_2^2\sigma^2}{2r_1 r_2}\right)\right. \\ &\qquad \left. \times\Theta(r_1 + r_2 - f_2)\Theta(|r_1 - r_2| - f_2)\right], \end{aligned}$$

where I used the notation $[f(x)]_a^b = f(b) - f(a)$.

The last remaining integral can then be computed as follows. First, I use an integration by parts to get a derivative of the arccos out. Then, I change variables first switching to $u = r_1^2$, and then to an angle φ such that: $u = u_- \cos^2\varphi + u_+ \sin^2\varphi$, where $u_\pm \equiv (f_2 \pm r_2)^2$. This allows me to derive an exact expression, that is a bit cumbersome to write here. The

integrals J_f and J_{ff} finally read

$$\begin{aligned} J_f &= \pi\sigma^4 \left[\pi f^2 - \sqrt{4-f^2} \left(\frac{f}{2} + \frac{f^3}{4} \right) \right. \\ &\quad + \arccos\left(1 - \frac{f^2}{2}\right) - f^2 \arcsin\left(\frac{f}{2}\right) \\ &\quad \left. - f^2 \arctan\left(\frac{f}{\sqrt{4-f^2}} \right) \right], \\ J_{ff} &= 4\pi^2\sigma^4 J_{ff}^L + 4\pi\sigma^4 J_{ff}^U, \end{aligned}$$

where

$$\begin{aligned} J_{ff}^L &= \frac{f^4}{4}\Theta\left(\frac{1}{2} - f\right) \\ &\quad + \frac{1}{24}\left(6f^4 - 16f^3 + 12f^2 - 1\right)\Theta\left(f - \frac{1}{2}\right), \\ J_{ff}^U &= \Theta\left(f - \frac{1}{2}\right)\left[\frac{\pi}{24} - \frac{\pi}{4}f^2 + \frac{2\pi}{3}f^3 - \frac{\pi}{4}f^4 \right. \\ &\quad - \frac{f^2}{8}\sqrt{4f^2-1} \\ &\quad - \frac{1}{16}\sqrt{4f^2-1} - \frac{f^2}{2}\arctan\left(\frac{1}{\sqrt{4f^2-1}}\right) \\ &\quad - \frac{1}{2}f^2\arccos\left(\frac{1}{2}\sqrt{\frac{1}{f}+2}\right) + \frac{1}{4}f^2\arccos\left(\frac{1}{2f}\right) \\ &\quad \left. + \frac{1}{4}f^4\arccos\left(1 - \frac{1}{2f^2}\right)\right]. \end{aligned}$$

Putting all these results together, I find that B_3 reads

$$\begin{aligned} B_3(h,T) &= -\frac{1}{24\pi^3 I_0(\beta h)^3}\left(I_2^{(3)}J_\triangle^{(3)} - 3I_2^{(2)}J_\triangle^{(2)} \right. \\ &\quad \left. + 3I_2^{(1)}J_\triangle^{(1)} - I_2^{(0)}J_\triangle^{(0)}\right), \end{aligned}$$

where we defined quite a few intermediary integrals,

$$\begin{aligned} I_2^{(3)} &= J_1 + 3(e^{-\beta u} - 1)J_f, \\ &\quad + 3(e^{-\beta u} - 1)^2 J_{ff} + (e^{-\beta u} - 1)^3 f^4 J_1, \\ I_2^{(2)} &= J_1 + 2(e^{-\beta u} - 1)J_f + (e^{-\beta u} - 1)^2 J_{ff}, \\ I_2^{(1)} &= J_1 + (e^{-\beta u} - 1)J_f, \\ I_2^{(0)} &= J_1, \end{aligned}$$

with J_1 the value of J_f for $f = 1$, and

$$
\begin{aligned}
J_{\triangle}^{(0)} &= 8\pi^3 I_0(\beta h)^3, \\
J_{\triangle}^{(1)} &= 8\pi^3 I_0(\beta h)\left[I_0(\beta j) I_0(\beta h)^2 + 2\sum_{n\geq 1} I_n(\beta j) I_n(\beta h)^2\right], \\
J_{\triangle}^{(2)} &= (2\pi I_0(\beta h))^3 I_0(\beta j)^2 + 32\pi^3 I_0(\beta j) I_0(\beta h) \sum_{n\geq 1} I_n(\beta j) I_n(\beta h)^2 \\
&+ 16\pi^3 \sum_{m,n\geq 1} I_m(\beta j) I_n(\beta j) I_m(\beta h) I_n(\beta h)(I_{m+n}(\beta h) + I_{m-n}(\beta h)), \\
J_{\triangle}^{(3)} &= 8\pi^3 (I_0(\beta h) I_0(\beta j))^3 + 48\pi^3 I_0(\beta h) I_0(\beta j)^2 \sum_{n=1}^{\infty} (I_n(\beta h))^2 I_n(\beta j) \\
&+ 48\pi^3 I_0(\beta j) \sum_{\epsilon=\pm 1} \sum_{m,n=1}^{\infty} I_m(\beta h) I_n(\beta h) I_{m+\epsilon n}(\beta h) I_m(\beta j) I_n(\beta j) \\
&+ 8\pi^3 \sum_{\epsilon,\eta,\nu=\pm 1} \sum_{m,n,p=1}^{\infty} I_{m+\epsilon n}(\beta h) I_{n+\eta p}(\beta h) I_{p+\nu m}(\beta h) I_m(\beta j) I_n(\beta j) I_p(\beta j) \\
&- 8\pi^3 \sum_{\epsilon,\eta,\nu=\pm 1} \epsilon\eta\nu \sum_{m,n,p=1}^{\infty} I_{m+\epsilon n}(\beta h) I_{n+\eta p}(\beta h) I_{p+\nu m}(\beta h) I_m(\beta j) I_n(\beta j) I_p(\beta j).
\end{aligned}
$$

Just like for B_2, I check that I recover the hard-disk limit given in the literature [133] for $u \to \infty, h \to 0$, and $j \to 0$,

$$
B_3^{HS} = \pi f^4 \sigma^4 \left(\frac{\pi}{3} - \frac{\sqrt{3}}{4}\right).
$$

Appendix C

Displacement correlations in a homogeneous rotating disk

> There's no such thing as simple.
> Simple is hard.
>
> Martin Scorsese

In the main text, I present numerical curves for the correlation function C_d. The corresponding exact calculation can be performed in the case of a disk with homogeneous density ρ_0 and radius R, rotating around its centre at a constant angular velocity Ω. In this case, the velocity field can be written in polar coordinates (with the origin at the center of the disk) as

$$\boldsymbol{v}(\boldsymbol{r}) = r\Omega\,\hat{\boldsymbol{e}}_\theta \ ,$$

where $\hat{\boldsymbol{e}}_\theta$ is the unit orthoradial vector at position $\boldsymbol{r}$. By construction, this velocity field has a zero sum over the whole disk. I seek to compute

$$C_d(r) = \frac{1}{c_0}\frac{\sum\limits_{i\neq j} \boldsymbol{v}_i\cdot\boldsymbol{v}_j\delta(r_{ij}-r)}{\sum\limits_{i\neq j}\delta(r_{ij}-r)} \ ,$$

where the sum is computed over the particles that constitute the disk, and c_0 ensures that $C_d(0)=1$. These sums can be approximated by integrals that run over the surface of the disk,

$$C_d(r) = \frac{1}{c_0}\frac{\int d^2\boldsymbol{r}_1 d^2\boldsymbol{r}_2\ \rho(\boldsymbol{r}_1)\rho(\boldsymbol{r}_2)\boldsymbol{v}(\boldsymbol{r}_1)\cdot\boldsymbol{v}(\boldsymbol{r}_2)\,\delta(r_{12}-r)}{\int d^2\boldsymbol{r}_1 d^2\boldsymbol{r}_2\ \rho(\boldsymbol{r}_1)\rho(\boldsymbol{r}_2)\,\delta(r_{12}-r)} \ .$$

Since I here assume the density to be homogeneous, a factor of ρ_0^2 comes out of both integrals, and the density disappears from the calculation altogether. The task at hand is then to compute the integrals in the numerator $\mathcal{N}$ and the denominator $\mathcal{D}$ of C_d, defined by

$$\mathcal{N}(r) \equiv \int d^2\boldsymbol{r}_1 d^2\boldsymbol{r}_2\ \boldsymbol{v}(\boldsymbol{r}_1)\cdot\boldsymbol{v}(\boldsymbol{r}_2)\,\delta(r_{12}-r) \ ,$$

$$\mathcal{D}(r) \equiv \int d^2\boldsymbol{r}_1 d^2\boldsymbol{r}_2\ \delta(r_{12}-r) \ .$$

I first focus on the denominator, $\mathcal{D}$. The geometric constraint encoded by the Dirac-δ can be rewritten explicitly in terms of the polar coordinates of the positions $\boldsymbol{r}_1$ and $\boldsymbol{r}_2$, leading to

$$\mathcal{D}(r) = \int_0^R dr_1 \int_0^R dr_2 \int_{-\pi}^{\pi} d\theta_1 \int_{-\pi}^{\pi} d\theta_2 \, r_1 r_2 \, \delta\left(\sqrt{r_1^2 + r_2^2 - 2r_1 r_2 \cos\theta_{12}} - r\right) ,$$

where $\theta_{12} = \theta_2 - \theta_1$. One can then use the change of variables $\theta_2 \to \theta + \theta_1$, integrate over θ_1, and use the periodicity and parity of the cosine to write

$$\mathcal{D}(r) = 4\pi \int_0^R dr_1 \int_0^R dr_2 \int_0^{\pi} d\theta \, r_1 r_2 \, \delta\left(\sqrt{r_1^2 + r_2^2 - 2r_1 r_2 \cos\theta} - r\right) . \tag{C.1}$$

The integral over the remaining angle can then be computed, using the fact that for any function g with a single zero at a point x_0, one has [257]

$$\int_a^b dx \; f(x) \, \delta\left(g(x)\right) = \frac{f(x_0)}{|g'(x_0)|} \, \mathbb{1}\left(a \leq x_0 \leq b\right) ,$$

where $\mathbb{1}$ is a Boolean function which takes the value 1 if its argument is true, and is 0 otherwise. Since the cosine is a bijection from $[0;\pi]$ to $[-1;1]$, there is *at most* one value θ_0 of θ that verifies the condition imposed by the δ in Eq. (C.1). This value is given by

$$\theta_0 = \arccos\left[\frac{r_1^2 + r_2^2 - r^2}{2r_1 r_2}\right] ,$$

and there is such a value in $[0;\pi]$ if and only if the argument of the arccos is indeed in $[-1;1]$, implying the conditions

$$(r_1 - r_2)^2 \leq r^2 \leq (r_1 + r_2)^2 .$$

Furthermore, I compute the derivative $g'(\theta_0)$ of the argument $g(\theta)$ of the Dirac-δ,

$$g'(\theta_0) = \frac{r_1 r_2}{r} \sqrt{1 - \left(\frac{r_1^2 + r_2^2 - r^2}{2r_1 r_2}\right)^2} .$$

All in all, integrating over θ in Eq. (C.1) yields

$$\mathcal{D}(r) = 4\pi r \int_0^R dr_1 \int_0^R dr_2 \, \frac{\mathbb{1}\left[(r_1 - r_2)^2 \leq r^2 \leq (r_1 + r_2)^2\right]}{\sqrt{1 - \left(\frac{r_1^2 + r_2^2 - r^2}{2r_1 r_2}\right)^2}} .$$

An equivalent expression is obtained by multiplying the numerator and denominator of the integrand by $2r_1 r_2$,

$$\mathcal{D}(r) = 8\pi r \int_0^R dr_1 \, r_1 \int_0^R dr_2 \, r_2 \frac{\mathbb{1}\left[(r_1 - r_2)^2 \leq r^2 \leq (r_1 + r_2)^2\right]}{\sqrt{-r_2^4 + 2r_2^2\left(r_1^2 + r^2\right) - \left(r_1^2 - r^2\right)^2}} .$$

I then change variables according to $r_2 \to u = r_2^2$, and notice that the square root in the denominator is a degree-two polynomial in u, with roots $u_\pm = (r \pm r_1)^2$. Furthermore, the conditions in the numerator can be expressed as constraints on u rather than on r, yielding $u_- \leq u \leq u_+$ (which ensures that the content of the square root is positive), so that

$$\mathcal{D}(r) = 4\pi r \int_0^R dr_1\, r_1 \int_0^{R^2} du \frac{\mathbb{1}\left[u_- \leq u \leq u_+\right]}{\sqrt{-\left(u-u_+\right)\left(u-u_-\right)}} \,.$$

It is now convenient to use the conditions in the Boolean function to split the integral over u into several domains. First, since $u_- \geq 0$, the lower bound of the integral over u is in fact always u_-. Furthermore, for the integration domain to have a finite extent, one should have $u_- \leq R^2$, which imposes $r_1 \geq r - R$. Finally, the upper bound of the integral over u, is the lower of the two values R^2 and u_+. Stating that $u_+ \leq R^2$ is equivalent to stating that $r_1 \leq R - r$. Therefore, the $2d$ integration domain naturally splits into two parts: one such that $r_1 \leq R - r$ (provided that $r \leq R$) so that u reaches u_+; and one such that $r_1 \geq R - r$ (regardless of the value of r) so that u reaches R^2 before u_+. In the end, one gets

$$\mathcal{D}(r) = 4\pi r \left[\mathbb{1}\left(r \leq R\right) \int_0^{R-r} dr_1\, r_1 \int_{u_-}^{u_+} du \frac{1}{\sqrt{-\left(u-u_+\right)\left(u-u_-\right)}} + \int_{|R-r|}^{R} dr_1\, r_1 \int_{u_-}^{R^2} du \frac{1}{\sqrt{-\left(u-u_+\right)\left(u-u_-\right)}} \right] . \tag{C.2}$$

To compute the integrals over u, I introduce the change of variables $u = u_- \cos^2\phi + u_+ \sin^2\phi$. The corresponding differential elements are related by the equation

$$du = 2\cos\phi\sin\phi\left(u_+ - u_-\right)\, d\phi \,,$$

and the polynomial in the square root can be rewritten as

$$-(u-u_+)(u-u_-) = \left(u_+ - u_-\right)^2 \cos^2\phi \sin^2\phi.$$

Finally, the bounds of the integral are given by

$$\begin{aligned} \phi_R &= \arcsin\left[\sqrt{\frac{R^2-u_-}{u_+-u_-}}\right], \\ \phi_- &= 0 \,, \\ \phi_+ &= \frac{\pi}{2} \,, \end{aligned}$$

when $u = R^2$, $u = u_-$, and $u = u_+$, respectively. With all these transformations, Eq. (C.2) can be rewritten as

$$\mathcal{D}(r) = 8\pi r \left[\mathbb{1}\left(r \leq R\right) \int_0^{R-r} dr_1\, r_1 \int_0^{\pi/2} d\phi + \int_{|R-r|}^{R} dr_1\, r_1 \int_0^{\phi_R} d\phi \right] .$$

The first term is an elementary integration, while the second one, that I shall call $\mathcal{I}$, is a bit more challenging. It reads

$$\mathcal{I} \equiv \int_{|R-r|}^{R} dr_1\, r_1 \arcsin\left[\sqrt{\frac{R^2-(r-r_1)^2}{4rr_1}}\right].$$

An integration by parts, as well as some simplifications yield

$$\mathcal{I} = \left[\frac{r_1^2}{2}\arcsin\left[\sqrt{\frac{R^2-(r-r_1)^2}{4rr_1}}\right]\right]_{|r-R|}^{R} - \frac{1}{2}\int_{|R-r|}^{R} dr_1 r_1 \frac{r^2-R^2-r_1^2}{\sqrt{-r_1^4+2r_1^2(R^2+r^2)-(R^2-r^2)^2}}.$$

The last remaining integral can, like before, be treated by first introducing the variable $v = r_1^2$ and then writing $v = v_- \cos^2\phi + v_+ \sin^2\phi$, with $v_\pm \equiv (r \pm R)^2$. Applying these changes one can finally calculate the remaining integral and obtain an explicit expression for the denominator $\mathcal{D}$,

$$\mathcal{D}(r) = \pi r R^2 \left(\pi - \frac{r}{R}\sqrt{4-\frac{r^2}{R^2}} + 4\,\mathrm{arccsc}\frac{2}{\sqrt{2-r/R}} - 2\arctan\frac{r/R}{\sqrt{4-r^2/R^2}}\right).$$

Note that this function is closely related to the pair correlation function in the disk. The latter is essentially recovered by dividing $\mathcal{D}$ by a factor of $2\pi r$.

I now turn my attention to the numerator $\mathcal{N}(r)$. Following the same steps that led to Eq. (C.1) one deduces

$$\mathcal{N}(r) = 4\pi\omega^2 \int_0^R dr_1 \int_0^R dr_2 \int_0^\pi d\theta\, r_1^2 r_2^2 \cos\theta\, \delta\left(\sqrt{r_1^2+r_2^2+2r_1r_2\cos\theta} - r\right).$$

The integration over θ can be treated in the same way as for $\mathcal{D}$, leading to the expression

$$\mathcal{N}(r) = 2\pi r\omega^2 \int_0^R dr_1 \int_0^R dr_2 \frac{r_1^2+r_2^2-r^2}{\sqrt{1-\left(\frac{r_1^2+r_2^2-r^2}{2r_1r_2}\right)^2}}\, \mathbb{1}\left[(r_1-r_2)^2 \le r^2 \le (r_1+r_2)^2\right].$$

The changes of variables $u = r_2^2$ and $u = u_- \cos^2\phi + u_+ \sin^2\phi$, with the same definitions as before, then leads to

$$\begin{aligned}\mathcal{N}(r) = {} & 4\pi r\omega^2 \int_0^{R-r} dr_1 r_1 \int_0^{\pi/2} d\phi \left[\left(r_1^2-r^2\right) + u_- \cos^2\phi + u_+ \sin^2\phi\right] \mathbb{1}\left[r \le R\right] \\ & + 4\pi r\omega^2 \int_{|R-r|}^{R} dr_1 r_1 \int_0^{\phi_R} d\phi \left[\left(r_1^2-r^2\right) + u_- \cos^2\phi + u_+ \sin^2\phi\right].\end{aligned}$$

The first integral is, again, simple to compute. The second one, that I shall call $\mathcal{J}$, can be rewritten using the expression of ϕ_R and some trigonometry ($\sin 2\theta_R = 2\cos\theta_R \sin\theta_R$ and $\cos\arcsin x = \sqrt{1-x^2}$),

$$\begin{aligned}\mathcal{J} &\equiv \int_{|R-r|}^{R} dr_1 r_1 \int_0^{\phi_R} d\phi \left[\left(r_1^2 - r^2\right) + u_- \cos^2\phi + u_+ \sin^2\phi\right] \\ &= 2\int_{|R-r|}^{R} dr_1\, r_1^3 \arcsin\sqrt{\frac{R^2-(r-r_1)^2}{4rr_1}} - 2r\int_{|R-r|}^{R} dr_1\, r_1^2 \sqrt{1-\frac{R^2-(r-r_1)^2}{4rr_1}}\sqrt{\frac{R^2-(r-r_1)^2}{4rr_1}}\,.\end{aligned}$$

The first term in $\mathcal{J}$ is similar to $\mathcal{I}$: the only difference is that there is an extra factor of r_1^2. The second term, on the other hand, can be rewritten using the variable $v = r_1^2$, as

$$\int_{|R-r|}^{R} dr_1 r_1^2 \sqrt{1-\frac{R^2-(r-r_1)^2}{4rr_1}}\sqrt{\frac{R^2-(r-r_1)^2}{4rr_1}} = \frac{1}{8r}\int_{(R-r)^2}^{R^2} dv\sqrt{-(v-v_+)(v-v_-)}$$

and can be integrated using techniques similar to those presented above. The numerator $\mathcal{N}$ can then be written as

$$\begin{aligned}\mathcal{N}(r) \;=\; & \frac{\pi\omega^2 R^4}{4} r\left[\pi\left(2-4\frac{r^2}{R^2}\right) + \frac{r}{R}\sqrt{4-\frac{r^2}{R^2}}\left(\frac{r^2}{R^2}-6\right) + 16\frac{r^2}{R^2}\operatorname{arccot}\sqrt{\frac{2-r/R}{2+r/R}}\right. \\ & \left. + 8\operatorname{arccsc}\frac{2}{\sqrt{2-r/R}} - 4\left(1+2\frac{r^2}{R^2}\right)\arctan\frac{r/R}{\sqrt{4-r^2/R^2}}\right].\end{aligned}$$

One can check that $\int_0^{2R} dr\,\mathcal{N}(r) = 0$, which follows from $\sum_i \boldsymbol{v}_i = \boldsymbol{0}$. [11]

Putting $\mathcal{N}$ and $\mathcal{D}$ back together, I derive an expression for C_d. In order to have $C_d(0) = 1$, one should set $c_0 = R^2\omega^2/4$. When replacing c_0 by this value, the expression for C_d turns out to only depend on $x = r/(2R)$, and it can be written as

$$C_d(x) = \frac{\pi\left(1-8x^2\right) + 4x\sqrt{1-x^2}\left(2x^2-3\right) + 32x^2\operatorname{arccot}\sqrt{\frac{1-x}{1+x}} + 4\arcsin\sqrt{\frac{1-x}{2}} - 2\left(1+8x^2\right)\arctan\frac{x}{\sqrt{1-x^2}}}{3\pi - 4x\sqrt{1-x^2} - 4\operatorname{arcsec}\frac{2}{\sqrt{2-2x}} - 2\arctan\frac{x}{\sqrt{1-x^2}}}\,. \tag{C.4}$$

As mentioned in the main text, this function only depends on distance through its ratio to the size of the system. Since this function is rather cumbersome, one can also Taylor-expand it around 0 up to order 2, finding

$$C_d(x) \approx 1 - \frac{4}{\pi}x - \frac{16}{\pi^2}x^2\,. \tag{C.5}$$

This expression is a rather good approximation of C_d in the $[0;1]$ interval. In particular, it has a root at

$$x_0 = \frac{\pi}{8}\left(\sqrt{5}-1\right) \approx 0.485\,.$$

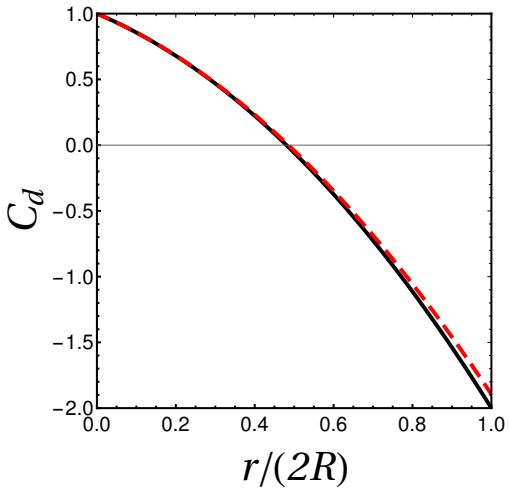

Fig. C.1 **Exact displacement-displacement correlations in a rotating homogenous disk.** I show here a plot of the exact expression (C.4) (black line), and its Taylor expansion to second order around 0 (dashed red line), as given by Eq. (C.5).

It is tempting to reproduce the calculation above in the case of the speed-speed correlation C_{sp}. In the case of a homogeneous disk, noticing that

$$\frac{1}{N}\sum_i v_i \approx \frac{1}{\pi R^2}\int d^2\boldsymbol{r}\; r\omega = \frac{2}{3}R\omega\,,$$

the full speed-speed correlation can be written as

$$\begin{aligned} C_{sp}(r) &= \frac{\omega^2}{c_{0,sp}\mathcal{D}(r)}\int d^2\boldsymbol{r}_1 d^2\boldsymbol{r}_2 \left(r_1 - \frac{2}{3}R\right)\left(r_2 - \frac{2}{3}R\right)\delta\left(r_{12} - r\right) \\ &= \frac{\omega^2}{c_{0,sp}\mathcal{D}(r)}\int d^2\boldsymbol{r}_1 d^2\boldsymbol{r}_2 \left(r_1 r_2 - \frac{4}{3}Rr_1 + \frac{4}{9}R^2\right)\delta\left(r_{12} - r\right)\,. \end{aligned}$$

While the last two terms in the integral in the numerator can be computed using the strategies used for C_d, the first term is in fact much less tractable. Indeed, if I call

$$\mathcal{N}^1_{sp}(r) \equiv \omega^2 \int d^2\boldsymbol{r}_1 d^2\boldsymbol{r}_2\; r_1 r_2\, \delta\left(r_{12} - r\right),$$

following the same route as for $\mathcal{N}$ yields

$$\mathcal{N}^1_{sp}(r) = 8\pi r\omega^2 \int_0^R dr_1\; r_1^2 \int_0^{R^2} du\; \frac{\sqrt{u}}{\sqrt{-\left(u-u_+\right)\left(u-u_-\right)}}\; \mathbb{1}\left[u_- \le u \le u_+\right].$$

Here, the most convenient change of variable is the one used for the other integrals, but where u_+ and u_- are swapped,

$$u = u_+ \cos^2\phi + u_- \sin^2\phi.$$

Indeed, using this definition, after some more algebra, one finds

$$\mathcal{N}^1_{sp}(r) = 8\pi r\omega^2 \int_0^{R-r} dr_1\, r_1^2\,(r+r_1)\, E\left(\frac{4rr_1}{(r+r_1)^2}\right) \mathbb{1}\left[r \leq R\right] \\ + 8\pi r\omega^2 \int_{|r-R|}^{R} dr_1\, r_1^2\,(r+r_1) \left[E\left(\frac{4rr_1}{(r+r_1)^2}\right) - E\left(\varphi_R, \frac{4rr_1}{(r+r_1)^2}\right)\right],$$

where $E(\varphi, x)$ is the incomplete elliptic integral of the second kind, [101] $E(x) = E(\pi/2, x)$ is the elliptic integral of the second kind, and

$$\varphi_R \equiv \arcsin\sqrt{\frac{u_+ - R^2}{u_+ - u_-}}\,.$$

Since elliptic functions are in general hard and cumbersome to treat analytically, there is little hope of writing a tractable expression for C_{sp} using this integration strategy. However, one still expects an expression that only depends on $r/(2R)$: changing variables following $r_{1,2} \to 2Rx_{1,2}$ in every integral of C_{sp} yields a $R^2\omega^2$ prefactor that should be absorbed by $c_{0,sp}$, like in the case of C_d.

Appendix D

First Steps towards a hydrodynamic description.

> "I couldn't get you to the ocean, but there was nothing stopping me bringing the ocean to you."
>
> Neil Gaiman, *The Ocean at the End of the Lane.*

In this appendix, I describe the first steps I have undertaken in deriving a hydrodynamic theory for spin-velocity coupled models, starting from the microscopic Hamiltonian. Following standard textbook methods [82, 258], in Sec. D.1 I derive the Boltzmann equation corresponding to a spin fluid with a linear spin-velocity coupling, and in Sec. D.2 I show how to use the conservation rules of the system to derive an Euler-level hydrodynamic equation.

D.1 Boltzmann's equation and kinetic theory

D.1.1 Derivation of the Boltzmann equation

I here study the system defined by the Hamiltonian:

$$H = \sum_{i=1}^{N} \left[\frac{1}{2}{\omega_i}^2 + \frac{1}{2}{p_i}^2 - K\left(\boldsymbol{p_i}\cdot\boldsymbol{s_i}\right) - \frac{1}{2}\sum_{k\neq i}\left[J(r_{ik})\boldsymbol{s_i}\cdot\boldsymbol{s_k} - U(r_{ik})\right] \right],$$

corresponding to the Hamiltonian equations of motion

$$\begin{aligned}
\dot{\boldsymbol{r}}_{\boldsymbol{i}} &= \partial_{\boldsymbol{p_i}} H = \boldsymbol{p_i} - K\boldsymbol{s_i}, \\
\dot{\boldsymbol{p}}_{\boldsymbol{i}} &= -\partial_{\boldsymbol{r_i}} H = \sum_{k\neq i} \partial_{\boldsymbol{r_i}} \left(j(r_{ik})\cos\theta_{ik} - U(r_{ik}) \right), \\
\dot{\theta}_i &= \partial_{\omega_i} H = \omega_i, \\
\dot{\omega}_i &= -\partial_{\theta_i} H = K\boldsymbol{p_i}\cdot\boldsymbol{s_i^{\perp}} + \sum_{k\neq i} j(r_{ik})\sin\theta_{ik}.
\end{aligned}$$

I introduce the phase space density of the system ρ, defined by

$$\rho(\boldsymbol{r},\boldsymbol{p},\theta,\omega,t) \equiv \sum_{i=1}^{N} \delta\left(\boldsymbol{r_i}(t)-\boldsymbol{r}\right)\delta\left(\boldsymbol{p_i}(t)-\boldsymbol{p}\right)\delta\left(\theta_i(t)-\theta\right)\delta\left(\omega_i(t)-\omega\right).$$

Considering the evolution of the system in an infinitesimal time interval, and using the Hamiltonian equations of motion, one can show (see, for instance, Kardar [82] or Reichl [83]) that the volume of an element of phase space does not change under Hamiltonian dynamics or, in other words that

$$\frac{d\rho}{dt} = 0.$$

This result, known as the Liouville equation, can be rewritten in terms of the Hamiltonian,

$$\frac{\partial\rho}{\partial t} = \sum_{i,a}\left(\frac{\partial\rho}{\partial p_{i,a}}\frac{\partial\mathcal{H}}{\partial q_{i,a}} - \frac{\partial\rho}{\partial q_{i,a}}\frac{\partial\mathcal{H}}{\partial p_{i,a}}\right),$$

and is often noted using so-called Poisson brackets,

$$\frac{\partial\rho}{\partial t} = -\left\{\rho,\mathcal{H}\right\}.$$

Replacing the Hamiltonian with its actual expression yields

$$\begin{aligned}\partial_t\rho = &-\sum_{i=1}^{N}\left(\boldsymbol{p_i}-K\boldsymbol{s_i}\right)\partial_{\boldsymbol{r_i}}\rho_i + \sum_{i=1}^{N}\partial_{\boldsymbol{p_i}}\rho_i\sum_{k\neq i}\partial_{\boldsymbol{r_i}}\left(j(r_{ik})\cos\theta_{ik}-U(r_{ik})\right)\\ &-\sum_{i=1}^{N}\omega_i\partial_{\theta_i}\rho_i + \sum_{i=1}^{N}\partial_{\omega_i}\rho_i\left((K\boldsymbol{p_i})\cdot\boldsymbol{s_i^{\perp}} + \sum_{k\neq i}j(r_{ik})\sin\theta_{ik}\right).\end{aligned}$$

In the last expression, I use the definition of ρ to express all the terms as functions of the coordinates in phase space only, and I rewrite the derivatives of the total potential as an integral over all of phase space, following standard rewritings [82],

$$\begin{aligned}\partial_t\rho = &-\left(\boldsymbol{p}-K\boldsymbol{s}\right)\partial_{\boldsymbol{r}}\rho - \omega\partial_\theta\rho + \partial_\omega\rho\left(K\boldsymbol{p}\right)\cdot\boldsymbol{s}^{\perp}\\ &+\partial_{\boldsymbol{p}}\rho\int d\boldsymbol{r'}d\boldsymbol{p'}d\theta'd\omega'\rho(\boldsymbol{r'},\boldsymbol{p'},\theta',\omega',t)\nabla_{\boldsymbol{r}}V(\boldsymbol{r}-\boldsymbol{r'},\theta-\theta')\\ &+\partial_\omega\rho\int d\boldsymbol{r'}d\boldsymbol{p'}d\theta'd\omega'\rho(\boldsymbol{r'},\boldsymbol{p'},\theta',\omega',t)\nabla_\theta V(\boldsymbol{r}-\boldsymbol{r'},\theta-\theta'),\end{aligned}$$

where:

$$\begin{aligned}\nabla_{\boldsymbol{r}}V(\boldsymbol{r}-\boldsymbol{r_k},\theta-\theta_k) &\equiv \partial_{\boldsymbol{u}}\left(j(\boldsymbol{u})\cos(\theta-\theta_k)-U(\boldsymbol{u})\right)\big|_{\boldsymbol{u}=\boldsymbol{r}-\boldsymbol{r_k}}\\ \nabla_\theta V(\boldsymbol{r}-\boldsymbol{r_k},\theta-\theta_k) &\equiv j(\boldsymbol{r}-\boldsymbol{r_k})\sin(\theta-\theta_k).\end{aligned}$$

Using hypothesis that ρ is symmetric under the permutation of any two particles, I

define the s-body phase space probability density f_s through

$$\begin{aligned} f_1(\boldsymbol{X_1};t) &\equiv N \int \left[\prod_{i=2}^{N} d\boldsymbol{X_i}\right] \rho\left(\boldsymbol{X_1};\boldsymbol{X_2},\ldots,\boldsymbol{X_N};t\right) \\ f_2(\boldsymbol{X_1},\boldsymbol{X_2};t) &\equiv N(N-1) \int \left[\prod_{i=3}^{N} d\boldsymbol{X_i}\right] \rho\left(\boldsymbol{X_1},\boldsymbol{X_2};\boldsymbol{X_3},\ldots,\boldsymbol{X_N};t\right) \\ &\vdots \\ f_s(\boldsymbol{X_1},\ldots,\boldsymbol{X_s};t) &\equiv \frac{N!}{(N-s)!} \int \left[\prod_{i=s+1}^{N} d\boldsymbol{X_i}\right] \rho\left(\boldsymbol{X_1},\ldots,\boldsymbol{X_s};\boldsymbol{X_{s+1}},\ldots,\boldsymbol{X_N};t\right), \end{aligned}$$

where I call $\boldsymbol{X_i} \equiv \{\boldsymbol{r_i},\boldsymbol{p_i},\theta_i,\omega_i\})$ a full set of coordinates in phase space. Furthermore, I define the unconditional s-body PDFs ρ_s as:

$$\begin{aligned} \rho_s(\boldsymbol{X_1},\ldots,\boldsymbol{X_s};t) &\equiv \frac{(N-s)!}{N!} f_s(\boldsymbol{X_1},\ldots,\boldsymbol{X_s};t) \\ &= \int \left[\prod_{i=s+1}^{N} d\boldsymbol{X_i}\right] \rho\left(\boldsymbol{X_1},\ldots,\boldsymbol{X_s};\boldsymbol{X_{s+1}},\ldots,\boldsymbol{X_N};t\right) \end{aligned}$$

In order to use these definitions in a convenient way, I decompose the Hamiltonian into three parts:

$$H = H_s + H_{N-s} + H'$$

where the first two terms correspond to Hamiltonians with the same definition as before, but restricted to a subsystem of size s and a subsystem of size $N-s$. The last part therefore contains all the interactions between these two subsystems[1]:

$$H' = \sum_{i=1}^{s} \sum_{k=s+1}^{N} \left[U(r_{ik}) - j(r_{ik}) \boldsymbol{s_i} \cdot \boldsymbol{s_k}\right]$$

Then, for the subsystem with size s:

$$\frac{\partial \rho_s}{\partial t} = \int \left[\prod_{i=s+1}^{N} d\boldsymbol{X_i}\right] \frac{\partial \rho}{\partial t} = -\int \left[\prod_{i=s+1}^{N} d\boldsymbol{X_i}\right] \{\rho, H_s + H_{N-s} + H'\} \tag{D.1}$$

I now focus on each term of this decomposition separately. The first one simply reads

$$\int \left[\prod_{i=s+1}^{N} d\boldsymbol{X_i}\right] \{\rho, H_s\} = \{\rho_s, H_s\}$$

[1]The factor of $\frac{1}{2}$ disappears when considering the two parts contributing to H'

The second one, which I henceforth call I_{N-s}, on the other hand, reads

$$\begin{aligned} I_{N-s} &= -\int \left[\prod_{i=s+1}^{N} d\boldsymbol{X_i}\right] \{\rho, H_{N-s}\} \\ &= \int \left[\prod_{i=s+1}^{N} d\boldsymbol{X_i}\right] \sum_{j=1}^{N} \left(\partial_{\boldsymbol{r_j}} H_{N-s} \partial_{\boldsymbol{p_j}} \rho - \partial_{\boldsymbol{p_j}} H_{N-s} \partial_{\boldsymbol{r_j}} \rho + \partial_{\theta_j} H_{N-s} \partial_{\omega_j} \rho - \partial_{\omega_j} H_{N-s} \partial_{\theta_j} \rho\right) \\ &= \int \left[\prod_{i=s+1}^{N} d\boldsymbol{X_i}\right] \sum_{j=s+1}^{N} \left(\partial_{\boldsymbol{r_j}} H_{N-s} \partial_{\boldsymbol{p_j}} \rho - \partial_{\boldsymbol{p_j}} H_{N-s} \partial_{\boldsymbol{r_j}} \rho + \partial_{\theta_j} H_{N-s} \partial_{\omega_j} \rho - \partial_{\omega_j} H_{N-s} \partial_{\theta_j} \rho\right) \end{aligned}$$

Just like for regular gases [82], I can integrate by parts for each couple of conjugated variables and find that this term integrates to $I_{N-s} = 0$. Finally, the third term, that I call I', reads:

$$\begin{aligned} I' &= -\int \left[\prod_{i=s+1}^{N} d\boldsymbol{X_i}\right] \{\rho, H'\} \\ &= \int \left[\prod_{i=s+1}^{N} d\boldsymbol{X_i}\right] \sum_{j=1}^{N} \left(\partial_{\boldsymbol{r_j}} H' \partial_{\boldsymbol{p_j}} \rho - \partial_{\boldsymbol{p_j}} H' \partial_{\boldsymbol{r_j}} \rho + \partial_{\theta_j} H' \partial_{\omega_j} \rho - \partial_{\omega_j} H' \partial_{\theta_j} \rho\right) \\ &= \int \left[\prod_{i=s+1}^{N} d\boldsymbol{X_i}\right] \sum_{j=1}^{N} \left(\partial_{\boldsymbol{r_j}} H' \partial_{\boldsymbol{p_j}} \rho + \partial_{\theta_j} H' \partial_{\omega_j} \rho\right) \\ &= \int \left[\prod_{i=s+1}^{N} d\boldsymbol{X_i}\right] \left(\sum_{j=1}^{s} \partial_{\boldsymbol{p_j}} \rho \cdot \sum_{k=s+1}^{N} \partial_{\boldsymbol{r_k}} \left[U(r_{jk}) - j(r_{jk}) \boldsymbol{s_j} \cdot \boldsymbol{s_k}\right] + \sum_{j=1}^{s} \partial_{\omega_j} \rho \sum_{k=s+1}^{N} j(r_{jk}) \sin\theta_{jk}\right) \\ &\quad + \int \left[\prod_{i=s+1}^{N} d\boldsymbol{X_i}\right] \left(\sum_{j=s+1}^{N} \partial_{\boldsymbol{p_j}} \rho \cdot \sum_{k=1}^{s} \partial_{\boldsymbol{r_k}} \left[U(r_{jk}) - j(r_{jk}) \boldsymbol{s_j} \cdot \boldsymbol{s_k}\right] + \sum_{j=s+1}^{N} \partial_{\omega_j} \rho \sum_{k=1}^{s} j(r_{jk}) \sin\theta_{jk}.\right) \end{aligned}$$

Just like before, an integration by parts shows that the second integral is simply 0, so that, using the isotropy of all the couplings, I find

$$\begin{aligned} I' &= \int \left[\prod_{i=s+1}^{N} d\boldsymbol{X_i}\right] \left(\sum_{j=1}^{s} \partial_{\boldsymbol{p_j}} \rho \cdot \sum_{k=s+1}^{N} \partial_{\boldsymbol{r_k}} \left[U(r_{jk}) - j(r_{jk}) \boldsymbol{s_j} \cdot \boldsymbol{s_k}\right] + \sum_{j=1}^{s} \partial_{\omega_j} \rho \sum_{k=s+1}^{N} j(r_{jk}) \sin\theta_{jk}\right) \\ &= (N-s) \sum_{j=1}^{s} \int d\boldsymbol{X_{s+1}} \left(\partial_{\boldsymbol{p_j}} \rho_{s+1} \cdot \partial_{\boldsymbol{r_j}} \left[U(r_{j,s+1}) - j(r_{j,s+1}) \boldsymbol{s_j} \cdot \boldsymbol{s_{s+1}}\right] + \partial_{\omega_j} \rho_{s+1} j(r_{j,s+1}) \sin\theta_{j,s+1}\right). \end{aligned}$$

Putting all three parts of Eq. (D.1) back together, one finds, for all values of s, an

equation that links ρ_s to ρ_{s+1},

$$\frac{\partial \rho_s}{\partial t} - \{H_s, \rho_s\} = (N-s) \sum_{n=1}^{s} \int d\boldsymbol{X_{s+1}} \left(\frac{\partial \rho_{s+1}}{\partial \boldsymbol{p_n}} \cdot \frac{\partial}{\partial \boldsymbol{r_n}} V_{n,s+1} + \frac{\partial \rho_{s+1}}{\partial \omega_n} \frac{\partial}{\partial \theta_n} V_{n,s+1} \right),$$

where I introduced the short-hand notation

$$V_{n,s+1} \equiv \left[U(r_{n,s+1}) - j(r_{n,s+1}) \boldsymbol{s_n} \cdot \boldsymbol{s_{s+1}} \right].$$

This hierarchy of equations can equivalently be written on the f_s's,

$$\frac{\partial f_s}{\partial t} - \{H_s, f_s\} = \sum_{n=1}^{s} \int d\boldsymbol{X_{s+1}} \left(\frac{\partial f_{s+1}}{\partial \boldsymbol{p_n}} \cdot \frac{\partial}{\partial \boldsymbol{r_n}} V_{n,s+1} + \frac{\partial f_{s+1}}{\partial \omega_n} \frac{\partial}{\partial \theta_n} V_{n,s+1} \right)$$

and is called the Born-Bogoliubov-Green-Kubo-Yvon (BBGKY) hierarchy [82]. They are exact equations, that describe the evolution of the $s-$body density in phase space in terms of $s+1$-body interactions, but they are in practice impossible to use without resorting to an approximation that yields a (small) finite number of equations instead.

To do so, one generally focuses on the first two equations of the BBGKY hierarchy,

$$\begin{aligned}
\frac{\partial f_1}{\partial t} - \{H_1, f_1\} &= \int d\boldsymbol{X_2} \left(\frac{\partial f_2}{\partial \boldsymbol{p_1}} \cdot \frac{\partial}{\partial \boldsymbol{r_1}} V_{1,2} + \frac{\partial f_2}{\partial \omega_1} \frac{\partial}{\partial \theta_1} V_{1,2} \right) \\
\frac{\partial f_2}{\partial t} - \{H_2, f_2\} &= \sum_{n=1}^{2} \int d\boldsymbol{X_3} \left(\frac{\partial f_3}{\partial \boldsymbol{p_n}} \cdot \frac{\partial}{\partial \boldsymbol{r_n}} V_{n,3} + \frac{\partial f_3}{\partial \omega_n} \frac{\partial}{\partial \theta_n} V_{n,3} \right),
\end{aligned}$$

and introduces a closure relation that simplifies the second equation. The most common such procedure consists in neglecting all s-body collisions as soon as $s > 2$, so that the right-hand side of the second equation is assumed to be zero [82], yielding the simpler system of equations

$$\begin{aligned}
\frac{\partial f_1}{\partial t} - \{H_1, f_1\} &= \int d\boldsymbol{X_2} \left(\frac{\partial f_2}{\partial \boldsymbol{p_1}} \cdot \frac{\partial}{\partial \boldsymbol{r_1}} V_{1,2} + \frac{\partial f_2}{\partial \omega_1} \frac{\partial}{\partial \theta_1} V_{1,2} \right) \\
\frac{\partial f_2}{\partial t} - \{H_2, f_2\} &= 0.
\end{aligned}$$

I will here use this closure relation. Using the definition of the Poisson bracket, as well as the fact that the one-particle Hamiltonian does not depend on the position of the particle, I write that

$$\begin{aligned}
\{H_1, f_1\} &= -\partial_{\boldsymbol{p_1}} H_1 \partial_{\boldsymbol{r_1}} f_1 + \partial_{\theta_1} H_1 \partial_{\omega_1} f_1 - \partial_{\omega_1} H_1 \partial_{\theta_1} f_1 \\
&= -\dot{\boldsymbol{r}}_{\boldsymbol{1}} \cdot \partial_{\boldsymbol{r_1}} f_1 - \dot{\omega}_1 \partial_{\omega_1} f_1 - \dot{\theta}_1 \partial_{\theta_1} f_1.
\end{aligned}$$

This equation can be used to rewrite the equation on f_1 as

$$\left[\frac{\partial}{\partial t} + \dot{\boldsymbol{r}}_{\boldsymbol{1}} \cdot \frac{\partial}{\partial \boldsymbol{r_1}} + \dot{\omega}_1 \frac{\partial}{\omega_1} + \dot{\theta}_1 \frac{\partial}{\partial \theta_1} \right] f_1 = \int d\boldsymbol{X_2} \left(\frac{\partial f_2}{\partial \boldsymbol{p_1}} \cdot \frac{\partial}{\partial \boldsymbol{r_1}} V_{1,2} + \frac{\partial f_2}{\partial \omega_1} \frac{\partial}{\partial \theta_1} V_{1,2} \right).$$

The right-hand side of this equation is often called a collision integral, as it describes the evolution of the one-body probability density in phase space in terms of two-body interactions, so that I introduce the short-hand notation

$$\left[\frac{\partial}{\partial t} + \dot{\boldsymbol{r}}_{\boldsymbol{1}} \cdot \frac{\partial}{\partial \boldsymbol{r_1}} + \dot{\omega}_1 \frac{\partial}{\omega_1} + \dot{\theta}_1 \frac{\partial}{\partial \theta_1} \right] f_1 \equiv \left. \frac{df_1}{dt} \right|_{coll}.$$

Using this more compact notation, I write

$$\left.\frac{df_1}{dt}\right|_{coll} = \int d\boldsymbol{X_2} \left(\frac{\partial f_2}{\partial \boldsymbol{p_1}} \cdot \frac{\partial}{\partial \boldsymbol{r_1}} V_{1,2} + \frac{\partial f_2}{\partial \omega_1} \frac{\partial}{\partial \theta_1} V_{1,2} \right).$$

This equation can be symmetrized by adding terms that integrate to 0,

$$\left.\frac{df_1}{dt}\right|_{coll} = \int d\boldsymbol{X_2} \left(\left(\frac{\partial}{\partial \boldsymbol{p_1}} - \frac{\partial}{\partial \boldsymbol{p_2}} \right) f_2 \cdot \frac{\partial}{\partial \boldsymbol{r_1}} V_{1,2} + \left(\frac{\partial}{\partial \omega_1} - \frac{\partial}{\partial \omega_2} \right) f_2 \frac{\partial}{\partial \theta_1} V_{1,2} \right).$$

Then, a usual hypothesis is that f_2 should be a slow function of $\boldsymbol{R} \equiv \frac{\boldsymbol{r_1}+\boldsymbol{r_2}}{2}$ but a fast function of $\boldsymbol{r} \equiv \boldsymbol{r_2} - \boldsymbol{r_1}$ [82], so that:

$$\begin{aligned} \frac{\partial f_2}{\partial \boldsymbol{R}} &\ll \frac{\partial f_2}{\partial \boldsymbol{r}} \\ \frac{\partial f_2}{\partial \boldsymbol{r_2}} &\approx -\frac{\partial f_2}{\partial \boldsymbol{r_1}} \approx \frac{\partial f_2}{\partial \boldsymbol{r}} \end{aligned}$$

Likewise, I expect that, if $\Theta = \frac{\theta_1+\theta_2}{2}$ and $\theta = \theta_2 - \theta_1$,

$$\begin{aligned} \frac{\partial f_2}{\partial \Theta} &\ll \frac{\partial f_2}{\partial \theta} \\ \frac{\partial f_2}{\partial \theta_2} &\approx -\frac{\partial f_2}{\partial \theta_1} \approx \frac{\partial f_2}{\partial \theta} \end{aligned}$$

In order to use these approximations, I furthermore assume that the dependence of f_2 in the relative coordinates is well-approximated by its steady-state behaviour:

$$\begin{aligned} 0 &= -\{H_2, f_2\} \\ &= \left[\dot{\boldsymbol{r}}_{\boldsymbol{1}} \cdot \frac{\partial}{\partial \boldsymbol{r_1}} + \dot{\boldsymbol{r}}_{\boldsymbol{2}} \cdot \frac{\partial}{\partial \boldsymbol{r_2}} + \omega_1 \frac{\partial}{\partial \theta_1} + \omega_2 \frac{\partial}{\partial \theta_2} \right] f_2 \\ &\quad - \left[\frac{1}{2} \frac{\partial}{\partial \boldsymbol{r_1}} V_{1,2} \left(\frac{\partial}{\partial \boldsymbol{p_1}} - \frac{\partial}{\partial \boldsymbol{p_2}} \right) + \frac{1}{2} \frac{\partial}{\partial \theta_1} V_{1,2} \left(\frac{\partial}{\partial \omega_1} - \frac{\partial}{\partial \omega_2} \right) \right] f_2 \end{aligned}$$

Using the approximations mentioned above for relative coordinates, I get:

$$\left[\frac{1}{2} \frac{\partial}{\partial \boldsymbol{r_1}} V_{1,2} \left(\frac{\partial}{\partial \boldsymbol{p_1}} - \frac{\partial}{\partial \boldsymbol{p_2}} \right) + \frac{1}{2} \frac{\partial}{\partial \theta_1} V_{1,2} \left(\frac{\partial}{\partial \omega_1} - \frac{\partial}{\partial \omega_2} \right) \right] f_2 \approx \left[(\dot{\boldsymbol{r}}_{\boldsymbol{2}} - \dot{\boldsymbol{r}}_{\boldsymbol{1}}) \cdot \frac{\partial}{\partial \boldsymbol{r}} + (\omega_2 - \omega_1) \frac{\partial}{\partial \theta} \right] f_2$$

In this last equation, note that the difference of velocities, when expressed in terms of the canonical Hamiltonian variables, takes the unusual form

$$\dot{\boldsymbol{r}}_{\boldsymbol{2}} - \dot{\boldsymbol{r}}_{\boldsymbol{1}} = \boldsymbol{p_2} - \boldsymbol{p_1} - K\left(\boldsymbol{s_2} - \boldsymbol{s_1}\right).$$

Finally, the collision equation can be written as:

$$\begin{aligned} \left.\frac{df_1}{dt}\right|_{coll} &= \int d\boldsymbol{X_2} \left[(\dot{\boldsymbol{r}}_{\boldsymbol{2}} - \dot{\boldsymbol{r}}_{\boldsymbol{1}}) \cdot \frac{\partial}{\partial \boldsymbol{r}} + (\omega_2 - \omega_1) \frac{\partial}{\partial \theta} \right] f_2 \\ &= \int d\boldsymbol{X_2} \left[(\boldsymbol{p_2} - \boldsymbol{p_1} - K\left(\boldsymbol{s_2} - \boldsymbol{s_1}\right)) \cdot \frac{\partial}{\partial \boldsymbol{r}} + (\omega_2 - \omega_1) \frac{\partial}{\partial \theta} \right] f_2 \end{aligned}$$

In 2 dimensions of space, which is the case I am most concerned with in the context of this thesis, the rotational part integrates to zero, since $\theta \in \mathbb{R}\backslash 2\pi$ [2]. Therefore, here, I only have:

$$\begin{aligned}\left.\frac{df_1}{dt}\right|_{coll} &= \int d\boldsymbol{X_2}\left[(\dot{\boldsymbol{r}}_\mathbf{2}-\dot{\boldsymbol{r}}_\mathbf{1})\cdot\frac{\partial}{\partial \boldsymbol{r}}\right] f_2 \\ &= \int d\boldsymbol{X_2}\left[(\boldsymbol{p_2}-\boldsymbol{p_1}-K\left(\boldsymbol{s_2}-\boldsymbol{s_1}\right))\cdot\frac{\partial}{\partial \boldsymbol{r}}\right] f_2\end{aligned}$$

This is the usual definition of the so-called Boltzmann equation [82]. At this point, one generally introduces cylindrical coordinates along the (straight) trajectory of particle 2, as seen from the frame associated to particle 1, before the collision. In the case of the present model, an additional difficulty is that the free particle trajectories are not straight lines (see Fig. II.1). I nevertheless assume that the trajectories of free particles are rectilinear enough at the time scale of interactions that I can use the usual definition of the Boltzmann cylinder. I therefore define $d\boldsymbol{X_2} = d\boldsymbol{r}d\boldsymbol{\Gamma_2}$, and integrate over the space coordinate that is along the axis of the cylinder, so that the Boltzmann equation takes its more conventional form:

$$\left.\frac{df_1}{dt}\right|_{coll} = \int dbd\boldsymbol{\Gamma_2}\left|\dot{\boldsymbol{r}}_\mathbf{2}-\dot{\boldsymbol{r}}_\mathbf{1}\right|\left(f_2^+-f_2^-\right)\delta(\text{rules}), \tag{D.2}$$

where b is the collision parameter (coordinate perpendicular to the revolution axis of the cylinder), $+$ and $-$ superscripts correspond to states of the system after and before the collision, and δ(rules) is here used as a simple reminder that several conservation rules should be enforced (notably momentum conservation), thereby linking f_2^+ to f_2^-. This equation is generally used to predict the evolution of observables due to binary collisions. Consider the evolution of an observable $\boldsymbol{A}$ (e.g. the total magnetisation of the fluid) due to a binary collision in the N-particle fluid, and $\boldsymbol{a}$ its microscopic 2-particle counterpart (e.g. the total magnetisation of the binary system, $\boldsymbol{s} = \boldsymbol{s_1} + \boldsymbol{s_2}$). I can immediately write that $\frac{d\boldsymbol{A}}{dt} = \frac{d}{dt}\int f_1 \boldsymbol{a} d\boldsymbol{X_1}$ Using the Boltzmann equation, I furthermore find that:

$$\frac{d\boldsymbol{A}}{dt} = \int dbd\boldsymbol{\Gamma_2}d\boldsymbol{X_1}\left|\dot{\boldsymbol{r}}_\mathbf{2}-\dot{\boldsymbol{r}}_\mathbf{1}\right|\boldsymbol{a}\left(f_2^+-f_2^-\right)\delta(\text{rules}),$$

This can be rewritten by introducing the values of the microscopic observable before and after a collision, and factorizing the two-body distribution before the collision:

$$\frac{d\boldsymbol{A}}{dt} = \int dbd\boldsymbol{\Gamma_2}d\boldsymbol{X_1}\left|\dot{\boldsymbol{r}}_\mathbf{2}-\dot{\boldsymbol{r}}_\mathbf{1}\right| f_2^-\left(\boldsymbol{a}'-\boldsymbol{a}\right)\delta(\text{rules}).$$

In order to use this equation, one needs to predict a shape for f_2. This task is generally strenuous, so that it is common to make additional assumptions to approximate it:

(i) I assume that I am studying homogeneous dilute phases, so that the space density factorizes,

$$f_2(\boldsymbol{r}_1,\boldsymbol{p}_1,\theta_1,\omega_1,\boldsymbol{r}_2|_{|a|\to\infty},\boldsymbol{p_2},\theta_2,\omega_2) \simeq \rho^2\tilde{f}_2(\boldsymbol{p}_1,\theta_1,\omega_1,\boldsymbol{p_2},\theta_2,\omega_2).$$

[2] In higher dimensions, however, only one angular integration on the hypersphere is performed on the whole $[0;2\pi]$ interval.

(ii) I assume "molecular chaos", meaning that particles are completely independent except at the instant of the collision, so that

$$\tilde{f}_2(\boldsymbol{p}_1, \theta_1, \omega_1, \boldsymbol{p_2}, \theta_2, \omega_2) \simeq \tilde{f}_1(\boldsymbol{p}_1, \theta_1, \omega_1)\tilde{f}_1(\boldsymbol{p_2}, \theta_2, \omega_2)$$

Using those hypotheses, I get:

$$\frac{d\boldsymbol{A}}{dt} = N\rho \int dbd\boldsymbol{\Gamma_2} d\boldsymbol{\Gamma_1} \, |\dot{\boldsymbol{r}}_{\boldsymbol{2}} - \dot{\boldsymbol{r}}_{\boldsymbol{1}}| \, \tilde{f}_1(\boldsymbol{p}_1, \theta_1, \omega_1)\tilde{f}_1(\boldsymbol{p_2}, \theta_2, \omega_2)(\boldsymbol{a}' - \boldsymbol{a})\delta(\text{rules}).$$

I also assume for simplicity that the angular velocity distribution factorizes and that the collision rules do not depend to much on angular velocities, so that I can integrate them out:

$$\frac{d\boldsymbol{A}}{dt} = N\rho \int dbd\boldsymbol{p}_2 d\boldsymbol{p}_1 d\theta_1 d\theta_2 \, |\dot{\boldsymbol{r}}_{\boldsymbol{2}} - \dot{\boldsymbol{r}}_{\boldsymbol{1}}| \, f_1(\boldsymbol{p}_1, \theta_1) f_1(\boldsymbol{p_2}, \theta_2)(\boldsymbol{a}' - \boldsymbol{a})\delta(\text{rules}). \quad \text{(D.3)}$$

D.1.2 Kinetic theory with a simple ansatz

Having established the Boltzmann equation (D.2), and the resulting evolution equation for observables (D.3) under simple hypotheses, that only depends on f_1, I can seek a simple ansatz for the shape of distribution f_1 to get a feeling of the physics of the system as viewed from kinetic theorety. I assume that I am studying two particles in a magnetised fluid, with intensive magnetisation $\boldsymbol{m}$ and a velocity of the centre of mass $\boldsymbol{v_G}$. A reasonable mean-field-like form for f_1 would be:

$$f_1(\boldsymbol{p}, \boldsymbol{s}) = \frac{1}{\mathcal{N}} \exp\left[-\beta\left(\frac{p^2}{2} - K\boldsymbol{p}\cdot\boldsymbol{s} - \boldsymbol{v_G}\cdot\boldsymbol{p} - J\boldsymbol{s}\cdot\boldsymbol{m}\right)\right], \quad \text{(D.4)}$$

where $\mathcal{N}$ is a normalization constant, β is the inverse temperature of the surrounding fluid and J is an effective ferromagnetic constant. This distribution contains, following the order of terms in the exponential: the two momentum-dependent terms of the Hamiltonian, the part of the Gibbs measure that ensures conservation of momentum, and an effective, mean-field-like term for the distribution of spins.

I first check that the behaviour of this distribution makes sense consdering what I learned on the model in this thesis. Integrating f_1 over momenta yields a distribution of spin orientations:

$$\begin{aligned} f_1(\boldsymbol{s}) &= \int d^2\boldsymbol{p} f_1(\boldsymbol{p}, \boldsymbol{s}), \\ &= \frac{1}{\mathcal{N}}\frac{2\pi}{\beta} e^{\beta J \boldsymbol{s}\cdot\boldsymbol{m}} e^{\frac{1}{2}\beta(K\boldsymbol{s}+\boldsymbol{v_G})^2}, \\ &= \frac{2\pi}{\beta\mathcal{N}} e^{\frac{1}{2}\beta(K^2+v_G^2)} e^{\beta\boldsymbol{s}\cdot(J\boldsymbol{m}+K\boldsymbol{v_G})}, \\ &= \frac{2\pi}{\beta\mathcal{N}} e^{\frac{1}{2}\beta(K^2+v_G^2)} e^{\beta\boldsymbol{s}\cdot\boldsymbol{h}_{eff}}, \end{aligned}$$

where I defined $\boldsymbol{h}_{eff} \equiv J\boldsymbol{m} + K\boldsymbol{v_G}$, the effective field acting on spins in the distribution. From this distribution, I compute the zeroth and first moment of the spin distribution.

The zeroth moment is just a normalization of the probability distribution function:

$$\begin{aligned} 1 &= \int d\theta f_1(\boldsymbol{s}), \\ &= \frac{2\pi}{\beta\mathcal{N}} e^{\frac{1}{2}\beta(K^2+v_G^2)} 2\pi I_0(\beta h_{eff}), \end{aligned}$$

which yields an expression for the normalization:

$$\mathcal{N} = \frac{4\pi^2}{\beta} e^{\frac{1}{2}\beta(K^2+v_G^2)} I_0(\beta h_{eff}).$$

Using this expression for $\mathcal{N}$ in the definition of $f_1(\boldsymbol{s})$ yields a much simpler Von Mises form:

$$f_1(\boldsymbol{s}) = \frac{e^{\beta \boldsymbol{h}_{eff}\cdot\boldsymbol{s}}}{2\pi I_0(\beta h_{eff})}.$$

The first moment then yields a self-consistent equation on the magnetisation:

$$\begin{aligned} \boldsymbol{m} &= \int d\theta \boldsymbol{s} f_1(\boldsymbol{s}), \\ &= \frac{I_1(\beta h_{eff})}{I_0(\beta h_{eff})}, \\ &= \frac{I_1(\beta\,|J\boldsymbol{m} + K\boldsymbol{v_G}|)}{I_0(\beta\,|J\boldsymbol{m} + K\boldsymbol{v_G}|)}. \end{aligned}$$

This expression is exactly that found in the fully-connected description presented in Sec. II.3.

The momentum part of the distribution is a priori harder to study, as a naïve integration over spins yields:

$$f_1(\boldsymbol{p}) = \frac{1}{\mathcal{N}} e^{-\beta\left(\frac{p^2}{2} - \boldsymbol{v_G}\cdot p\right)} 2\pi I_0\left(\beta\,|K\boldsymbol{p} + J\boldsymbol{m}|\right)$$

However, recalling that $\boldsymbol{p} = \boldsymbol{v} + K\boldsymbol{s}$ for any one particle, so that a change of variables yields

$$f_1(\boldsymbol{v}, \boldsymbol{s}) = \frac{1}{\mathcal{N}} \exp\left[-\beta\left(\frac{v^2}{2} - K\boldsymbol{v_G}\cdot\boldsymbol{s} - \boldsymbol{v_G}\cdot\boldsymbol{v} - J\boldsymbol{s}\cdot\boldsymbol{m}\right)\right],$$

where I absorbed a constant factor of $e^{\beta K^2/2}$ into the normalization. Using this expression, I get a distribution of velocities by integrating out the spins,

$$f_1(\boldsymbol{v}) = \frac{1}{\mathcal{N}} \exp\left[-\beta\left(\frac{v^2}{2} - \boldsymbol{v_G}\cdot\boldsymbol{v}\right)\right] 2\pi I_0(\beta h_{eff})$$

Computing the zeroth moment, I recover the same value for $\mathcal{N}$ as before (recalling that I absorbed a constant into $\mathcal{N}$ already). The average value of $\boldsymbol{v}$, on the other hand, yields $\boldsymbol{v_G}$ as expected. In summary, using a shape for f_1 that was directly inspired by the Gibbs measure of the system at mean-field level, I find that spins are drawn from a Von Mises distribution around $\boldsymbol{m}$ and velocities from a Gaussian centered on $\boldsymbol{v_G}$. As the determinant

of the Jacobian of the transformation $(\boldsymbol{p}, \boldsymbol{s}) \mapsto (\boldsymbol{v}, \boldsymbol{s})$ is 1, the Boltzmann equation can be rewritten using this ansatz for f_1 in $\boldsymbol{v}, \boldsymbol{s}$ variables:

$$\frac{d\boldsymbol{A}}{dt} = N\rho \int dbd\boldsymbol{v}_2 d\boldsymbol{v}_1 d\theta_1 d\theta_2 \, |\boldsymbol{v_2} - \boldsymbol{v_1}| \, f_1(\boldsymbol{v}_1, \theta_1) f_1(\boldsymbol{v_2}, \theta_2)(\boldsymbol{a'} - \boldsymbol{a})\delta(\text{rules}),$$

What remains to be done is defining some collision rules for microscopic variables. The variables in the problem at hand are velocities and spins, whose evolution is constrained by conservation of momentum during the collision. An exact but cumbersome way to deal with these collision rules would be to integrate the equations of motion by sampling initial conditions. Instead, in order to get qualitative results, I assume some simpler rules. I call $\overline{\theta} = \text{Arg}\left[e^{i\theta_1} + e^{i\theta_2}\right]$ the bisector angle of incoming spins. The interest of defining rules on the spin in this model becomes clear when trying to compute the modification of velocity during a collision:

$$\frac{d\boldsymbol{V}}{dt} = N\rho \int dbd\boldsymbol{v}_2 d\boldsymbol{v}_1 d\theta_1 d\theta_2 \, |\boldsymbol{v_2} - \boldsymbol{v_1}| \, f_1(\boldsymbol{v}_1, \theta_1) f_1(\boldsymbol{v_2}, \theta_2)(\boldsymbol{v'} - \boldsymbol{v})\delta(\boldsymbol{p'} - \boldsymbol{p}),$$
$$\frac{d\boldsymbol{V}}{dt} = N\rho \int dbd\boldsymbol{v}_2 d\boldsymbol{v}_1 d\theta_1 d\theta_2 \, |\boldsymbol{v_2} - \boldsymbol{v_1}| \, f_1(\boldsymbol{v}_1, \theta_1) f_1(\boldsymbol{v_2}, \theta_2) K(\boldsymbol{s} - \boldsymbol{s'}).$$

Indeed, in this form, momentum conservation enables to convert the change of velocity into a change of magnetisation. Note that the interaction rule could a priori encompass some two-range interactions with a short-range hardcore exclusion that simply reverses velocities and thereby conserves the "usual" momentum $\boldsymbol{v}$: then, only the change in spins can modify velocity alignment. Following the gist of the original Vicsek model [52], I assume that during a collision, spins align onto $\overline{\theta}$ with some noise η drawn from a distribution $\mathbb{P}(\eta)$:

$$\boldsymbol{s_1'} = \hat{\boldsymbol{e}}(\overline{\theta} + \eta),$$
$$\boldsymbol{s_2'} = \hat{\boldsymbol{e}}(\overline{\theta} - \eta).$$

An additional integration is then needed as part of the collision rules to count all possible values of η:

$$\frac{d\boldsymbol{V}}{dt} = N\rho \int dbd\boldsymbol{v}_2 d\boldsymbol{v}_1 d\theta_1 d\theta_2 d\eta \, |\boldsymbol{v_2} - \boldsymbol{v_1}| \, f_1(\boldsymbol{v}_1, \theta_1) f_1(\boldsymbol{v_2}, \theta_2) K(\boldsymbol{s} - \boldsymbol{s'}(\eta))\mathbb{P}(\eta).$$

I assume that magnetic interactions have a finite (short) range σ. Using some basic trigonometry at the instant when particles are exactly separated by a distance σ, the integral over the impact parameter b can be turned into an integral over an angle γ [38, 259]:

$$\int_{-\sigma}^{\sigma} db = \sigma \int_{-\pi/2}^{\pi/2} d\gamma \, |sin\gamma|$$

As the rules we chose do not depend on γ, I simply get a factor of 2σ in front of the integral.

$$\frac{d\boldsymbol{V}}{dt} = 2NK\rho\sigma \int d\boldsymbol{v}_2 d\boldsymbol{v}_1 d\theta_1 d\theta_2 d\eta \, |\boldsymbol{v_2} - \boldsymbol{v_1}| \, f_1(\boldsymbol{v}_1, \theta_1) f_1(\boldsymbol{v_2}, \theta_2)(\boldsymbol{s} - \boldsymbol{s'}(\eta))\mathbb{P}(\eta).$$

I furthermore assume a simple form for $\mathbb{P}(\eta)$, e.g.

$$\mathbb{P}(\eta) = \frac{e^{-\eta^2/2\sigma_\eta^2}}{\sqrt{2\pi\sigma_\eta^2}},$$

so that:

$$\frac{d\boldsymbol{V}}{dt} = 2NK\rho\sigma \int d\boldsymbol{v}_2 d\boldsymbol{v}_1 d\theta_1 d\theta_2 \, |\boldsymbol{v_2} - \boldsymbol{v_1}| \, f_1(\boldsymbol{v}_1, \theta_1) f_1(\boldsymbol{v_2}, \theta_2)(\boldsymbol{s} - 2\hat{\boldsymbol{e}}(\overline{\theta}) e^{-\sigma_\eta^2/2}).$$

I then introduce the ansatz (D.4) on the one-body distributions:

$$\begin{aligned}\frac{d\boldsymbol{V}}{dt} = \frac{2N}{\mathcal{N}^2} K\rho\sigma \int d\boldsymbol{v}_2 d\boldsymbol{v}_1 d\theta_1 d\theta_2 \, |\boldsymbol{v_2} - \boldsymbol{v_1}| \, (\boldsymbol{s} - 2\hat{\boldsymbol{e}}(\overline{\theta}) e^{-\sigma_\eta^2/2}) \\ \times e^{-\beta\left(\frac{v_1^2}{2} - K\boldsymbol{v_G}\cdot\boldsymbol{s_1} - \boldsymbol{v_G}\cdot\boldsymbol{v_1} - J\boldsymbol{s_1}\cdot\boldsymbol{m}\right)} e^{-\beta\left(\frac{v_2^2}{2} - K\boldsymbol{v_G}\cdot\boldsymbol{s_2} - \boldsymbol{v_G}\cdot\boldsymbol{v_2} - J\boldsymbol{s_2}\cdot\boldsymbol{m}\right)}\end{aligned}$$

Notice than the integrals over velocities and spins are decoupled, so that I can consider them separately. In order to make computations easier to follow, I factorize the distribution by a constant to rewrite the velocity distributions explicitly as gaussians centered on $\boldsymbol{v_G}$:

$$\begin{aligned}\frac{d\boldsymbol{V}}{dt} = \frac{2N}{\mathcal{N}^2} K\rho\sigma e^{\beta v_G^2} \int d\boldsymbol{v}_2 d\boldsymbol{v}_1 e^{-\frac{\beta}{2}(\boldsymbol{v_2} - \boldsymbol{v_G})^2 - \frac{\beta}{2}(\boldsymbol{v_1} - \boldsymbol{v_G})^2} \, |\boldsymbol{v_2} - \boldsymbol{v_1}| \\ \times \int d\theta_1 d\theta_2 (\boldsymbol{s} - 2\hat{\boldsymbol{e}}(\overline{\theta}) e^{-\sigma_\eta^2/2}) e^{+\beta(K\boldsymbol{v_G}\cdot\boldsymbol{s} + J\boldsymbol{s}\cdot\boldsymbol{m})}\end{aligned}$$

The integral over velocities can then be computed by introducing $\boldsymbol{u} = \boldsymbol{v_2} - \boldsymbol{v_1}$ and $\boldsymbol{w} = \boldsymbol{v_1} + \boldsymbol{v_2}$:

$$\begin{aligned}\mathcal{J} &\equiv \int d\boldsymbol{v}_2 d\boldsymbol{v}_1 e^{-\frac{\beta}{2}(\boldsymbol{v_2} - \boldsymbol{v_G})^2 - \frac{\beta}{2}(\boldsymbol{v_1} - \boldsymbol{v_G})^2} \, |\boldsymbol{v_2} - \boldsymbol{v_1}| \\ &= 2 \int d\boldsymbol{u} d\boldsymbol{w} u e^{-\frac{\beta}{2}((\boldsymbol{w} - \boldsymbol{u})/2 - \boldsymbol{v_G})^2 - \frac{\beta}{2}((\boldsymbol{w} + \boldsymbol{u})/2 - \boldsymbol{v_G})^2} \\ &= 2e^{-\beta v_G^2} \int d\boldsymbol{u} d\boldsymbol{w} u e^{-\frac{\beta}{4}u^2} e^{-\frac{\beta}{2}\left(\frac{w^2}{2} - 2\boldsymbol{w}\cdot\boldsymbol{v_G}\right)}.\end{aligned}$$

Some algebra yields:

$$\begin{aligned}\int d\boldsymbol{u} u e^{-\frac{\beta}{4}u^2} &= 4\left(\frac{\pi}{\beta}\right)^{3/2} \\ \int d\boldsymbol{w} e^{-\frac{\beta}{2}\left(\frac{w^2}{2} - 2\boldsymbol{w}\cdot\boldsymbol{v_G}\right)} &= 4e^{\beta v_G^2} \frac{\pi}{\beta},\end{aligned}$$

so that:

$$\begin{aligned}\frac{d\boldsymbol{V}}{dt} = \frac{2N}{\mathcal{N}^2} K\rho\sigma e^{\beta v_G^2} \left(\frac{\pi}{\beta}\right)^{5/2} \\ \times \int d\theta_1 d\theta_2 (\boldsymbol{s} - 2\hat{\boldsymbol{e}}(\overline{\theta}) e^{-\sigma_\eta^2/2}) e^{+\beta(K\boldsymbol{v_G}\cdot\boldsymbol{s} + J\boldsymbol{s}\cdot\boldsymbol{m})}.\end{aligned}$$

I now write explicitly the form of the normalization to cast the equation into the shape

$$\frac{d\boldsymbol{V}}{dt} = \frac{N}{2}\pi^{1/2}\beta^{1/2}K\rho\sigma \times \frac{1}{4\pi^2 I_0(\beta h_{eff})^2}\int d\theta_1 d\theta_2 (\boldsymbol{s} - 2\hat{\boldsymbol{e}}(\overline{\theta})e^{-\sigma_\eta^2/2})e^{+\beta \boldsymbol{s}\cdot\boldsymbol{h}_{eff}}.$$

Computing the integration of $\boldsymbol{s}$ yields

$$\frac{d\boldsymbol{V}}{dt} = \frac{N}{2}\pi^{1/2}\beta^{1/2}K\rho\sigma \times \left[\boldsymbol{m} - \frac{1}{2\pi^2 I_0(\beta h_{eff})^2}\int d\theta_1 d\theta_2 \hat{\boldsymbol{e}}(\overline{\theta})e^{-\sigma_\eta^2/2}e^{+\beta \boldsymbol{s}\cdot\boldsymbol{h}_{eff}}\right].$$

The only integral left is *a priori* hard to compute. I can nevertheless check the two extreme limits of the width of the distribution of angles,

(i) $\beta h_{eff} \to 0$, so that spins are flatly distributed on the circle ($\boldsymbol{m} = \boldsymbol{0}$), leading to a zero integration over both angles and no velocity buildup.

(ii) $\beta h_{eff} \to \infty$, so that spins are delta-distributed, and

$$\frac{d\boldsymbol{V}}{dt} = \frac{N}{2}\pi^{1/2}\beta^{1/2}K\rho\sigma \times \boldsymbol{m}\left[1 - e^{-\sigma_\eta^2/2}\right]$$

$$\frac{d\boldsymbol{m}}{dt} = -\frac{1}{2}\pi^{1/2}\beta^{1/2}\rho\sigma \times \boldsymbol{m}\left[1 - e^{-\sigma_\eta^2/2}\right]$$

In that case, each collision disaligns spins because of the noise, so that the modulus of the magnetisation decreases and the velocity grows in return, due to the conservation of momentum.

These very simple results are globally in agreement with intuition on the model, and it would be interesting to explore other ansatz and hypotheses, that could lead to richer results and, perhaps, new predictions on the model.

D.2 Zeroth-order Hydrodynamics and Euler's equation

Another possible output of the Boltzmann equation is a set of continuum equations, that describe the hydrodynamics of the considered fluid [82, 258]. One way to do so [258] is to write that the collision integral in the Boltzmann equation should not be able to modify the macroscopic values of the quantities that are conserved by the dynamics: the number of particles N, energy E, momentum $\boldsymbol{P}$, and angular momentum of particles $\boldsymbol{L}$ in a macroscopic volume. In this Section, I introduce a compact notation for the collision integral,

$$C(\boldsymbol{r_1}, \boldsymbol{\Gamma_1}; t) \equiv \int d\boldsymbol{X_2}\left[(\dot{\boldsymbol{r}}_{\boldsymbol{2}} - \dot{\boldsymbol{r}}_{\boldsymbol{1}})\cdot\frac{\partial}{\partial \boldsymbol{r}}\right] f_2\left(\{\boldsymbol{r_1}, \boldsymbol{\Gamma_1}\}, \{\boldsymbol{r_2}, \boldsymbol{\Gamma_2}\}; t\right),$$

which can here be considered in its full form, prior to the approximations of the joint distribution f_2. Stating that N, E, $\boldsymbol{p}$, and $\boldsymbol{L}$ are conserved by collisions is tantamount to writing the equations

$$\int C(\boldsymbol{r}, \boldsymbol{\Gamma}; t) d\boldsymbol{\Gamma} = 0, \tag{D.5}$$

$$\int \mathcal{H} C(\boldsymbol{r}, \boldsymbol{\Gamma}; t) d\boldsymbol{\Gamma} = 0, \tag{D.6}$$

$$\int \boldsymbol{p} C(\boldsymbol{r}, \boldsymbol{\Gamma}; t) d\boldsymbol{\Gamma} = \boldsymbol{0}, \tag{D.7}$$

$$\int \boldsymbol{L} C(\boldsymbol{r}, \boldsymbol{\Gamma}; t) d\boldsymbol{\Gamma} = \boldsymbol{0}, \tag{D.8}$$

respectively. These equations, through Eq. (D.3) yield equations on the macroscopic density ρ, velocity field $\boldsymbol{u}$, magnetisation field $\boldsymbol{m}$, kinetic energy density e, momentum density $\boldsymbol{\pi}$, and angular momentum density $\boldsymbol{\ell}$ in the fluid, as defined by

$$\rho(\boldsymbol{r}, t) \equiv \int f_1(\boldsymbol{r}, \boldsymbol{\Gamma}; t) d\boldsymbol{\Gamma}, \tag{D.9}$$

$$\rho(\boldsymbol{r}, t) \boldsymbol{u}(\boldsymbol{r}, t) \equiv \int \dot{\boldsymbol{r}} f_1(\boldsymbol{r}, \boldsymbol{\Gamma}; t) d\boldsymbol{\Gamma}, \tag{D.10}$$

$$\rho(\boldsymbol{r}, t) \boldsymbol{m}(\boldsymbol{r}, t) \equiv \int \boldsymbol{s} f_1(\boldsymbol{r}, \boldsymbol{\Gamma}; t) d\boldsymbol{\Gamma},$$

$$e(\boldsymbol{r}, t) \equiv \frac{1}{N} \int \mathcal{H}_1 f_1(\boldsymbol{r}, \boldsymbol{\Gamma}; t) d\boldsymbol{\Gamma}, \tag{D.11}$$

$$\rho(\boldsymbol{r}, t) \boldsymbol{\pi}(\boldsymbol{r}, t) \equiv \int \boldsymbol{p} f_1(\boldsymbol{r}, \boldsymbol{\Gamma}; t) d\boldsymbol{\Gamma}, \tag{D.12}$$

$$\rho(\boldsymbol{r}, t) \boldsymbol{\ell}(\boldsymbol{r}, t) \equiv \int (\omega \boldsymbol{e_z} + \boldsymbol{r} \wedge \boldsymbol{p}) f_1(\boldsymbol{r}, \boldsymbol{\Gamma}; t) d\boldsymbol{\Gamma}, \tag{D.13}$$

where I introduced the one-particle Hamiltonian $\mathcal{H}_1$. Note that, by definition of the momentum, and thanks to the linearity of the integral,

$$\boldsymbol{u} = \boldsymbol{\pi} - K\boldsymbol{m}.$$

In the following, I discuss each conservation law separately.

D.2.1 Mass Conservation Equation

Combining Eqs. (D.3), (D.5), and (D.9) yields the so-called mass conservation equation,

$$\frac{\partial \rho}{\partial t} + \boldsymbol{\nabla} \cdot (\rho \boldsymbol{u}) = \boldsymbol{0}$$

This is the usual equation for the conservation of the number of particles in a fluid, although here one should heed the difference between the momentum and velocity.

D.2.2 Momentum conservation equation

Combining Eqs. (D.3), (D.7), and (D.12) yields one equation for each component a of the momentum,

$$0 = \frac{\partial}{\partial t} (\rho \pi_a) + \frac{\partial}{\partial x_b} \sigma_{ab}(\boldsymbol{r}, t),$$

where x_b is the $b-$th spatial coordinate, and $\overline{\overline{\sigma}}$ is a momentum flux tensor, defined by

$$\sigma_{ab} \equiv \int v_b p_a f_1(\boldsymbol{r}, \boldsymbol{\Gamma}; t) d\boldsymbol{\Gamma}.$$

Notice that the distinction between velocity and momentum is here important in the definition of $\overline{\overline{\sigma}}$.

D.2.3 Energy conservation equation

Combining Eqs. (D.3), (D.6), and (D.11) this time yields the equation

$$\frac{\partial e}{\partial t} + \boldsymbol{\nabla} \cdot \boldsymbol{q_e} + I_\theta + I_\omega = 0$$

where I defined an energy flux q_e and two integrals, I_θ and I_ω through

$$\begin{aligned}
\boldsymbol{q_e} &\equiv \frac{1}{N} \int \mathcal{H}_1 \boldsymbol{v} f_1(\boldsymbol{r}, \boldsymbol{\Gamma}; t) d\boldsymbol{\Gamma}, \\
I_\theta &\equiv \frac{1}{N} \int \mathcal{H}_1 \omega \frac{\partial}{\partial \theta} f_1(\boldsymbol{r}, \boldsymbol{\Gamma}; t) d\boldsymbol{\Gamma}, \\
I_\omega &\equiv \frac{1}{N} \int d\boldsymbol{\Gamma} \mathcal{H}_1 \dot{\omega} \frac{\partial}{\partial \omega} f_1(\boldsymbol{r}, \boldsymbol{\Gamma}; t).
\end{aligned}$$

The first of these is simply an energy current related to the advection of particles, while the other two require a more in-depth study. First, one can rewrite I_ω in terms of a local field,

$$\begin{aligned}
I_\omega &= \frac{1}{N} \int \frac{\omega^2}{2} \dot{\omega} \frac{\partial}{\partial \omega} f_1(\boldsymbol{r}, \boldsymbol{\Gamma}; t) d\boldsymbol{\Gamma}, \\
&= -\frac{1}{N} \int \omega \dot{\omega} f_1(\boldsymbol{r}, \boldsymbol{\Gamma}; t) d\boldsymbol{\Gamma}, \\
&= -\frac{1}{N} \int \frac{\partial}{\partial t} (\frac{\omega^2}{2}) f_1(\boldsymbol{r}, \boldsymbol{\Gamma}; t) d\boldsymbol{\Gamma}.
\end{aligned}$$

This field represents a variation of rotational kinetic energy per unit volume, which I henceforth call

$$k_{rot}(\boldsymbol{r}; t) \equiv \frac{1}{N} \int \omega \dot{\omega} f_1(\boldsymbol{r}, \boldsymbol{\Gamma}; t) d\boldsymbol{\Gamma}.$$

I_θ, on the other hand, can be rewritten using an integration by parts,

$$\begin{aligned}
I_\theta &= -\frac{1}{N} \int K \boldsymbol{p} \cdot \boldsymbol{s} \omega \frac{\partial}{\partial \theta} f_1(\boldsymbol{r}, \boldsymbol{\Gamma}; t) d\boldsymbol{\Gamma}, \\
&= -\frac{K}{N} \int d\boldsymbol{\Gamma} p \omega \int_0^{2\pi} d\theta \cos\theta \frac{\partial}{\partial \theta} f_1(\boldsymbol{r}, \boldsymbol{\Gamma}; t), \\
&= -\frac{K}{N} \int d\boldsymbol{\Gamma} p \omega \int_0^{2\pi} d\theta \sin\theta f_1(\boldsymbol{r}, \boldsymbol{\Gamma}; t), \\
&= -\frac{K}{N} \int (\boldsymbol{p} \wedge \boldsymbol{s}) \cdot \boldsymbol{e_z} \omega f_1(\boldsymbol{r}, \boldsymbol{\Gamma}; t) d\boldsymbol{\Gamma}.
\end{aligned}$$

This more unusual field counts how energy might be locally modified by a change of alignment between $\boldsymbol{p}$ and $\boldsymbol{s}$ due to a nonzero value of ω (a rotation of $\boldsymbol{s}$ at fixed $\boldsymbol{p}$). I call the associated local field the self-disalignment field D, defined by

$$D(\boldsymbol{r};t) \equiv \frac{1}{N}\int d\boldsymbol{\Gamma}\omega(\boldsymbol{p}\wedge\boldsymbol{s})\cdot\boldsymbol{e_z}f_1(\boldsymbol{r},\boldsymbol{\Gamma};t).$$

Altogether, the energy conservation equation can be rewritten as

$$\frac{\partial e}{\partial t} + \boldsymbol{\nabla}\cdot\boldsymbol{q_e} - KD(\boldsymbol{r};t) - k_{rot}(\boldsymbol{r};t) = 0.$$

D.2.4 Angular momentum conservation equation

Finally, combining Eqs. (D.3), (D.8), and (D.13) yields

$$\frac{\partial}{\partial t}(\rho\boldsymbol{\ell}) + \boldsymbol{\nabla}\cdot(q_L) + \boldsymbol{I_L} = \boldsymbol{0}$$

where I defined the angular momentum flux q_L and the integral I_L through

$$\begin{aligned} q_L &\equiv \int(\omega\boldsymbol{e_z}+\boldsymbol{r}\wedge\boldsymbol{p})\cdot\boldsymbol{v}f_1(\boldsymbol{r},\boldsymbol{\Gamma};t)d\boldsymbol{\Gamma} = 0,\\ \boldsymbol{I_L} &\equiv \int(\omega\boldsymbol{e_z}+\boldsymbol{r}\wedge\boldsymbol{p})\dot{\omega}\frac{\partial}{\partial\omega}f_1(\boldsymbol{r},\boldsymbol{\Gamma};t)d\boldsymbol{\Gamma}. \end{aligned}$$

Like in the case of the energy, q_L simply represents the advection of the angular momentum field, while the integral I_L can be rewritten as:

$$\begin{aligned} I_L &= \int\omega\dot{\omega}\frac{\partial}{\partial\omega}f_1(\boldsymbol{r},\boldsymbol{\Gamma};t)d\boldsymbol{\Gamma}\boldsymbol{e_z} + \boldsymbol{r}\wedge\int\boldsymbol{p}\dot{\omega}\frac{\partial}{\partial\omega}f_1(\boldsymbol{r},\boldsymbol{\Gamma};t)d\boldsymbol{\Gamma},\\ &= \int\omega\dot{\omega}\frac{\partial}{\partial\omega}f_1(\boldsymbol{r},\boldsymbol{\Gamma};t)d\boldsymbol{\Gamma}\boldsymbol{e_z},\\ &= -\int\dot{\omega}f_1(\boldsymbol{r},\boldsymbol{\Gamma};t)d\boldsymbol{\Gamma}\boldsymbol{e_z}, \end{aligned}$$

where I assumed that $[\omega f_1]_{-\infty}^{\infty}$ vanishes. This should be true because of two arguments: first, the Hamiltonian is even in ω, so that there should be no imbalance between positive and negative values and, second, f_1 should vanish for large values of ω. Having thus written I_L as a local field, I introduce the macroscopic angular acceleration field $\boldsymbol{\tau}$ through

$$\rho(\boldsymbol{r},t)\boldsymbol{\tau}(\boldsymbol{r},t) \equiv \int\dot{\omega}f_1(\boldsymbol{r},\boldsymbol{\Gamma};t)d\boldsymbol{\Gamma}\boldsymbol{e_z}.$$

In the end, the angular momentum conservation law reads

$$\frac{\partial}{\partial t}(\rho\boldsymbol{\ell}) - \rho(\boldsymbol{r},t)\boldsymbol{\tau}(\boldsymbol{r},t) = \boldsymbol{0}.$$

D.2.5 Euler's equation

Using conservation arguments, I have found continuum mechanics equations verified by the local fields in the fluid,

$$\begin{aligned}
\mathbf{0} &= \frac{\partial \rho}{\partial t} + \boldsymbol{\nabla} \cdot (\rho \boldsymbol{u}), \\
0 &= \frac{\partial}{\partial t}(\rho \pi_a) + \frac{\partial}{\partial x_b}\sigma_{ab}(\boldsymbol{r},t), \\
0 &= \frac{\partial e}{\partial t} + \boldsymbol{\nabla} \cdot \boldsymbol{q_e} - KD(\boldsymbol{r};t) - k_{rot}(\boldsymbol{r};t), \\
\mathbf{0} &= \frac{\partial}{\partial t}(\rho \boldsymbol{\ell}) - \rho(\boldsymbol{r},t)\boldsymbol{\tau}(\boldsymbol{r},t).
\end{aligned}$$

These equations are still quite different from standard hydrodynamical equations, as they are still written in terms of microscopic fields, and not macroscopic quantities like the pressure or the temperature. In order to introduce such quantities, and to find more usual macroscopic equations, one usually focuses on the mass and momentum conservation equations [258]. Here, the only quantity that seems out of place in these equations is the momentum flux tensor, which I need to express in terms of simpler quantities. In order to do so, I introduce the notation

$$\langle \cdot \rangle_1 \equiv \int (\cdot) f_1(\boldsymbol{r}, \boldsymbol{\Gamma}; t) d\boldsymbol{\Gamma},$$

so that, for instance, $\sigma_{ab}(\boldsymbol{r},t) \equiv \langle p_a v_b \rangle_1$. I then use the definition of the momentum in terms of velocities and spins to write that

$$\sigma_{ab}(\boldsymbol{r},t) = \langle v_a v_b \rangle_1 + K \langle s_a v_b \rangle_1.$$

I now decompose the velocity field as $\boldsymbol{v} = \boldsymbol{u} + \boldsymbol{v'}$, where $\boldsymbol{u}$ is the mean velocity defined in Eq. (D.10). Using this decomposition, the momentum flux tensor can be rewritten as

$$\sigma_{ab}(\boldsymbol{r},t) = \langle u_a u_b \rangle_1 + K \langle s_a u_b \rangle_1 + \langle v'_a v'_b \rangle_1 + K \langle s_a v'_b \rangle_1 + \langle u_a v'_b \rangle_1 + \langle v'_a u_b \rangle_1.$$

In this expression, one can take advantage of the definition of $\boldsymbol{u}$ to write that

$$\begin{aligned}
\langle u_a u_b \rangle_1 &= \rho(\boldsymbol{r};t) u_a u_b, \\
\langle s_a u_b \rangle_1 &= \rho(\boldsymbol{r};t) u_b m_a(\boldsymbol{r};t).
\end{aligned}$$

Furthermore, I assume that the field $\boldsymbol{v'}$ is not ordered macroscopically, so that

$$\begin{aligned}
\langle u_a v'_b \rangle_1 &= u_a \langle v'_b \rangle_1 = 0, \\
\langle v'_a u_b \rangle_1 &= 0,
\end{aligned}$$

and that the components of the velocity fluctuations are independent of each other, so that

$$\langle v'_a v'_b \rangle_1 = \langle {v'_a}^2 \rangle_1 \delta_{ab}.$$

This last equation is, in fact, a very strong approximation: I am hereby assuming that the f distribution is purely Gaussian with respects to the velocities at the hydrodynamic scale (it is in that sense that one calls this description "zeroth order"[82]), so that the velocity correlation tensor is purely diagonal. As a consequence, if the system is set in motion with a shear flow, the flow will persist forever [82]. Using these expressions anyway, the momentum flux tensor can be rewritten as

$$\sigma_{ab}(\boldsymbol{r},t) = \rho(\boldsymbol{r};t)u_a u_b + K\rho(\boldsymbol{r};t)u_b m_a(\boldsymbol{r};t) + \langle {v'_a}^2\rangle_1 \delta_{ab} + K\langle s_a v'_b\rangle_1.$$

In order to rewrite the remaining mean values in terms of macroscopic quantities, I resort to the equipartition relation associated to the momentum in the microscopic model, that was established in Ref. [69] and presented in Sec. II.2,

$$\langle {p_a}^2\rangle - \langle p_a\rangle^2 - K^2(\langle s_a^2\rangle - \langle s_a\rangle^2) = k_B T,$$

where $\langle\cdot\rangle$ is here the mean value with respect to the Boltzmann-Gibbs measure in the canonical ensemble. I know assume that the fluid is locally at equilibrium, which ensures that $\rho\langle\cdot\rangle = \langle\cdot\rangle_1$. This equipartition relation can then be rewritten in terms of the velocity fluctuations $\boldsymbol{v}'$, leading to

$$\langle {v'_a}^2\rangle_1 + 2K\langle v'_a s_a\rangle_1 = \rho k_B T.$$

As a result, I can use the equipartition relation to write

$$\sigma_{ab}(\boldsymbol{r},t) = \rho(\boldsymbol{r};t)\left(u_a u_b + K u_b m_a(\boldsymbol{r};t) + k_B T\delta_{ab} + K\langle s_a v'_b\rangle - 2K\langle s_a v'_a\rangle\delta_{ab}\right).$$

In order to use this equation, I finally make a strong hypothesis: I assume that I study the system close to a perfectly ordered collectively-moving state, and that the collective part of the velocity essentially contains all the correlation between the velocities and the magnetisation. In simpler terms, I assume that $\langle \boldsymbol{v'}\cdot\boldsymbol{s}\rangle \approx 0$, which is consistent with a purely Gaussian distribution of the velocity fluctuations. Under that (probably very crude) hypothesis, I find

$$\sigma_{ab}(\boldsymbol{r},t) = \delta_{ab}\rho(\boldsymbol{r};t)k_B T + \rho(\boldsymbol{r};t)u_b\left(u_a + K m_a(\boldsymbol{r};t)\right),$$

so that

$$\frac{\partial}{\partial x_b}\sigma_{ab}(\boldsymbol{r},t) = \frac{\partial}{\partial x_a}\rho(\boldsymbol{r};t)k_B T + \frac{\partial}{\partial x_b}\left[\rho(\boldsymbol{r};t)u_b\left(u_a + K m_a(\boldsymbol{r};t)\right)\right]$$

and, in vector form,

$$\frac{\partial}{\partial t}\rho\boldsymbol{\pi} + \rho\left(\boldsymbol{u}\cdot\boldsymbol{\nabla}\right)\left(\boldsymbol{u} + K_1\boldsymbol{m}\right) + \left(\boldsymbol{\alpha} + K_1\boldsymbol{m}\right)\cdot\left(\boldsymbol{\nabla}\cdot(\rho\boldsymbol{u})\right) = -\boldsymbol{\nabla}(\rho k_B T).$$

Therefore, when recalling that $\boldsymbol{\pi} = \boldsymbol{u} + K_1\boldsymbol{m}$, I get the equations

$$\frac{\partial}{\partial t}\rho + \boldsymbol{\nabla}\rho\boldsymbol{u} = 0,$$
$$\frac{\partial}{\partial t}\rho\boldsymbol{\pi} + \rho\left(\boldsymbol{u}\cdot\boldsymbol{\nabla}\right)\boldsymbol{\pi} + \boldsymbol{\pi}\cdot\left(\boldsymbol{\nabla}\rho\boldsymbol{u}\right) = -\boldsymbol{\nabla}(\rho k_B T).$$

The mass conservation equation can be used to cancel out two terms of the second equation, which leads to the two equations:

$$\frac{\partial}{\partial t}\rho + \boldsymbol{\nabla}\rho\boldsymbol{u} = 0,$$
$$\left[\frac{\partial}{\partial t} + \boldsymbol{u}\cdot\boldsymbol{\nabla}\right]\boldsymbol{\pi} = -\frac{1}{\rho}\boldsymbol{\nabla}(\rho k_B T).$$

The second equation is Euler's flow equation in this system, with $P = \rho k_B T$ the pressure of an ideal fluid, emphasizing that this description neglects most of the interactions inside of the fluid. The difference with the standard Euler's equation is that here it is not simply the velocity that is advected, but the momentum, that also contains the magnetisation field. At this level of description, I do not find an equation for the dynamics of the magnetisation field alone, although one could introduce an effective Ginzburg-Landau-like dynamics, following works on the hydrodynamic description of systems of self-propelled particles [59]. Interestingly, in hydrodynamic descriptions of active systems, authors often argue that the non-Galilean character of a model leads to an additional factor in front of the advection term [250], that is here absent.

Bibliography

> Quizá me engañen la vejez y el temor, pero sospecho que la especie humana - la única - está por extinguirse y que la Biblioteca perdurará: iluminada, solitaria, infinita, perfectamente inmóvil, armada de volúmenes preciosos, inútil, incorruptible, secreta.
>
> Jorge Luis Borges, *La biblioteca de Babel*

[1] J.-P. Hansen and I. R. McDonald, *Theory of simple liquids*. Elsevier Academic Press, 2006. 1, 22, 68, 71, 72, 73, 75, 76, 78, 79, 80, 83, 84, 85, 90, 98, 100, 108, 123, 126, 127, 129, 193

[2] M. Kardar, *Statistical Physics of Fields*. Cambridge University Press, 2007. 1, 14, 43, 46, 48, 54, 57, 59, 62, 64, 128

[3] S. Chandrasekhar, *Liquid crystals*. Cambridge University Press, 1977. 1, 70

[4] P. M. Chaikin and T. C. Lubensky, *Principles of Condensed Matter Physics*. Cambridge University Press, 1995. 1, 47, 50, 57, 70, 80

[5] M. Mézard and A. Montanari, *Information, Physics, and Computation*. Oxford University Press, 2009. 1, 85, 120

[6] J.-P. Bouchaud, "An introduction to statistical finance," *Physica A: Statistical Mechanics and its Applications*, vol. 313, pp. 238—-251, 2002. 1

[7] G. L. Vasconcelos, "A Guided Walk Down Wall Street: An Introduction to Econophysics," *Brazilian Journal of Physics*, vol. 34, no. 3B, pp. 1039—-1065, 2004. 1

[8] C. Castellano, S. Fortunato, and V. Loreto, "Statistical physics of social dynamics," *Reviews of Modern Physics*, vol. 81, no. 2, pp. 591—-646, 2009. 1

[9] T. D. Lee and C. N. Yang, "Statistical theory of equations of state and phase transitions. II. Lattice gas and ising model," *Physical Review*, vol. 87, no. 3, p. 410, 1952. 2, 68, 108, 114

[10] M. Ballerini, N. Cabibbo, R. Candelier, A. Cavagna, E. Cisbani, I. Giardina, A. Orlandi, G. Parisi, A. Procaccini, M. Viale, and V. Zdravkovic, "Empirical investigation of starling flocks: a benchmark study in collective animal behaviour," *Animal Behaviour*, vol. 76, no. 1, pp. 201–215, 2008. 2, 4, 181

[11] A. Cavagna, A. Cimarelli, I. Giardina, G. Parisi, R. Santagati, F. Stefanini, and M. Viale, "Scale-free correlations in starling flocks," *Proceedings of the National Academy of Sciences*, vol. 107, no. 26, pp. 11865–11870, 2010. 3, 4, 17, 153, 168, 179, 180, 181, 182, 183, 205

[12] A. Cavagna, S. M. D. Queiros, I. Giardina, F. Stefanini, and M. Viale, "Diffusion of individual birds in starling flocks," *Proceedings of the Royal Society B: Biological Sciences*, vol. 280, no. 1756, pp. 20122484–20122484, 2013. 170, 173, 174, 181, 188

[13] A. Cavagna and I. Giardina, "Bird Flocks as Condensed Matter," *Annual Review of Condensed Matter Physics*, vol. 5, no. 1, pp. 183–207, 2014. 3, 4

[14] A. Cavagna, I. Giardina, and T. S. Grigera, "The physics of flocking: Correlation as a compass from experiments to theory," *Physics Reports*, vol. 728, pp. 1–62, 2018. 2, 3, 167, 181, 183

[15] W. Bialek, A. Cavagna, I. Giardina, T. Mora, E. Silvestri, M. Viale, and A. M. Walczak, "Statistical mechanics for natural flocks of birds," *Proceedings of the National Academy of Sciences*, vol. 109, no. 13, pp. 4786–4791, 2012. 3, 183, 184

[16] J. R. Stowers, M. Hofbauer, R. Bastien, J. Griessner, P. Higgins, S. Farooqui, R. M. Fischer, K. Nowikovsky, W. Haubensak, I. D. Couzin, K. Tessmar-Raible, and A. D. Straw, "Virtual reality for freely moving animals," *Nature Methods*, vol. 14, no. 10, pp. 995–1002, 2017. 3

[17] A. Attanasi, A. Cavagna, L. Del Castello, I. Giardina, S. Melillo, L. Parisi, O. Pohl, B. Rossaro, E. Shen, E. Silvestri, and M. Viale, "Collective Behaviour without Collective Order in Wild Swarms of Midges," *PLoS Computational Biology*, vol. 10, no. 7, p. e1003697, 2014. 3

[18] A. Cavagna, D. Conti, C. Creato, L. Del Castello, I. Giardina, T. S. Grigera, S. Melillo, L. Parisi, and M. Viale, "Dynamic scaling in natural swarms," *Nature Physics*, vol. 13, no. 9, pp. 914–918, 2017. 4

[19] R. Ni and N. T. Ouellette, "Velocity correlations in laboratory insect swarms," *European Physical Journal: Special Topics*, vol. 224, no. 17-18, pp. 3271–3277, 2015.

[20] D. Gorbonos, R. Ianconescu, J. G. Puckett, R. Ni, N. T. Ouellette, and N. S. Gov, "Long-range acoustic interactions in insect swarms: an adaptive gravity model," *New Journal of Physics*, vol. 18, no. 7, p. 073042, 2016. 4

[21] D. Gorbonos and N. S. Gov, "Stable swarming using adaptive long-range interactions," *Physical Review E*, vol. 95, no. 4, p. 042405, 2017.

[22] A. M. Reynolds, M. Sinhuber, and N. T. Ouellette, "Are midge swarms bound together by an effective velocity-dependent gravity?," *European Physical Journal E*, vol. 40, no. 4, p. 46, 2017. 3, 4

[23] O. Feinerman, I. Pinkoviezky, A. Gelblum, E. Fonio, and N. S. Gov, "The physics of cooperative transport in groups of ants," *Nature Physics*, vol. 14, no. 7, pp. 683–693, 2018. 4

[24] J. Buhl, D. J. Sumpter, I. D. Couzin, J. J. Hale, E. Despland, E. R. Miller, and S. J. Simpson, "From disorder to order in marching locusts," *Science*, vol. 312, no. 5778, pp. 1402–1406, 2006. 4

[25] H. P. Zhang, A. Be'er, E.-L. Florin, and H. L. Swinney, "Collective motion and density fluctuations in bacterial colonies," *Proceedings of the National Academy of Sciences*, vol. 107, no. 31, pp. 13626–13630, 2010. 5

[26] M. C. Marchetti, J. F. Joanny, S. Ramaswamy, T. B. Liverpool, J. Prost, M. Rao, and R. A. Simha, "Hydrodynamics of soft active matter," *Reviews of Modern Physics*, vol. 85, no. 3, p. 1143(47), 2013. 4, 5, 14

[27] C. Dombrowski, L. Cisneros, S. Chatkaew, R. E. Goldstein, and J. O. Kessler, "Self-concentration and large-scale coherence in bacterial dynamics," *Physical Review Letters*, vol. 93, no. 9, p. 098103, 2004. 5, 6

[28] S. Ramaswamy, "The Mechanics and Statistics of Active Matter," *Annual Review of Condensed Matter Physics*, vol. 1, pp. 323–345, 2010. 4, 187

[29] C. Bechinger, R. Di Leonardo, H. Löwen, C. Reichhardt, G. Volpe, and G. Volpe, "Active particles in complex and crowded environments," *Reviews of Modern Physics*, vol. 88, no. 4, pp. 1–57, 2016. 4, 189, 190

[30] T. Sugi, H. Ito, M. Nishimura, and K. H. Nagai, "C. elegans collectively forms dynamical networks," *Nature Communications*, vol. 10, no. 1, p. 683, 2019. 4, 13, 17, 176

[31] A. Sokolov, I. S. Aranson, J. O. Kessler, and R. E. Goldstein, "Concentration dependence of the collective dynamics of swimming bacteria," *Physical Review Letters*, vol. 98, no. 15, p. 158102, 2007. 5

[32] A. Sokolov and I. S. Aranson, "Reduction of viscosity in suspension of swimming bacteria," *Physical Review Letters*, vol. 103, no. 14, p. 148101, 2009. 6

[33] H. M. López, J. Gachelin, C. Douarche, H. Auradou, and E. Clément, "Turning Bacteria Suspensions into Superfluids," *Phys. Rev. Lett.*, vol. 115, no. 2, p. 28301, 2015. 6

[34] E. Ferrante, A. E. Turgut, C. Huepe, A. Stranieri, C. Pinciroli, and M. Dorigo, "Self-organized flocking with a mobile robot swarm: A novel motion control method," *Adaptive Behavior*, vol. 20, no. 6, pp. 460–477, 2012. 6

[35] J. Deseigne, O. Dauchot, and H. Chaté, "Collective motion of vibrated polar disks," *Physical Review Letters*, vol. 105, no. 9, p. 098001, 2010. 6, 7

[36] N. Kumar, H. Soni, S. Ramaswamy, and A. K. Sood, "Flocking at a distance in active granular matter," *Nature Communications*, vol. 5, p. 4688, 2014. 6

[37] J. Deseigne, S. Léonard, O. Dauchot, and H. Chaté, "Vibrated polar disks: Spontaneous motion, binary collisions, and collective dynamics," *Soft Matter*, vol. 8, no. 20, pp. 5629–5639, 2012. 7

[38] K. D. N. T. Lam, M. Schindler, and O. Dauchot, "Self-propelled hard disks: Implicit alignment and transition to collective motion," *New Journal of Physics*, vol. 17, no. 11, p. 113056, 2015. 7, 218

[39] G. Briand and O. Dauchot, "Crystallization of Self-Propelled Hard Discs," *Physical Review Letters*, vol. 117, no. 9, p. 098004, 2016. 7

[40] G. Briand, M. Schindler, and O. Dauchot, "Spontaneously Flowing Crystal of Self-Propelled Particles," *Physical Review Letters*, vol. 120, no. 20, p. 208001, 2018. 7, 179, 183

[41] J. Palacci, S. Sacanna, A. P. Steinberg, D. J. Pine, and P. M. Chaikin, "Living crystals of light-activated colloidal surfers," *Science*, vol. 339, no. 6122, pp. 936–940, 2013. 7, 8

[42] A. Walther and A. H. Müller, "Janus particles," *Soft Matter*, vol. 4, no. 4, pp. 663–668, 2008. 8

[43] L. F. Valadares, Y. G. Tao, N. S. Zacharia, V. Kitaev, F. Galembeck, R. Kapral, and G. A. Ozin, "Catalytic nanomotors: Self-propelled sphere dimers," *Small*, vol. 6, no. 4, pp. 565–572, 2010. 8

[44] H. R. Jiang, N. Yoshinaga, and M. Sano, "Active motion of a Janus particle by self-thermophoresis in a defocused laser beam," *Physical Review Letters*, vol. 105, no. 26, p. 268302, 2010. 8

[45] Z. Izri, M. N. Van Der Linden, S. Michelin, and O. Dauchot, "Self-propulsion of pure water droplets by spontaneous marangoni-stress-driven motion," *Physical Review Letters*, vol. 113, no. 24, p. 248302, 2014. 8, 190

[46] E. Heisler, N. J. Suematsu, A. Awazu, and H. Nishimori, "Swarming of self-propelled camphor boats," *Physical Review E - Statistical, Nonlinear, and Soft Matter Physics*, vol. 85, no. 5, p. 055201, 2012. 8

[47] A. Bricard, J.-B. Caussin, N. Desreumaux, O. Dauchot, and D. Bartolo, "Emergence of macroscopic directed motion in populations of motile colloids," *Nature*, vol. 503, no. 7474, pp. 95–98, 2013. 8, 9

[48] Y. Sumino, K. H. Nagai, Y. Shitaka, D. Tanaka, K. Yoshikawa, H. Chaté, and K. Oiwa, "Large-scale vortex lattice emerging from collectively moving microtubules," *Nature*, vol. 483, no. 7390, pp. 448–452, 2012. 9, 10, 17, 166, 176

[49] S. J. Kron and J. A. Spudich, "Fluorescent actin filaments move on myosin fixed to a glass surface," *Proceedings of the National Academy of Sciences of the United States of America*, vol. 83, no. 17, pp. 6272–6276, 1986. 9

[50] T. Sanchez, D. T. Chen, S. J. Decamp, M. Heymann, and Z. Dogic, "Spontaneous motion in hierarchically assembled active matter," *Nature*, vol. 491, no. 7424, pp. 431–434, 2012. 10

[51] Z. Csahok and T. Vicsek, "Lattice-gas model for collective biological motion," *Physical Review E*, vol. 52, no. 5, p. 5297, 1995. 10

[52] T. Vicsek, A. Czirók, E. Ben-Jacob, I. Cohen, and O. Shochet, "Novel Type of Phase Transition in a System of Self-Driven Particles," *Physical Review Letters*, vol. 75, no. 6, p. 1226, 1995. 10, 11, 71, 155, 218

[53] F. Ginelli, "The Physics of the Vicsek model," *European Physical Journal: Special Topics*, vol. 225, no. 11-12, pp. 2099–2117, 2016. 11, 12

[54] N. D. Mermin and H. Wagner, "Absence of ferromagnetism or antiferromagnetism in one- or two-dimensional isotropic Heisenberg models," *Physical Review Letters*, vol. 17, p. 1133, 1966. 11, 34, 58, 68, 98, 101

[55] N. D. Mermin, "Absence of ordering in certain classical systems," *Journal of Mathematical Physics*, vol. 8, no. 5, pp. 1061–1064, 1967. 11, 34, 58, 68, 98, 101

[56] H. Chaté, F. Ginelli, G. Grégoire, F. Peruani, and F. Raynaud, "Modeling collective motion: Variations on the Vicsek model," *European Physical Journal B*, vol. 64, no. 3-4, pp. 451–456, 2008. 11, 188

[57] A. P. Solon, H. Chaté, and J. Tailleur, "From phase to microphase separation in flocking models: The essential role of nonequilibrium fluctuations," *Phys. Rev. Lett.*, 2015. 11, 12, 188

[58] A. P. Solon and J. Tailleur, "Flocking with discrete symmetry: The two-dimensional active Ising model," *Physical Review E - Statistical, Nonlinear, and Soft Matter Physics*, vol. 92, p. 042119, 2015. 11, 12, 71

[59] E. Bertin, M. Droz, and G. Grégoire, "Boltzmann and hydrodynamic description for self-propelled particles," *Physical Review E - Statistical, Nonlinear, and Soft Matter Physics*, vol. 74, no. 2, p. 022101, 2006. 11, 188, 226

[60] Y. Fily and M. C. Marchetti, "Athermal phase separation of self-propelled particles with no alignment," *Physical Review Letters*, vol. 108, no. 23, p. 235702, 2012. 12, 13, 93, 176, 183

[61] M. E. Cates and J. Tailleur, "Motility-Induced Phase Separation," *Annual Review of Condensed Matter Physics*, vol. 6, pp. 219–244, 2014. 13, 71

[62] A. P. Solon, J. Stenhammar, M. E. Cates, Y. Kafri, and J. Tailleur, "Generalized Thermodynamics of Phase Equilibria in Scalar Active Matter," *Physical Review E*, vol. 97, p. 020602(R), sep 2016. 13

[63] T. F. Farage, P. Krinninger, and J. M. Brader, "Effective interactions in active Brownian suspensions," *Physical Review E - Statistical, Nonlinear, and Soft Matter Physics*, vol. 91, no. 4, p. 042310, 2015. 13, 71

[64] L. F. Cugliandolo, P. Digregorio, G. Gonnella, and A. Suma, "Phase Coexistence in Two-Dimensional Passive and Active Dumbbell Systems," *Physical Review Letters*, vol. 119, p. 268002, 2017. 13, 16, 70, 179, 183

[65] P. Digregorio, D. Levis, A. Suma, L. F. Cugliandolo, G. Gonnella, and I. Pagonabarraga, "Full Phase Diagram of Active Brownian Disks: From Melting to Motility-Induced Phase Separation," *Physical Review Letters*, vol. 121, no. 9, p. 98003, 2018. 13, 16, 70, 179, 183

[66] F. D. Farrell, M. C. Marchetti, D. Marenduzzo, and J. Tailleur, "Pattern formation in self-propelled particles with density-dependent motility," *Physical Review Letters*, vol. 108, no. 24, p. 248101, 2012. 13, 71, 165, 189

[67] K. H. Nagai, Y. Sumino, R. Montagne, I. S. Aranson, and H. Chaté, "Collective motion of self-propelled particles with memory," *Physical Review Letters*, vol. 114, no. 16, p. 168001, 2015. 17, 166, 176

[68] D. Nishiguchi, K. H. Nagai, H. Chaté, and M. Sano, "Long-range nematic order and anomalous fluctuations in suspensions of swimming filamentous bacteria," *Physical Review E*, vol. 95, no. 2, p. 020601(R), 2017. 13

[69] S. L. Bore, M. Schindler, K.-D. N. T. Lam, E. Bertin, and O. Dauchot, "Coupling spin to velocity: collective motion of Hamiltonian polar particles," *J. Stat. Mech.: Theory and Experiments*, vol. 2016, no. 3, p. 033305, 2016. 14, 15, 16, 17, 27, 28, 29, 31, 36, 40, 49, 53, 137, 138, 139, 146, 160, 225

[70] G. Mussardo, *Statistical Field Theory: An Introduction to Exactly Solved Models in Statistical Physics*. Oxford University Press, 2009. 14

[71] J. M. Kosterlitz and D. J. Thouless, "Ordering, metastability and phase transitions in two-dimensional systems," *Journal of Physics C: Solid State Physics*, vol. 6, p. 1181, 1973. 17, 21, 58, 59, 98

[72] J. M. Kosterlitz and D. J. Thouless, "Ordering, metastability and phase transitions in two-dimensional systems," *J. Phys. C: Solid State Phys.*, vol. 6, p. 1181, 1973. 140, 142, 143, 145

[73] J. M. Kosterlitz, "The critical properties of the two-dimensional xy model," *J. Phys. C : Solid State Phys*, vol. 7, no. 6, p. 1046, 1974. 58, 59, 60, 98, 148

[74] J. M. Kosterlitz, "Kosterlitz-Thouless physics: a review of key issues," *Reports on Progress in Physics*, vol. 79, no. 2, p. 026001, 2016. 17, 21, 108

[75] M. Casiulis, M. Tarzia, L. F. Cugliandolo, and O. Dauchot, "Ferromagnetism-induced phase separation in a 2d spin fluid," *Journal of Chemical Physics*, vol. 150, no. 15, p. 154501, 2019. 18, 97, 148, 149, 151, 152, 171, 174

[76] M. Casiulis, M. Tarzia, L. F. Cugliandolo, and O. Dauchot, "Order by disorder: saving collective motion from topological defects in a conservative model," *Journal of Statistical Mechanics: Theory and Experiment*, vol. 2020, no. 1, p. 013209, 2020. 18, 138, 170

[77] M. Casiulis, M. Tarzia, L. F. Cugliandolo, and O. Dauchot, "Velocity and Speed Correlations in Hamiltonian Flocks," *Physical Review Letters*, vol. 124, no. 19, p. 198001, 2020. 18, 168

[78] V. L. Berezinskii, "Destruction of long-range order in one-dimensional and two-dimensional systems having a continuous symmetry group I. classical systems," *Sov. Phys. JETP*, vol. 32, no. 3, p. 493, 1971. 21, 58, 98

[79] L. D. Landau and E. M. Lifshitz, *Course of Theoretical Physics Vol. 1: Mechanics*. Butterworth-Heinemann, 3rd ed., 1976. 22, 23

[80] L. D. Landau and E. M. Lifshitz, *Course of Theoretical Physics Vol. 5: Statistical Physics, Part I*. Pergamon Press, 3rd ed., 1980. 26, 90

[81] B. Diu, C. Guthmann, D. Lederer, and B. Roulet, *Physique Statistique*. Hermann, 1996. 26, 28, 30, 33, 73, 92

[82] M. Kardar, *Statistical Physics of Particles*. Cambridge University Press, 2007. 26, 30, 92, 209, 210, 212, 213, 214, 215, 220, 225

[83] Reichl L.E., *A modern course in statistical physics*. Wiley, 2nd ed ed., 1998. 26, 71, 80, 90, 210

[84] D. Mukamel, "Statistical mechanics of systems with long range interactions," *Lecture Notes of the Les Houches Summer School – Long-Range Interacting Systems*, vol. 90, pp. 22–38, 2008. 27

[85] P. Attard, *Thermodynamics and statistical mechanics: equilibrium by entropy maximisation*. London: Academic Press, 2002. 28

[86] H. H. Chi and H. J. He, "Single-valued Hamiltonian via Legendre-Fenchel transformation and time translation symmetry," *Nuclear Physics B*, vol. 885, pp. 448–458, 2014. 35, 166, 191, 192

[87] B. Mahault, X.-c. Jiang, E. Bertin, Y.-q. Ma, A. Patelli, X.-q. Shi, and H. Chaté, "Self-Propelled Particles with Velocity reversals and Ferromagnetic Alignment: Active Matter Class with Second-Order Transition to Quasi-Long-Range Polar Order," *Physical Review Letters*, vol. 120, p. 258002, 2018. 36, 160, 166, 189

[88] S. Henkes, M. C. Marchetti, and R. Sknepnek, "Dynamical patterns in nematic active matter on a sphere," *Physical Review E*, vol. 97, no. 4, p. 042605, 2018. 36

[89] E. W. Weisstein, "Runge-Kutta Method," *From MathWorld—A Wolfram Web Resource*. 37

[90] L. Verlet, “Computer "Experiments" on Classical Fluids. I. Thermodynamical Properties of Lennard, -Jones Molecules,” *Physical Review*, vol. 159, no. 2, pp. 183–195, 1967. 38

[91] L. Berthier, P. C. W. Holdsworth, and M. Sellitto, “Non-equilibrium critical dynamics of the two-dimensional XY model,” *Journal of Physics A: Mathematical and Theoretical*, vol. 34, no. 01, pp. 1805–1824, 2001. 40

[92] G. Biroli, L. F. Cugliandolo, and A. Sicilia, “Kibble-Zurek mechanism and infinitely slow annealing through critical points,” *Physical Review E - Statistical, Nonlinear, and Soft Matter Physics*, vol. 81, no. 5, p. 050101(R), 2010.

[93] A. Jelic and L. F. Cugliandolo, “Quench dynamics of the 2D XY model,” *Journal of Statistical Mechanics: Theory and Experiment*, vol. 2011, no. 02, p. P02032, 2011. 108, 111

[94] V. Raban, C. T. Suen, L. Berthier, and P. C. Holdsworth, “Multiple symmetry sustaining phase transitions in spin ice,” *Physical Review B*, vol. 99, no. 22, p. 224425, 2019. 40

[95] J.-P. Vest, G. Tarjus, and P. Viot, “Dynamics of a monodisperse Lennard-Jones system on a sphere,” *Molecular Physics*, vol. 112, no. 112, pp. 9–10, 2014. 41

[96] F. D. Nobre and C. Tsallis, “Classical infinite-range-interaction Heisenberg ferromagnetic model: Metastability and sensitivity to initial conditions,” *Phys. Rev. E*, vol. 68, no. 036115, 2003. 41

[97] M. E. Fisher, “Correlation functions and the critical region of simple fluids,” *Journal of Mathematical Physics*, vol. 5, no. 7, pp. 944–962, 1964. 43, 44

[98] B. Widom, “Surface tension and molecular correlations near the critical point,” *The Journal of Chemical Physics*, vol. 43, no. 11, pp. 3892–3897, 1965. 44

[99] L. P. Kadanoff, “More is the same; phase transitions and mean field theories,” *Journal of Statistical Physics*, vol. 137, no. 5, pp. 777–797, 2009. 44

[100] P. Weiss, “L’Hypothèse du Champ Moléculaire et la Propriété Ferromagnétique,” *Journal de Physique Théorique et Appliquée*, vol. 6, no. 1, pp. 661–690, 1907. 44, 122

[101] M. Abramowitz and I. A. Stegun, *Handbook of Mathematical Functions*. National Bureau of Standards, Applied Mathematics Series, 1972. 45, 51, 122, 128, 158, 160, 176, 196, 207

[102] R. Peierls, “On Ising’s model of ferromagnetism,” *Mathematical Proceedings of the Cambridge Philosophical Society*, vol. 32, no. 3, pp. 477–481, 1936. 54, 59

[103] C. Rulquin, P. Urbani, G. Biroli, G. Tarjus, and M. Tarzia, “Nonperturbative fluctuations and metastability in a simple model: From observables to microscopic theory and back,” *Journal of Statistical Mechanics: Theory and Experiment*, vol. 2016, no. 2, p. 023209, 2016. 54, 106

[104] C. N. Yang, "The spontaneous magnetization of a two-dimensional Ising model," *Physical Review*, vol. 85, no. 5, pp. 808–816, 1952. 54

[105] R. J. Baxter, *Exactly solved models in statistical mechanics*. Academic Press, 1982. 54, 85, 86

[106] A. L. Talapov and H. W. J. Blöte, "The magnetization for the 3D Ising model," *J. Phys. A: Math. Gen.*, vol. 29, pp. 5727–5733, 1996. 54

[107] M. Campostrini, A. Pelissetto, P. Rossi, and E. Vicari, "25th-order high-temperature expansion results for three-dimensional Ising-like systems on the simple-cubic lattice," *Physical Review E - Statistical Physics, Plasmas, Fluids, and Related Interdisciplinary Topics*, vol. 65, no. 6, p. 066127, 2002. 54

[108] H. W. Blöte and R. H. Swendsen, "Critical behavior of the four-dimensional Ising model," *Physical Review B*, vol. 22, no. 9, pp. 4481–4483, 1980. 54

[109] N. Aktekin, "Simulation of the three-dimensional ising model on the creutz cellular automaton," *Physica A: Statistical Mechanics and its Applications*, vol. 219, no. 3-4, pp. 436–446, 1995. 54

[110] J. Cardy, *Scaling and Renormalization in Statistical Physics*. Cambridge University Press, 1996. 55

[111] D. P. Landau and K. Binder, *A Guide to Monte Carlo Simulations in Statistical Physics, Second Edition*. Cambridge University Press, 2005. 55

[112] G. A. Canova, Y. Levin, and J. J. Arenzon, "Kosterlitz-Thouless and Potts transitions in a generalized XY model," *Physical Review E*, vol. 89, no. 1, p. 012126, 2014. 56, 66

[113] D. R. Nelson and R. A. Pelcovits, "Momentum-shell recursion relations, anisotropic spins, and liquid crystals in $2+\epsilon$ dimensions," *Physical Review B*, vol. 16, no. 5, p. 2191, 1977. 58, 102, 107

[114] L. F. Cugliandolo and G. Gonnella, "Phases of active matter in two dimensions," in *Lecture Notes of the Les Houches Summer School – Active Matter And Non-Equilibrium Statistical Physics*, 2018. 58, 68, 70

[115] J. P. Sethna, *Entropy, Order Parameters, and Complexity*. Oxford University Press, 2017. 58, 70

[116] P. Archambault, S. T. Bramwell, and P. C. W. Holdsworth, "Magnetic Fluctuations in a finite two-dimensional XY model," *Journal of Physics A: Mathematical and General*, vol. 30, p. 8363, 1997. 60, 61, 62, 64, 65, 66, 101, 104, 106, 148, 152

[117] V. L. Pokrovsky and G. V. Uimin, "Magnetic Properties of Two-Dimensional and Layered Systems," *Physics Letters A*, vol. 45, no. 6, pp. 467–468, 1973. 63

[118] P. C. W. Holdsworth and S. T. Bramwell, "Magnetization: A characteristic of the Kosterlitz-Thouless-Berezinskii transition," *Physical Review B*, vol. 49, no. 13, pp. 8811–8814, 1994. 63, 102

[119] G. M. Wysin, A. R. Pereira, I. A. Marques, S. A. Leonel, and P. Z. Coura, "Extinction of the Berezinskii-Kosterlitz-Thouless phase transition by nonmagnetic disorder in planar symmetry spin models," *Physical Review B - Condensed Matter and Materials Physics*, vol. 72, no. 9, p. 094418, 2005. 63, 98, 108

[120] D. R. Nelson and B. I. Halperin, "Dislocation-mediated melting in two dimensions," *Physical Review B*, vol. 19, no. 5, pp. 2457–2484, 1979. 68

[121] A. P. Young, "Melting and Vector Coulomb Gas in Two Dimensions," *Physical Review B*, vol. 19, no. 4, p. 1855, 1979. 68

[122] G. Aeppli and R. Bruinsma, "Hexatic order and liquid density fluctuations," *Physical Review Letters*, vol. 53, no. 22, pp. 2133–2136, 1984. 69, 174

[123] U. Gasser, C. Eisenmann, G. Maret, and P. Keim, "Melting of crystals in two dimensions," *ChemPhysChem*, vol. 11, no. 5, pp. 963–970, 2010. 70

[124] E. P. Bernard and W. Krauth, "Two-Step Melting in Two Dimensions: First-Order Liquid-Hexatic Transition," *Physical Review Letters*, vol. 107, p. 155704, oct 2011. 70, 106

[125] M. Engel, J. A. Anderson, S. C. Glotzer, M. Isobe, E. P. Bernard, and W. Krauth, "Hard-disk equation of state: First-order liquid-hexatic transition in two dimensions with three simulation methods," *Physical Review E - Statistical, Nonlinear, and Soft Matter Physics*, vol. 87, p. 042134, 2013.

[126] S. C. Kapfer and W. Krauth, "Two-Dimensional Melting: From Liquid-Hexatic Coexistence to Continuous Transitions," *Physical Review Letters*, vol. 114, no. 3, p. 035702, 2015. 70

[127] A. L. Thorneywork, J. L. Abbott, D. G. Aarts, and R. P. Dullens, "Two-Dimensional Melting of Colloidal Hard Spheres," *Physical Review Letters*, vol. 118, p. 158001, 2017. 70

[128] P. Gallo, D. Corradini, and M. Rovere, "Widom line and dynamical crossovers as routes to understand supercritical water," *Nature Communications*, vol. 5, p. 5806, 2014. 70, 128

[129] A. P. Solon and J. Tailleur, "Revisiting the Flocking Transition Using Active Spins," *Phys. Rev. Lett.*, vol. 111, no. 7, p. 78101, 2013. 71

[130] F. Reif, *Fundamentals of statistical and thermal physics*. McGraw-Hill series in fundamentals of physics, 1965. 71, 90

[131] L. Peliti, *Statistical Mechanics in a Nutshell*. Princeton University Press, 2003.

[132] J. E. Mayer and M. Goeppert-Mayer, *Statistical Mechanics*. New York: John Wiley & Sons, 1st ed., 1940. 71, 72, 75, 76, 77

[133] P. C. Hemmer, "Virial Coefficients for the Hard-Core Gas in Two Dimensions," *The Journal of Chemical Physics*, vol. 42, no. 3, p. 1116, 1965. 77, 128, 196, 199

[134] F. H. Ree and W. G. Hoover, "Fifth and Sixth Virial Coefficients for Hard Spheres and Hard Disks," *The Journal of Chemical Physics*, vol. 40, no. 4, p. 939, 1964.

[135] E. J. Janse and V. Rensburgt, "Virial coefficients for hard discs and hard spheres," *J. Phys. A: Math. Gen. Gen*, vol. 26, no. 26, pp. 4805–4818, 1993.

[136] N. Clisby and B. M. McCoy, "Ninth and tenth order virial coefficients for hard spheres in D dimensions," *Journal of Statistical Physics*, vol. 122, no. 1, pp. 15–57, 2006. 77

[137] J. C. Maxwell, "On the Dynamical Evidence of the Molecular Constitution of Bodies," *Nature*, vol. 11, pp. 357–359, 1875. 79

[138] J. K. Percus and G. J. Yevick, "Analysis of Classical Statistical Mechanics by Means of Collective Coordinates," *Physical Review*, vol. 110, no. 1, pp. 1–13, 1958. 80, 83

[139] L. S. Ornstein and F. Zernike, "Accidental deviations of density and opalescence at the critical point of a single substance," *Proc. Akad. Sci.(Amsterdam)*, vol. XVII, no. September, pp. 793–806, 1914. 82

[140] E. Thiele, "Equation of state for hard spheres," *The Journal of Chemical Physics*, vol. 39, no. 2, p. 474, 1963. 84

[141] M. S. Wertheim, "Exact solution of the percus-yevick integral equation for hard spheres," *Physical Review Letters*, vol. 10, no. 8, pp. 321–323, 1963.

[142] M. S. Wertheim, "Analytic Solutions of the Percus-Yevick Equation," *Journal of Mathematical Physics*, vol. 5, p. 643, 1964. 84

[143] N. F. Carnahan and K. E. Starling, "Equation of state for non-attracting spheres," *J. Chem. Phys*, vol. 51, pp. 635–636, 1969. 84

[144] M. S. Ripoll and C. F. Tejero, "Approximate analytical expression for the direct correlation function of hard discs within the Percus-Yevick equation," *Molecular Physics*, vol. 85, no. 2, pp. 423–428, 1995. 84, 123

[145] H. A. Bethe, "Statistical Theory of Superlattices," *Proceedings of the Royal Society of London A*, vol. 150, pp. 552–558, 1935. 85

[146] R. Peierls, "Statistical Theory of Superlattices with Unequal Concentrations of the Components," *Proceedings of the Royal Society of London A*, vol. 154, no. 881, pp. 207–222, 1936. 85

[147] P. R. Weiss, "The Application of the Bethe-Peierls Method to Ferromagnetism," *Physical Review*, vol. 74, no. 10, pp. 1493–1504, 1948. 85

[148] M. Mézard and M. A. Virasoro, "The microstructure of ultrametricity," *Journal de Physique*, vol. 46, no. 8, pp. 1293–1307, 1985. 85

[149] M. Mézard, G. Parisi, and M. A. Virasoro, "SK Model : The Replica Solution without Replicas," *Europhysics Letters*, vol. 1, no. 2, pp. 77–82, 1986. 85

[150] L. Zdeborová and F. Krzakala, "Phase transitions in the coloring of random graphs," *Physical Review E - Statistical, Nonlinear, and Soft Matter Physics*, vol. 76, no. 3, p. 031131, 2007. 85, 120

[151] O. Rivoire, G. Biroli, O. C. Martin, and M. Mézard, "Glass models on bethe lattices," *European Physical Journal B*, vol. 37, no. 1, pp. 55–78, 2004. 85, 86, 87, 89

[152] M. Tarzia, "On the absence of the glass transition in two dimensional hard disks," *Journal of Statistical Mechanics: Theory and Experiment*, vol. 2007, no. 1, p. P01010, 2007. 89, 119, 120

[153] F. Krzakala, M. Tarzia, and L. Zdeborová, "Lattice model for colloidal gels and glasses," *Physical Review Letters*, vol. 101, no. 16, p. 165702, 2008. 85, 119, 120

[154] N. Wormald, "Models of random regular graphs," *London Mathematical Society Lecture Note Series*, pp. 239–298, 1999. 86

[155] P. Erdős and A. Rényi, "On the evolution of random graphs," *Publications of the Mathematical Institute of the Hungarian Academy of Sciences*, vol. 5, pp. 17–61, 1960. 86

[156] M. Mézard and G. Parisi, "The Bethe lattice spin glass revisited," *Eur. Phys. J. B*, vol. 20, pp. 217–233, 2001. 87

[157] B. Mantisi and M. Micoulaut, "Premelting and cation mobility in simple silicates: Contrasting the dynamics in the crystalline and molten state," *Journal of Non-Crystalline Solids*, vol. 440, pp. 1–6, 2016. 91

[158] W. van Megen, T. C. Mortensen, S. R. Williams, and J. Müller, "Measurement of the self-intermediate scattering function of suspensions of hard spherical particles near the glass transition," *Physical Review E - Statistical Physics, Plasmas, Fluids, and Related Interdisciplinary Topics*, vol. 58, no. 5, pp. 6073–6085, 1998. 91

[159] F. Sausset, G. Biroli, and J. Kurchan, "Do Solids Flow?," *Journal of Statistical Physics*, vol. 140, no. 4, pp. 718–727, 2010. 91

[160] N. D. Mermin, "Crystalline Order in Two Dimensions," *Physical Review*, vol. 176, no. 1, pp. 250–254, 1968. 91

[161] M. J. Sánchez-Miranda, B. Bonilla-Capilla, E. Sarmiento-Gómez, E. Lázaro-Lázaro, A. Ramírez-Saito, M. Medina-Noyola, and J. L. Arauz-Lara, "Transition from diffusive to subdiffusive motion in colloidal liquids," *Soft Matter*, vol. 11, no. 4, pp. 655–658, 2015. 91

[162] V. M. Bedanov, G. V. Gadiyak, and Y. E. Lozovik, "On a modified Lindemann-like criterion for 2D melting," *Physics Letters A*, vol. 109A, no. 6, pp. 289–291, 1985. 91

[163] X. H. Zheng and J. C. Earnshaw, "On the Lindemann criterion in 2D," *Europhysics Letters*, vol. 41, no. 6, pp. 635–640, 1998.

[164] K. Zahn and G. Maret, "Dynamic criteria for melting in two dimensions," *Physical Review Letters*, vol. 85, no. 17, pp. 3656–3659, 2000. 91

[165] P. Langevin, "Sur la théorie du mouvement brownien 146 , 530–533 (1908)]," *Comptes-Rendus de l'Académie des Sciences (Paris)*, vol. 146, pp. 530–533, 1908. 91

[166] C. Gardiner, *Handbook of Stochastic Methods*. Berlin: Springer, 1983. 92, 94

[167] A. Einstein, "On the Motion of Small Particles Suspended in a Stationary Liquid, as Required by the Molecular Kinetic Theory of Heat," *Ann. d. Phys.*, vol. 17, pp. 549–560, 1905. 93

[168] M. von Smoluchowski, "On the kinetic theory of Brownian motion and suspensions," *Annalen der Physik*, vol. 326, no. 14, pp. 756–780, 1906. 93

[169] W. Sutherland, "A dynamical theory of diffusion for non-electrolytes and the molecular mass of albumin," *Philosophical Magazine*, vol. 6, no. 9:54, pp. 781–785, 1905. 93

[170] R. G. Winkler, A. Wysocki, and G. Gompper, "Virial pressure in systems of spherical active Brownian particles," *Soft Matter*, vol. 11, no. 33, pp. 6680–6691, 2015. 94, 176

[171] P. K. Ghosh, Y. Li, G. Marchegiani, and F. Marchesoni, "Communication: Memory effects and active Brownian diffusion," *Journal of Chemical Physics*, vol. 143, no. 21, p. 211101, 2015. 95, 176

[172] J. M. Tavares, M. M. Telo Da Gama, P. I. Teixeira, J. J. Weis, and M. J. Nijmeijer, "Phase diagram and critical behavior of the ferromagnetic Heisenberg fluid from density-functional theory," *Physical Review E*, vol. 52, no. 2, pp. 1915—-1929, 1995. 97, 108, 117

[173] E. Lomba, J. J. Weis, and C. F. Tejero, "Liquid-solid transition of the ferromagnetic Heisenberg fluid: Simulation, density functional, and perturbation theories," *Physical Review E*, vol. 58, no. 3, pp. 3426—-3435, 1998. 97, 98, 108, 117

[174] N. B. Wilding, "Continuous demixing at liquid-vapor coexistence in a symmetrical binary fluid mixture," *Physical Review E - Statistical Physics, Plasmas, Fluids, and Related Interdisciplinary Topics*, vol. 67, no. 5, p. 052503, 2003. 97

[175] S. K. Das, J. Horbach, K. Binder, M. E. Fisher, and J. V. Sengers, "Static and dynamic critical behavior of a symmetrical binary fluid: A computer simulation," *Journal of Chemical Physics*, vol. 125, no. 2, p. 024506, 2006.

[176] F. Puosi, D. L. Cardozo, S. Ciliberto, and P. C. Holdsworth, "Direct calculation of the critical Casimir force in a binary fluid," *Physical Review E*, vol. 94, no. 4, p. 040102(R), 2016. 97

[177] I. P. Omelyan, R. Folk, A. Kovalenko, W. Fenz, and I. M. Mryglod, "Liquid-vapor interfaces in XY -spin fluids: An inhomogeneous anisotropic integral-equation approach," *Physical Review E*, vol. 79, no. 1, p. 011123, 2009. 97, 100, 108, 117

[178] J. L. Barrat, J. P. Hansen, G. Pastore, and E. M. Waisman, "Density functional theory of soft sphere freezing," *The Journal of Chemical Physics*, vol. 86, no. 11, pp. 6360–6365, 1987. 98

[179] S. Lepri and S. Ruffo, "Finite-size effects on the Hamiltonian dynamics of the XY-model," *Europhysics Letters*, vol. 55, no. 4, pp. 512–517, 2001. 98

[180] G.-B. Jo, Y.-R. Lee, J.-H. Choi, C. A. Christensen, T. H. Kim, J. H. Thywissen, D. E. Pritchard, and W. Ketterle, "Itinerant Ferromagnetism in a Fermi Gas of Ultracold Atoms," *Science*, vol. 325, no. 5947, pp. 1521–1524, 2009. 98, 135

[181] A. K. Boudalis, G. Rogez, B. Heinrich, R. G. Raptis, and P. Turek, "Towards ionic liquids with tailored magnetic properties: bmim + salts of ferro- and antiferromagnetic CuII3 triangles," *Dalton Transactions*, vol. 46, no. 36, pp. 12263–12273, 2017. 98, 135

[182] E. W. Weisstein, "Circle Packing," *From MathWorld—A Wolfram Web Resource*. 99

[183] J. Tobochnik and G. V. Chester, "Monte Carlo study of the planar spin model," *Physical Review B*, vol. 20, no. 9, pp. 3761–3769, 1979. 101, 104, 106, 140, 148, 152, 174

[184] A. Hanbury, "Constructing cylindrical coordinate colour spaces," *Pattern Recognition Letters*, vol. 29, no. 4, pp. 494–500, 2008. 102

[185] D. J. Amit, Y. Y. Goldschmidt, and G. Grinstein, "Renormalisation group analysis of the phase transition in the 2D Coulomb gas, Sine-Gordon theory and XY-model," *J. Phys. A: Math. Gen.*, vol. 13, no. 2, p. 585, 1980. 102

[186] W. Janke and K. Nather, "Numerical evidence for Kosterlitz-Thouless transition in the 2D XY Villain model," *Physics Letters A*, vol. 157, no. 1, pp. 11–16, 1991. 104

[187] S. K. Baek, P. Minnhagen, and B. J. Kim, "Phase transition of XY model in heptagonal lattice," *Europhysics Letters*, vol. 79, no. 2, p. 26002, 2007. 108

[188] C. Holm, W. Janke, T. Matsui, and K. Sakakibara, "Monte Carlo Study of Asymmetric 2D XY Model," *Physica A*, vol. 246, p. 633, 1997. 108

[189] E. Domany, M. Schick, and R. H. Swendsen, "First-order transition in an xy model with nearest-neighbor interactions," *Physical Review Letters*, vol. 52, no. 17, pp. 1535–1538, 1984. 108

[190] A. C. van Enter and S. B. Shlosman, "First-Order Transitions for n-Vector Models in Two and More Dimensions: Rigorous Proof," *Physical Review Letters*, vol. 89, no. 28, p. 285702, 2002. 108

[191] M. Rovere, D. W. Heermann, and K. Binder, "The gas-liquid transition of the two-dimensional Lennard-Jones fluid," *Journal of Physics of Condensed Matter*, vol. 2, pp. 7009–7032, 1990. 108

[192] B. Widom, "Tricritical Points in Three- and Four-Component Fluid Mixtures," *Journal of Physical Chemistry*, vol. 77, no. 18, pp. 2196–2200, 1973. 108

[193] M. E. Fisher and B. Widom, "Decay of correlations in linear systems," *The Journal of Chemical Physics*, vol. 50, no. 9, pp. 3756–3772, 1969. 111

[194] S. K. Das, S. Roy, and J. Midya, "Coarsening in fluid phase transitions," *Comptes Rendus Physique*, vol. 16, no. 3, pp. 303–315, 2015. 111, 112

[195] A. Onuki, *Phase Transition Dynamics*. Cambridge University Press, 2004. 111, 112

[196] P. Hohenberg and B. Halperin, "Theory of dynamic critical phenomena," *Reviews of Modern Physics*, vol. 49, no. 3, pp. 435–479, 1977. 112

[197] A. J. Bray, "Theory of phase-ordering kinetics," *Advances in Physics*, vol. 43, no. 3, pp. 357–459, 1994. 112

[198] A. J. Bray and K. Humayun, "Growth of order in vector spin systems: scaling and universality," *Journal of Physics A: Mathematical and General*, vol. 23, pp. 5897–5913, 1990. 116

[199] A. J. Bray and J. G. Kissner, "Phase ordering from off-critical quenches and the measurement of the dynamic exponent λ," *Journal of Physics A: Mathematical and General*, vol. 25, no. 1, pp. 31–45, 1992. 116

[200] S. N. Majumdar, D. A. Huse, and B. D. Lubachevsky, "Growth of Long-Range Correlations after a Quench in conserved-Order-Parameter Systems," *Physical Review Letters*, vol. 73, no. 1, p. 182, 1994. 116

[201] M. Blume, "Theory of the First-Order Magnetic Phase Change in UO$_2$," *Physical Review*, vol. 141, no. 2, pp. 517–524, 1966. 117

[202] H. W. Capel, "On the Possibility of First-Order Phase Transitions in Ising Systems of Triplet Ions with Zero-Field Splitting," *Physica*, vol. 32, pp. 966–988, 1966. 117

[203] M. Blume, V. J. Emery, and R. B. Griffiths, "Ising Model for the λ Transition and Phase Separation in He3-He4 Mixtures," *Phys. Rev. A*, vol. 4, no. 3, pp. 1071–1077, 1971. 117, 120

[204] N. B. Wilding and P. Nielaba, "Tricritical universality in a two-dimensional spin fluid," *Physical Review E*, vol. 53, no. 1, pp. 926–934, 1996. 117

[205] M. Pica Ciamarra, M. Tarzia, A. De Candia, and A. Coniglio, "Lattice glass model with no tendency to crystallize," *Physical Review E*, vol. 67, no. 5, p. 057105, 2003. 119

[206] C. Kittel, "Physical theory of ferromagnetic domains," *Reviews of Modern Physics*, vol. 21, no. 4, p. 541, 1949. 122

[207] M. Evans, N. Hastings, and B. Peacock, *Statistical Distributions*. Wiley, 4th ed., 2000. 127

[208] G. Franzese and H. E. Stanley, "The Widom line of supercooled water," *Journal of Physics Condensed Matter*, vol. 19, no. 20, p. 205126, 2007. 128

[209] P. Gallo, K. Amann-Winkel, C. A. Angell, M. A. Anisimov, F. Caupin, C. Chakravarty, E. Lascaris, T. Loerting, A. Z. Panagiotopoulos, J. Russo, J. A. Sellberg, H. E. Stanley, H. Tanaka, C. Vega, L. Xu, and L. G. M. Pettersson, "Water: A Tale of Two Liquids," *Chemical Reviews*, vol. 116, no. 13, pp. 7463–7500, 2016. 133, 135

[210] M. C. Rechtsman, F. H. Stillinger, and S. Torquato, "Negative Thermal Expansion in Single-Component Systems with Isotropic Interactions," *Journal of Physical Chemistry A*, vol. 111, no. 49, pp. 12816–12821, 2007. 133

[211] E. Zaccarelli, F. Sciortino, S. V. Buldyrev, and P. Tartaglia, "Short-ranged attractive colloids: What is the gel state?," in *Unifying Concepts in Granular Media and Glasses* (A. Coniglio, A. Fierro, H. J. Herman, and M. Nicodemi, eds.), pp. 181–194, Amsterdam: Elsevier, 2004. 133

[212] H. Yoshino, "Translational and orientational glass transitions in the large-dimensional limit : a generalized replicated liquid theory and an application to patchy colloids," *Arxiv Preprint*, p. 1807.04095, 2018. 133

[213] R. J. Baxter, "Percus-Yevick equation for hard spheres with surface adhesion," *The Journal of Chemical Physics*, vol. 49, no. 6, pp. 2770–2774, 1968. 133

[214] M. Höfler, *The Berezinskii-Kosterlitz-Thouless transition of mobile Hamiltonian polar particles Masterarbeit*. PhD thesis, 2019. 134

[215] J. W. Cahn, "On spinodal decomposition," *Acta Metallurgica*, vol. 9, no. 9, pp. 795–801, 1961. 135

[216] K. P. O'Keeffe, H. Hong, and S. H. Strogatz, "Oscillators that sync and swarm," *Nature Communications*, vol. 8, p. 1504, 2017. 135

[217] J. Villain, R. Bidaux, J.-P. Carton, and R. Conte, "Order as an effect of disorder," *J. Physique*, vol. 41, pp. 1263–1272, 1980. 139, 149

[218] E. F. Shender and P. C. W. Holdsworth, "Order by Disorder and Topology in Frustrated Magnetic Systems," in *Fluctuations and Order: The New Synthesis* (M. Millonas, ed.), pp. 259–279, New York, NY: Springer US, 1996. 139, 149

[219] D. S. Dean, "Langevin equation for the density of a system of interacting Langevin processes," *Journal of Physics A: Mathematical and General*, vol. 29, pp. L613–L617, dec 1996. 142

[220] A. Barone, F. Esposito, C. J. Magee, and A. C. Scott, "Theory and applications of the sine-gordon equation," *La Rivista del Nuovo Cimento (1971-1977)*, vol. 1, no. 2, pp. 227–267, 1971. 143

[221] M. E. Gouvea, F. G. Mertens, A. R. Bishop, and G. M. Wysin, "The classical two-dimensional XY model with in-plane magnetic field," *Journal of Physics: Condensed Matter*, vol. 2, pp. 1853–1868, 1990. 143, 145

[222] B. A. Malomed, "Dynamics of quasi-one-dimensional kinks in the two-dimensional sine-Gordon model," *Physica D: Nonlinear Phenomena*, vol. 52, no. 2-3, pp. 157–170, 1991. 143

[223] A. G. Shagalov, "Singular solutions of the elliptic \text{Sine-Gordon} equation: models of defects," *Physics Letters A*, vol. 165, no. 5, pp. 412–416, 1992. 143

[224] V. E. Sinitsyn, I. G. Bostrem, and A. S. Ovchinnikov, "Numerical study of spirals in a two-dimensional \text{XY} model with in-plane magnetic field," *Journal of Physics: Condensed Matter*, vol. 16, no. 20, p. 3445, 2004. 143

[225] P. C. Guruciaga, M. Tarzia, M. V. Ferreyra, L. F. Cugliandolo, S. A. Grigera, and R. A. Borzi, "Field-Tuned Order by Disorder in Frustrated Ising Magnets with Antiferromagnetic Interactions," *Physical Review Letters*, vol. 117, no. 16, p. 167203, 2016. 149

[226] K. K. Rao and P. R. Nott, *An Introduction to Granular Flow*. Cambridge University Press, 2008. 156

[227] H. C. Berg and E. M. Purcell, "Physics of chemoreception," *Biophysical Journal*, vol. 20, no. 2, pp. 193–219, 1977. 156

[228] F. Sausset and G. Tarjus, "Periodic boundary conditions on the pseudosphere," *Journal of Physics A: Mathematical and Theoretical*, vol. 40, no. 43, pp. 12873–12899, 2007. 161

[229] M. Z. Hasan and C. L. Kane, "Colloquium: Topological insulators," *Reviews of Modern Physics*, vol. 82, no. 4, pp. 3045–3067, 2010. 166

[230] B. Loewe, A. Souslov, and P. M. Goldbart, "Flocking from a quantum analogy: Spin-orbit coupling in an active fluid," *New Journal of Physics*, vol. 20, p. 013020, 2018. 166, 187

[231] P. J. Ackerman and I. I. Smalyukh, "Diversity of knot solitons in liquid crystals manifested by linking of preimages in torons and hopfions," *Physical Review X*, vol. 7, no. 1, p. 011006, 2017. 166

[232] S. J. DeCamp, G. S. Redner, A. Baskaran, M. F. Hagan, and Z. Dogic, "Orientational order of motile defects in active nematics," *Nature Materials*, vol. 14, no. 11, pp. 1110–1115, 2015. 166, 190

[233] E. Putzig, G. S. Redner, A. Baskaran, and A. Baskaran, "Instabilities, defects, and defect ordering in an overdamped active nematic," *Soft Matter*, vol. 12, no. 17, pp. 3854–3859, 2016. 190

[234] A. Patelli, I. Djafer-Cherif, I. S. Aranson, E. Bertin, and H. Chaté, "Understanding dense active nematics from microscopic models," *Arxiv Preprint*, 2019. 166

[235] A. Cavagna, A. Cimarelli, I. Giardina, A. Orlandi, G. Parisi, A. Procaccini, R. Santagati, and F. Stefanini, "New statistical tools for analyzing the structure of animal groups," *Mathematical Biosciences*, vol. 214, no. 1-2, pp. 32–37, 2008. 167, 184

[236] A. Cavagna, I. Giardina, and M. Viale, "Comment on "Velocity and Speed Correlations in Hamiltonian Flocks" by M. Casiulis et al. [arXiv:1911.06042]," *Arxiv Preprint*, p. 1912.07056v1, 2019. 168

[237] M. Casiulis, M. Tarzia, L. F. Cugliandolo, and O. Dauchot, "Reply to "Comment on "Velocity and Speed Correlations in Hamiltonian Flocks""," *Arxiv Preprint*, vol. 1911.06042, 2019. 168

[238] F. Peruani and L. G. Morelli, "Self-propelled particles with fluctuating speed and direction of motion in two dimensions," *Physical Review Letters*, vol. 99, no. 1, pp. 1–4, 2007. 173

[239] C. Chen, S. Liu, X. Q. Shi, H. Chaté, and Y. Wu, "Weak synchronization and large-scale collective oscillation in dense bacterial suspensions," *Nature*, vol. 542, no. 7640, pp. 210–214, 2017. 176

[240] E. Borel, "Mémoire sur les séries divergentes," *Annales Scientifiques de l'E.N.S.*, vol. 3, no. 16, pp. 9–131, 1899. 176

[241] T. W. Burkhardt, "The random acceleration process in bounded geometries," *Journal of Statistical Mechanics: Theory and Experiment*, no. 7, p. P07004, 2007. 177

[242] W. T. Kranz and R. Golestanian, "Trail-mediated self-interaction," *The Journal of Chemical Physics*, vol. 150, no. 21, p. 214111, 2019. 177, 190

[243] K. Copenhagen, G. Scita, N. Gov, W. Yu, A. Gopinathan, and G. Malet-Engra, "Frustration-induced phases in migrating cell clusters," *Science Advances*, vol. 4, no. 9, p. eaar8483, 2018. 179, 183

[244] I. Petrelli, P. Digregorio, L. F. Cugliandolo, G. Gonnella, and A. Suma, "Active dumbbells: dynamics and morphology in the coexisting region," *European Physical Journal E*, vol. 41, p. 128, 2018. 179, 183

[245] A. Cavagna, I. Giardina, T. S. Grigera, A. Jelic, D. Levine, S. Ramaswamy, and M. Viale, "Silent flocks: Constraints on signal propagation across biological groups," *Physical Review Letters*, vol. 114, no. 21, p. 218101, 2015. 181

[246] L. D. Landau and E. M. Lifshitz, *Course of Theoretical Physics Vol. 7: Theory of Elasticity*. Pergamon Press, 3rd ed., 1986. 183

[247] S. Henkes, Y. Fily, and M. C. Marchetti, "Active jamming: Self-propelled soft particles at high density," *Physical Review E - Statistical, Nonlinear, and Soft Matter Physics*, vol. 84, no. 4, p. 040301(R), 2011. 183

[248] C. Ruscher, J. Baschnagel, and J. Farago, "The Voronoi Liquid," *Europhysics Letters*, vol. 112, no. 6, p. 66003, 2015. 184

[249] C. Ruscher, J. Baschnagel, and J. Farago, "Voronoi glass-forming liquids: A structural study," *Physical Review E*, vol. 97, no. 3, p. 032132, 2018. 184

[250] J. Toner and Y. Tu, "Long-range order in a two-dimensional dynamical XY model: How birds fly together," *Physical Review Letters*, vol. 75, no. 23, pp. 4326–4329, 1995. 187, 188, 226

[251] J. Toner and Y. Tu, "Flocks, herds, and schools: A quantitative theory of flocking," *Physical Review E*, vol. 58, no. 4, p. 4828, 1998.

[252] Y. Tu, J. Toner, and M. Ulm, "Sound waves and the absence of galilean invariance in flocks," *Physical Review Letters*, vol. 80, no. 21, pp. 4819–4822, 1998. 188

[253] A. P. Solon, Y. Fily, A. Baskaran, M. E. Cates, Y. Kafri, M. Kardar, and J. Tailleur, "Pressure is not a state function for generic active fluids," *Nature Physics*, vol. 11, no. 8, pp. 673–678, 2015. 189

[254] N. Nikola, A. P. Solon, Y. Kafri, M. Kardar, J. Tailleur, and R. Voituriez, "Active Particles with Soft and Curved Walls: Equation of State, Ratchets, and Instabilities," *Physical Review Letters*, vol. 117, no. 9, p. 098001, 2016.

[255] Y. Ben Dor, Y. Kafri, and J. Tailleur, "Forces in dry active matter," in *Lecture Notes of the Les Houches Summer School – Active Matter And Non-Equilibrium Statistical Physics*, 2018. 189

[256] M. M. Genkin, A. Sokolov, O. D. Lavrentovich, and I. S. Aranson, "Topological defects in a living nematic ensnare swimming bacteria," *Physical Review X*, vol. 7, no. 1, p. 011029, 2017. 189

[257] I. Gel'Fand and G. Shilov, *Generalized Functions, Vol. 1.* Academic Press, 1968. 202

[258] L. D. Landau and E. Lifshitz, *Course of Theorectical Physics Vol.10: Physical Kinetics.* Pergamon Press, 1981. 209, 220, 224

[259] T. Hanke, C. A. Weber, and E. Frey, "Understanding Collective Dynamics of Soft Active Colloids by Binary Scattering," *Physical Review E*, vol. 88, p. 052309, 2013. 218

Mathias Casiulis **21 novembre 2019**

Sujet : Etude d'un modèle Hamiltonien de liquide non-Galiléen : du mouvement collectif sans activité

Résumé : Le mouvement collectif, l'ordre spontané des vitesses dans un système macroscopique, est une propriété marquante des systèmes vivants tels que les vols d'oiseaux. Il est prédit par des modèles de particules auto-propulsées, qui sont actives : elles ne conservent ni énergie, ni impulsion. Dans ma thèse, j'étudie un modèle conservatif de mouvement collectif, composé de particules portant des spins couplés à leur vitesse, en m'aidant de notions de physique des liquides, de magnétisme, et de mécanique statistique. Je montre que l'alignement des spins génère une attraction effective, qui est responsable d'une séparation de phase entre un gaz isotrope et un ferroliquide se terminant en un point triple, d'où émerge la ligne de Curie. Je dresse ensuite le diagramme des phases du modèle en présence d'un couplage spin-vitesse, en faisant varier son intensité, le nombre de particules, la densité, et la température. La conservation de l'impulsion impose que les phases polaire soient en mouvement collectif. A basse température et basse densité, je montre que le système peut créer spontanément des défauts d'alignement pour ne pas avoir à se mouvoir et ainsi échapper à un coût élevé en énergie cinétique. Je montre que le système peut transiter d'un état apolaire vers un état polaire lorsque la température augmente, trahissant un phénomène d'ordre par le désordre. Enfin, je montre que le mouvement du système est bien décrit par un modèle effectif de particules auto-propulsées avec de l'inertie de rotation, qui augmente fortement à la transition de rigidité. A haute inertie, le système présente des virages et des rotations spontanées dus à la conservation du moment cinétique.

Mots clés : Mouvement Collectif, Matière Active, Systèmes Hamiltoniens, Magnétisme de Spins, Défauts Topologiques, Ordre par le Désordre

Subject : Study of a non-Galilean Hamiltonian liquid: collective motion without activity

Abstract: Collective motion, the spontaneous ordering of the velocities across a macroscopic system, is a hallmark of living systems like flocks of birds. It is captured by models of self-propelled particles, that are usually active: they do not conserve energy nor momentum. In my thesis, using notions from the theory of liquids, magnetism, and statistical mechanics, I study a conservative model of collective motion, composed of particles that carry spins, which are coupled to their velocities. I show that the alignment of spins creates an effective attraction, that is responsible for a phase separation between an isotropic gas and a ferroliquid. This phase separation ends in a tricritical point, from which stems the Curie line. I then establish the full phase diagram of the model with a spin-velocity coupling, varying its amplitude, the number of particles, the density, and the temperature. The conservation of momentum imposes that all polar phases move collectively. At low temperatures and densities, I show that the system spontaneously generates alignment defects so as to stop moving, and thus escapes a high kinetic energy cost. I also show that the system can go from an apolar state to a polar one as the temperature increases, betraying an order-by-disorder phenomenon. Finally, I show that the dynamics of the system is well described by an effective model of self-propelled particles, with a rotational inertia that soars at the rigidity transition. At high inertia, the system moves with spontaneous turns and rotations caused by the conservation of angular momentum.

Keywords : Collective Motion, Active Matter, Hamiltonian Systems, Spin Magnetism, Topological Defects, Order by Disorder